



Bangkok, THAILAND



The 20th Asian Chemical Congress (ASIACHEM 2025)

Proceedings

ISBN (E-book) 978-616-93355-1-1

1st Edition November 2025 (PDF only)

(available from https://acc2025thailand.com)

Published by The Chemical Society of Thailand under the Patronage of

Professor Dr. Her Royal Highness Princess Chulabhorn Krom

Phra Srisavangavadhana

Editorial Information

Editor-in-chief: Tirayut Vilaivan Editorial Assistant: Pornpan Pungpo Editorial Assistant: Supakorn Boonyuen Editorial Board: see committees pages

Disclaimer

The contents of this proceedings book are provided for informational purposes only. The conference volunteers serving as chairs, co-chairs, reviewers, committee members, as well as the editor and typesetter, have diligently adhered to academic, ethical, and legal standards to ensure accuracy and quality. Nevertheless, the information presented may still contain errors or omissions. Any missing or incorrect information should be addressed to the organizer at:

acc2025thailand@gmail.com



WELCOME MESSAGES





Prof. Dr. Supa Hannongbua

Chairperson of the 20th Asian Chemical Congress (20ACC) or ASIACHEM2025

Message from the Chairperson of the 20th Asian Chemical Congress

On behalf of the organizing committee, I am delighted to welcome you all to the 20th Asian Chemical Congress (20ACC) or ASIACHEM2025, taking place from June 22nd to 26th, 2025, at the Berkeley Hotel Pratunam in the heart of Bangkok, Thailand.

For nearly four decades, the Asian Chemical Congress has served as a significant international platform in the field of chemistry, bringing together researchers and scientists from across Asia and around the world. It offers a valuable opportunity to present the latest research, exchange ideas, explore new scientific directions, and foster collaborations in both pure and applied chemistry. The Chemical Society of Thailand jointly organizes the 20th Asian Chemical Congress (ACC) under the Patronage of Her Royal Highness Princess Chulabhorn Krom Phra Srisavangavadhana and under the auspices of the Federation of Asian Chemical Societies (FACS). We are also profoundly grateful for the generous support of various local and international organizations whose contributions have been instrumental in making this congress possible.

The 20ACC stands out for its emphasis on the theme "Responsible Chemical Sciences for World Sustainability," underscoring its greater significance in today's context. This congress is particularly well-aligned with the evolving role of chemistry and the chemical sciences in addressing pressing global challenges related to the environment, health, and energy. The congress brings together almost nine hundred participants from both Thailand and abroad, representing 45 countries. Among the distinguished speakers are seven plenary lecturers, including Nobel Laureate in Chemistry (2004) Prof. Dr. Aaron Ciechanover, IUPAC President Prof. Dr. Ehud Keinan, and other renowned scientists. Additionally, approximately 200 invited speakers from 25 countries will share their expertise. The latest advancements in chemical research, development, and education will be showcased across 11 regular sessions, 15 specialized symposia, and two side events designed to inspire and engage the younger generation with a passion for science. The program highlights progress in both pure and applied chemistry, emphasizing their contributions to technological innovation. Moreover, the congress will feature three poster presentation sessions and a comprehensive exhibition on chemicals and scientific instrumentation.

Organizing an event of this scale would not have been possible without the dedication and outstanding teamwork of many individuals who contributed generously in various capacities. I sincerely hope that the presentations and discussions held during the congress will foster continued academic advancement and promote deeper research collaboration both within the region and globally. Notably, the congress also provided scholarships and valuable opportunities for young chemists and scientists to engage with leading experts in their respective fields, encouraging the exchange of knowledge and the passing of research experience from one generation to the next. Aside from the congress, you will have the chance to experience a myriad of Thailand's exceptional and exotic tourist and cultural attractions. You will find the congress both valuable and enjoyable.

Last but not least, I am confident that, with your active participation and valuable contributions, the 20th Asian Chemical Congress will be among the most successful in its history. I sincerely wish you a memorable and rewarding experience during your stay in Bangkok.

With warmest regards,

Prof. Dr. Supa Hannongbua

Chairperson of the 20th Asian Chemical Congress (20ACC) or ASIACHEM2025



WELCOME MESSAGES





Prof. Dr. Vudhichai Parasuk

President of Chemical Society of Thailand

Message from the President of the Chemical Society of Thailand

It is my great pleasure to welcome you to the 20th Asian Chemical Congress (20ACC) and to host the 22nd FACS General Assembly, which takes place from June 22 to 26, 2025, at The Berkeley Hotel Pratunam in the vibrant city of Bangkok, Thailand. This prestigious biennial event brings together chemists and researchers from across Asia and around the world to share their latest discoveries and innovations.

As President of the Chemical Society of Thailand, the proud host of this year's congress, I am honored to welcome you to what promises to be an inspiring and intellectually enriching event. The 20ACC serves as a premier platform for presenting groundbreaking research, fostering international collaborations, and cultivating lasting professional networks across all areas of chemistry.

In addition to the academic exchange, Bangkok offers a remarkable experience with its rich cultural heritage, renowned hospitality, and an array of leisure and culinary delights. We encourage you to take some time to explore and enjoy all that this dynamic city has to offer.

I wish you productive discussions, meaningful connections, and a memorable experience both at the congress and throughout your stay in Thailand.

With warmest regards,

Professor Dr. Vudhichai Parasuk

President of the Chemical Society of Thailand





INTERNATIONAL ADVISORY COMMITTEE

Supawan Tantayanont Chulalongkorn University, Thailand (Chair)
David Winkler Royal Australian Chemical Institute, Australia

Dien Pandaman Pidilite Innovation Center, Singapore

Edward Juan Joon Ching University Malaya, Malaysia

Ehud Keinan International Union of Pure & Applied Chemistry &

Technion - Israel Institute of Technology, Israel

Hamdan Mohammad Alajmi Kuwait Chemical Society, Kuwait

Jumras Limtrakul Vidyasirimedhi Institute of Science and Technology,

Thailand

Mary Garson The University of Queensland, Australia

Minoru Isobe Chemical Society of Japan/Nagoya University, Japan Mustafa Culha Sabanci University Nanotechnology Research and

Application Center, Türkiye

Onder Metin Koç University, Türkiye

Reuben Jih-Ru Hwu National Tsing Hua University, Taiwan

Seokmin Shin Korean Chemical Society/Seoul National University,

Korea

Surin Laosooksathit Nanotechnology Society of Thailand, Thailand

Thanuttkhul Science Society of Thailand, Thailand

Mongkolaussavarat

Ting Kueh Soon Institut Kimia Malaysia, Malaysia Uday Maitra Indian Institute of Science, India

Wai-yeung Wong The Hong Kong Polytechnic University, Hong Kong

Xiaoguang Lei Peking University, China

LOCAL ORGANIZING COMMITTEE

Vudhichai Parasuk President of Chemical Society Advisor

of Thailand

Supa Hannongbua Kasetsart University Conference Chair Supakorn Boonyuen Thammasat University General Secretary Sutasinee Kityakarn Kasetsart University General Secretary Duangruthai Sridaeng Rangsit University Assistant Secretary

General

Singto Sakulkhaemaruethai Rajamangala University of Assistant Secretary

Technology Thanyaburi General

Pornpan Pungpo Ubon Ratchathani University Assistant Secretary

General

Tirayut Vilaivan Chulalongkorn University Scientific Program

Waraporn Parasuk Kasetsart University, Thailand Registration





LOCAL ORGANIZING COMMITTEE

Boonnak Sukhummek	King Mongkut's University of Technology North Bangkok	Treasurer
Narumol Kreua-ongarjnukool	King Mongkut's University of Technology North Bangkok	Protocol & Social Event
Thitinun Karpkird	Kasetsart University	Protocol & Social
		Event
Chanat Aonbangkhen	Chulalongkorn University	Facility Management
Peera Atcharasathian	Thammasat University	Facility Management
Singto Sakulkhaemaruethai	Rajamangala University of Technology Thanyaburi	Public Relations
Suchada Chantrapromma	Prince of Songkla University	Public Relations
Sutasinee Kityakarn	Kasetsart University	Exhibition
Songwut Suramitr	Kasetsart University	Exhibition
Supakit Achiwawanich	Kasetsart University	Audio and
•	•	Visualization
Pipat Khongpracha	Kasetsart University	Audio and
	•	Visualization
Patraporn Luksirikul	Kasetsart University	Audio and
		Visualization
Ramida Rattanakam	Kasetsart University	Audio and
		Visualization
Duangjai Nakapreecha	Mahidol University	Sponsor
Ekasith Somsook	Mahidol University	CST committee
Monthip Sriratana Tabucanon	Digital Belt and Road Program	CST committee
Phoosak Hirunyatrakul	MD Bara Scientific Co., Ltd.	CST committee
Siwaporn Meejoo Smith	Mahidol University	CST committee
Kanit Tapasa	Department of Science Service	CST committee
Rungnapa Kohkaew	Chemical Society of Thailand	CST committee
Purim Jarujamrus	Ubon Ratchathani University	CST committee

SCIENTIFIC COMMITTEE

Tirayut Vilaivan	Chulalongkorn University, Thailand (Chair)
Alvin Lim	University Putra Malaysia Kampus Bintulu Sarawak,
	Malaysia
Amornpon Changsuphan	Department of Science Service, Thailand
Auradee Punkvang	Nakorn Panom University
Boodsarin Sawatlon	Chulalongkorn University, Thailand
Boonyaras Sookkheo	Rangsit University, Thailand
Braja Gopal Bag	Vidyasagar University, India





SCIENTIFIC COMMITTEE

Bunjerd Jongsomjit Chulalongkorn University, Thailand
Bussaba Pinchaipat Kasetsart University, Thailand
Chana Panyanon Rangsit University, Thailand
Chanatip Samart Thammasat University, Thailand
Chiravoot Pechyen Thammasat University, Thailand
Chongrak Polprasert Thammasat University, Thailand

Chularat Wattanakit Vidyasirimedhi Institute of Science and Technology,

Thailand

Dinesh Talwar Asian Chemical Editorial Society (ACES), Germany

Dinusha Udukala Institute of Chemistry Ceylon, Sri Lanka Dong-Myeong Shin University of Hong Kong, Hong Kong

Duangkamol Gleeson King Mongkut's Institute of Technology Ladkrabang,

Thailand

Duangruthai Sridaeng Rangsit University, Thailand Ekasith Somsook Mahidol University, Thailand

Hongyi Gao University of Science and Technology Beijing, China

Itthipon Jeerapan Prince of Songkla University, Thailand

Ittipat Meewan Mahidol University, Thailand

Jan J. Weigand Technische Universität Dresden, Germany

Janitha LiyanageUniversity of Kelaniya, Sri LankaJaroon JakmuneeChiang Mai University, ThailandJeewantha PremarathnaUniversity of Kelaniya, Sri Lanka

Jidapa Sangswan Ubon Ratchathani University, Thailand Iorge Ibanez Ibero American University, Spain

Jorge Ibanez Ibero American University, Spa Juan Joon Ching University of Malaya, Malaysia Jyoti Giri Tribhuvan University, Nepal

Kampanart Chayajarus Ubon Ratchathani University, Thailand

Kampol Poophawatanakij Food Matrix Global Co., Ltd., Thailand Kanet Wongravee Chulalongkorn University, Thailand

Kanit Tapasa Department of Science Service, Thailand

Karthikeyan Sathrugnan Frontier Laboratories, Singapore
Kittipong Chainok Thammasat University, Thailand
Krittiya Khuenpet Thammasat University, Thailand
Kuntawit Witthayolankowit Kasetsart University, Thailand
Luckhana Lawtrakul Thammasat University, Thailand

Malee Prajubsuk Ubon Ratchathani University, Thailand

Manthana Jariyaboon Mahidol University, Thailand





SCIENTIFIC COMMITTEE

Mathew Paul Gleeson King Mongkut's Institute of Technology Ladkrabang,

Thailand

Mathi Kandiah BMS University, Sri Lanka Metta Chareonpanich Kasetsart University, Thailand

Monthip Sriratana Tabucanon Chemical Society of Thailand, Thailand

Namploy Pinyan Rangsit University, Thailand
Nanthawat Wannarit Thammasat University, Thailand
Narisra Komalawardhana Mahidol University, Thailand
Nawee Kungwan Chiang Mai University, Thailand

Nguyen Deinj Trun GT Innovation Company Limited, Vietnam

Nobuto Yoshinari Osaka University, Japan

Nopparat Plucktaveesak Thammasat University, Thailand Ong-art Thanetnit Chulalongkorn University, Thailand

Ornjira Aruksakunwong Rangsit University, Thailand
Panumart Thongyoo Thammasat University, Thailand
Panuwat Padungros Chulalongkorn University, Thailand

Paptawan Thongdee National Science and Technology Development

Agency, Thailand

Paramasivam Shanmugam Thammasat University, Thailand Pariya Na Nakorn Thammasat University, Thailand Patchreenart Saparpakorn Kasetsart University, Thailand Peera Atcharasathian Thammasat University, Thailand

Pinit Kidkhunthod Synchrotron Light Research Institute, Thailand

Pornpan Pungpo Ubon Ratchathani University, Thailand

Pranorm Khaomek Rangsit University, Thailand
Prapasri Theprugsa Thammasat University, Thailand
Priyani Paranagama University of Kelaniya, Sri Lanka
Pumidech Puthongkham Chulalongkorn University, Thailand
Ratanon Chotima Naresuan University, Thailand

Ratchakrich Rangsit University, Thailand

Patthamasopasakul

Reuben Jih-Ru Hwu National Tsing Hua University, Taiwan

Ruwan Perera University of Kelaniya, Sri Lanka Sa-Ad Riyajan Thammasat University, Thailand Saad Riyajan Thammasat University, Thailand

Sagarika Ekanayake University of Sri Jayewardenepura, Sri Lanka

Saisamorn Lumlong Ubon Ratchathani University, Thailand

Seiji Mori Ibaraki University, Japan





SCIENTIFIC COMMITTEE

Shuchen Hsieh National Sun Yat-sen University, Taiwan Siriporn Jungsuttiwong Ubon Ratchathani University, Thailand

Sirirat Kokpol Chulalongkorn University, Thailand

Siwaporn Meejoo Smith Mahidol University & ACS Thailand Chapter, Thailand

Somjintana Taweepanich Ubon Ratchathani University, Thailand Sudkanueng Singto National Nanotechnology Center, Thailand

Sunisa Akkarasamiyo Kasetsart University, Thailand Supacha Wirojsaengthong Chulalongkorn University, Thailand

Supakorn Boonyuen Thammasat University, Thailand
Supareak Praserthdam Chulalongkorn University, Thailand

Supavadee Kiatisevi Mahidol University, Thailand

Supawadee Namuangruk National Science and Technology Development

Agency, Thailand

Suranga Wickramarachchi University of Kelaniya, Sri Lanka Suratsawadee Sukeesan Kasetsart University, Thailand Suwabun Chirachanchai Chulalongkorn University, Thailand Suwadee Kongparakul Thammasat University, Thailand

Tawan Sooknoi King Mongkut's Institute of Technology Ladkrabang,

Thailand

Taweetham Limpanuparb Mahidol University, Thailand

Teeraphan Laomettachit King Mongkut's University of Technology Thonburi,

Thailand

Thelma Abeshinghe The Open University of Sri Lanka, Sri Lanka

Thidarat Imyen Kasetsart University, Thailand Thitinat Sukonket Suan Dusit University, Thailand

Uday Maitra Indian Institute of Science, Bangalore, India

Usa Jeenjenkit Amnuay Silpa School, Thailand

Vatcharin Rukachaisirikul Prince of Songkla University, Thailand

Vinich Promarak Vidyasirimedhi Institute of Science and Technology,

Thailand

Waleeporn Donphai Kasetsart University, Thailand
Wannisa Sukjee Kasetsart University, Thailand
Wantanee Sittiwong Thammasat University, Thailand

Weiliang Zhu Shanghai Institute of Materia Medica, China

Worapong Sangprasert kul Srinakharinwirot University, Thailand Worawan Bhanthumnavin Chulalongkorn University, Thailand

Yasuhiro Funahashi Osaka University, Japan

Yodchai Tangjaideborisut Food Matrix Global Co., Ltd., Thailand





SCIENTIFIC COMMITTEE

Yoichi M. A. Yamada RIKEN, Japan

Yoshito Andou Kyushu Institute of Technology, Japan Yuki Shirosaki Kyushu Institute of Technology, Japan Zhijian Xu Shanghai Institute of Materia Medica, China Zuriati Zakaria Universiti Teknologi Malaysia, Malaysia



TABLE OF CONTENTS



CE: Chemistry for Energy and Environment	
Study on the conversion of residual lithium titanate oxide into lithium ion sieve adsorbents Hsiu-Mei Chiu, Wen-Hua Chen, An-Ya Lo	1-5
FA: Food, Agriculture, and Cosmetics	
Carbohydrate content test of tofu liquid waste as an alternative media for the growth of <i>Streptococcus mutans</i> Ni'matul Murtafiah, Aziz Ansori Wahid, Suci Rizki Nurul Aeni, Fitri Nurhamidah	6-9
FE: Future in Chemical Education	
Implementing LDR to assist disabled students in reaction rate practicum Nurul Cholis	10-13
Implementation SSC (Small Scale Chemistry) in the practical work on making carbon dioxide gas from egg shells to improve student creativity in stoichiometry material <i>Laurensia</i>	14–17
MN: Materials Science and Nanotechnology	
MoSe ₂ -PEDOT nanocomposite for ultrasensitive electrochemical sensing of nitroaromatic compounds <i>Shivam Kashyap, Anjana Sarkar</i>	18-22
OM: Organic Synthesis and Medicinal Chemistry	
Enhanced Biginelli reaction via synergistic action of squaramide and TBAB ionic liquid Pinanong Bunthaisong, Peera Acharasatian	23–26
Synthetic study of benzoquinolizidine alkaloids: Functionalization of the piperidine ring by oxidative addition to the unsaturated lactam Sasipa Booranamonthol, Duangkamon Namborisut, Punlop Kuntiyong	27–30
Total synthesis of piperlongumine and its analogs from L-glutamine <i>Phongsathon Khlongkhlaeo, Punlop Kuntiyong</i>	31-34
PC: Polymers and Bio-based Materials	
Cellular responses of MC3T3-E1 on peptide-functionalized chitosan Chatchai Purananunak, Pichamon Kiatwuthinon, Chantiga Choochottiros, Weeraphat Pon- On, Chomdao Sinthuvanich	35–39
PT: Physical and Theoretical Chemistry	
Computational insights into sulfonamide-modified cannabinoids as selective COX-2 inhibitors: Binding affinity and drug-like properties Watcharin Kumaeum, Panichakorn Jaiyong	40-45
S5: AI in Drug Discovery Research	
Rational design of InhA inhibitors from damnacanthal using molecular docking calculations Thimpika Pornprom, Bongkochawan Phakamwong, Darunee Sukchit, Khemmisara Sawatdee, Masayuki Yuguchi, Nagomi Chimura, Auradee Punkvang, Khomson Suttisintong, Prasat Kittakoop, Noriyuki Kurita, Pornpan Pungpo	46-49
Quantitative structure activity relationship and molecular docking calculations of xanthone derivatives as anti-tuberculosis agents Wannasa Upom, Bongkochawan Phakamwong, Thimpika Pornprom, Darunee Sukchit, Khemmisara Sawatdee, Auradee Punkvang, Khomson Suttisintong, Prasat Kittakoop, Pornpan Pungpo	50-53



TABLE OF CONTENTS



70 - 73

78-81

S5: AI in Drug Discovery Research (cont.)

Investigation of the bioactivities of Caesalpinia pulcherrima (L.) SW wood extracts and 54-57 in silico analysis of stigmasterol as an InhA inhibitor Pritsana Srisaengmueang, Darunee Sukchit, Khemmisara sawatdee, Thimpika Pornprom, Bongkochawan Pakamwong, Paptawan Thongdee, Somjintana Taveepanich, Kampanat Chayajarus, Saisamorn Lumlong, Prajakkit Rawee, Jitlada Dechatiwong, Jidapa Sangswan, Kanjana Pangjit, Auradee Punkvang, Khomson Suttisintong, Prasat Kittakoop, Pornpan Pungpo

S6: Advances in Nutraceutical Chemistry Shaping the Future of Disease Prevention in Asia

Bioactive extraction from bamboo, roselle, and monk fruit for a fiber-rich wellness drink with sustainable packaging Ratchaphong Katerung, Narissara Uthai, Duangrutai Thumrongchote, Supakorn Boonyuen	58-62
Preparation of bioactive ionic liquids for extraction of polyhydroxylated fatty alcohols from avocado (<i>Persea americana</i>) Kristoffer Rem Labing-isa, Sanya Sureram, Chulabhorn Mahidol, Somsak Ruchirawat, Prasat Kittakoop	63-66
Shellfish "Royal Purple" pigment discovered via HPLC on a 2,500-year old marble jar of the Persian King Darius the Great <i>Zvi C. Koren</i>	67-69
S8: Green Chemistry; Paving the Way to a Sustainable Future	

extraction using microwave hydro-distillation Patar Jonathan Sipahutar, Mahfud	
Catalytic ethanol dehydration to ethylene over zeolite A synthesized from sugarcane bagasse ash Darunee Sukchit, Saisamorn Lumlong, Malee Prajuabsuk, Chan Inntam, Supakorn Boonyuen, Duangkamol Gleeson, Auradee Punkvang, Sasijuta Wattanarach, Parjaree Thavorniti, Bunjerd Jongsomjit, Pornpan Pungpo	74–77

Kluai 'Namwa' for antibacterial activity Khemmisara Sawatdee, Pritsana Srisaengmueang, Darunee Sukchit, Bongkochawan Pakamwong, Thimpika Pornprom, Kampanat Chayajarus, Saisamorn Lumlong, Prajakkit Rawee, Jitlada Dechatiwong, Jidapa Sangswan, Auradee Punkvang, Paptawan Thongdee, Khomson Suttisintong, Pornpan Pungpo

Green synthesis of silver nanoparticles using crude extract from peels of *Musa ABB cv.*

Kinetic model comparison and analysis in citronella leaves (*Cymbopogon winterianus*)

IIS: Future Chemistry Research Presentation for Undergraduate Students

03. Future chemistry Research Fresentation for Ondergraduate Students	
Magnetic $CoFe_2O_4/MIL-53/carbon$ aerogel composite for efficient organic dye adsorption in wastewater treatment Kamonphat Narkwan, Paramasivam Shanmugam, Supakorn Boonyuen	82-89
Sustainable carbon aerogel/graphene oxide composite for efficient dye removal from wastewater Nuntikan Kongkharat, Paramasivam Shanmugam, Supakorn Boonyuen	90-95

Impact of electron beam irradiation on physicochemical properties of okara powder 96-100 Danita Sornkeawthanadet, Thajanyawan Sahaspornchaikul, Krittiya Khuenpet

Green synthesis of silver nanoparticles using *Caesalpinia pulcherrima* flower extracts: 101-108 Evaluating their phytochemicals and antioxidant activity

Neethiyarasu Dhino Dhithesh, Mathi Kandiah





Study on the conversion of residual lithium titanium oxide into lithium ion sieve adsorbents

Hsiu-Mei Chiu, 1 Wen-Hua Chen, 1,* An-Ya Lo²

¹Department of Chemistry, National Atomic Research Institute, Taiwan (R.O.C.)
²Institute and Undergraduate Program of Electro-Optical Engineering, National Taiwan Normal University,
Taiwan (R.O.C.)

*E-mail: wenhua@nari.org.tw

Abstract:

This study utilized industrial residual lithium titanium oxide (LTO) from battery manufacturing to develop hydrogen titanium oxide (HTO) adsorbents via hydrochloric acid leaching. The optimal condition (0.1 M HCl, 48 h at room temperature) was determined based on efficient lithium removal with minimal titanium loss. The resulting HTO exhibited Li⁺ adsorption capacities up to 27.5 mg/g in simulated lithium solution and 3.9 mg/g in pretreated brine. Despite a high Na⁺/K⁺ background, the adsorbent maintained favorable selectivity. The use of residual LTO material and a simple leaching process provides a sustainable and low-cost pathway for lithium recovery from brine.

1. Introduction

As global demand for lithium continues to rise, conventional extraction methods such as mining and evaporation ponds are increasingly seen as unsustainable due to their inefficiency and environmental impact. Direct lithium extraction (DLE) technologies have gained attention for their fast kinetics, high selectivity, and potential environmental advantages.¹

Among the various DLE approaches, adsorption stands out due to its operational simplicity and high ion selectivity. Lithium-ion sieves (LISs) are among the most representative adsorbents, offering selective uptake and release of Li⁺ ions.² Depending on their structure and synthesis routes, LISs can be broadly categorized into manganese-based and titanium-based materials. Notably, titanium-based LISs—such as hydrogen titanium oxide (HTO)—exhibit excellent acid resistance and structural stability, making them strong candidates for practical applications.³

In this study, residual lithium titanium oxide (LTO) from battery manufacturing was utilized as a precursor to synthesize HTO via acid leaching with dilute HCl. Unlike most reports that rely on high-purity reagents and test in concentrated lithium solutions, this work evaluates the adsorption performance of HTO in real pretreated brine containing 12 mg/L Li⁺, after Mg²⁺ and Ca²⁺ removal. This strategy combines resource circularity and real-world applicability, offering a new pathway for the development of sustainable lithium recovery materials.

2. Experimental Procedure and Overview

The experimental workflow consisted of two major stages: acid leaching of LTO and lithium adsorption testing. A schematic overview of the process is provided in Figure 1. Both the acid leaching and lithium adsorption procedures were designed with reference to the conditions reported by Zhao et al. (2020).4 In the acid leaching stage, LTO powder was treated with hydrochloric acid (HCl) solutions of varying concentrations (0.1–1.0 M) for up to 48 hours at room temperature, using a solid-to-liquid ratio of 0.1 g per 10 mL (2 g/L, hereafter referred to as S/L). The mixtures were shaken at 150 rpm throughout the leaching process to investigate the effects of acid concentration. Only the sample leached under the optimal condition was subsequently washed with deionized water until neutral pH and dried in a vacuum oven at 60 °C for 8 hours, vielding the HTO adsorbent for further lithium adsorption experiments. Lithium adsorption tests were conducted using both simulated lithium chloride (LiCl) solutions (8.09, 151, and 636 mg/L Li⁺) and pretreated brine. In each test, 0.1 g of HTO was added to 50 mL of solution (adjusted to pH ~12) and shaken at room temperature for 24 hours. The lithium concentration in the supernatant was analyzed at predetermined time intervals to evaluate adsorption performance.

2.1 Adsorption data analysis

The adsorption capacity at time t (q_t , mg/g) and at equilibrium (q_e , mg/g) was calculated using the following equation:







Figure 1. HTO preparation and Li⁺ adsorption process

$$q_e = \frac{(C_0 - C_t) \cdot V}{m}$$
 Eq 1

where C_0 and C_t (mg/L) are the initial and residual Li^+ concentrations at time t, V(L) is the volume of

the solution, and m (g) is the mass of the adsorbent.

To analyze the adsorption kinetics, the experimental data were fitted using two commonly used models: the pseudo-first-order (PFO) and pseudo-second-order (PSO) models, expressed as:

PFO model
$$\ln(q_e - q_t) = \ln q_e - K_1 t$$
 Eq 2

PSO model
$$\frac{t}{q_t} = \frac{1}{K_2 q_e^2} + \frac{t}{q_e}$$
 Eq 3

where q_e and q_t are as defined above, and k_l (1/h) and k_2 (g/mg·h) are the respective rate constants.

To evaluate Li^+ selectivity, the distribution coefficient (K_d , mL/g) was calculated as:

$$K_d = \frac{(C_0 - C_e) \cdot V}{C_{e} \cdot m}$$
 Eq 4

The separation factor (α) between Li⁺ and other competing ions (e.g., Mg²⁺, Ca²⁺) was defined as:

$$\alpha_M^{Li} = \frac{Kd_{Li}}{Kd}$$
 Eq 5

2.2 Characterization

The phase and composition of the residual LTO and acid-leached products were characterized by X-ray diffraction (XRD) and inductively coupled plasma optical emission spectrometry (ICP-OES, HORIBA Scientific, ULTIMA 2). XRD was used to monitor phase changes before and after acid leaching, and the resulting diffraction patterns were compared with JCPDS reference data cited in the literature. ICP-OES was applied to determine the lithium and titanium concentrations in both solid samples and leachates.

3. Results & Discussion

3.1 Phase and composition of LTO

The industrial residual LTO powder was initially of unknown phase and composition. It was therefore characterized by XRD and ICP-OES. XRD revealed diffraction peaks matching the standard Li₄Ti₅O₁₂ pattern (JCPDS card #49-0207), indicating a typical spinel structure (Figure 2). ICP-OES further showed lithium titanium contents of 67,327 542,943 mg/kg, respectively, corresponding to a Li:Ti atomic ratio of approximately 0.855, close to the theoretical 4:5 ratio, supporting its identification as Li₄Ti₅O₁₂. Figure 2 also presents the XRD pattern of the HTO sample prepared under the optimized leaching condition (0.1 M HCl, 48 h), with major peaks remaining consistent with those of LTO, indicating that the spinel structure was largely retained after acid leaching.





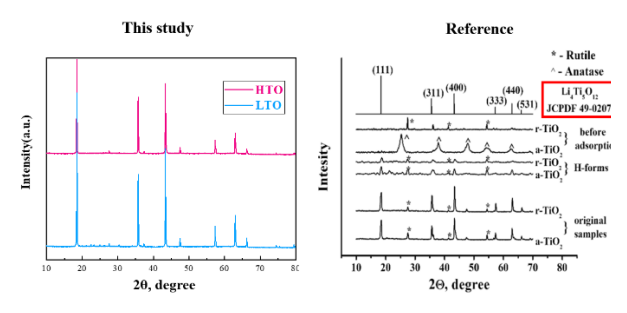


Figure 2. XRD patterns of LTO and HTO (this study) with reference Li₄Ti₅O₁₂ peaks (JCPDS #49-0207, from Ivanets et al., 2024).⁵

3.2 Brine composition analysis

The parent brine contained 16.9 mg/L of ions (Li⁺), along with concentrations of coexisting cations including Na⁺ (44,440 mg/L), Mg²⁺ (40,890 mg/L), Ca²⁺ (8,740 mg/L), and K^+ (38,843 mg/L), as summarized in Table 1. To reduce interferences and simplify the system, the brine was treated with NaOH to precipitate Mg²⁺ and Ca²⁺ as hydroxides, which were subsequently removed by filtration. ICP-OES analysis showed that Mg²⁺ was almost completely removed (<1 mg/L), and Ca²⁺ was reduced to 2.7 mg/L. Due to NaOH addition, Na+ increased to 86,142 mg/L, while Li⁺ slightly decreased to 12 mg/L, indicating that lithium was largely retained in solution. This pretreatment effectively simplified the ionic background for subsequent adsorption evaluation.

Table 1. Composition of parent and pretreated brine (mg/L)

Sample	Li ⁺	$\mathrm{Mg}^{2^{+}}$	Ca ²⁺	Na ⁺	K ⁺
Parent brine	16.9	40,890	8,740	44,440	38,843
Pretreated brine	12	<1	2.7	86,142	22,698

3.3 Acid leaching optimization

To improve the adsorption performance of recycled LTO, acid leaching conditions were optimized. Leaching facilitates lithium removal and phase transformation, influencing adsorbent formation and selectivity. Various HCl concentrations and durations were compared to balance lithium extraction and material stability.

As shown in Figure 3, lithium extraction from LTO gradually increased with time and reached ~35% at 48 h across all tested HCl concentrations. The differences in Li⁺ removal between 0.1–1.0 M were minimal, indicating that acid concentration had limited effect on delithiation efficiency within this range. In contrast, Figure 4 shows that Ti dissolution significantly increased with HCl concentration. At 1.0 M, Ti loss reached 1.8%, while remaining below 0.2% under 0.1 M, suggesting that higher acidity may compromise the structural integrity of the material. Considering both lithium removal and titanium retention, 0.1 M HCl was identified as the optimal leaching condition, balancing extraction efficiency with structural stability subsequent HTO synthesis. This selection was based on two key criteria: (i) achieving a lithium extraction efficiency of at least 30% to sufficient delithiation, and (ii) maintaining titanium loss below 0.2% to preserve the material's structural stability. These thresholds were established to optimize precursor transformation while minimizing structural degradation prior to HTO synthesis.

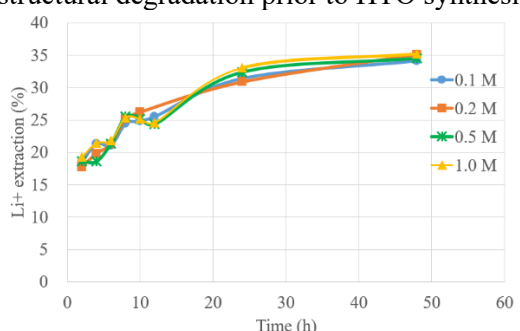


Figure 3. Li⁺ extraction (%) from LTO under various HCl concentrations

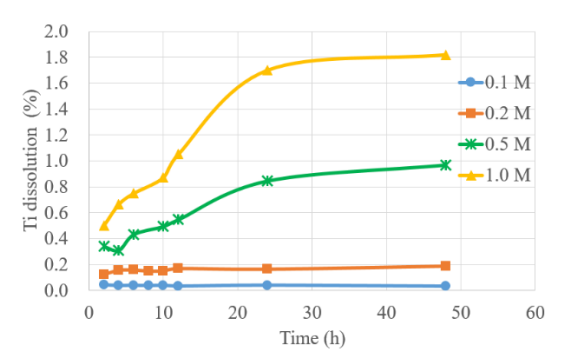


Figure 4. Ti dissolution (%) from LTO under various HCl concentrations



Table 2. Comparison of kinetic parameters for pretreated brine and simulated Li solution

System	C_0 , Li^+	q _{e,exp}	Pseudo-First-Order (PFO) Pseudo-Sec			econd-Orde	er(PSO)	
	(mg/L)	(mg/L)	q _e (mg/g)	$K_1(1/h)$	\mathbb{R}^2	$q_e(mg/g)$ $K_2(1/h)$	\mathbb{R}^2	
Pretreated brine	12	3.90	1.122	0.002	0.991	4.026	0.004	0.999
Simulated Li solution	8.09	2.28	0.929	0.001	0.666	2.325	0.005	0.965

Table 3. Selectivity of HTO toward metal ions

Metal ions	K_{d} (mL/g)	α
Li ⁺	0.96	1.00
$\mathrm{Na}^{^{+}}$	0.02	48.71
K^+	0.03	32.73
Ca^{2+}	0.25	3.85

3.4 Adsorption rate and capacity

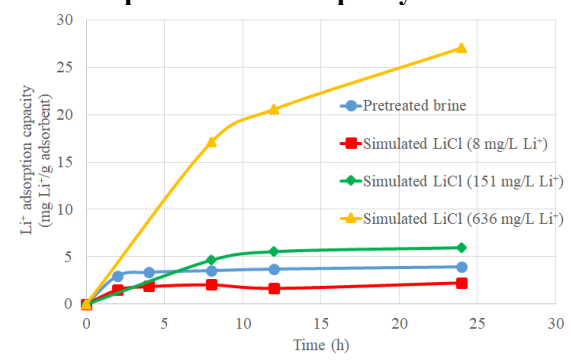


Figure 5. Li⁺ Uptake behavior in pretreated brine and simulated LiCl solutions

As shown in Figure 5, the adsorption process showed a rapid increase in Li⁺ uptake during the first 4-8 hours. As the initial concentration increased, the equilibrium adsorption capacity (qe) also rose, reaching a maximum of 27.5 mg/g at 636 mg/L. Notably, the pretreated brine system (12 mg/L) achieved higher q_e than the simulated 8.09 mg/L solution, indicating strong Li+ uptake even in the presence of competing ions. To further evaluate the performance of the HTO adsorbent developed in this study, a comparison was made with literature reports using high-purity precursors. Pu et al. (2021)⁶ synthesized Li₂TiO₃ using lithium acetate dihydrate and TiO2 as starting materials. After acid leaching, the resulting HTO exhibited an equilibrium Li+ adsorption capacity of 29.98 mg/g under a lithium concentration of 1000 mg/L (S/L = 3). In comparison, the HTO synthesized from residual LTO in this study achieved 27.5 mg/g at 636 mg/L Li^+ (S/L = 2), demonstrating comparable adsorption performance under high-concentration conditions while offering additional advantages in sustainability and costeffectiveness.

3.5 Adsorption kinetics and selectivity

The adsorption kinetics were evaluated using pseudo-first-order (PFO) and pseudo-second-order (PSO) models. For both the pretreated brine and the simulated 8 mg/L systems, the PSO model provided a better fit ($R^2 \ge 0.965$) and more accurate estimation of the equilibrium adsorption capacity (q_e), indicating that chemisorption was likely the rate-limiting step. In contrast, the PFO model underestimated q_e and yielded lower R^2 values, particularly under low-concentration conditions.

The detailed kinetic parameters, including rate constants and model-predicted q_e values, are summarized in Table 2.

As shown in Table 3, the distribution coefficient (K_d) for Li^+ was significantly higher than those of the competing ions, and all calculated separation factors (α) exceeded 1, confirming the preferential adsorption of Li^+ over Na^+ , K^+ , and Ca^{2+} .

4. Conclusions

A low-cost synthesis route for HTO was successfully developed by utilizing industrial residual LTO from battery manufacturing as the titanium source. The resulting HTO exhibited promising lithium adsorption performance, with a maximum uptake of 27.5 mg/g in simulated LiCl solution and 3.9 mg/g in pretreated brine. These findings suggest that battery-derived residual LTO is a viable candidate for producing effective HTO





adsorbents for lithium recovery, particularly under low-concentration conditions in brine.

References

- 1. Farahbakhsh, J.; Arshadi, F.; Mofidi, Z.; Mohseni-Dargah, M.; Kök, C.; Assefi, M.; Soozanipour, A.; Zargar, M.; Asadnia, M.; Boroumand, Y.; Presser, V.; Razmjou, A. *Desalination* **2024**, *575*, 117249.
- 2. Murphy, M.; Haji, S. Front. Chem. Eng. **2022**, *2*, 1008680.

- 3. Chen, Q.; Chen, Z.; Li, H.; Ni, B.-J. *Sustain. Horiz.* **2024**, *9*, 100093.
- Zhao, B.; Guo, M.; Qian, F.; Qian, Z.; Xu, N.; Wu, Z.; Liu, Z. RSC Adv. 2020, 10, 3312–3320.
- 5. Ivanets, A.; Bicheva, E.; Prozorovich, V.; Kouznetsova, T.; Aimbetova, I. O.; Su, X. *Sep. Purif. Technol.* **2024**, *335*, 125986.
- 6. Pu, X.; Du, X.; Wang, G.; Zhang, Y.; Wang, Q.; Wu, H. *Multipurpose Utilization of Mineral Resources* **2021**, *4*, 176–180.





Carbohydrate content test of tofu liquid waste as an alternative media for the growth of Streptococcus mutans

Ni'matul Murtafiah,* Aziz Ansori Wahid, Suci Rizki Nurul Aeni, Fitri Nurhamidah Medical Laboratory Technology, Faculty of Health, Rajawali Health Institute, Bandung, Indonesia *E-mail: nimatul.murtafiah@yahoo.co.id

Abstract:

Alternative media for bacterial growth using liquid tofu waste, the nutrient content in liquid tofu waste has the potential as a source of nutrients for the growth of bacteria. To see the carbohydrate content in tofu liquid waste, qualitative tests (Benedict) and quantitative tests using the DNS method were carried out. The growth of *Streptococcus mutans* isolates alternative media also carried out. The method used is an experimental method with sampling technique in the form of Purposive Sampling. Qualitative test results were carried out using Benedict method from 8 test samples, 4 positive samples showed the presence of carbohydrates marked by a color change to green. Further quantitative test using the DNS method, test samples with the highest carbohydrate content tofu liquid waste at 20%, 50%, and 80% concentrations supported the growth of *Streptococcus mutans*. Among them, the 20% concentration proved most effective due to its more favorable pH and sufficient carbohydrate content because the pH of the medium is close to the optimum pH of the bacteria.

1. Introduction

Dental caries is a disease characterized by damage to the enamel layer of the tooth that can extend to the nerves, caused by the bacteria *Streptococcus mutans*. This bacterium is a gram-positive type that is acidogenic and acidic, able to survive in an acidic environment and produce an unpleasant odor in the mouth (Juariah et al., 2022).

Bacterial culture media, which consists of a mixture of essential nutrients, is crucial for the isolation, identification, and pure culture of microorganisms. Optimal growth requires controlled conditions including humidity, pH, aeration, sterility, and nutrient availability (Toruan et al., 2023). Agar blood, a nutrientrich medium commonly used for *Streptococcus* sp., has limited cost and availability, especially due to the need for sheep blood (Nurhidayanti, 2019). The high cost of conventional media and suboptimal waste utilization encourage the exploration of economical alternatives.

Tofu industrial liquid contains significant concentrations of organic compounds, particularly proteins (40–50%) and carbohydrates (25-50%), which have the potential to be a source of nutrients for bacterial growth (Juriah & Sari, 2021). Carbohydrates, organic compounds made up of carbon, hydrogen, and oxygen, are the main source of energy. Food processing can modify the composition of carbohydrates, and heating can increase its bioavailability (W. Benedict

test is used for the qualitative detection of reducing sugars, while UV-Vis spectrophotometry allows accurate quantification of carbohydrates at low concentrations (Putri, 2018). Therefore, this study aims to evaluate tofu liquid waste as an economical sustainable and alternative medium for Streptococcus mutans culture, while contributing to waste management and improving oral health.

2. Method

This study uses an experimental method with purposive sampling techniques. carbohydrate qualitative test was carried out using the Benedict method, while the quantitative test was carried out using the DNS method. The growth of Streptococcus mutans in alternative media of tofu liquid waste was observed at various concentrations (20%, 50%, and 80%). The pH measurement of the media is also carried out. The materials used include tofu liquid waste obtained from the tofu industry which is rich in nutrients such as protein and carbohydrates, so that it has the potential to be an alternative medium for the growth of Streptococcus mutans (Juriah & Sari, 2021).

3. Results & Discussion

This study aims to produce carbohydrate levels in tofu liquid waste and the potential of this medium as the growth of *Streptococcus mutans*.





Table 1. Results of a qualitative test of carbohydrate content (*Benedict*)

Sample Code	Measureme About Re		Color	
	1	2		
LTA	-	-	Blue	
LTB	+	+	Green	
LTC	+	+	Green	
LTD	-	-	Blue	
LTE	-	-	Blue	
LTF	+	+	Green	
LTG	+	+	Green	
LTH	-	-	Blue	

^{*}Information: -: Contains no carbohydrates (Negative)

Table 2. Quantitative test of carbohydrate content (DNS method)

Sample	Concentration	Abso	Absorbance Flat		Up to Carbohydrates	Up to Carbohydrates
Code	%	Repetition		-flat		
		1	2		(ppm)	(%)
	20%	0.061	0.061	0.061	59.83	0.005983%
LTA	50%	0.074	0.074	0.074	64.03	0.006403%
	80%	0.089	0.089	0.089	68.87	0.006887%
	20%	0.070	0.072	0.071	63.06	0.006306%
LTB	50%	0.153	0.153	0.153	89.51	0.008951%
	80%	0.296	0.296	0.296	135.64	0.013564%
	20%	0.078	0.078	0.078	65.32	0.006532%
LTC	50%	0.170	0.170	0.170	95	0.0095%
	80%	0.337	0.339	0.338	149.19	0.014919%
	20%	0.056	0.056	0.056	58.22	0.005822%
LTD	50%	0.065	0.067	0.066	61.45	0.006145%
	80%	0.101	0.101	0.101	75	0.0075%
	20%	0.056	0.056	0.056	58.22	0.005822%
LTE	50%	0.079	0.079	0.079	65.64	0.006564%
	80%	0.108	0.108	0.108	72.74	0.007274%
	20%	0.087	0.087	0.087	68.22	0.006822%
LTF	50%	0.185	0.185	0.185	99.83	0.009983%
	80%	0.430	0.434	0.432	179.19	0.017919%
	20%	0.074	0.079	0.076	64.67	0.006467%
LTG	50%	0.170	0.172	0.171	95.32	0.009532%
	80%	0.335	0.339	0.337	148.87	0.014887%
	20%	0.068	0.068	0.068	62.09	0.006209%
LTH	50%	0.079	0.079	0.079	65.64	0.006564%
	80%	0.097	0.097	0.097	71.45	0.007145%

The results of the study consisted of qualitative tests, quantitative tests, and bacterial colony growth. The results of the qualitative test carried out using the Benedict method showed that out of eight samples of tofu liquid waste, four samples contained carbohydrates, characterized by a change in color to green

(Table 1). This shows that tofu liquid waste still stores nutrients that can be utilized by microorganisms. According to Dasyanti (2013), the Benedict test is effective in detecting the presence of reducing sugars, which is an important indicator in determining the nutritional potential of a medium.

^{+:} Contains carbohydrates (Positive)





LTF samples at 80% concentrations showed the highest carbohydrate content of 0.017919%, while at concentrations of 20% and 50%, they had levels of 0.006822% and 0.009983%, respectively (Table 2).

The standard curve is obtained from the preparation of standard glucose solutions with concentrations of 200 ppm, 400 ppm, 600 ppm, 800 ppm and 1000 ppm. The result of the determination coefficient (R^2) is 0.9958. R^2 has a value between 0-1 provided that the closer to 1 the better and the equation y = 0.0031x - 0.1245 is obtained as displayed as in the following curve in Figure 1.

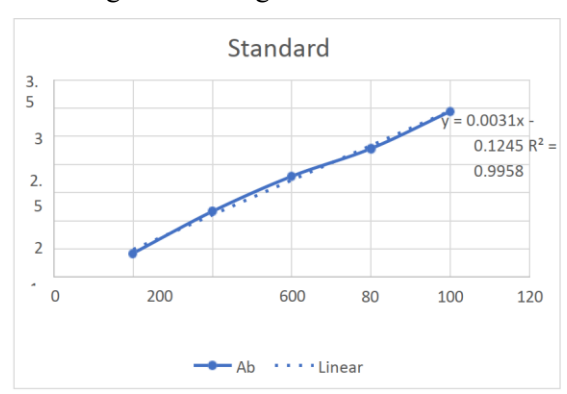


Figure 1. Standard curve of glucose concentration (200–1000 ppm) based on DNS method with absorbance measurement.

pH measurements are carried out to ensure that the pH content in the liquid tofu waste is in accordance with the growth *Streptococcus mutans*. Acidity level (pH) is a value that indicates whether an ingredient is acidic (<7), alkaline (>7) or neutral (7). The results of the measurement of liquid tofu waste were obtained at concentrations of 20%, 50% and 80% indicating an acidic pH (<7) as shown in Table 3.

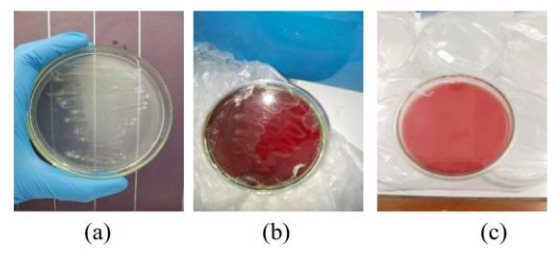


Figure 2. Colony growth results (a) positive sample, (b) positive control, (c) negative control

The results showed that *Streptococcus mutans* grew well on alternative media made from tofu liquid waste. All concentrations tested (20%, 50%, and 80%) showed positive colony growth. However, a concentration of 20% with a pH of 5.08 proved to be most effective for bacterial growth. Previous research has shown that *Streptococcus mutans* has an optimal pH of about 6.0, but is able to adapt and grow at a lower pH (Lemos et al., 2019).

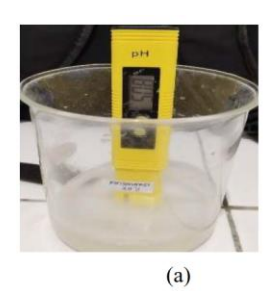
Table 3. Growth results of Streptococcus mutans colonies

Sample Code	Growth Media	Incubated Mouth	Repetition		Incubation Time (Hours)
	Growth Media		1	2	` ,
LTF	Tofu liquid waste concentration 20%	37°	✓	✓	24 Hours
	Tofu liquid waste Concentration 50%	37°	✓	✓	24 Hours
	Tofu liquid waste Concentration 80%	37°	✓	✓	24 Hours
LTF	Tofu liquid waste concentration 20%	37°	✓	✓	48 Hours
	Tofu liquid waste Concentration 50%	37°	✓ ✓	✓ ✓	48 Hours
	Tofu liquid waste Concentration 80%	37°	✓	✓	48 Hours
Controls+	Media BAP	37°	-	-	
Control-	Media BAP	37°	-	-	



Table 4. pH measurement results

Sample Code	Concentration (%)	Ph	Information
LT F	20%	5.08	Sour
	50%	4.78	Sour
	80%	4.69	Sour



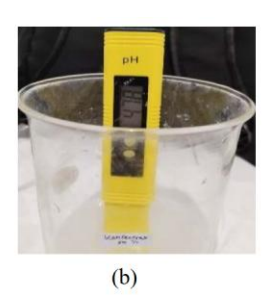




Figure 3. pH measurement results (a) 20% concentration, (b) 50% concentration, (c) 80% concentration Source: Personal Documentation (2024)

The results showed that *Streptococcus mutans* grew well on alternative media made from tofu liquid waste. All concentrations tested (20%, 50%, and 80%) showed positive colony growth. However, a concentration of 20% with a pH of 5.08 proved to be most effective for bacterial growth. Previous research has shown that *Streptococcus mutans* has an optimal pH of about 6.0, but is able to adapt and grow at a lower pH (Lemos et al., 2019).

4. Conclusion

Alternative media derived from tofu liquid waste showed variations in carbohydrate content and pH that affected bacterial growth. Although higher concentrations (50% and 80%) had more carbohydrates, their low pH levels were less suitable for *S. mutans*. The 20% concentration offered a better balance, supporting optimal growth conditions. These findings imply that tofu liquid waste, particularly at 20%, can serve as a practical, low-cost, and sustainable alternative culture medium, especially in resource-limited microbiological laboratories.

References

- 1. Juariah; Sari, W. P. *Health Analyst Science* **2021**, *10*, 8–12.
- Toruan, S. A. L.; Manu, T. T.; Evriarti, P. R. Journal of Indonesian Medical Laboratory and Science 2023, 4, 25–36.

- 3. Putri, A. S. Quantitative Carbohydrate Test on Rice. https://www.academia.edu/42898512/Uji _Karbohidrat_pada_Nasi_secara_Kuantit atif (accessed May 7, 2025).
- 4. Dasyanti, N. L. M. Ministry of Health of the Republic of Indonesia, Denpasar Polytechnic: Denpasar, 2013.
- Pratiwi, Y. H.; Ratnayani, O.; Wirajana, I. N. J. Kim. 2018, 12, 134–139.





Implementing LDR to assist disabled students in reaction rate practicum

Nurul Cholis*

SMAN 1 Campaka Purwakarta West Java, Indonesia *E-mail: cholisnurul70@gmail.com

Abstract:

This study explores the use of a Light Dependent Resistor (LDR) as an assistive tool to enhance accessibility and engagement for students with disabilities in class XI MIPA semester 3 at SMAN 1 Bungursari Purwakarta, particularly those with visual impairments, in a reaction rate practicum, and serves as a continuation of the work "Utilization of Light Dependent Resistor as a Tool to Measure the Accuracy of Reaction Time and Reaction Rate," presented at ICCE 2024. The experiment involved measuring the reaction rate between sodium thiosulphate and hydrochloric acid using an LDR system, which detected changes in light intensity caused by the color change in the solution and converted them into electrical signals. The methodology included preparing tools and materials, setting up the system, conducting the chemical reaction, and analyzing data to evaluate the effectiveness of the LDR system. The findings showed that the LDR system successfully detected light intensity changes corresponding to the reaction rate, providing accessible feedback to visually impaired students. However, the study was limited to a single chemical reaction, and further research is needed to assess the system's applicability to other reactions, its scalability in diverse educational settings, and its long-term impact on learning outcomes, especially in resource-constrained environments. The results suggest that LDR technology holds promise as a practical tool for promoting inclusivity in science education, particularly for students with disabilities.

1. Introduction

Implementing Light Dependent Resistor (LDR) sensors in reaction rate practicums can significantly enhance accessibility for students with disabilities, particularly those with visual impairments.²

LDR sensors can detect changes in light intensity, which can be translated into auditory signals. For instance, a system can emit varying tones or vibrations based on the amount of light detected, aiding visually impaired students in perceiving and responding to stimuli during reaction time tests.⁷

Combining LDR sensors with vibration motors can provide tactile feedback. As light intensity changes, the vibration pattern can vary, offering a non-visual cue to students, which is especially beneficial for those with both visual and auditory impairments.

Using microcontrollers like Arduino, LDR sensors can process light changes in real-time, allowing for immediate auditory or tactile feedback. This instant response is crucial in reaction time experiments where prompt feedback is necessary.⁶

This innovative prop is an original creation of the author and, to our knowledge, it has never been made by anyone else before. By using these props, students will be exposed to new inquiry experiences. Not only in terms of making props but also when conducting their own experiments. So, the learning activities carried out can not only improve the quality of students but also provide them with a learning experience to foster the carrying out of independent activities. This will students the opportunity to exercise and develop various inquiry skills.^{1,4}

2. Methods

2.1 Implementing learning/Teaching aids

The implementation of this teaching aid for fostering inquiry learning consists of several steps:

Title: Reaction Rate

Objective: Determine the reaction rate of reagents for the reaction between hydrochloric acid solution (HCl) and sodium thiosulfate solution (Na₂S₂O₃) according to the following reaction equation.

2 HCl (aq) + Na₂S₂O₃ (aq) \longrightarrow 2 NaCl (aq) + H₂O(l) + SO₂(g) + 1/8 S₈(s)

Tools: 2 small test tubes, light sensor (LDR) 1 piece, clock/stopwatch, and sufficient pipettes **Ingredients**: 0.1 M HCl solution 2 mL, 0.2 M HCl solution 2 mL, 0.1 M Na₂S₂O₃ solution 2 mL, 0.2 M Na₂S₂O₃ solution 2 mL

Working methods: Pour 2 mL of 0.1 M HCl solution into a small test tube. Insert the tube





into the light sensor. Then add 2 mL of 0.2 M Na₂S₂O₃ solution. Note the time from pouring the Na₂S₂O₃ solution until the light comes on and the buzzer sounds. Repeat the experiment with 2 mL of 0.1 M Na₂S₂O₃ solution. Complete the observation table with data from your experimental results. Repeat experiment no. 1 and 3 using 25 mL of 0.2 M HCl solution with 2 mL of 0.2 M Na₂S₂O₃ solution. Note the time from pouring the Na₂S₂O₃ solution until the light turns on and the buzzer sounds.

2.2 Observation

Table 1. Fill in the observation data

No	[HCl]/M	$[Na_2S_2O_3]/M$	Time/s
1			
2			
3			

By answering the following questions, it is expected that stundets can draw the right conclusions.

- Determine the order of HCl
- Determine the order of Na₂S₂O₃
- Determine the reaction rate or the overall reaction order
- Write the reaction rate equation
- Calculate the value of k

Place and arrange the components as shown in the following scheme :

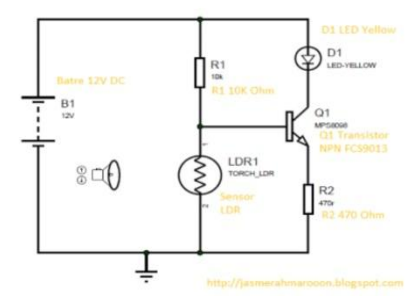


Figure 1. device circuit schematic

The tools and materials needed to make the props are:

- 1. PCB
- 2. Tin
- 3. Cable
- 4. Transistors
- 5. Resistors
- 6. Buzzer
- 7. LED

- 8. LDR
- 9. Thick paper or thick plastic for wrapping

2.3 How to use props

Props designed and made by the author as shown in the following picture.

- Connect the tool to a 12 V power supply or 8 batteries @ 1.5 V
- Pay attention to whether the LED indicator inside is on or not
- Insert the test tube into the prepared hole
- The blue LED indicator will light up when the reaction ends
- Record the time using a clock or stopwatch.

For more information, see the video clip: https://youtu.be/FkTlv2BgNf4

This approach aligns with meaningful and contextual learning strategies that emphasize active student participation and hands-on experience.^{5,6}

3. Result & Discussion

3.1 Observation result

Table 2. Observation data

No	[HCl]/M	$[Na_2S_2O_3]/M$	Time/s
1	0.1	0.1	240
2	0.1	0.2	120
3	0.2	0.1	60

3.2 Determining HCl reaction order

The calculation results from the observation data show that the rate of reaction for HCl is 2^{nd} order. From the experimental data, graph the HCl concentration against time units:

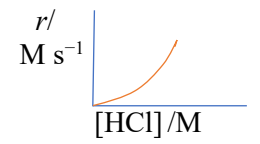


Figure 2. Schematic graph of HCl reaction order



3.3 Determining Na₂S₂O₃ reaction order

The calculation results from the observation data show that the rate of reaction for Na₂S₂O₃ is 1st order. Using the experimental data, graph the Na₂S₂O₃ concentration against time units:

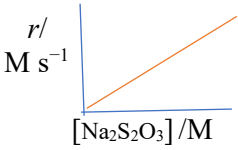


Figure 3. Schematic graph of Na₂S₂O₃ reaction order

3.4 Determining the total order of reaction

The total reaction order from the experiment above is 3.

3.5 Writing down the reaction rate equation The reaction equation is as follows:

 $r = k \text{ [HCl]}^2 \text{[Na}_2 \text{S}_2 \text{O}_3 \text{]}$

3.6 Calculate the value of k

Next, the value can be calculated from the reaction rate equation, and the result obtained is 0.06

It is expected that the use of this teaching aid will make it easier for teachers to teach the concept of reaction rate. With LED indicators and buzzers, students with special needs can be helped so that they can do practical work. Hopefully, this article will also be a source of inspiration for teachers to design, make and use personally perfected teaching aids. The use of teaching aids in learning is intended to increase the competence and achievement of students.² In addition, it is also about developing scientific attitudes and improving the quality and independence of students so that these can then be applied in everyday life.^{4,7}

The results of this classroom action research show changes in student learning outcomes. Before using the tool, the student's results were 65% and after using the tool, there was an increase to 76%. The percentage of student learning performance can be described in the following diagram:

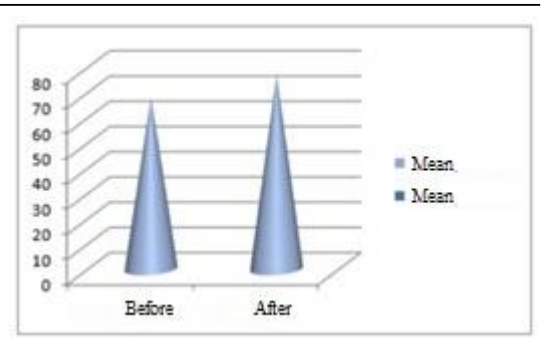


Figure 4. Diagram student learning performance

Next, some feedback from colleagues on the Implementing LDR to assist disabled students in reaction rate practicum:

1. Student A

Response: "Interesting learning can encourage students to be more active".

Suggestion: "Teachers should always provide feedback at the end of each learning."

2. Student B

Response: "Practical learning can improve students' learning motivation, increase their curiosity and explore their critical thinking skills."

Suggestion: "Examples of student worksheets related to learning objectives can be displayed."

3. Student C

Response: "That chemistry practicums can be done without laboratory equipment."

Suggestion: "It is very good and can be adapted by other chemistry teachers."

4. Conclusions and Suggestions

These studies delve into the development and application of assistive devices that enhance accessibility for students with disabilities, providing valuable information implementing inclusive educational practices. The use of LDR in reaction rate practicums allows: Inclusive and participatory learning. Use of sensors microcontrollers as adaptive learning aids. Students with disabilities can still experience direct observation of chemical processes.

Learning props are very useful for making the real world accessible in class, especially reaction rates that are difficult to observe directly. Of course, this presents a challenge for teachers to create appropriate teaching aids





since many teachers find it difficult to meet their needs for these teaching aids.

Simple props designed and made by the author can serve as an alternative to overcome the problem of scarcity of props. The tool presented here can be used to measure the exact time at which the reaction ends, allowing accurate data to be obtained from measuring the speed of the reaction rate. This tool can also be used for students with special needs, such as those who cannot hear or see. Since it is made from materials that are easily available anywhere, the manufacturing cost is very affordable. In addition, this tool can be created by students in a short time so that it can be used in classroom teaching.

Due to the various advantages of these teaching aids, it is recommended that their use be disseminated to all schools, both high school and middle school.

References

- 1. Abdurrahman. *Meaningful Learning Reinvention of Meaningful Learning*; Student Library: Yogyakarta, 2007.
- 2. Adeyanju, L. Teachers Perception of the Effects and Use of Learning Aids in Teaching: A Case Study of Winneba Primary and Secondary Schools; http://ultibase.rmit.edu.au/Articles/nov03/adeyanju1.htm (accessed August 16, 2011).
- 3. Budi Utami, et al. *Chemistry for SMA/MA Class XI*; Department of National Education: Jakarta, 2010.
- 4. De Porter, B., et al. *Quantum Teaching Practicing Quantum Learning in Classrooms*; Kaifa: Bandung, 2004.
- 5. First Directorate of Further Education. Contextual Approach (Contextual Teaching and Learning, CTL);
 Department of National Education:
 Jakarta, 2003.
- 6. Nurhadi, et al. *Contextual Learning and its Application in KBK*, 2nd ed.; Malang State University Publishers (UM Press): Malang, 2004.
- 7. Suyatno. *Exploring Innovative Learning*; Masmedia Buana Pustaka: Sidoarjo, 2009.





Implementation SSC (Small Scale Chemistry) in the practical work on making carbon dioxide gas from egg shells to improve student creativity in stoichiometry material

Laurensia*

MAN 3 Jakarta Pusat, Jakarta, Indonesia *E-mail: laurensiaumi73@gmail.com

Abstract:

This study aims to apply the small-scale chemistry (SSC) approach in laboratory practice on carbon dioxide (CO₂) production from eggshells to encourage student creativity in stoichiometry subjects. The SSC approach is suitable for high school level because it uses minimal chemicals, simple equipment, and safe techniques. This type of research is classroom action research in the form of quantitative descriptive. Respondents are student of grade XI IPA who have taken stoichiometry learning. Student creativity data were collected through observation, interviews, and rubrics and then analyzed quantitatively descriptively. Kampung chicken eggs, domestic chicken eggs, and duck eggs were used in the experiment. The results showed that student creativity increased when SSC was applied in laboratory practice of making carbon dioxide from eggshells. The use of kampung chicken eggshells produced (an average of 24 mL CO₂) higher than domestic chicken (an average of 20 mL CO₂) and duck eggs (an average of 18 mL CO₂). After practicing using SSC in class, students were able to understand the concept of stoichiometry more effectively. The implementation of SSC technique practicum has been proven to have an effect on creativity with the results of pretest (average 78%) and posttest cycle 1 (average 84%), cycle 2 (average 95%) which experienced significant changes. It is concluded that the implementation of the SSC approach makes chemistry learning about stoichiometry more interesting and relevant and increases student' creativity and understanding.

1. Introduction

Chemistry learning in schools has developed over time. This is in line with the independent curriculum launched by the government with an emphasis on deep learning. Every school has certainly conducted training in implementing the independent curriculum to improve the quality of educator professionalism, so that they are able to implement the independent curriculum in the teaching and learning process. The implementation of SSC (Small Scale Chemistry) is one effort to make learning meaningful. SSC is also a learning process by utilizing environmentally friendly, safe and easily obtained tools and materials and in accordance with the principles of green chemistry. According to Manahan,1 chemical experiments by maximizing the benefits of nature while eliminating or at least reducing its negative impacts are known as green chemistry. Green chemistry aims to develop chemical processes and chemical products that are environmentally friendly and in accordance with sustainable development.²

2. Methods

This research is a Classroom Action Research conducted by teachers to overcome various learning problems experienced by student in the classroom. What is meant by action here is a movement of this research activity in the form of a series of activity cycles as a means of improving learning and increasing student creativity by using media, methods, models or learning aids that are more interesting, creative, and innovative so that they can be used as a reference in quality learning activities. While class means a group of student in a particular class who receive lessons from a teacher. Classroom action research is a study that explains the cause and effect of treatment, while explaining what happens when the treatment is given, and explaining the entire process from the beginning of the treatment to the impact of the treatment.³ In this study, an experimental method was also used in the laboratory, namely by using eggshell material which was reacted with acetic acid using the SSC technique, namely with two syringes or injections connected by a rubber hose, then the CO₂ gas produced is recorded in the observation table, then with the concept of stoichiometric



calculations student can calculate how much carbon dioxide gas is produced and compared with theoretical calculations.

2.1 Population and Sample

This research was conducted at MAN 3 Central Jakarta, Cempaka Putih District, Central Jakarta, in the 2025/2026 academic year. The population in this study were student of class XI MAN 3 Central Jakarta. The sample in this study was class XI-2 which consisted of 35 student with details of 6 male student and 29 female student.

2.2 Experimental procedure

The resulting CO₂ concentration data were obtained as follows:

- 1. Place 1 gram of eggshell sample into a 30 mL syringe. Carefully attach the plunger while expelling the air from the syringe.
- 2. Carefully add 10 mL of the eggshell sample to the syringe. Attach the rubber tubing to the end of the syringe and close the tubing with a paper clip. Allow the two solutions to react. Once CO2 gas has formed, slowly pour the liquid into a plastic waste container and connect it to a second syringe to drain the CO₂ gas.
- 3. Measure the volume of CO₂ formed and record it in the observation table.
- 4. The CO₂ gas that is formed is tested by flowing CO2 gas into a beaker containing 2 mL of Ca(OH)2. If the solution becomes cloudy, it is proven that the gas produced is CO₂ gas.





Figure 1. a) Syring with CO₂ b) CO₂ gas test

2.3 Data Analysis Techniques, Evaluation, and Reflection

In addition to observing student learning activities in the laboratory, the teacher also collected primary data on student creativity. The data was collected through observation activities to collect data on student creativity using Google Forms. The collected data will be analyzed to determine student average scores

and improve learning outcomes using the following analysis techniques:

2.4 Average student grades

The researcher added up the scores obtained by the student and then divided them by the number of student in class XI-2 to obtain the formula for the average score of the formative test according to Arikunto⁴ as follows:

$$X = \frac{\sum X}{\sum N}$$

Information:

X : Average Value

ΣΧ : Number of all student grades

 ΣN : Number of student

2.5 Improved learning outcomes

According to Aqib⁵ to determine the improvement of student learning outcomes, quantitative analysis is used with the formula

$$A = \frac{\text{Total score all student}}{\text{Number of Student}} \times 100\%$$

Information:

: Average

Total Score All Student : All student' grades Number of student : Total number of student in the class

For reflection analysis: the student creativity evaluation score obtained from the total score before the implementation of learning with the total score after learning in cycle 1 and cycle 2 obtained the percentage of improvement. The results obtained and problems that arise during the implementation of the action are evaluated by the researcher, usually by involving students as well, so that it can be used as a basis for reimplementation in cycle II if the results of cycle I have not been achieved. For example, in cycle 1 there are still groups of students who lose CO₂ gas due to being less careful in transferring CO₂ from syringe 1 to syringe 2. in cycle 1 students only measure CO₂ samples on free-range chicken eggshells, in cycle 2 they want to be creative with other eggs. The hope is of course that cycle 2 is better than cycle 1.

In this study, a practical activity involving the reaction between eggshells and acetic acid solution provides students with the opportunity directly understand the concept stoichiometry. Students learn to calculate the number of moles of eggshells (CaCO₃) and





acetic acid (CH₃COOH) used in the reaction. By using the stoichiometric formula, they can calculate the amount of CO₂ produced based on the amount of reactants used. Students not only learn theory but also gain practical experience. They can see firsthand how chemical reactions occur and how CO₂ gas is formed. Students can see the relationship between reactants and products in chemical reactions. This experience makes learning more interesting and easier to remember.

3. Results & Discussion

Table 1. List of pretest, posttest I and posttest II scores

Entries	Pretest	Cycle 1	Cycle 2
1	78	82	94
2	79	80	92
3	75	83	92
4	78	82	96
5	76	84	95
6	78	80	96
7	79	84	89
8	80	85	95
9	78	84	94
10	75	84	89
11	78	82	92
12	78	84	94
13	78	82	94
14	76	82	95
15	78	83	94
16	78	84	96
17	78	84	94
18	79	84	95
19	78	85	96
20	78	84	89
21	74	85	95
22	78	84	96
23	79	84	96
24	78	85	95
25	80	88	96
26	78	84	97
27	76	84	97
28	78	84	96
29	77	84	95
30	75	84	97
31	78	82	96
32	79	85	96

Entries	Pretest	Cycle 1	Cycle 2
33	79	86	97
34	78	84	96
35	78	82	96
SUM	2720	2927	3312
AVERAGE RATING	78%	84%	95%

Table 2. CO₂ gas data in cycles 1 and 2

	Average	Average
Material	Cycle 1	Cycle 2
kampung chicken eggs	23.90 mL	24.00 mL
domestic chicken eggs	-	20.00 mL
duck eggs	-	18.00 mL

From the results of the data analysis obtained above, it can be proven that:

- 1. From Table 1 the application of SSC (Small Scale Chemistry) in the Practical Work on Making Carbon Dioxide Gas from Eggshells to Improve Student Creativity in Stoichiometry Material for the 2025/2026 academic year, namely by increasing the average value of student creativity before the Action by 78% to 84% in cycle I and increasing again by 95% in cycle II. After the Action using the CO₂ gas making practicum method with the SSC technique.
- 2. From Tabel 2 with the Application of SSC (Small Scale Chemistry) in the Practical Work on Making Carbon Dioxide Gas from Eggshells, student experience an increase in understanding and creativity, because they learn according to their wishes and abilities, student in cycle 1 only use free-range chicken eggs but they are creative by comparing them with domestic chicken eggs and duck eggs. From the data they obtained, it turned out that free-range chicken eggs produce more carbon dioxide gas.

The researcher conducted two cycles of research and found that the results of observations on student creativity increased. The increase in student creativity can be seen from the increase in the average class creativity score in the two cycles compared to before the action. The application of SSC in the practicum of making CO₂ gas from eggshells in class XI MAN 3 Central Jakarta has been proven to increase student creativity. The increase in





student creativity is presented in the histogram for cycle 1 and cycle 2 below:

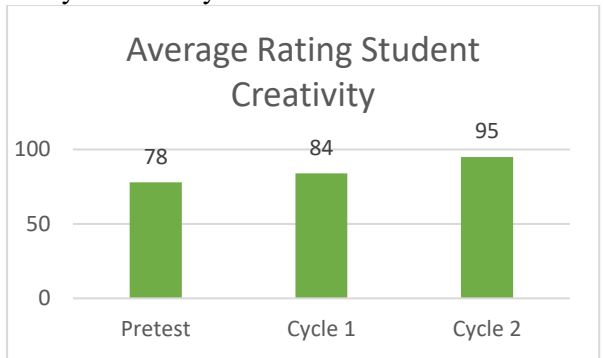


Figure 2. Histogram of student creativity through cycle 1 and cycle 2 tests

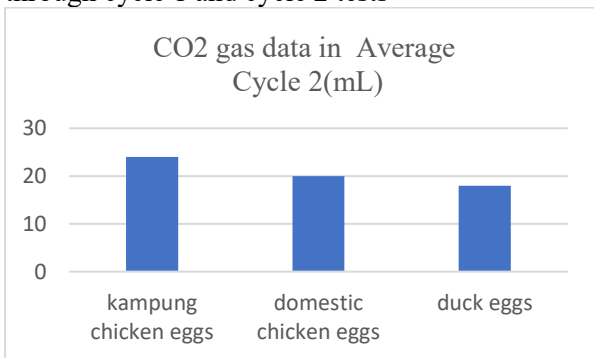


Figure 3. Histogram of student creativity through cycle 1 and cycle 2 tests

4. Conclusion

From the learning outcomes that have been implemented by applying SSC (Small Scale Chemistry) to the carbon dioxide gas production practicum and based on all the discussions and data analysis that have been carried out, it can be concluded that the learning implemented by applying SSC (Small Scale Chemistry) to the Carbon Dioxide Gas Production Practicum from Eggshells to Improve the Creativity of MAN 3 Central Jakarta Class XI 2 Student in Stoichiometry Material, which is marked by an increase in student creativity before the Action 78% increased to 84% in cycle I and increased again to 95% in cycle II. From the research results obtained from the previous description in order for the chemistry learning process to be more effective, innovative and creative and able to provide optimal results for student, the following suggestions are submitted: 1) To implement/implement small scale chemistry (SSC) thorough preparation is needed so that the practicum runs smoothly and the materials used are easy to obtain and safe, 2) Further research is needed because this research was only conducted in one class at MAN 3 Central Jakarta so it would be better if it was also implemented in other schools, 3) For similar research, improvements need to be made in various things in order to obtain better results.

References

- Manahan, S. E. Environmental Science and Technology: A Sustainable Approach to Green Science and Technology, CRC: Boca Raton, 2006.
- 2. Ulfah, M.; Mulyazmi; Burmawi; Praputri, E.; Sundari, E.; Firdaus. *IOP Conf. Ser.: Mater. Sci. Eng.* **2018**, *334*, 012006.
- 3. Arikunto, S; Suhardjono, dan Supardi Penelitian Tindakan Kelas. Malang: PT Bumi Aksara, 2015.
- 4. Arikunto, S. *Research Procedure for a Practical Approach*, Jakarta: Rineka Cipta, 2010.
- Aqib, Z. et al. Pendidikan Karakter: Membangun Perilaku Positif Anak Bangsa, Yrama Widya, 2011.
- 6. Abrahams, I.; Millar, R. *International Journal of Science Education* **2008**, *30* (14), 1945–1969.
- 7. Adadan, E.; Irving, K. E.; Trujillo, T. *Chemistry Education Research and Practice*, **2009**, *10*(1), 23–31.
- 8. Bodner, G. M. *Journal of Chemical Education* **1986**, *63*(10), 873.
- 9. Csikszentmihalyi, M. Creativity: Flow and the psychology of discovery and invention. Harper Perennial, 1996.
- 10. Guilford, J. P. *American Psychologist* **1950**, *5*(9), 444–454.
- 11. Herron, J. D. *The Chemistry Classroom:* Formulas for Successful Teaching. American Chemical Society: Washington, DC, 1996.
- 12. Laurensia. (2021) *Small Scale Chemistry* Suatu Pendekatan Baru Dalam Praktikum Kimia, Pustaka Media Guru, 2021.
- 13. Lunetta, V. N.; Hofstein, A.; Clough, M. P. Learning and Teaching in the School Science Laboratory: An Analysis of Research, Theory, and Practice. In *Handbook of Research on Science Education*; S. K. Abell & N. G. Lederman (Eds.); Lawrence Erlbaum Associates, 2007; pp. 393–441.





MoSe₂-PEDOT nanocomposite for ultrasensitive electrochemical sensing of nitroaromatic compounds

Shivam Kashyap, Anjana Sarkar*

Department of Chemistry, Netaji Subhas University of Technology, Azad Hind Fauj Marg, Dwarka Sector-3, New Delhi, India – 110078.

*E-mail: anjana.sarkar@nsut.ac.in

Abstract:

Nitroaromatic compounds (NACs) are widely used in industry and as explosives precursors, posing health and environmental risks. Environmental monitoring and security require sensitive and selective electrochemical NAC sensors. We develop a high-performance electrochemical sensor for NAC reduction using a hydrothermally synthesised MoSe₂-PEDOT nanocomposite. MoSe₂'s rich active site, PEDOT's excellent conductivity, and processable polymer matrix together enable outstanding electrocatalytic activity towards NACs like nitrobenzene (NB), 2,4-dinitrotoluene (DNT), etc. The MoSe₂-PEDOT nanocomposite was synthesised using a hydrothermal technique and in-situ polymerisation, resulting in a synergistic combination. XRD, FESEM, and BET confirmed its structural and morphological features. Cyclic voltammetry (CV), electrochemical impedance spectroscopy (EIS), and differential pulse voltammetry (DPV) showed that the MoSe₂-PEDOT modified electrode reduced representative NACs better than bare and single-component modified electrodes. His synergy increased peak currents and decreased reduction potentials. The sensor had good selectivity, sensitivity, repeatability, and low detection limit. Synergy between MoSe₂'s catalytic activity and PEDOT's charge transport improves performance. These results suggest that hydrothermally synthesised MoSe₂-PEDOT nanocomposites could be used to make sensitive electrochemical sensors for toxic NACs.

1. Introduction

Industrial effluents are releasing nitroaromatic pollutants, especially nitrotoluene, into aquatic ecosystems in ever-growing amounts, which is a major environmental and public health issue. Classified as a priority pollutant by the U.S. Environmental Protection Agency (EPA), 2,4-DNT is a stubborn chemical with great toxicity endocrine-disrupting properties. nitrotoluene can remain in the environment for long durations because of its chemical stability and resistance to microbial breakdown, which causes bioaccumulation and negative environmental effects. Traditional analytical techniques like gas chromatography, highperformance liquid chromatography, and mass spectrometry provide excellent sensitivity; however, they are hindered by factors such as high costs, complexity, and the need for thorough sample preparation. Conversely, electrochemical methods have surfaced as formidable options owing to their exceptional sensitivity, affordability, swift response times, portability.1 and The efficacy electrochemical sensors is significantly influenced by the characteristics of the electrode material.

Transition metal dichalcogenides (TMDCs), particularly molybdenum diselenide (MoSe₂), have attracted considerable interest owing to their layered two-dimensional architecture, elevated surface-to-volume ratio, adjustable electrical characteristics, and inherent catalytic efficacy. Nonetheless, MoSe₂ exhibits low and electrical conductivity inadequate dispersion in wet environments, constraining its direct utilisation in electrochemical sensing. To mitigate these limitations, we have synthesised MoSe₂–PEDOT nanocomposite integrating the conductive polymer PEDOT into the MoSe₂ matrix. PEDOT provides superior conductivity, mechanical flexibility, environmental stability, and processability, conjugated π -electron system while its enhances effective electron transmission at the MoSe₂ contact.²

In this investigation, we developed a MoSe₂-PEDOT nanocomposite and utilised it to fabricate a modified GCE for the precise and targeted detection of 2.4-DNT. The behaviour electrochemical of the nanocomposite in relation to the reduction of 2,4-DNT was examined through the application of CV and DPV techniques. Additionally, we investigated the electrode's ability





electrochemically degrade 2,4-DNT, thus providing a dual-functional platform for both sensing and remediation. The exceptional capabilities of the MoSe₂–PEDOT sensor highlight its promising applications in environmental monitoring and water purification technologies.

2. Experimental Section

2.1 Materials and Reagents

molybdate Sodium dihydrate (Na₂MoO₄·2H₂O), selenium powder (Se), Sodium Borohydride (NaBH₄) were purchased Loba Chemie Pvt Ltd. (EDOT) ethylenedioxythiophene was purchased from Tokyo Chemical Industry Ammonium Persulphate Cetyltrimethylammonium bromide (CTAB), Acetone, Ethanol, and 2,4-dinitrotoluene (2,4-DNT) (≥99%) were procured from SRL Chemicals. All chemicals were used without further purification. Phosphate-buffered saline (PBS, 0.1 M, pH 7.0) was used as the supporting electrolyte. Ultrapure (resistivity $\geq 18.2 \text{ M}\Omega \cdot \text{cm}$) was obtained from a Milli-Q purification system.

2.2 Synthesis of MoSe₂ Nanosheets

MoSe₂ Nanosheets were synthesised using the hydrothermal method. Briefly, 0.05 mmol of Na₂MoO₄.2H₂O was added to 25 ml DI water, and continued to be stirred for 15 min, then 0.1 mmol Se powder was added and sonicated for 30 min to thoroughly disperse the Se powder. 0.1 mol NaBH₄ was added to the above solution and continued to be stirred for 30 min till the colour changed to dark brown. The reaction mixture was transferred to a 100 ml stainless steel hydrothermal autoclave at 200 °C for 24 hrs. After 24 hrs, the autoclave is allowed to cool automatically to room temperature, and the synthesised product is washed with DI and ethanol to remove unreacted reactant and impurities.3

2.3 Synthesis of PEDOT

The precursor solution was prepared by adding 3 mmol of EDOT to a 30 ml solution of ethanol and water in a 1:1 ratio and stirring for 30 min. Another solution of 7.5 mmol APS was prepared by dissolving it into a mixture of 20 ml ethanol and water (1:1) and mixing with the precursor solution, and continued to stir for the next 1 hr. The solution was transferred to a 100 ml stainless steel hydrothermal autoclave at 200

°C for 24 hrs. The autoclave was slowly cooled until it reached room temperature. The synthesised PEDOT was rinsed multiple times with deionized water and ethanol to eliminate any remaining unreacted compounds.⁴

2.4 Synthesis of MoSe₂-PEDOT Nanocomposite

The composite was synthesised via an in situ hydrothermal method. A mixture of 0.01 mol Na₂MoO₄.2H₂O and 0.02 mol Se powder was prepared in a solution containing 50 ml of ethanol and DI (1:1). 0.015 gm NaBH₄ was added to the above solution after 30 min. Another solution is prepared, consisting of 0.1 mmol EDOT in a 50 ml solution of ethanol and DI (1:1), and is continued to stir for 30 min. 0.25 mmol APS was added to the EDOT solution as an initiator. The resultant solution was added to the solution containing the precursor solution of MoSe₂. The resultant solution was continued to stir for 30 min at ambient temperature and then transferred to a 200 ml hydrothermal autoclave and heated at 200 °C for 24 hrs. After cooling, the resultant MoSe₂-PEDOT nanocomposite was subjected to ethanol and DI for washing to remove unreacted reactants.5

2.5 Characterization Techniques

The structural, optical, and morphological properties of the synthesised MoSe₂-PEDOT nanocomposite were systematically characterized using advanced analytical techniques. X-ray diffraction (XRD) analysis was conducted on a Rigaku Miniflex tabletop XRD equipped with Cu (Ka) ($\lambda = 1.54 \text{ Å}$) to investigate the crystallinity and phase composition of the synthesised materials. The diffraction pattern was recorded over a 2θ range of 5°- 70° at a scan rate of 2° per min. Complementing the structural insights, morphological analysis was performed using field emission scanning electron microscopy (FESEM) using a JEOL JSM 6500F electron microscope operated at 15 kV. FTIR spectroscopy was subsequently performed using a Bruker Alpha-II spectrophotometer to evaluate the functional groups.

2.6 Electrochemical Measurements

A three-electrode CH Instruments 660E electrochemical workstation was used for electrochemical experiments. A MoSe₂–PEDOT-modified glassy carbon electrode (GCE) was used as the working electrode, along





with an Ag/AgCl (3 M KCl) reference electrode and a platinum wire counter electrode. To ensure reproducibility, the GCE surface was polished with 0.3 µm alumina slurry and ultrasonically cleaned in ethanol before modification. The active nanocomposite layer was built by drop-casting $10~\mu L$ of a homogeneous MoSe₂-PEDOT suspension (2 mg/mL in ethanol) onto the GCE surface and drying under ambient conditions to establish a stable, uniform coating. Cyclic voltammetry (CV) and differential pulse voltammetry (DPV) were used to evaluate electrochemical sensing performance in 0.1 M PBS (PBS, pH 7.4) with varying 2,4-DNT concentrations. CV scans were performed at 10-150 mV/s to study reaction kinetics and interfacial charge transfer. To improve sensitivity and signal resolution in DPV, settings were carefully optimised using a pulse amplitude of 25 mV, a pulse width of 50 mS, and a step potential of 10 mV. The nanocomposite's resistance to passivation and structural degradation was demonstrated by repeated CV cycling in an electrolyte containing 2,4-DNT.

3. Results and Discussion

3.1 XRD Analysis: The crystallographic structure of pristine MoSe₂, PEDOT, and the MoSe₂-PEDOT nanocomposite investigated using X-Ray Diffraction (XRD), and the corresponding patterns are presented in Figure 1. The XRD analysis confirms the synthesis of MoSe₂-PEDOT successful nanocomposite. Pristine MoSe₂ shows sharp peaks at $2\theta = 13.7$, 29.4, 33.5, and 58.5, corresponding to the (002), (004), (100), and (110) planes of hexagonal MoSe₂, indicating good crystallinity. PEDOT shows a broad, amorphous hump around 20-30, characteristic of π - π * stacking in polymer chains. The composite retains the major crystalline peaks of MoSe₂ with slight broadening and reduced intensity, along with the broad feature of PEDOT, confirming successful integration. These structural features suggest strong interfacial interaction and partial exfoliation of MoSe₂, which are beneficial for enhancing electrochemical performance in 2,4-DNT sensing.

3.2 FTIR Analysis: The effective synthesis of MoSe₂–PEDOT is confirmed by the FTIR spectra shown in **Figure 2** of MoSe₂, PEDOT,

and their nanocomposite. Because of its layered inorganic structure, MoSe₂ exhibits little IR activity; deposited moisture is responsible for the broad absorption near 3400 cm⁻¹. Along with broad bands matching to C-H stretching vibrations, PEDOT has characteristic peaks at ~1130–3100 cm⁻¹ (C–O–C stretching), ~1270– 3100 cm⁻¹ (C–C inter-ring), and ~1510–1600 cm⁻¹ (C=C stretching). All main functional groups of PEDOT are kept in the composite spectrum with minor variations in intensity and retention, showing effective interaction between MoSe₂ and PEDOT. Near 3400 cm⁻¹, the large O-H/N-H stretching band points to surface-adsorbed species or hydrogen bonding. These spectrum characteristics support the synthesis of a chemically interacting nanocomposite, projected to offer improved conductivity and active surface functions for the selective electrochemical detection of 2,4-

3.3 Morphological Analysis: The FESEM images demonstrate different morphological characteristics of MoSe₂, PEDOT, and their nanocomposite, shown in Figure 3. Pristing MoSe₂'s layered, flake-like structures with uneven edges and great surface roughness reflect its exfoliated nanosheet form. Typical of polymeric microspheres developed during oxidative polymerisation, PEDOT shows homogeneous spherical particles with smooth surfaces. Micrographs in the MoSe₂–PEDOT composite exhibit a hybrid design whereby PEDOT microspheres are consistently embedded inside and ornamented by MoSe₂ nanosheets. Strong interfacial contact between the conducting polymer and the inorganic phase is established, and the surface area is improved by this integrated structure. High surface roughness from MoSe₂ and good electrical conductivity from PEDOT are expected to promote fast electron transport and enlarged active areas for interaction with nitroaromatic analytes. Such a synergistic shape greatly helps the composite to have better electrochemical performance for the sensitive detection of 2,4-DNT.

3.4 Electrochemical Analysis: The electrochemical behavior of MoSe₂ and MoSe₂–PEDOT nanocomposite was thoroughly investigated to evaluate their sensing performance toward 2,4-dinitrotoluene (2,4-DNT). Cyclic voltammetry (CV) in PBS



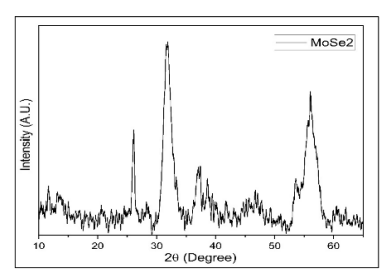


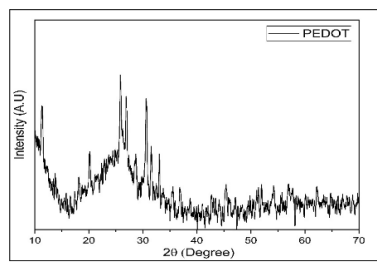
(Figure 4 A-C) reveals that the bare GCE exhibits negligible current response, while the MoSe₂-modified GCE displays improved redox activity. Notably, the MoSe₂-PEDOT nanocomposite-modified GCE demonstrates pronounced redox peaks with significantly higher current, reflecting enhanced charge transfer kinetics due to the synergistic interaction between the conductive PEDOT matrix and electroactive MoSe₂ layers. In the presence of 2,4-DNT (Figure 4 D-E), the composite exhibits a sharper and more intense cathodic peak compared to MoSe₂ alone, confirming superior electrocatalytic reduction capability. Scan rate studies (Figure 4 F) show linear current increase with scan rate, indicating a diffusion-controlled process. DPV analysis (Figure 4 G-I) reveals two distinct reduction peaks for the composite, with increasing current response proportional to 2,4-DNT

concentration. The sensor demonstrates excellent sensitivity and a calculated limit of detection (LOD) of 4 μ M, making the MoSe₂–PEDOT nanocomposite a highly promising material for nitroaromatic pollutant detection in environmental applications.

4. Conclusions

The MoSe₂–PEDOT nanocomposite was successfully synthesized via a hydrothermal in situ polymerization route and evaluated for its electrochemical sensing performance toward 2,4-dinitrotoluene (2,4-DNT). Structural analysis (XRD, FTIR) confirmed the formation of a chemically integrated hybrid with strong interfacial interaction, while FESEM revealed a well-distributed, high-surface-area morphology ideal for analyte interaction. Electrochemical studies using cyclic voltammetry (CV) and differential pulse voltammetry (DPV)





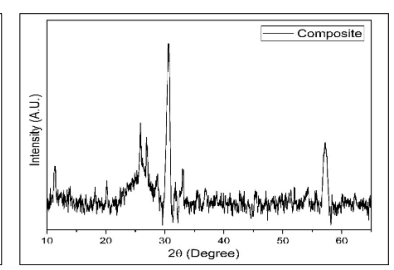
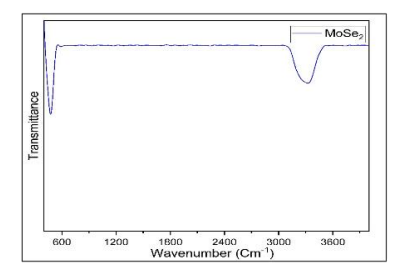
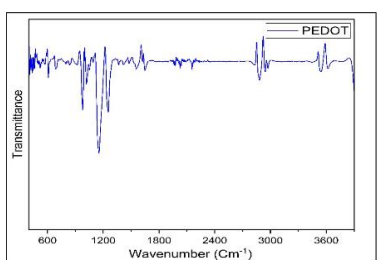


Figure (1): -Above image represents the XRD pattern of MoSe₂, PEDOT and composite material.





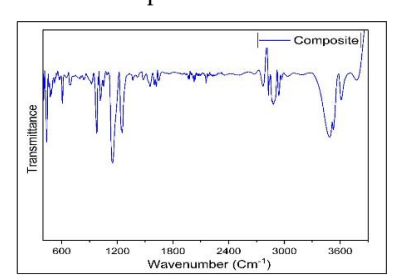
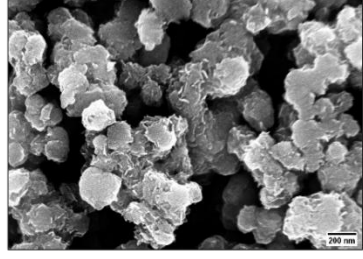
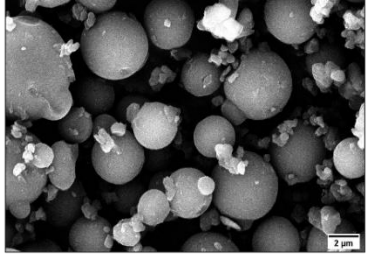


Figure (2): -Above image represents the FTIR spectra of MoSe₂, PEDOT and composite material.





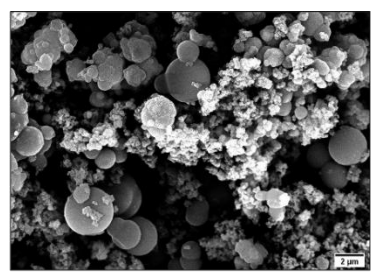


Figure (3): -The Above image represents the FESEM images of MoSe2, PEDOT, and composite material (from left to right).





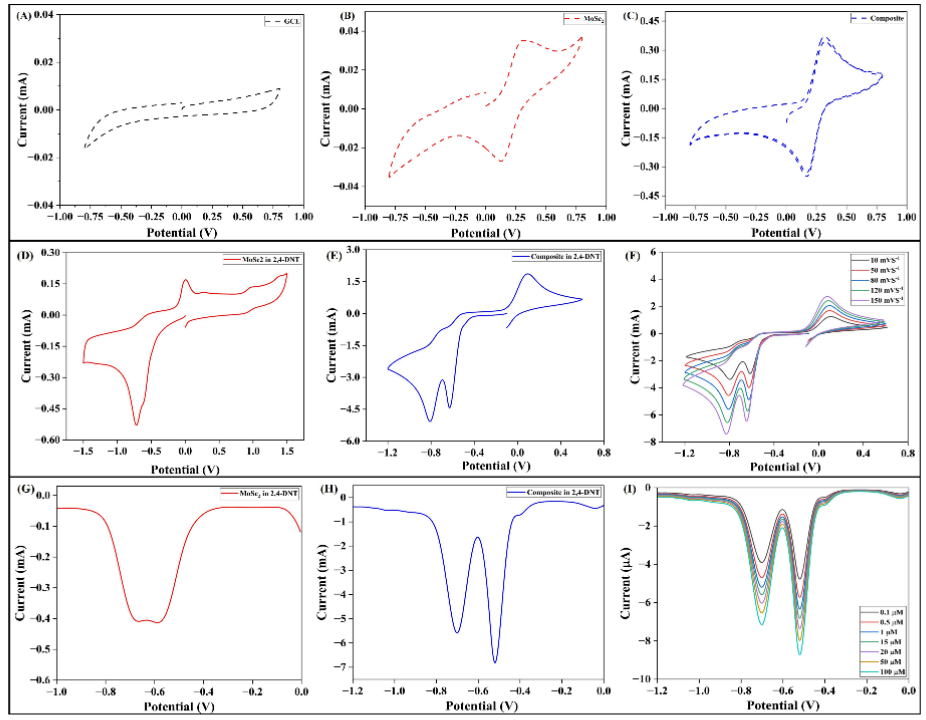


Figure (4): - (A), and (B) represents the CV of $MoSe_2$, and Composite (c) depicts the CV of the composite at different scan rates in 5mM $K_4[Fe(Cn_6)]$ and 0.1M KCl, (D), and (E) represents the CV of $MoSe_2$, and Composite (F) depict the CV of the composite at different scan rate in μ M 2,4-DNT PBS pH 7, (G), and (F) represents the DPV of $MoSe_2$, and Composite in 15 μ M 2,4-DNT PBS pH 7, (G) depict the DPV of Composite in different concentration of 2,4-DNT PBS pH 7.

demonstrated enhanced electron transfer and high current responses at the nanocompositemodified electrode compared to bare and single-component electrodes. The composite showed a strong, selective electrocatalytic response to 2,4-DNT with a clearly defined reduction peak and diffusion-controlled behavior. Importantly, the developed sensor achieved a low limit of detection (LOD) of 4 μM, highlighting its high sensitivity. These MoSe₂–PEDOT confirm the results nanocomposite as a promising material for efficient, selective, and sensitive electrochemical detection of nitroaromatic pollutants, with potential applications in environmental monitoring and water safety.

Acknowledgement

The authors gratefully acknowledge the organizers of AsiaChem 2025 for providing a prestigious platform to present and share our research work with a diverse and esteemed scientific community. The opportunity to engage with fellow researchers and gain valuable feedback has been immensely enriching. We would also like to express our

heartfelt appreciation to Netaji Subhas University of Technology (NSUT), New Delhi, for their unwavering support in terms of research infrastructure, laboratory facilities, and financial assistance. Their continued encouragement and provision of necessary resources played a crucial role in enabling our active participation in AsiaChem 2025.

References

- 1. Prasertying, P.; Suvaporn, N.; Keawmamuang, C.; Fukana, N.; Buking, S.; Wilairat, P.; Nacapricha, D. *ACS Sens.* **2025**, *10*, 2919–2927.
- Kashyap, S.; Ansari, U.; Poddar, D.; Singh, A.; Sarkar, A.; Jain, D. *Inorg. Chem. Commun.* 2025, 144, 113570.
- 3. Singh, A.; Poddar, D.; Thakur, S.; Jha, R. *Mater. Chem. Phys.* **2021**, *273*, 125043.
- 4. Ljubek, G.; Kraljić Roković, M. *J. Appl. Electrochem.* **2025**, 55, 889–904.
- Insawang, M.; Voraud, A.; Seetawan, T.; Muntini, M. S. M.; Phan, T. B.; Kumar, M. *J. Electron. Mater.* 2025, 54, 3494–3500.



E-Proceedings



Enhanced Biginelli reaction via synergistic action of squaramide and TBAB ionic liquid

Pinanong Bunthaisong, Peera Acharasatian*

Department of Chemistry, Faculty of Science and Technology, Thammasat University 99 Paholyothin Road, Prathumthani, 12120, Thailand *E-mail: peera@tu.ac.th

Abstract:

Multicomponent reactions (MCRs) have emerged as powerful tools in modern organic and medicinal chemistry for their efficiency, atom economy, and structural diversity. Among these, the Biginelli reaction—a one-pot, acid-catalyzed cyclocondensation of ethyl acetoacetate, benzaldehyde, and urea—remains a cornerstone method for synthesizing dihydropyrimidinones (DHPMs), valuable scaffolds in drug development. Traditionally, reactions were performed under reflux in ethanol with hydrochloric acid. In this study, we unveil a highly efficient alternative by leveraging the synergistic catalytic effect of squaramide derivatives and tetrabutylammonium bromide (TBAB), an ionic liquid, in the Biginelli reaction. A comparative screening of squaric acid and squaramides identified squaramide 5 as the most effective catalyst. Under optimized conditions—using TBAB as the solvent and squaramide 5 in catalytic amounts—the reaction proceeded smoothly to afford DHPM in an impressive 95% yield. In stark contrast, omitting squaramide 5 from the TBAB system resulted in a drastically lower yield (38%), and performing the reaction in ethanol with squaramide 5 gave only 34%. These findings underscore the remarkable synergy between squaramide 5 and TBAB, highlighting a potent, eco-friendly organocatalytic system for the Biginelli condensation and offering promising potential for broader synthetic applications.

1. Introduction

Multicomponent reactions¹ (MCRs), which involve the combination of three or more reactants in a single vessel to form products incorporating elements from each starting material, hold great significance in organic and medicinal chemistry. Their appeal lies in synthetic efficiency, atom economy, and the molecular diversity they offer, all of which are vital for the discovery of new lead compounds. Over the past two decades, MCRs have gained increasing attention due to their ability to generate complex molecular architectures in a one-pot manner, minimizing reaction steps, reducing waste, and simplifying procedures making them both cost-effective environmentally friendly.

Among MCRs, the Biginelli reaction stands out as a powerful method for synthesizing multifunctionalized 3,4-dihydropyrimidin-2(1H)-ones (DHPMs).² These DHPMs exhibit a broad range of biological activities, including anticancer,³ and antimicrobial⁴ properties. Originally reported by Pietro Biginelli in 1893, this reaction involves a simple one-pot condensation of benzaldehyde (1), urea (2), and ethyl acetoacetate (3) in the presence of an acid catalyst, typically under reflux to yield DHPM 4 (Scheme 1).

Traditionally, Brønsted acids have been used to catalyze the Biginelli reaction. However, recent developments have introduced a variety of catalysts, each offering improvements in reaction efficiency or selectivity.⁵ Chiral Brønsted acids, particularly chiral phosphoric acids,⁶ have shown exceptional potential in asymmetric Biginelli reactions, enhancing yields by 20–50% and delivering high enantioselectivity (ee ~94–99%).⁷

Scheme 1. Biginelli reaction implemented in the synthesis of DHPM **4**.

Of particular interest are hydrogen-bonding organocatalysts, including squaramides, which exhibit unique bifunctional activation properties. These catalysts facilitate reaction pathways through dual hydrogen bonding interactions, thereby improving both reaction rates and stereoselectivity. Kesavan *et al.* have demonstrated that squaramide-based





bifunctional catalysts are highly effective in promoting MCRs with excellent outcomes.9 In parallel, task-specific ionic liquids (TSILs) have emerged as green alternatives to conventional solvents and catalysts. 10 TSILs possess several advantageous properties: low toxicity, non-volatility, high thermal stability, broad liquid range, recyclability, and excellent solubilizing capabilities. They function not only as solvents but also as catalysts, aligning well with the principles of green chemistry.¹¹ In this study, we explore the synergistic catalytic effect of a squaramide-based organocatalyst (compounds 5 and 6) combined with tetrabutylammonium bromide (TBAB), an ionic liquid, to enhance the Biginelli reaction. This combined system aims to deliver improved yields and environmentally friendly conditions for synthesizing biologically relevant DHPM derivatives.

2. Experimental Section

General Information. Benzaldehyde, urea, ethyl acetoacetate, squaric acid, and tetrabutyl ammonium bromide were procured from Sigma-Aldrich, and organic solvents were purchased from commercial suppliers without Squaramide-based further purification. bifunctional hydrogen-bonding catalysts (compounds 5 and 6) were synthesized according to previously reported procedures.¹² Analysis of ¹H NMR and ¹³C NMR was recorded using a Bruker AVANCE NEO 400 MHz spectrometer.

General Procedure for the Synthesis of Compound 4 in TBAB. A mixture of benzaldehyde (1, 0.2122 g, 2.0 mmol), urea (2, 0.1210 g, 2.0 mmol), ethyl acetoacetate (3, 0.2656 g, 2.0 mmol), and the catalyst (0.5 mmol, 0.25 equiv) was added to a 25 mL round-bottom flask containing TBAB (350 mg) as the reaction medium. The mixture was stirred and heated at 105 °C for 4 h. Upon completion, the reaction mixture was cooled to room temperature and poured into water to precipitate the product. The solid was collected by

filtration and purified by recrystallization from EtOH to afford compound 4.

Characterization of *ethyl 6-methyl-2-oxo-4-phenyl-1,2,3,4-tetrahydropyrimidine-5-*

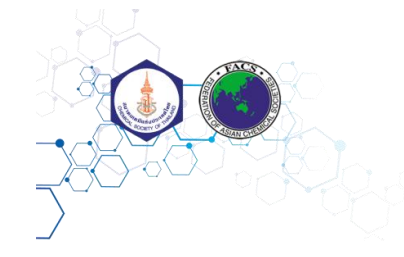
carboxylate (4): Yield: white powder (catalyst **5**: 95%; catalyst **6**: 93; catalyst **7**: 61%; catalyst-free: 38%), m.p. 211-212 °C, ¹H NMR (400 MHz, DMSO- d_6)¹³ δ 9.15 (s, 1H), 7.71 (s, 1H), 7.35–7.19 (m, 5H), 5.13 (s, 1H), 3.95 (q, J=7.1 Hz, 2H), 3.32 (s, 3H), 1.07 (t, J=7.1 Hz, 3H) ppm; ¹³C NMR (400 MHz, DMSO- d_6) δ 165.8, 152.6, 148.8, 145.3, 138.8, 137.6, 136.7, 99.8, 59.6, 54.5, 18.2, 14.5 ppm.

The experiments were reproduced using increased TBAB (700 mg). Yield: (catalyst 5: 66%; catalyst 6: 55; catalyst 7: 44%; catalyst-free: 32%).

Synthesis of Compound 4 in EtOH. To a 25 mL round-bottom flask, benzaldehyde (0.2122 g, 2.0 mmol), urea (0.1210 g, 2.0 mmol), ethyl acetoacetate (0.2656 g, 2.0 mmol), and catalyst 5 (0.5 mmol, 0.25 equiv) were added in 20 mL of ethanol. The mixture was stirred and refluxed for 4 h. After cooling, the reaction mixture was poured into water to precipitate the product. The solid was collected by filtration and recrystallized from EtOH. Characterization of compound 4: Yield: white powder (catalyst 5: 34%; catalyst-free: 34%), m.p. 211-212 °C, ¹H NMR (400 MHz, DMSO- d_6) δ 9.15 (s, 1H), 7.71 (s, 1H), 7.35–7.19 (m, 5H), 5.13 (s, 1H), 3.95 (q, J = 7.1 Hz, 2H), 3.32 (s, 3H), 1.07 (t, J) $= 7.1 \text{ Hz}, 3\text{H}) \text{ ppm}; ^{13}\text{C NMR} (400 \text{ MHz},$ DMSO- *d*₆) δ 165.8, 152.6, 148.8, 145.3, 138.8, 137.6, 136.7, 99.8, 59.6, 54.5, 18.2, 14.5 ppm.

3. Results & Discussion

The Biginelli reaction catalyzed by squaramide derivatives in TBAB as the reaction medium yielded excellent results. Initial experiments were conducted using 350 mg of TBAB. Under these conditions, squaramide catalysts 5 and 6 produced remarkably high yields of compound 4—95% and 93%, respectively (Table 1). The similar performance of 5 and 6 suggests that electron-donating and electronwithdrawing substituents are compatible with the catalytic function of squaramides in this system. Notably, 6, which contains nitro groups that are typically expected to reduce electron density on the squaramide framework, still afforded a high yield of 93%. This implies that electron-withdrawing nature





substituents does not impair catalytic activity. In contrast, the use of squaric acid (7) as a catalyst resulted in a significantly lower yield of 61%. Squaramides possess two NH groups capable of forming strong, directional bifurcated hydrogen bonds with electrophilic intermediates. These hydrogen bonds help stabilize the transition state, lower the activation energy, and increase the reaction rate. Squaric acid, on the other hand, has hydroxyl groups that can also donate hydrogen bonds but lacks the same directional and bifurcated bonding geometry, preventing effective dual-point interaction with the reaction intermediate. Consequently, catalytic performance is less efficient. The catalyst-free reaction afforded only a 38% yield. These results clearly indicate that squaramides 5 and 6 exhibit superior catalytic activity in promoting the Biginelli reaction under the studied conditions.

Table 1. Biginelli Reaction in TBAB.

Interestingly, when the amount of TBAB was increased to 700 mg, a notable decrease in product yield was observed across all conditions. Specifically, the yields dropped to 66% (catalyst 5), 55% (catalyst 6), 44% (catalyst 7), and 32% (no catalyst). This decline suggests that the catalytic performance is highly sensitive to the composition of the reaction medium. Doubling the amount of TBAB without adjusting the catalyst quantity effectively halved the molar concentration of the catalyst relative to the medium. Although the dilution factor was only two-fold, the decline in yield was disproportionately large, indicating that squaramide catalysts require a local concentration microenvironment to function effectively. It is possible that excess TBAB alters solvation

dynamics or induces changes in the aggregation state of the catalyst-substrate complex, reducing the frequency or stability of productive interactions. Therefore, the decrease in yield is likely due to catalyst dilution, which leads to diminished catalytic efficiency. These findings highlight the importance of maintaining an optimal catalyst-to-medium ratio to ensure high reactivity.

Further investigations involved replacing TBAB with EtOH as the reaction solvent while keeping other conditions constant. When the reaction was conducted in EtOH using squaramide 5 as the catalyst, the product yield dramatically decreased to 34%, which matched vield obtained under catalyst-free conditions (Table 2). This surprising result suggests that squaramide 5 is highly effective only in the presence of TBAB and not in EtOH. The dramatic decrease in yield when using EtOH (from 95% to 34%) can be attributed to the absence of the synergistic interaction between the squaramide catalyst and the TBAB ionic liquid. In TBAB, the squaramide catalyst is proposed to form bifurcated hydrogen bonds with the iminium ion intermediate, while the bromide anion stabilizes this intermediate through ion pairing. This cooperative interaction enhances both the reaction rate and product yield. In contrast, ethanol lacks this ionic environment and, therefore, cannot support the key stabilizing interactions, particularly the ion pairing. As a result, the catalytic activity of squaramide 5 significantly diminished in EtOH, yielding amounts comparable to the catalyst-free condition.

Table 2. Biginelli Reaction in EtOH.

The reduced catalytic activity observed when the catalyst concentration in TBAB was too diluted, along with the complete loss of activity when using 5 in EtOH (without TBAB), supports the hypothesis of a synergistic





interaction between **5** and the TBAB ionic liquid. It is proposed that **5** facilitates the reaction via bifurcated hydrogen bonding with the iminium ion intermediate. ¹⁴ Simultaneously, the bromide anion from TBAB likely stabilizes the intermediate via ion pairing and possibly through aggregate formation, as illustrated in Figure 1. This cooperative mechanism¹⁵ enhances the overall stabilization of key intermediates, thereby accelerating the reaction.

In the TBAB reaction medium, the absence of a squaramide catalyst results in low product yields, and substituting TBAB with ethanol fails to improve the reaction outcome. In contrast, the combination of 5 and TBAB forms a highly efficient catalytic system for the Biginelli reaction, underscoring the essential and synergistic roles of both components in facilitating this transformation.

Figure 1. Stabilization of the iminium ion intermediate via dual hydrogen bonding interactions and ion pairing.

4. Conclusions

Squaramide derivatives in TBAB have been demonstrated to be highly efficient catalysts for the Biginelli reaction, affording excellent product yields of up to 93–95%. Compared to squaric acid, squaramides exhibited significantly greater catalytic activity under identical conditions. The catalytic performance was found to be highly dependent on the concentration of the squaramide in the ionic liquid medium—excessive dilution resulted in markedly reduced yields. The data suggest a synergistic interaction between squaramide and TBAB, likely through combined dual hydrogen bonding interactions and ion-pair stabilization of the iminium ion intermediate. Notably, the use of either squaramide in EtOH or TBAB without a catalyst led to poor outcomes, with yields ranging from 34% to 38%. For future investigations, the optimized condition employing 25 mol% of catalyst 5 and 350 mg

of TBAB will be applied to the Biginelli reaction using a broader range of starting materials to further explore the scope and limitations of this catalytic system.

Acknowledgements

This work was partially supported by the Department of Chemistry, Thammasat University.

References

- 1. Domling, A. Chem. Rev. 2006, 106, 17–89.
- Alvim, H. G. O.; Lima, T. B.; de Oliveira, A. L.; de Oliveira, H. C. B.; Silva, F. M.; Gozzo, F. C.; Souza, R. Y.; da Silva, W. A.; Neto B. A. D. *J. Org. Chem.* 2014, 79, 3383-3397.
- 3. Bijani, S.; Shaikh, F.; Mirza, S.; Siu, S.; Jain, N.; Rawal, R.; Richards, N. G. J.; Shah, A.; Radadiya, A. *ACS Omega* **2022**, 7, 16278–16287.
- Parmar, M. P.; Das, A.; Vala, D. P.; Bhalodiya, S. S.; Patel, C. D.; Balachandran, S.; Kandukuri, N. K.; Kashyap, S.; Khan, A. N.; González-Bakker, A.; Arumugam, M. K.; Padrón, J. M.; Nandi, A.; Banerjee, S.; Patel, H. M. ACS Omega 2025, 10, 7013-7026.
- Oliverio, M.; Costanzo, P.; Nardi, M.; Rivalta, I.; Procopio, A. *ACS Sustain. Chem. Eng.* 2014, 2, 1228–1233.
 Chen, X.; Xu, X.; Liu, H.; Cun, L.; Gong, 1228.
- Chen, X.; Xu, X.; Liu, H.; Cun, L.; Gong, L. J. Am. Chem. Soc. 2006, 128, 14802–14803.
- 7. Saha, S.; Moorthy, J. N. J. Org. Chem. **2011**, 76, 396–402.
- 8. Hahn, R.; Raabe, G.; Enders. D. *Org. Lett.* **2014**, *16*, 3636–3639.
- 9. Kumarswamyreddy, N.; Kesavan, V. *Org. Lett.* **2016**, *18*, 1354–1357.
- Alvim, H. G. O.; de Lima, T. B.; de Oliveira, H. C. B.; Gozzo, F. C.; de Macedo, J. L.; Abdelnur, P. V.; Silva, W. A.; Neto, B. A. D. *ACS Catal.* 2013, 3, 1420–1430.
- 11. Davanagere, P. M.; Maiti, B. *ACS Omega* **2021**, *6*, 26035–26047.
- 12. Soonthonhut, S.; Acharasatian, P. *Synlett* **2022**, *33*, 1347–1352.
- 13. Yao, B-J.; Wu, W-X.; Ding, L-G.; Dong, Y-B. *J. Org. Chem.* **2021**, *86*, 3024–3032.
- 14. KAPPE, C. O. Acc. Chem. Res. **2000**, *33*, 879–888.
- **15.** Alvim, H. G. O.; Pinheiro, D. L. J.; Carvalho-Silva, V. H.; Fioramonte, M.; Gozzo, F. C.; da Silva, W. A. Amarante, G. W.; Neto, B. A. D. *J. Org. Chem.* **2018**, *83*, 12143–12153.





Synthetic study of benzoquinolizidine alkaloids: Functionalization of the piperidine ring by oxidative addition to the unsaturated lactam

Sasipa Booranamonthol, Duangkamon Namborisut, Punlop Kuntiyong*
Department of Chemistry, Faculty of Science, Silpakorn University, Sanamchandra Palace,
Muang, Nakhon Pathom, Thailand
*E-mail: kuntiyong p@su.ac.th

Abstract:

Benzoquinolizidine is an important structural feature found in many biologically active alkaloids. Herein, we discuss a synthetic study of benzoquinolizidine alkaloid emetine, focusing on the installation of a substituent on the C ring of benzoquinolizidine system using the oxidative bond formation. Emetine is a cytotoxic benzoquinolizidine alkaloid found in the root of *Psychotria ipecacuanha*. Our synthetic study led to benzoquinolizidinyl ethyl malonate ester 9 as the key precursor. We envision the installation of a malonate moiety on the piperidone C ring to be achieved by oxidative vinylogous Mannich reaction of the unsaturated lactam 9 via *N*-acyliminium ion A. DDQ was used as an oxidant while cesium carbonate was used as a base to affect the diastereoselective formation of lactone C. In addition, in a synthetic study of related compound tetrabenazine, oxygenation of the benzoquinolizidine precursor 10 was accomplished using Wacker type reaction.

1. Introduction

Benzoquinolizidine alkaloids are a prominent class of natural and synthetic compounds that exhibit diverse and potent biological activities, making them attractive scaffolds for medicinal chemistry and drug discovery. Notable examples include emetine, historically used as an anti-amoebic agent and more recently recognized for its antiviral and anticancer activities via inhibition of protein synthesis and induction of apoptosis.1 Its biosynthetic precursor, protoemetinol, although studied, shares the core structure and presents a simplified scaffold for further drug development. Synthetic derivatives such as tetrabenazine (a VMAT2 inhibitor for Huntington's disease)² and carmegliptin (a DPP-4 inhibitor for type 2 diabetes)³ further highlight the therapeutic relevance of this scaffold. Additionally, tetrahydropalmatine demonstrates sedative and analgesic effects, with potential applications in anxiety and addiction treatment.⁴ The chemical structures of these representative compounds are shown in Figure 1. These examples underscore the pharmacological significance benzoquinolizidines and the need for efficient synthetic methodologies to access them.

We have previously reported synthesis of benzoquinolizidine 1 via diastereoselective *N*-acyliminium ions cyclization. The chiral *N*-acyliminium ion was derived from 2-(3,5-dihydroxyphenyl) ethylamine and derivative of

L-glutamic acid as a starting material. The dibenzylamino group gave stereocontrol in the reaction. After reaction the key dibenzylamino group was removed using Cope elimination to give conjugated unsaturated lactam 2 which could readily be converted to the allylated benzoquinolizidine 3 and methyl ether 4 via conjugate nucleophilic addition.⁵ On the other hand, we also reported Cope elimination of benzoquinolizidines 5 and 6 giving non-conjugated unsaturated lactams 7 and 8. Installation of a substituent on the lactam C ring in this case cannot proceed via conjugate addition.6

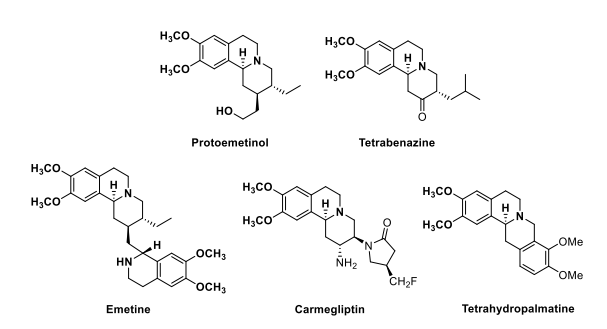


Figure 1. Examples of bioactive molecules of benzoquinolizidine skeleton.

In this work, we discuss a synthetic study of emetine via protoemetinol as the key precursor. Installation of the substituent on the unsaturated lactam C ring would employ the oxidative vinylogous Mannich reaction. This strategy was an adaptation from a one-pot





transformation strategy reported by Jung and Min.⁷ They synthesized benzoquinolizidine via the aza-Michael and oxidative Mannich process, in which DDQ was a key oxidant with high diastereoselectivity. In addition, in a synthetic study of related compound tetrabenazine, oxygenation of the benzoquinolizidine precursor was accomplished using Wacker-type reaction.

Our previous work

Scheme 1. Our previous reports on synthesis of benzoquinolizidines

Scheme 2. Functionalization of the piperidine ring by oxidative addition to the unsaturated lactam

2. Experimental Methods

All reagents and starting materials were obtained from commercial sources and used without further purification. Reaction progress was monitored by TLC on Fluka silica gel 60 F-254 plates (0.2 mm) and visualized under UV light or by heating after staining with 1%

vanillin in 0.1 M H₂SO₄/EtOH. Flash chromatography was performed using 40 μm silica gel (Scientific Absorbents Inc.). NMR spectra (¹H and ¹³C) were recorded on a Bruker Avance-300 spectrometer in CDCl₃ with TMS as the internal standard.

2.1.(*R*)-1-((3*S*,11b*S*)-9,10-dimethoxy-4-oxo-3,6,7,11b-tetrahydro-4*H*-pyrido[2,1-*a*]iso-quinolin-3-yl)ethyl methyl malonate (9)

Malonic acid was dissolved in a mixture of HCl/MeOH. The reaction mixture was then concentrated under reduced pressure. To a solution of alcohol 7 (20.0 mg, 0.07 mmol) in 5 mL CH₂Cl₂, EDCI (50.6 mg, 0.26 mmol), DMAP (1.2 mg, 0.01 mmol), and an excess of malonate was added. The reaction mixture was stirred at room temperature overnight. The reaction was quenched with sat. aq. NaHCO₃ (10 mL) and extracted with CH₂Cl₂ (3×10 mL). The combined organic layers were dried over anh. Na₂SO₄, filtered and evaporated under reduced pressure. Purification of the crude material by thin layer chromatography (silica gel, 1:2 Hexane/EtOAc) produced malonate 9 (32 mg, 88%) as a yellow oil. ¹H NMR (300 MHz, CDCl₃) δ: 6.76 (s, 1H), 6.64 (s, 1H), 6.42 (dd J = 10.0, 4.86 Hz, 1H), 6.04 (d J = 10.0 Hz, 1H), 5.25 (m, 1H), 4.65 (m,2H), 3.90 (s, 3H), 3.88 (s, 3H), 3.71 (s, 3H), 3.43 (s, 2H), 3.25-3.24 (m, 1H), 3.06-3.01 (m, 2H), 2.67-2.62 (m, 1H), 1.41 (d J = 6.4 Hz, 3H): ¹³C NMR (75 MHz, CDCl₃) δ: 166.8, 165.8, 163.3, 148.3, 147.4, 136.6, 128.5, 127.9, 126.1, 112.3, 107.5, 72.8, 56.7, 56.3, 55.9, 52.6, 42.2, 41.9, 41.5, 27.6, 16.6.

2.2 Methyl (8a*S*,9*R*,12a*S*)-2,3-dimethoxy-9-methyl-8,11-dioxo-5,8a,9,11,12,12a-hexa-hydro-6*H*,8*H*-pyrano[4',3':4,5]pyrido[2,1-*a*]isoquinoline-12-carboxylate (11).

To a solution of lactam 9 (6.5 mg, 0.02 mmol) in CH₂Cl₂ (5 mL) was added DDQ (17.0 mg, 0.08 mmol), and Cs₂CO₃ (20 mg, 0.24 mmol). The mixture was heated to reflux for 2 days. The reaction was quenched with 1M NaOH and extracted with CH₂Cl₂ (3x10 mL). The organic phase was washed with water and brine, dried over anh. Na₂SO₄, filtered and evaporated under reduced pressure. Purification of the crude material preparative thin layer chromatography (silica gel, 1:2 Hexane/EtOAc) produced lactone 11 (3.2 mg, 49%, dr = 10:1) as a yellow oil along with alcohol 7 (2.3 mg, 47%). ¹H NMR (300





MHz, CDCl₃) δ : 6.88 (s, 1H), 6.84 (s, 1H), 5.67 (d J = 6.7 Hz, 1H), 4.76-4.66 (m, 1H), 3.85 (s, 3H), 3.75 (s, 3H), 3.66 (s, 3H), 3.56-3.52 (m, 3H), 3.26 (d J = 7.3 Hz, 1H), 3.22-3.15 (m, 2H), 2.70-2.61 (m, 1H), 1.80 (d J = 7.3 Hz, 3H); ¹³C (75 MHz, CDCl₃) δ : 170.0, 169.9, 163.4, 148.9, 146.9, 134.9, 129.4, 128.0, 111.4, 109.7, 100.2, 70.0, 56.2, 56.1, 51.9, 50.6, 48.9, 44.0, 27.2, 24.2, 16.8.

2.3 Benzoquinolizidine acetate 10

To a solution of alcohol 8 (46.5 mg, 0.14 mmol) in dried CH₂Cl₂ (1 mL) was added pyridine (1 drop) under an argon atmosphere. To this solution was added excess Ac₂O (0.50mL) and stirred overnight. The reaction was quenched with sat. aq. NaHCO3 and extracted with CH₂Cl₂ (3 x 5 mL). The combined organic layers were dried over anh. Na₂SO₄, filtered and evaporated under reduced pressure to give the product 10 (quantitative yield) as a yellow oil. ¹H NMR (300 MHz, CDCl₃) δ : 6.70 (s, 1H), 6.62 (s, 1H), 6.40 (dd J = 6.7, 2.3 Hz, 1H), 5.95 (d J = 6.7 Hz, 1H), 5.18 (m, 1H), 4.68 (m, 1H), 4.50 (s, 1H), 3.89 (s, 3H), 3.85 (s, 3H), 3.20 (m, 2H), 3.05 (m, 1H), 2.65 (m, 1H), 2.12 (s, 3H), 2.05 (m, 1H), 1.08 (d J = 7.0 Hz, 2H), 0.98 (d J = 7.0 Hz, 2H); ¹³C NMR (75 MHz, CDCl₃) δ: 169.8, 146.2, 145.2, 138.5, 128.2, 127.33, 126.6, 126.3, 124.7, 109.3, 107.0, 67.3, 55.9, 54.1, 53.40, 41.1, 40.6, 23.9, 27.4, 19.3.

2.4 Benzoquinolizidine vinyl acetate 12

A solution of unsaturated lactam-acetate 10 (20 mg, 0.05 mmol) in toluene (5 mL) was treated with Pd(OAc)₂ (13 mg, 0.06 mmol) and Na₂CO₃ (14 mg, 0.12 mmol) and the mixture was heated to reflux for 12 hours. The reaction was concentrated under reduced pressure and water (10 mL) was added. The mixture was extracted with CH₂Cl₂ (3×10 mL). The combined organic layers were dried over anh. Na₂SO₄, filtered and evaporated under reduced pressure. Purification of the crude material by preparative thin layer chromatography (silica gel, 1:2 Hexane/EtOAc) produced vinyl acetate 12 (13.4 mg, 67%) as a yellow oil. ¹H NMR (300 MHz, CDCl₃) δ: 7.49 (s, 1H), 6.71 (s, 1H), 6.05 (dd J = 5.1, 1.5 Hz, 1H), 5.59 (s, 1H), 4.28 (d J = 1.5 Hz 1H), 3.96 (s, 3H), 3.86(s, 3H), 3.84-3.80 (m, 1H), 3.54-3.50 (m, 1H), 2.99-2.84 (m, 1H), 2.17 (s, 3H), 2.14-2.10 (m, 1H), 1.02 (d J = 6.9 Hz, 3H), 0.99 (d J = 6.9Hz, 3H); ¹³C NMR (75 MHz, CDCl₃) δ: 168.0,

157.0, 148.0, 146.8, 146.7, 140.8, 132.4, 129.5, 125.9, 111.5, 109.5, 100.6, 56.3, 56.1 (2C), 45.7, 29.3, 24.6, 22.3 (2C), 21.2.

3. Results and Discussion

The synthesis of functionalized benzoquinolizidine started with conversion of the alcohol 7 to malonate ester 9 via EDCImediated esterification with methyl malonate monoester in the presence of DMAP in dichloromethane. This key precursor underwent oxidative vinylogous Mannich cyclization under the influence of DDO, via single-electron oxidation at the nitrogen center to generate an N-acyliminium ion intermediate **A**. This electrophilic species was attacked by the enolizable malonate side chain at the vinylogous site, resulting diastereoselective ring closure to form lactone 11. DDQ plays a critical role in forming the iminium intermediate under mild, metal-free conditions. Cs₂CO₃ served as a mild, nonnucleophilic base that facilitated deprotonation of the malonate side chain, thereby enhancing its nucleophilicity and promoting efficient C-C bond formation. Unfortunately, the product was obtained in moderate yield due to partial hydrolysis of the malonate ester to give alcohol 7 as the undesired side product. In a related study of the synthesis of tetrabenazine, alcohol 8 with an isopropyl group was converted to acetate 10 in a standard procedure. Treatment of this compound with palladium acetate resulted in addition of the acetyl group to the unsaturated lactam ring in a Wacker type reaction to give vinyl acetate 12 via organopalladium intermediate **B**. This compound will be used for the synthesis of commercial drug tetrabenazine.

Scheme 3. Oxidative vinylogous Mannich reaction of unsaturated lactam **9**





$$\begin{array}{c} \text{H}_3\text{CO} \\ \text{H}_3\text{C$$

Scheme 4. Oxygenation of the unsaturated lactam **10** via Wacker-type reaction

4. Conclusions

In this study, we demonstrated the synthesis of benzoquinolizidine scaffold via oxidative vinylogous Mannich reaction unsaturated lactam 9 derived from L-glutamic acid. The key transformation involved the diastereoselective formation of lactone 11 using DDQ as an oxidant and cesium carbonate as a base. Based on the structural framework obtained, it is expected that lactone 11 can be further converted to protoemetinol through decarboxylation followed by directed reduction. In addition, in a synthetic study of unsaturated tetrabenazine, lactam underwent intramolecular Wacker-type reaction in which the acetate group added to the C=C bond in the presence of palladium acetate. The product 12 has the desired functionality for the synthesis of commercial drug tetrabenazine. This synthetic strategy provides a promising platform for the preparation of emetine analogs and highlights the utility of amino acid-derived intermediates in alkaloid synthesis.

Acknowledgments

This work was financially supported by Thailand Science Research and Innovation (TSRI)'s Fundamental Fund (FF67) and the Faculty of Science, Silpakorn University's Grant SRF-JRG-2566-13. SB is supported by a scholarship for Master Student Research Assistant from the Faculty of Science, Silpakorn University.

References

1. Kumar, R.; Afsar, M.; Khandelwal, N.; Chander, Y.; Riyesh, T.; Dedar, R.; Gulati, B. R.; Pal, Y.; Barua, S.; Tripathi,

- B. N.; Hussain, T.; Kumar, N. *Antiviral Res.* **2021**, *189*, 105056.
- 2. Paleacu, D. *Neuropsychiatr. Dis. Treat.* **2007**, *3*, 743–748.
- Mattei, P.; Boehringer, M.; Di Giorgio, P.; Fischer, H.; Hennig, M.; Huwyler, J.; Koçer, B.; Kuhn, B.; Loeffler, B. M.; MacDonald, A.; Narquizian, R.; Rauber, E.; Sebokova, E.; Sprecher, U. Bioorg. Med. Chem. Lett. 2010, 20, 1109–1113.
- 4. Du, Q.; Meng, X.; Wang, S. Front. *Pharmacol.* **2022**, *13*, 890078.
- 5. Kuntiyong, P.; Piboonsrinakara, N.; Bunrod, P.; Namborisut, D.; Akkarasamiyo, S.; Songthammawat, P.; Hemmara, C.; Buaphan, A.; Kongkathip, B. *Heterocycles* **2014**, *89*, 437–452.
- 6. Kuntiyong, P.; Namborisut, D.; Phakdeeyothin, K.; Chatpreecha, R.; Thammapichai, K. *Molecules* **2021**, *26*, 5866
- 7. Jung, A.; Min, S.-J. *Asian J. Org. Chem.* **2019,** *8*, 1617–1620.





Total synthesis of piperlongumine and its analogs from L-glutamine

Phongsathon Khlongkhlaeo, Punlop Kuntiyong*

Department of Chemistry, Faculty of Science, Silpakorn University, Sanamchandra Palace, Muang,
Nakhon Pathom, Thailand
*E-mail: kuntiyong p@su.ac.th

Abstract:

Piperlongumine, a potent cytotoxic amide alkaloid from long pepper, *Piper longum*, was synthesized along with its 3-dibenzylaminopiperlogumine analog from L-glutamine and 3,4,5-trimethoxycinnamic acid. The key intermediate (3S)-dibenzylaminoglutarimide was formed in 2 steps from L-glutamine via *N*-benzylation and 1,1'-carbonyldiimidazole (CDI)-mediated cyclization. Reduction of one of the glutarimide carbonyl with Lithium Aluminum Hydride (LAH) gave 3-dibenzylamino- δ -lactam along with 3-dibenzylaminopiperidine. Cope elimination of the dibenzylamino group gave the unsaturated δ -lactam. Coupling reaction of the lactam with 3,4,5-trimethoxycinnamic acid would give piperlongumine. In addition, amide formation of 3-dibenzylaminopiperidine with 3,4,5-trimethoxycinnamic acid gave the dibenzylamino analog of piperlongumine which could be converted to the natural product by Cope elimination and amide oxidation. In addition, the amino group will provide a variation point for further synthesis of other analogs of piperlongumine for evaluation of medicinal properties of the synthetic compounds in the future.

1. Introduction

Piperlongumine is a cytotoxic alkaloid found in Piper longum (deepli) which has been used as spice and medicinal herb in Thailand and other countries in South and South East Asia. Deepli is used for remedies for indigestion, other respiratory-related cough abnormality as well as intestinal worm and hemorrhoid. It can also be mixed with other herbs in medicine ball for local muscle aches and bruises. Studies of chemical constituents of deepli extract showed that piperlongumine and piperine are important ingredients which exhibit anti-colon and liver cancers as well as anti-bacterial, anti-inflammatory and antiplatelet aggregate activities. Piperlongumine was extracted from roots of Piper longum in 1% w/w amount. To date, there are several reports regarding biological activities of piperlongumine, its derivatives and analogs especially as anti-cancer agents. However, it has not been developed into a cancer drug in climical. addition. piperine and found piperlongumine were in Piper retrofractum Vahl as reported Wattanapiromsakul along with other alkaloids such as salvatine, piperlonguminine and methyl piperate.1 They also reported that piperine and piperlonguminine inhibited M. tuberculosis with MIC of 50.00 µg/mL. whereas methyl piperate and sylvatine were

inactive. The compounds were tested against lung cancer cells (SCLC-H22 and NCI-H187) and human gingival fibroblasts (HGF). Piperine, piperlonguminine, methyl piperate and sylvatine were active against SCLC-H22 and NCI-H187 but less active against human gingival fibroblasts (HGF) (% inhibition less than 20 % at 5 µg/mL or % inhibition less than 50 % at 50 µg/mL). In addition, a methanol extract was moderately active against NCI-H187 and human gingival fibroblasts (HGF) with IC₅₀ of 20.98 µg/mL and % inhibition = 57 at 25 µg/mL concentration, respectively² (Figure 1).

Figure 1. The chemical constituents of *Piper longum*





a previously reported synthesis piperlogumine and derivatives by Bradshaw and Moses, unsaturated δ-lactam 5 was synthesized from δ -valerolactam (1) in 5 steps which involve N-protection to give N-Boc carbamate 2, α-thinoylation for phenylsulfide 3 and oxidation of the sulfide and subsequent elimination of benzenesulfonyl to give intermediate 4 and deprotection of Boc carbamate with hydrochloric acid. Amide formation of the unsaturated lactam 5 with trimethoxycinnamoyl chloride gave piperlongumine.³ In addition, Schrieber reported a two-step synthesis of unsaturated lactam 5 from butenylamine hydrocholirde (7) and acryloyl chloride (8) to obtain Nbutenylacrylamide **(9)**. Ring closing metathesis of this diene gave unsaturated δ lactam 5 in 2 steps. However, the amine starting material 7 is expensive and acryloyl chloride is a highly toxic irritant (Scheme 1).4 In this work, we developed a new synthetic route for unsaturated lactam 5 for the synthesis of piperlongumine and its 3-dibenzylamino analogs from cheap and readily available starting material L-glutamine and 3,4,5trimethoxycinnamic acid.

Bradshaw and Moses

Scheme 1. Previously reported syntheses of piperlongumine

2.Methods and Experimental 2.1 Materials

1g = 3.900 Baht

Starting materials and reagents were obtained from commercial sources and were used without further purifications. Solvents were dried by distillation from the appropriate drying reagents. Tetrahydrofuran (THF) was distilled from sodium and benzophenone under argon. Moisture and air sensitive reactions were carried out under an atmosphere of argon. Reaction flasks and glassware were oven dried at 105 °C overnight. Unless otherwise stated, concentration was performed under reduced pressure. Analytical thin layer chromatography (TLC) was conducted using Fluka precoated TLC plates (0.2 mm layer thickness of silica gel 60 F-254). Compounds were visualized by ultraviolet light or by heating the plate after dipping in a 1% solution of vanillin in 0.1 M sulfuric acid in EtOH. Flash chromatography was carried out using Scientific Absorbents Inc. silica gel (40 mm particle size)

2.2 Spectroscopic measurement

Proton and carbon nuclear magnetic resonance (NMR) spectra were obtained using a Bruker Avance-300 spectrometer.

2.3 Synthesis of compounds

2.3.1 Synthesis of *N*,*N*-dibenzylaminoglutarimide 10

To a solution of N,N-dibenzyl L-glutamine (611 mg, 1.80 mmol) in CH₂Cl₂ was added N,N-carbonyldiimidazole (CDI) (875 mg, 5.39 mmol), 4-dimethylaminopyridine (DAMP) (22.0 mg, 0.180 mmol), triethylamine (Et₃N) (1.00 mL, 5.39 mmol) and the mixture was stirred for 12 hours at room temperature under argon atmosphere. To this mixture was added water and the mixture was extracted with CH₂Cl₂ (3 x 20 mL). The combined organic layers were dried over anhydrous Na₂SO₄, filtered, and concentrated under reduced pressure. The crude product was purified by chromatography (silica gel, hexanes/EtOAc) to give N,N-dibenzylamino glutarimide 10 (474 mg, 85%) as white amorphous solid.

Compound **10**; ¹H NMR (300 MHz, CDCl₃) δ : 8.34 (brs, NH), 7.57-7.21 (m, 10H), 4.00 (d J = 14.0 Hz, 2H), 3.76 (d, J = 14.0 Hz, 2H), 3.50 (dd J = 11.2, 6.5 Hz, 1H), 2.69 (dt J = 17.2, 3.2 Hz, 1H), 2.43 (dt J = 17.2, 3.2 Hz, 1H), 2.18-2.04 (m, 2H); ¹³C NMR (75 MHz, CDCl₃) δ : 23.1 (2C), 31.6 (2C), 55.1 (2C),





58.7 (1C), 127.4 (2C), 128.5 (4C), 128.8 (4C), 139.7 (2C), 173.0 (C=O), 173.7 (C=O).

2.3.2 Synthesis of 3-dibenzylamino-δ-lactam 11 and 3-dibenzylaminopiperidine 12

solution of *N*,*N*-dibenzylamino glutarimide 10 (171 mg, 0.56 mmol) in THF under argon atmosphere at 0 °C and was added LiAlH₄ (42 mg, 1.11 mmol) and the mixture was heated to reflux at 80 °C for 3 hours. After allowed to cool to room temperature, to this mixture was added dropwise sat. aq. NaHCO₃ (2 mL) water (8 mL) and the resulting mixture was extracted with EtOAc (3 x 10 mL). The combined organic layers were dried over anhydrous Na₂SO₄, filtered, and concentrated under reduced pressure. The crude product was purified by flash chromatography (silica 1:1 hexanes/EtOAc) to give dibenzylamino-δ-lactam 11 (30 mg, 18%) and 3-dibenzylaminopiperidine 12 (71 mg, 43%) Compound 11 ¹H NMR (300 MHz, CDCl₃) δ: 7.45-7.19 (m, 10H), 5.97 (brs, NH), 4.05 (d J = 14 Hz, 2H), 3.75 (d J = 14 Hz, 2H), 3.28 (dd J = 6.5, 11.0 Hz, 1H), 3.19(t J = 4.6 Hz, 2H), 2.20-2.00 (m, 2H), 1.85-1.75 (m, 2H); ¹³C NMR (75 MHz, CDCl₃) δ: 22.4 (1C), 27.2 (1C), 42.2 (1C), 55.4 (2C), 58.0 (1C), 126.8 (2C), 128.2 (4C), 128.6 (4C), 140.5 (2C), 173.4 (C=O).

Compound 12 ¹H NMR (300 MHz, CDCl₃) δ : 7.42-7.17 (m, 10H), 4.04 (brs, NH), 3.72 (d J = 14 Hz, 2H), 3.66 (d J = 14 Hz, 2H), 3.26 (d J = 11.0 Hz, 1H), 3.04 (d J = 12.1 Hz, 1H), 2.28-2.75 (m, 1H), 2.64 (t J= 11.5 Hz, 1H), 2.50-2.43 (m, 1H), 2.10-188 (m, 1H), 1.86-1.64 (m, 1H), 1.60-1.40 (m, 1H); ¹³C NMR (75 MHz, CDCl₃) δ : 23.0 (1C), 30.4 (1C), 45.5 (1C), 47.7 (1C), 55.4 (2C), 62.3 (1C), 127.0 (2C), 128.4 (4C), 128.9 (4C) 140.1 (2C).

2.3.3 Synthesis of unsaturated δ-lactam 5

To a solution of 3-dibenzylamino-δ-lactam 11 (60 mg, 0.20 mmol) in CH₂Cl₂ was added mchloroperbenzoic acid (m-CPBA) (70%, 74 mg, 0.30 mmol) and the mixture was stirred for 1 hour at room temperature. To this mixture was added sat. aq. Na₂CO₃ (10 mL) and the mixture was extracted with CH₂Cl₂ (3 x 10 mL). The combined organic layers were dried over anhydrous Na₂SO₄, filtered, and concentrated under reduced pressure. The purified crude product was by flash chromatography (silica gel, 1:2

hexanes/EtOAc) to give unsaturated δ -lactam 5 (12 mg, 63%) as a colorless oil.

Compound **5** ¹H NMR (300 MHz, CDCl₃) δ : 1H NMR (300 MHz, CDCl₃) δ : 6.67(dt J = 9.9, 4.11 Hz, 1H), 5.92 (d J = 1.7 Hz, 1H), 3.44(dt J = 7.04, 2.23 Hz, 2H), 2.40-2.34 (m, 2H) ¹³C NMR (75 MHz, CDCl₃) δ : 22.4 (1C), 37.5 (1C), 123.7 (1C), 140.5 (1C), 165.6 (C=O).

2.3.4 3-Dibenzylaminopiperlogumine 13

To a solution of 3.4.5-trimethoxycinnamic acid (43 mg, 0.18 mmol) in CH₂Cl₂ (10 mL) were added 3-dibenzylaminopiperidine 12 (50 mg, 0.18 mmol) and EDCI (83 mg, 0.53 mmol) and DMAP (5 mg) and the mixture was stirred at room temperature overnight. To this mixture was added water (10 mL) and it was extracted with CH₂Cl₂ (3 x 10 mL). The combined organic layers were dried over anhydrous Na₂SO₄, filtered, and concentrated under reduced pressure. The crude product purified by Preparative thin-layer chromatography (1:1 hexanes/EtOAc) to give 3-dibenzylamino analog 13 of piperlogumine (68 mg, 76%) as a colorless oil.

Compound **13** ¹H NMR (300 MHz, CDCl₃) δ : 7.29-7.21 (m, 10H), 7.32 (d J = 15.1 Hz, 1H), 7.03 d J = 15.1 Hz, 1H), 6.91 (s, 2H), 3.83 (s, 6H), 3.76 (s, 4H), 3.71 (s, 3H), 3.53-3.38 (m, 4H), 2.82-2.78 (m, 1H), 1.74-1.49 (m, 4H); ¹³C NMR (75 MHz, CDCl₃) δ : 23.3, 32.0, 47.2, 51.0, 56.1 (2C), 57.0 (2C), 60.8, 62.5, 103.8 (2C), 118.8, 127.2 (2C), 128.4 (4C), 128.8 (4C), 130.3, 138.4, 138.6 (2C), 141.7, 153.0 (2C), 166.3 (C=O).

3. Results and Discussion

The synthesis of unsaturated lactam 5 started from the benzylation of L-glutamine in under basic conditions using benzyl chloride, K₂CO₃, and NaOH in MeOH and H2O to give N,Ndibenzyl glutamine. This compound underwent CDI-mediated cyclization to give N,N-dibenzylamino glutarimide 10 in good yield. Reduction of the glutarimide with LAH in refluxing THF gave a mixture of 3dibenzylaminolactam 11 and dibenzylaminopiperidine 12 in a ca. 1:2 ratio. Cope elimination of the dibenzylamino group in lactam 11 gave unsaturated lactam 5 in a respectable yield (Scheme2).





The unsaturated lactam **5** was the key intermediate that could be converted to piperlongumine by coupling with 3,4,5-trimethoxycinnamoyl chloride according to the procedure reported by Bradshaw. In addition, 3-dibenzyl-aminopiperidine **12** underwent amide formation with 3,4,5-trimethoxycinnamic acid in the presence of EDCI and DMAP to give the dibenzylamino analog **13** of piperlongumine in good yield (Scheme 3).

Scheme 2. Synthesis of unsaturated δ -lactam 5

Scheme 3. Synthesis of 3-dibenzylaminopiperine analog **13**

In conclusion, we developed a new synthetic route for the unsaturated δ -lactam 5 for synthesis of piperlongumine and its 3dibenzylamino analog 13 from cheap and readily available starting material L-glutamine 3,4,5-trimethoxycinnamic acid. synthesis is shorter than the previously reported synthesis by Bradshaw comparable yield and used cheaper and greener starting material than both reported syntheses. In addition, the amino group will provide a variation point for further synthesis of other analogs of piperlongumine for evaluation of their medicinal properties in the future.

Acknowledgements

This work was financially supported by Thailand Science Research and Innovation (TSRI)'s Fundamental Fund (FF67) and the Faculty of Science, Silpakorn University's Grant SRF-JRG-2566-13. Phongsathon is supported by a scholarship for Master Student Research Assistant from the Faculty of Science, Silpakorn University.

Research Ethics/Declarations

Authors declare no conflict of interest.

References

- 1. Amad, S.; Yuenyongwad, S.; Wattanapiromsakul, C. *Walailak J. Sci. Tech.* **2017**, *14*, 731–739.
- 2. Tripathi, S. K.; Biswal, B. K. *Pharmacol. Res.* **2020**, *156*, 104772.
- 3. Han, L.; Stanley, P.; Wood, P.; Sharma, P.; Kuruppu, A.; Bradshaw, T.; Moses, J. *Org. Biomol. Chem.* **2016**, *14*, 7585–7593.
- Adam, D. J.; Dai, M.; Pellegrino, G.; Wagner, B. K.; Stern, A. M.; Shamji, A. F.; Schreiber, S. L. *Proc. Natl. Acad. Sci. U.S.A.* 2012, 109, 15115–15120.





Cellular responses of MC3T3-E1 on peptide-functionalized chitosan

<u>Chatchai Purananunak</u>, Pichamon Kiatwuthinon, Chantiga Choochottiros, Weeraphat Pon-On, Chomdao Sinthuvanich 1,2,*

¹Department of Biochemistry, Faculty of Science, Kasetsart University, Bangkok, Thailand ²Specialized center of Rubber and Polymer Materials in agriculture and industry (RPM), Faculty of Science, Kasetsart University, Bangkok, Thailand

³Department of Materials Science, Faculty of Science, Kasetsart University, Bangkok, Thailand ⁴Department of Physics, Faculty of Science, Kasetsart University, Bangkok, Thailand *E-mail: chomdao.si@ku.th

Abstract:

Chitosan, a biocompatible biomaterial, has been widely explored for bone regeneration applications, with chemical modifications enhancing its osteogenic properties. In this study, extracellular matrix (ECM)-derived peptides including RGD (RGD) and Ten2 (VFDNFVLK), derived from canonical ECM proteins, fibronectin and tenascin C, respectively, were used. These thiol-tagged peptides were covalently conjugated to chitosan via N-(m-maleimidobenzoyloxy)succinimide (MBS), resulting in maleimide-conjugated chitosan (MB-chitosan, control), as well as peptide-conjugated chitosan variants, including RGD-chitosan and Ten2-chitosan. This work aimed to investigate how specific functional peptide sequences influence biological responses at various levels, including cell morphology, adhesion, and mineralization. The results revealed that MB-chitosan, RGD-chitosan, and Ten2-chitosan effectively facilitated cell adhesion, with adhesion percentage of 100, 122 ± 14 , and 117 ±18, respectively. Moreover, morphological changes, including cell spreading and the formation of well-defined actin filament structures, were observed during initial interactions under serum-free conditions. Notably, Ten2-chitosan significantly enhanced mineralization over a 21-day culture period, as indicated by a higher normalized calcium content (4.04 ± 0.60 ng/ng total protein) compared to the mineralization control polystyrene (2.18 ±0.10 ng/ng total protein). Overall, improved cell adhesion and mineralization are indicative of osteoblast differentiation, implying the potential of the biomaterials to support bone regeneration.

1. Introduction

Chitosan has long been recognized as a valuable scaffold material for supporting bone development due to its inherent biocompatibility and ease of modification. Chitosan modification increasingly focused on enhancing osteogenic potential, particularly by addressing its limited capacity for cellular adhesion.1 However, a major limitation of chitosan in bone tissue engineering is its low cellular affinity, which hinders attachment cell and development.²

The application of peptide-conjugated materials, such as RGD-conjugated scaffolds, to enhance cell-adhesive properties has been extensively studied using various approaches, including chitosan-based scaffolds and titanium surfaces.^{3, 4} To covalently conjugate biologically derived peptides onto chitosan, the primary amine groups of chitosan were chemically modified using various linkers such as carbodiimide (EDC/NHS) coupling with N-

acetylcysteine and succinic anhydride, to introduce carboxyl groups.^{5, 6}

In this study, chitosan was chemically modified N-(m-maleimidobenzoyloxy)succinimide (MBS), which selectively reacts with primary amine groups to yield maleimidefunctionalized chitosan (MB-chitosan).⁷ This enables site-specific conjugation of cysteinecontaining peptides via a stable thiol-maleimide linkage under physiological conditions. ECMderived peptides, including RGD (RGD) and Ten2 (VFDNFVLK), derived from canonical ECM proteins, fibronectin and tenascin C, respectively, were covalently conjugated onto MB-chitosan.^{3, 8} Thus, peptide-functionalized chitosan represents a promising biomaterial for bone cell support due to its enhanced biocompatibility and tailored functionalization. Accordingly, this study aimed to evaluate the impact of functional peptide sequences on biological responses at multiple levels, including cell morphology, adhesion, and mineralization. The insights gained from this work are expected to support the development



and application of peptide-functionalized chitosan in bone tissue engineering.

2. Methods

2.1 Fabrication of peptide-functionalized chitosan

A schematic of surface modification is described in Figure 1. To start, chitosan film was prepared via a sequential surface modification strategy. A 0.5% (w/v) chitosan solution in 2% (v/v) acetic acid was cast into 24- or 8-well plates to achieve a coating density of 1.32 mg/cm², followed by drying in a hot-air oven at 37 °C for 24 hours to allow film formation. The dried films were treated with 0.25 M NaOH for 1 hour. The films were incubated with 1.33 mM MBS in 10% (v/v) dimethyl sulfoxide (DMSO) in 0.1 M phosphate buffer (PB) at pH 7.0 for 3 hours at room temperature in the dark, resulting in maleimide-conjugated chitosan (MB-chitosan). Peptide immobilization was carried out by reacting MB-chitosan with CGG-tagged RGD (CGGRGD) and Ten2 (CGGVFDNFVLK) peptides at 25 nmol/cm² in PB for 24 hours. Excess peptides were removed by triple washing, and residual maleimide groups were quenched with 800 μM β-mercaptoethanol (126 nmol/cm²). Functionalized films were sterilized with 70% ethanol, air-dried, and UVirradiated prior to cell culture assays.

2.2 Cell culture

MC3T3-E1 pre-osteoblasts were cultured in α-MEM with 10% fetal bovine serum (FBS) and 1% pen/strep until 80% confluency. For morphology analysis, cells were seeded at 3,000 cells/well on chambered cover-glass with or without FBS and incubated for 12 hours before fluorescent staining. For adhesion and mineralization studies, cells were seeded on peptide-functionalized chitosan in 96-well plates at 6,400 cells/well in 1% FBS. Adhesion was assessed after 24 hours. For mineralization, osteogenic medium was introduced at 72 hours post-seeding and replenished every three days for 21 days to evaluate calcium deposition.

2.3 Investigation of cell morphology via fluorescent staining

After seeding for 24 hours, the spent media was removed, followed by washing with phosphate

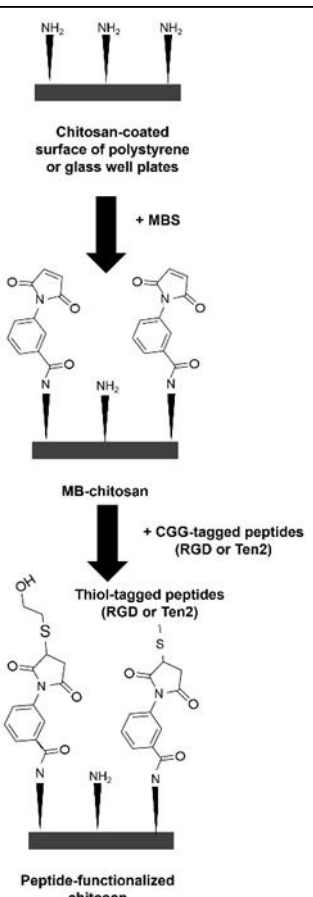


Figure 1. A schematic of surface modification and bond-line structural formulas of chemically modified chitosan.

buffer saline (PBS) at pH 7.4. Then fixation was performed by 1-hour incubation of 4% paraformaldehyde in PBS, followed by blocking with 0.1 M glycine in PBS for 5 minutes and washing with PBS once. Permeabilization was performed by 5-minute incubation of 0.1% (v/v) TritonX-100 for 3 minutes. Cellular structures, including the nucleus and actin filaments, were stained with DAPI (ab225549) and Phalloidin (ab176753) from Abcam (Cambridge, UK) in PBS for 1 hour in the dark, then washed with PBS three times. The cell morphology was observed using IX73 Inverted Microscope (OLYMPUS, Tokyo, Japan).

2.4 Investigation of cell adhesion via MTT

After 24 hours, the media was removed, followed by 3-hour incubation of 0.5 mg/mL MTT in complete media at 37 $^{\circ}$ C in a humidified atmosphere with 5% CO₂. Then the media was removed, and 100 μ L of DMSO was





added to solubilize the formazan crystal. The measurement and reference wavelengths were 570 nm and 630 nm, respectively. The viability percentage was calculated using the equation $((A_{565} - A_{630})_{experimental\ group}/(A_{565} - A_{630})_{control\ group})$ x 100. The experimental group was peptidefunctionalized chitosan, and the control group was MB-chitosan.

2.5 Calcium measurement

Calcium quantification was performed to mineralization peptideevaluate on functionalized chitosan.9 After 21 days of culture, cells were rinsed with PBS and decalcified using 0.6 M HCl at 4 °C for 24 hours. The supernatant was collected, and calcium content was measured using a colorimetric assay with O-cresolphthalein (OCPC). complexone Absorbance recorded at 570 nm. To normalize calcium levels, total protein content was determined from the decalcified cultures using 0.1 M NaOH with 0.1% SDS, followed by BCA protein assay.

2.6 Statistical Analysis

Statistical analysis was performed using oneway ANOVA followed by Tukey's Multiple Comparison Test in GraphPad Prism 5 (n = 3). p-values were reported to indicate statistical significance, with p < 0.05 considered significant (*).

3. Results & Discussion

3.1 Cellular response during initial interaction with chemically modified chitosan

To assess whether chemically modified chitosan effectively mimics a microenvironment conducive to bone cell adhesion, specific experimental conditions were optimized. In particular, to highlight the role of chemically modified chitosan in promoting cell adhesion during 12- to 24-hour assays, the concentration of FBS was reduced from 10% to 1%, and subsequently to serumfree conditions. This adjustment aimed to minimize the masking effect of serum proteins on the surface-bound peptides. ¹⁰

To investigate the role of chemically modified chitosan in promoting cell adhesion, an MTT assay was performed at 24 hours post-seeding. The cell adhesion percentages of adhered MC3T3-E1 cells on MB-chitosan, RGD-chitosan, and Ten2-chitosan were 100, 122 ±14,

117 ± 18 , respectively. In contrast, and unmodified chitosan showed no cell adhesion (data not shown), as shown in Figure 2A. Fluorescence imaging demonstrated that chemical modification of chitosan enhanced cell adhesion under serum-free conditions. To evaluate the impact of ECM-derived peptides on early MC3T3-E1 adhesion, fluorescent staining was performed 12 hours post-seeding to visualize nuclei and actin filaments, as shown in Figure 2B. Cells cultured on MB-chitosan, RGD-chitosan, and Ten2-chitosan displayed fibroblast-like morphology with organized actin structures. Residual maleimide groups were quenched using β -mercaptoethanol, which may further enhance adhesion through surface hydroxylation. Previous studies have shown that hydroxylated surfaces support integrinindependent cell attachment, even under serumfree conditions. suggesting that mercaptoethanol-modified surfaces contribute to improved cell adhesion beyond ligandreceptor interactions alone. These findings highlight the combined effect of chemical modification and surface properties on cellular behavior. 11, 12 Notably, these results indirectly indicate that cysteine-containing peptides and β-mercaptoethanol were successfully conjugated to MB-chitosan via site-specific thiol-maleimide linkage.

3.2 Mineralization under the influence of chemically modified chitosan

The measurement of calcium was performed after a 21-day osteogenic media treatment under the influence of chemically modified chitosan. The total protein content of MB-RGD-chitosan. Ten2-chitosan. mineralization control polystyrene, and nonmineralization control polystyrene $45,550.0\pm3,401.5$, $36,641.7\pm1,650.3$, 33,100.0 $\pm 6,263.2$, 61,866.7 $\pm 2,182.4$, and 50,116.7 $\pm 2,556.9$ ng/well, respectively (Figure 3A). The total calcium content of MB-chitosan, RGDchitosan, Ten2-chitosan, mineralization control polystyrene, and non-mineralization control polystyrene were 130.9 ± 13.3 , 104.7 ± 16.3 , 131.5 \pm 12.6, 134.8 \pm 4.7, and 66.7 \pm 15.9 ng/well, respectively (Figure 3B). normalized calcium content of MB-chitosan, RGD-chitosan, Ten2-chitosan, mineralization control polystyrene, and non-mineralization control polystyrene were 2.90 ±0.47, 2.87





 ± 0.58 , 4.04 ± 0.60 , 2.18 ± 0.10 , and 1.33 ± 0.26 ng/ng total protein, respectively (Figure 3C). The results showed that only Ten2-chitosan vielded significantly higher normalized calcium levels compared to the mineralization control polystyrene, as indicated in Figure 2C. Moreover, the total protein content indirectly indicated that the number of cells on Ten2chitosan was significantly lower than on the mineralization control polystyrene (Figure 2A). Notably, despite the lower cell number, Ten2chitosan facilitated cell adhesion and enhanced mineralization, highlighting its potential role in future bone substitute applications. Moreover, the hydroxylated surfaces of β-mercaptoethanol on MB-chitosan facilitated cell attachment through non-integrin mechanisms but were unable to enhance mineralization, a critical process in bone regeneration. For RGDchitosan, the epitope size of the functional sequences may play a critical role in cell recognition, thereby influencing cell adhesion and mineralization. It has been reported that the conformational epitope of a BMP2 dimer spans approximately 500-600 Å², offering a highaffinity interaction site. In contrast, the linear epitope of a BMP2 monomer presents a smaller area of around 200-250 Å², resulting in lower receptor-binding affinity.¹³ Consequently, the small peptide sequences of RGD may have limited ability to elicit effective cell recognition. Understanding how epitope size influences receptor binding and downstream

signaling could provide insights into optimizing peptide-functionalized chitosan for enhanced cellular responses.

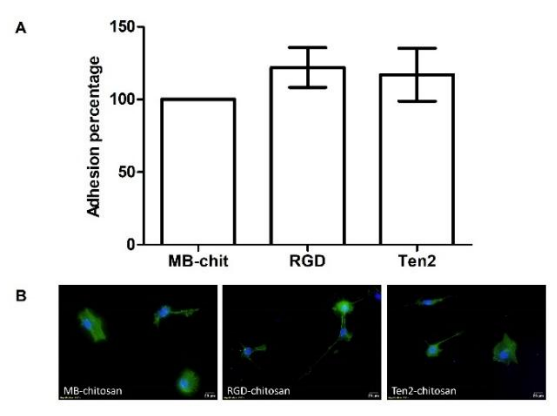


Figure 2. Cell adhesion and morphology: (A) MC3T3-E1 adhesion on chemically modified chitosan at 24 hours; (B) The fluorescent stain of nucleus (blue) and actin filament (green) of MC3T3-1 on chemically modified chitosan at 12 hours.

4. Conclusions

In conclusion, peptide-functionalized chitosan, particularly Ten2-chitosan, facilitated cell adhesion and significantly enhanced mineralization, suggesting its strong potential to promote osteoblast differentiation. These findings highlight the effectiveness of chemical modification in improving chitosan's bioactivity for bone regeneration applications.

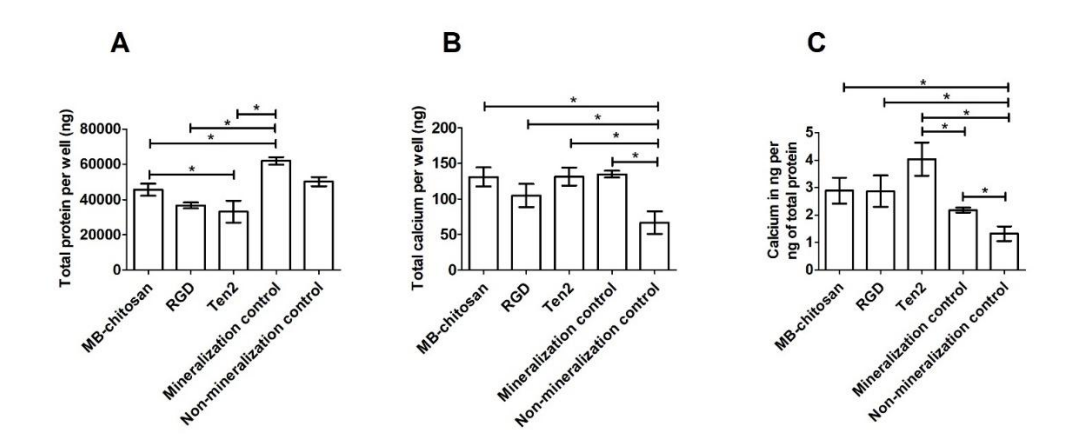


Figure 3. MC3T3-E1 mineralization on chemically modified chitosan after 21-day osteogenic media treatment: (A) Total protein; (B) Total calcium content; (C) Normalized calcium content. (*=p<0.05)





Acknowledgements

This work was supported by Program Management Unit for Human Resources & Institutional Development, Research and Innovation [grant number B05F640161]; Budget for International Academic Conference (BIAC_Student) from Faculty of Science, Kasetsart University; Graduate Studies Scholarship, Faculty of Science, Kasetsart University, Bangkok, Thailand.

References

- 1. Croisier, F.; Jérôme, C. *Eur. Polym. J.* **2013**, *49*, 780–792.
- 2. Wang, X.; Wang, G.; Liu, L.; Zhang, D. *Sci. Rep.* **2016**, *6*, 39322.
- 3. Tsai, W.-B.; Chen, Y.-R.; Liu, H.-L.; Lai, J.-Y. *Carbohydr. Polym.* **2011**, *85*, 129–137.
- 4. Liu, Q.; Limthongkul, W.; Sidhu, G.; Zhang, J.; Vaccaro, A.; Shenck, R.; Hickok, N.; Shapiro, I.; Freeman, T. *J. Orthop. Res.* **2012**, *30*, 1626–1633.
- Roque-Borda, C. A.; Antunes, B. F.; Toledo Borgues, A. B.; Costa de Pontes, J. T.; Meneguin, A. B.; Chorilli, M.; Trovatti, E.; Teixeira, S. R.; Pavan, F. R.; Vicente, E. F. ACS Omega 2022, 7, 28238–28247.
- Dubashynskaya, N. V.; Bokatyi, A. N.; Dobrodumov, A. V.; Kudryavtsev, I. V.; Trulioff, A. S.; Rubinstein, A. A.; Aquino, A. D.; Dubrovskii, Y. A.; Knyazeva, E. S.; Demyanova, E. V.; et al. *Int. J. Mol. Sci.* 2023, 24, 166.
- 7. Hozumi, K.; Nomizu, M. *Curr. Protoc. Cell Biol.* **2018**, *80*, e53.
- 8. Sever, M.; Mammadov, B.; Guler, M. O.; Tekinay, A. B. *Biomacromolecules* **2014**, *15*, 4480–4487.
- 9. Mathews, S.; Gupta, P. K.; Bhonde, R.; Totey, S. *Cell Prolif.* **2011**, *44*, 537–549.
- Kim, J. H.; Jekarl, D. W.; Kim, M.; Oh, E. J.; Kim, Y.; Park, I. Y.; Shin, J. C. *Int. J. Med. Sci.* 2014, 11, 298–308.
- 11. Curtis, A. S. G.; Forrester, J. V.; Clark, P. *J. Cell Sci.* **1986**, *86*, 9–24.
- 12. Hoshiba, T.; Tanaka, M. *Anal. Sci.* **2016**, *32*, 1151–1158.
- 13. Zhang, A.; Chen, Z.; Yu, X.; Zhang, L.; Song, Q. *Int. J. Pept. Res. Ther.* **2021**, *27*, 10058.





Computational insights into sulfonamide-modified cannabinoids as selective COX-2 inhibitors: Binding affinity and drug-like properties

Watcharin Kumaeum, Panichakorn Jaiyong*

Department of Chemistry, Faculty of Science and Technology, Thammasat University,
Pathum Thani 12120, Thailand
*E-mail: scpj@tu.ac.th

Abstract:

Cyclooxygenase (COX) is a key enzyme involved in inflammation and a major target for selective inhibition to reduce the adverse effects of nonsteroidal anti-inflammatory drugs (NSAIDs). This study employs a computational approach to evaluate the binding affinity and selectivity of sulfonamide-modified cannabinoids as potential COX-2 inhibitors. We applied semiempirical quantum mechanical (SQM) methods, particularly GFN2-xTB, to refine docked poses and predict binding free energies in implicit solvation ($\Delta G_{bind,solv}$). Within a fully relaxed COX-2 truncated pocket, noncovalent interactions of sulfonamide-modified cannabinoids contribute to $\Delta G_{bind,solv}$ values ranging from -35 to -64 kcal/mol, of which 27% to 49% is attributed to the sulfonamide group. These values indicate stronger binding than celecoxib ($\Delta G_{bind,solv} = -32.02$ kcal/mol), a known COX-2 selective NSAID. Additionally, drug-like properties and oral bioavailability predictions suggest favorable pharmacokinetics for these analogs. The findings highlight the potential of sulfonamide-modified cannabinoids as promising COX-2-selective inhibitors, providing valuable insights for the rational design of novel anti-inflammatory agents.

1. Introduction

Non-steroidal anti-inflammatory drugs (NSAIDs), such as celecoxib, diclofenac, and ibuprofen, are widely used to alleviate pain and inflammation by inhibiting cyclooxygenase (COX) enzymes. However, their long-term use is limited by side effects. Phytocannabinoids such as cannabidiol (CBD), cannabidiolic acid (CBDA), and cannabigerol (CBG) have shown inhibitory potency on COX and CB2 enzymes. Inhibitory potency on COX and CB2 enzymes.

In this study, we investigate the noncovalent binding interactions of selected natural cannabinoids with COX receptors using semiempirical quantum mechanical (SQM) potentials and a molecular docking technique. By incorporating empirical corrections for dispersion and hydrogen bonding, this approach offers a practical balance between computational efficiency and accuracy for modeling large protein-ligand complexes. To structure-affinity relationships, sulfonamide-modified cannabinoid analogs were designed and evaluated for their ability to enhance binding interactions within the fully relaxed COX-2 binding site.

2. Computational Methods

2.1 Protein and Ligand Preparation

Crystallographic structures of COX-1 (PDB code: 1EQH)⁵ and COX-2 (PDB code: 3LN1)⁶ were protonated at pH 7.4 using PROPKA plugin of APBS-PDB2PQR software suite.⁷ Structures of 6 natural cannabinoids (Δ⁹-THC, CBD, CBG, CBC, CBN, CBE, CBTA, CBL), their acid derivatives, and 7 NSIADs (etoricoxib, celecoxib, diclofenac, naproxen, ibuprofen, flurbiprofen, aspirin) were retrieved from the cannabis and ChEMBL databases and optimized with the MMFF94s force field using IQmol.⁸⁻¹⁰ SwissADME was used to predict drug-like properties of ligands.¹¹

Docking process was performed using AutoDock4 version 4.2.6 (grid box: 50 × 50 × 50 Å; grid spacing: 0.375 Å). ¹² Binding interactions were visualized using Discovery Studio Visualizer. ¹³

2.2 SQM Method Validation

We evaluated the performance of PM6-D3H4/X, DFTB3-D3H4/H5, and GFN2-xTB for computing noncovalent interaction energies (IEs), defined as:

 $IE = E_{\text{dimer}} - (E_{\text{monomer_a}} + E_{\text{monomer_b}})$ **Eq 1** Benchmark datasets included S66, HB375, X40, HB300SPX, and PLA15. All calculations employed default parameter settings for dispersion, hydrogen-bonding, and halogen bonding corrections. PM6 calculations were carried out using the



MOZYME module in MOPAC2016.²² DFTB3 calculations were performed with DFTB+ (v21.2).²³ GFN2-xTB calculations were performed using the xtb program (v6.6.0).²⁴

2.3 Binding Free Energy ($\Delta G_{\text{bind,solv}}$)

The ALPB implicit solvation model with GFN2-xTB method was used to reoptimize the docked poses of each NSAID in truncated binding pockets comprising 41 amino residues for COX-1 (657 atoms) and 38 amino residues for COX-2 (607 atoms), respectively, each assigned a net molecular charge of +1. This resulted in the uncorrected binding free energy ($\Delta G'_{\text{bind,solv}}$). The lowest-energy ligand–receptor complexes were then fully optimized at the same level of theory. Corrected binding free energy in implicit solvation ($\Delta G_{\text{bind,solv}}$) were computed at 298.15 K using Hessian-based thermostatistical contributions, according to:

$$\begin{split} \Delta G_{\text{bind,solv}} &= G_{\text{complex}} - (G_{\text{receptor}} + G_{\text{ligand}}) \\ &= \Delta E_{\text{bind,vac}} + \Delta \delta G_{\text{solv}} + \Delta G_{\text{TRVC}} \\ &= \Delta G'_{\text{bind,solv}} + \Delta G_{\text{TRVC}} \quad \textbf{Eq 2} \end{split}$$

where the total free energy (G) includes the single-point energy (E), solvation free energy (δG_{solv}) , and thermostatistical terms (G_{TRVC}) arising from translational, rotational, vibrational, and conformational degrees of freedom. 25, 26 Binding free energy (ΔG) of complex association was further converted to the inhibitory constant (K_i) using:

 $K_i = \exp(\Delta G/RT)$ Eq 3 where $R = 1.98 \text{ cal} \cdot \text{K}^{-1} \cdot \text{mol}^{-1}$ and T = 298.15 K. The COX-2/COX-1 selectivity index (SI) was calculated as:

 $SI_{\text{COX-2/COX-1}} = \log(K_i \text{ of COX-2/}K_i \text{ of COX-1})$ Eq 4

3. Results & Discussion

3.1 Benchmarking and SQM Method Accuracy

The performance of selected SQM methods for computing noncovalent IEs was benchmarked using established datasets. PM6-D3H4 and DFTB3-D3H5 showed comparable accuracy for non-halogenated systems in the S66 and HB375 datasets, with root mean square deviation (RMSD) values below 1 kcal/mol. PM6-D3H4X method improved predictive accuracy for halogenated systems in the X40 dataset, reducing RMSD to 2.31 kcal/mol. DFTB3-D3H5, which employs element-specific corrections to improve hydrogen bond

description, achieved the lowest RMSD of 1.24 kcal/mol on the HB375 dataset.²⁰

GFN2-xTB accurately reproduced IEs for small benchmark dimers in the X40 and HB300SPX datasets, with RMSDs of 1.06 and 1.40 kcal/mol, respectively. For larger protein—ligand systems containing hundreds of atoms in the PLA15 dataset, GFN2-xTB yielded the best performance among tested methods, with an RMSD of 13.27 kcal/mol, consistent with previous studies.

The optimized geometries of docked poses using GFN2-xTB in vacuum and ALPB solvation were well-aligned with experimental co-crystallized structures. For instance, AutoDock4 and GFN2-xTB methods accurately reproduced the native binding pose of celecoxib in COX-2, with the root mean square deviation (RMSD) below 1.0 Å (Figure 1).

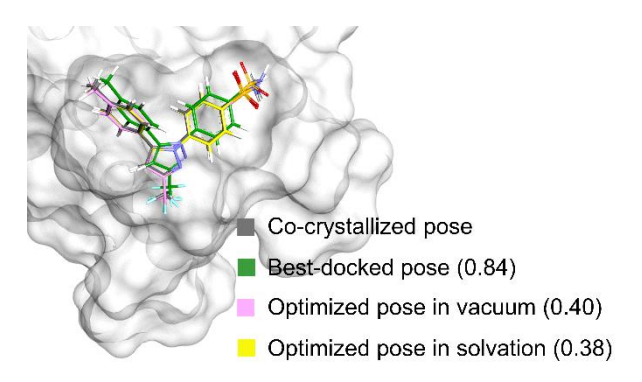


Figure 1. Overlays of co-crystallized celecoxib (gray stick) and best-docked pose (green stick) and optimized pose in vacuum (pink stick) and solvation (yellow stick) using the GFN2-xTB (ALPB) method in the COX-2. RMSD in angstrom are indicated in parentheses.

Geometry optimization using GFN2-xTB successfully resolved docking inaccuracies. For example, the best-docked pose of flurbiprofen was flipped relative to celecoxib, but after optimization, its carboxyl group aligned with the sulfonamide position of celecoxib. In addition, hydrogen bonds within 3 Å were formed between the carboxyl group of flurbiprofen's optimized pose and the amino groups of Arg499 and Phe504—the key residues essential for COX-2 selectivity (Figure 2).²⁷





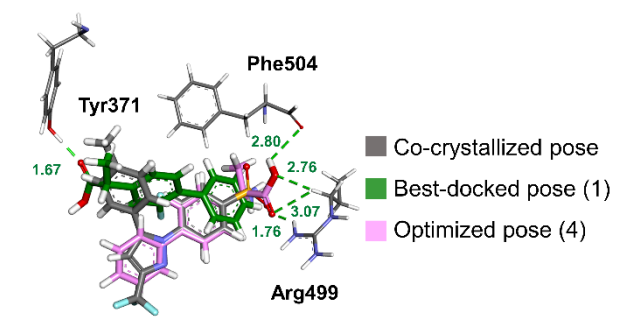


Figure 2. The lowest-energy GFN2-xTB optimized pose (pink stick) and best-docked pose (green stick) of flurbiprofen with key COX-2 residues. Hydrogen bonds (green dash lines) include distances in angstroms. The number of hydrogen bonds are indicated in parentheses.

Overall, GFN2-xTB combined with the ALPB solvation model demonstrated strong predictive performance in estimating binding free energies of NSAID. For 30 NSAIDs docked to a truncated crystallographic COX-2 structure, the Pearson correlation coefficient (r_p) between $\Delta G_{\text{bind,solv}}$ and experimental IC₅₀ values was indicating moderate predictive 0.35, accuracy.28, When thermostatistical corrections were included using the mRRHO model and fully relaxed receptor-ligand geometries, the r_p improved significantly to 0.54 for the $\Delta G_{\text{bind,solv}}$. 25, 26

3.2 Protein-Ligand Binding Affinity

The strength of protein–ligand binding is associated with the negative $\Delta G_{\text{bind,solv}}$ value, which is directly related to the equilibrium dissociation constant (K_d) as:

 $\Delta G_{\text{bind,solv}} = - \text{RTln} K_d = \text{RTln} K_a = \text{RTln} K_i \mathbf{Eq} \mathbf{5}$ Low values of the selectivity index ($SI_{COX-2/COX}$ -1), derived from the computed K_i values, indicate preferential binding to COX-2 over COX-1 and therefore suggest potential antiinflammatory selectivity. Compared with celecoxib, the COX-2 selective NSAID, several phytocannabinoids—CBCA, carboxylated CBNA, CBEA, CBTA, and CBLA—exhibited negative SI_{COX-2/COX-1} values, suggesting their potential as selective COX-2 ligands. For instance, carboxylic-containing cannabinoids bound more strongly to fully relaxed COX-2 than diclofenac, with $\Delta G_{\text{bind,solv}}$ values ranging from -19.59 to -22.80 kcal/mol (Table 1). In contrast, CBLA showed weaker binding affinity ($\Delta G_{\text{bind,solv}} = -15.52 \text{ kcal/mol}$).

Table 1. Uncorrected binding free energy $(\Delta G'_{\text{bind,solv}})$ and corrected binding free energy $(\Delta G_{\text{bind,solv}})$ for NSAIDs and the carboxylic group of cannabinoids with COX in a unit of kcal/mol, calculated using GFN2-xTB (ALPB) method.

	$\Delta oldsymbol{G'}_{ ext{bind,solv}}$		-	$\Delta G_{ ext{bind,solv}}$
Cannabinoids	COX-	COX-2	SI	Fully relaxed COX-2
Celecoxib	2.56	-43.86	-34.07	-32.02
Etoricoxib	3.01	-39.75	-31.38	-25.27
CBCA	4.97	-13.55	-13.59	-22.80
CBNA	1.41	-8.56	-7.31	-20.20
CBEA	22.74	-5.45	-20.68	-20.05
CBTA	14.61	-3.51	-13.30	-19.59
Diclofenac	-24.13	-23.81	0.24	-16.63
CBLA	20.45	2.28	-13.33	-15.52
Flurbiprofen	-25.29	-25.26	0.02	-18.26
Aspirin	-17.26	-19.02	-1.29	-10.53
Ibuprofen	-24.73	-21.70	2.23	-9.36
Naproxen	-26.73	-24.21	1.85	-8.32

To further improve binding affinity, a sulfonamide group was introduced at the alkyl side chain of each cannabinoid (Figure 3). This modification enhanced COX-2 binding affinity, resulting in $\Delta G_{\rm bind,solv}$ values more negative than celecoxib.

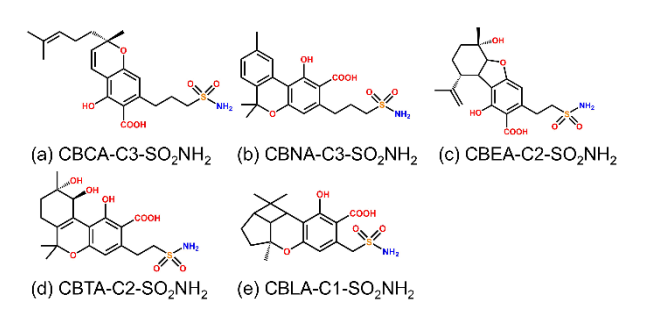


Figure 3. Chemical structures of sulfonamide-modified cannabinoid analogs: (a) CBCA-C3-SO₂NH₂, (b) CBNA-C3-SO₂NH₂, (c) CBEA-C2-SO₂NH₂, (d) CBTA-C2-SO₂NH₂, (e) CBLA-C1-SO₂NH₂.

Among these modified analogs, CBTA-C2- SO_2NH_2 demonstrated the strongest COX-2 interaction ($\Delta G_{bind,solv}$ of -63.85 kcal/mol), with 27.17% of the total binding energy attributed to the sulfonamide group (Figure 4). Energy decomposition analysis showed that this high affinity was supported by a network of hydrogen bonds involving Arg499, Ile503, Phe504, His75, Gln178, Arg106, Ser339, Ala513, and Glu510 (Figure 5d).²⁷ CBCA-C3-





 SO_2NH_2 ($\Delta G_{bind,solv} = -48.41$ kcal/mol) and CBEA-C2-SO₂NH₂ $(\Delta G_{\rm bind,solv})$ kcal/mol) showed stronger COX-2 binding than CBNA-C3-SO₂NH₂ $(\Delta G_{\rm bind,solv})$ kcal/mol), due to additional interactions with Met508 and Val102. Conversely, CBLA-C1- SO_2NH_2 had the weakest binding ($\Delta G_{bind,solv} =$ -34.71 kcal/mol), possibly due to the absence of favorable contacts with Ile503 (Figure 5). These sulfonamide-modified analogs showed favorable drug-like properties bioavailability, supporting their potential for drug development. They satisfied Lipinski's Rule of Five, with molecular weights <500 g/mol, ≤5 hydrogen bond donors, and ≤10

hydrogen bond acceptors.³⁰ Their predicted partition coefficients (log P) values were within the optimal range for oral bioavailability, with CBCA-C3-SO₂NH₂ (log P = 2.71) and CBNA-C3-SO₂NH₂ (log P = 2.64) comparable to celecoxib (log P = 3.40), further supporting their drug-like potential.

4. Conclusions

This study highlights the utility of SQM methods—specifically GFN2-xTB with the ALPB solvation model—for efficiently screening and identifying phytocannabinoids as potential anti-inflammatory agents. Benchmarking results confirmed its reliability for predicting binding free energies in both

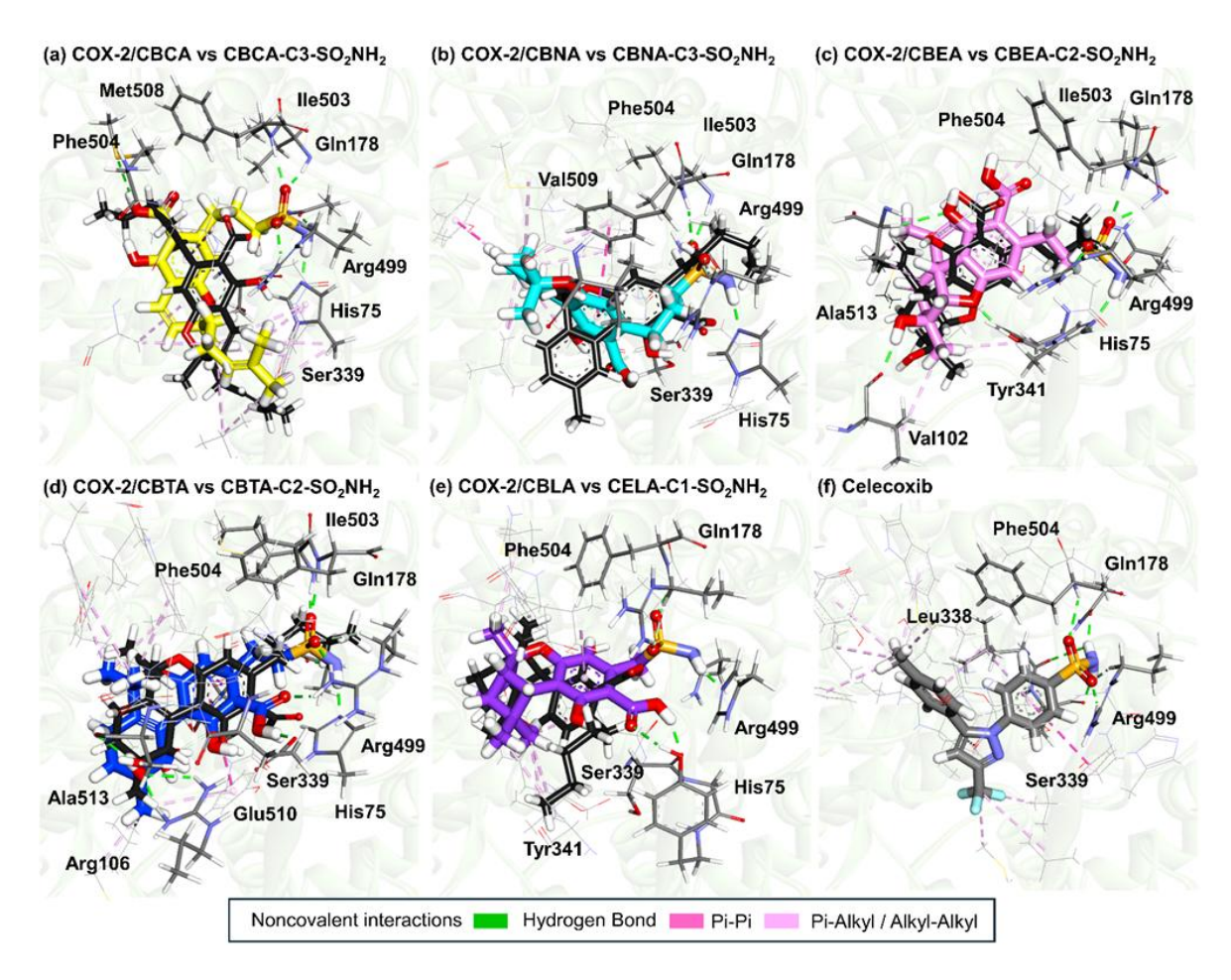


Figure 4. Energy components of COX-2 binding free energy ($\Delta G_{\text{bind,solv}}$), and relative binding free energy ($\Delta \Delta G_{\text{bind,solv}}$) in kcal/mol associated with the sulfonamide group of modified cannabinoids.





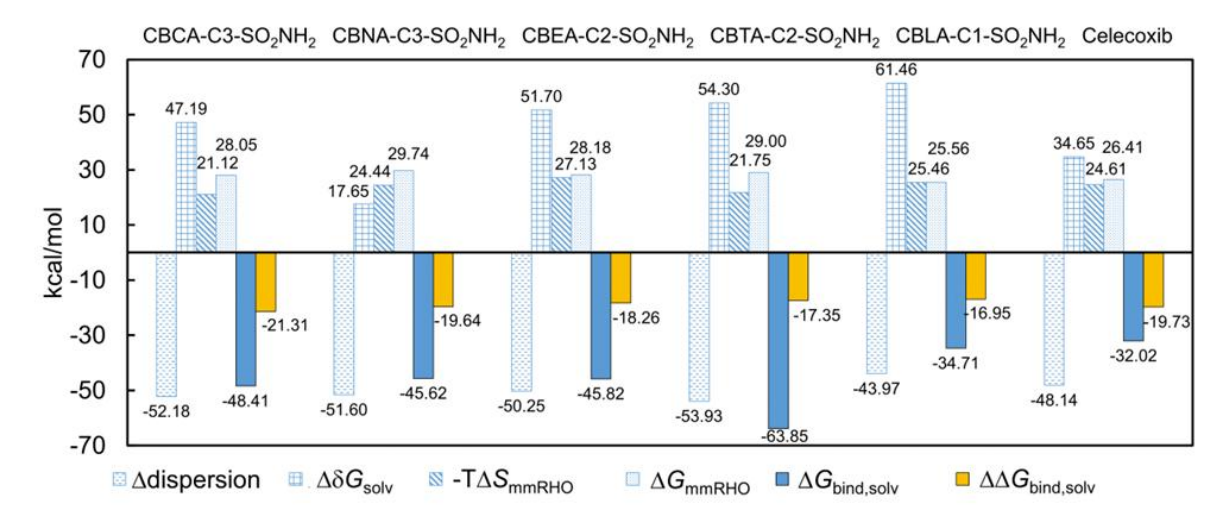


Figure 5. Binding interactions of sulfonamide-modified analogs: (a) CBCA-C3-SO₂NH₂, (b) CBNA-C3-SO₂NH₂, (c) CBEA-C2-SO₂NH₂, (d) CBTA-C2-SO₂NH₂, (e) CBLA-C1-SO₂NH₂, and (f) celecoxib with key residues in the fully relaxed COX-2 binding pocket, optimized using the GFN2-xTB (ALPB) method. Key noncovalent interactions include hydrogen bonding (green), π - π stacking (purple), and π -alkyl or alkyl-alkyl contacts (pink), depicted as dashed lines.

small molecule and protein-ligand systems. Carboxylic acid derivatives of cannabinoids demonstrated selective binding to COX-2, supporting their potential as promising leads for anti-inflammatory drug development. Sulfonamide modification further enhanced binding by reinforcing COX-2 affinity hydrogen bonding networks with key COX-2 residues. All modified analogs satisfied major drug-likeness criteria, including Lipinski's Rule of Five and predicted oral bioavailability, emphasizing their suitability for further development. These findings highlight the value of SQM-based approaches in rational drug design, particularly for selectively targeting COX-2.

Acknowledgements

The authors would like to acknowledge the Department of Chemistry, Faculty of Science and Technology, Thammasat University, for providing the necessary resources and support for this research. We also acknowledge the scholarship for talent students pursuing graduate studies at the Faculty of Science and Technology, Thammasat University (Contract No. TB 23/2563). This work was financially supported by the Thailand Science Research and Innovation (TSRI) Fundamental Fund for the fiscal year 2023.

References

- 1. Brewer, C.; Waddell, D. *J. Trainol.* **2012**, *I*, 45–52.
- 2. Rayar, A. M.; Lagarde, N.; Ferroud, C.; Zagury, J. F.; Montes, M.; Sylla-Iyarreta Veitia, M. *Curr. Top. Med. Chem.* **2017**, *17*, 2935–2956.
- Ruhaak, L. R.; Felth, J.; Karlsson, P. C.; Rafter, J. J.; Verpoorte, R.; Bohlin, L. *Biol. Pharm. Bull.* 2011, 34, 774–778.
- 4. Takeda, S.; Misawa, K.; Yamamoto, I.; Watanabe, K. *Drug Metab. Dispos.* **2008**, *36*(9), 1917–1921.
- Selinsky, B. S.; Gupta, K.; Sharkey, C. T.; Loll, P. J. *Biochemistry* 2001, 40, 5172–5180.
- Wang, J. L.; Limburg, D.; Graneto, M. J.; Springer, J.; Hamper, J. R. B.; Liao, S.; Pawlitz, J. L.; Kurumbail, R. G.; Maziasz, T.; Talley, J. J.; Kiefer, J. R.; Carter, J. Bioorg. Med. Chem. Lett. 2010, 20, 7159– 7163
- 7. Jurrus, E.; Engel, D.; Star, K.; Monson, K.; Brandi, J.; Felberg, L. E.; Brookes, D. H.; Wilson, L.; Chen, J.; Liles, K.; Chun, M.; Li, P.; Gohara, D. W.; Dolinsky, T.; Konecny, R.; Koes, D. R.; Nielsen, J. E.; Head-Gordon, T.; Geng, W.; Krasny, R.; Wei, G. W.; Holst, M. J.; McCammon, J. A.; Baker, N. A. *Protein Sci.* **2018**, *27*, 112–128.

- Mendez, D.; Gaulton, A.; Bento, A. P.; Chambers, J.; De Veij, M.; Félix, E.; Magariños, María P.; Mosquera, Juan F.; Mutowo, P.; Nowotka, M.; Gordillo-Marañón, M.; Hunter, F.; Junco, L.; Mugumbate, G.; Rodriguez-Lopez, M.; Atkinson, F.; Bosc, N.; Radoux, Chris J.; Segura-Cabrera, A.; Hersey, A.; Leach, Andrew R. Nucleic Acids Res. 2019, 47, D930-D940.
- 9. Wishart, D. S.; Ignatchenko, G.; Cao, X.; Guo, A. C.; Hiebert Giesbrecht, M.; LeVatte, M.; Liigand, J.; Wang, F.; Bhumireddy, S.; Wang, Y.; Zhang, J.; Mandal, R.; Dyck, J. Chemical composition of *Cannabis*. https://cannabisdatabase.ca/(accessed Feb 28, 2025).
- 10. IQmol. A molecular editor and visualization package. http://iqmol.org/ (accessed Feb 28, 2025).
- 11. Daina, A.; Michielin, O.; Zoete, V. *Sci. Rep.* **2017**, *7*, 42717.
- Morris, G. M.; Huey, R.; Lindstrom, W.; Sanner, M. F.; Belew, R. K.; Goodsell, D. S.; Olson, A. J. *J. Comput. Chem.* **2009**, *30*, 2785–2791.
- 13. Biovia, D. S. *Discovery Studio Modeling Environment*; Dassault Systèmes: San Diego, 2016.
- 14. Řezáč, J.; Riley, K. E.; Hobza, P. *J. Chem. Theory Comput.* **2011**, *7* (8), 2427–2438.
- 15. Rezac, J. J. Chem. Theory Comput. **2020**, 16, 2355–2368.
- 16. Řezáč, J.; Riley, K. E.; Hobza, P. *J. Chem. Theory Comput.* **2012**, *8*, 4285–4292.
- 17. Rezac, J. J. Chem. Theory Comput. **2020**, 16, 6305–6316.
- 18. Kříž, K.; Řezáč, J. *J. Chem. Inf. Model.* **2020**, *60*, 1453–1460.
- Miriyala, V. M.; Řezáč, J. J. Comput. Chem. 2017, 38, 688–697.
- 20. Řezáč, J. J. Chem. Theory Comput. **2017**, 13, 4804–4817.
- 21. Bannwarth, C.; Caldeweyher, E.; Ehlert, S.; Hansen, A.; Pracht, P.; Seibert, J.; Spicher,

- S.; Grimme, S. WIREs Comput. Mol. Sci. **2021**, 11, e1493.
- 22. Stewart, J. J. P. MOPAC2016. http://OpenMOPAC.net/ (accessed Feb 28, 2025).
- 23. Hourahine, B.; Aradi, B.; Blum, V.; Bonafé, F.; Buccheri, A.; Camacho, C.; Cevallos, C.; Deshaye, M. Y.; Dumitrică, T.; Dominguez, A.; Ehlert, S.; Elstner, M.; van der Heide, T.; Hermann, J.; Irle, S.; Kranz, J. J.; Köhler, C.; Kowalczyk, T.; Kubař, T.; Lee, I. S.; Lutsker, V.; Maurer, R. J.; Min, S. K.; Mitchell, I.; Negre, C.; Niehaus, T. A.; Niklasson, A. M. N.; Page, A. J.; Pecchia, A.; Penazzi, G.; Persson, M. P.; Řezáč, J.; Sánchez, C. G.; Sternberg, M.; Stöhr, M.; Stuckenberg, F.; Tkatchenko, A.; Yu, V. W.; Frauenheim, T. J. Chem. Phys. 2020, 152, 124101.
- 24. Bannwarth, C.; Ehlert, S.; Grimme, S. *J. Chem. Theory Comput.* **2019**, *15*, 1652–1671.
- 25. Spicher, S.; Grimme, S. *J. Phys. Chem. Lett.* **2020**, *11*, 6606–6611.
- Chen, Y. Q.; Sheng, Y. J.; Ma, Y. Q.; Ding, H. M. Phys. Chem. Chem. Phys. 2022, 24, 14339–14347.
- 27. Tavares, M. T.; Primi, M. C.; Silva, N. A. T. F.; Carvalho, C. F.; Cunha, M. R.; Parise-Filho, R. *J. Chem. Educ.* **2017**, *94*, 380–387.
- Riendeau, D.; Percival, M. D.; Brideau, C.; Charleson, S.; Dubé, D.; Ethier, D.; Falgueyret, J. P.; Friesen, R. W.; Gordon, R.; Greig, G.; Guay, J.; Mancini, J.; Ouellet, M.; Wong, E.; Xu, L.; Boyce, S.; Visco, D.; Girard, Y.; Prasit, P.; Zamboni, R.; Rodger, I. W.; Gresser, M.; Ford-Hutchinson, A. W.; Young, R. N.; Chan, C. C. J. Pharmacol. Exp. Ther. 2001, 296, 558–566.
- Warner, T. D.; Giuliano, F.; Vojnovic, I.; Bukasa, A.; Mitchell, J. A.; Vane, J. R. *Proc.* Natl. Acad. Sci. U.S.A. 1999, 96, 7563– 7568.
- 30. Lipinski, C. A.; Lombardo, F.; Dominy, B. W.; Feeney, P. J. *Adv. Drug Deliv. Rev.* **2001**, *46*, 3–26.





Rational design of InhA inhibitors from damnacanthal using molecular docking calculations

<u>Thimpika Pornprom</u>, ¹ Bongkochawan Phakamwong, ¹ Darunee Sukchit, ¹ Khemmisara Sawatdee, ¹ Masayuki Yuguchi, ² Nagomi Chimura, ² Auradee Punkvang, ³ Khomson Suttisintong, ⁴ Prasat Kittakoop, ^{5,6,7} Noriyuki Kurita, ² Pornpan Pungpo^{1,*}

¹Department of Chemistry and Center of Excellence for Innovation in Chemistry, Faculty of Science, Ubon Ratchathani University, Ubon Ratchathani, 34190, Thailand ²Department of Computer Science and Engineering, Toyohashi University of Technology, Tempaku-cho, Toyohashi, Aichi, 441-8580, Japan

³Division of Chemistry, Faculty of Science, Nakhon Phanom University, Nakhon Phanom, 48000, Thailand ⁴National Nanotechnology Center, NSTDA, 111 Thailand Science Park, Klong Luang, Pathum Thani, 12120, Thailand

⁵Chulabhorn Research Institute, Laksi, Bangkok 10210, Thailand

⁶Chulabhorn Graduate Institute, Program in Chemical Sciences, Bangkok 10210, Thailand

⁷Center of Excellence on Environmental Health and Toxicology (EHT), OPS, Ministry of Higher Education,

Science, Research and Innovation, Bangkok 10210, Thailand

*E-mail: pornpan.p@ubu.ac.th

Abstract:

Tuberculosis (TB) is a severe infectious disease in humans caused by *M. tuberculosis*. The enzyme enoyl-acyl carrier protein reductase (InhA) plays a crucial role in the biosynthesis of mycolic acids, which are essential for the survival of *M. tuberculosis*. As a result, InhA is a promising target for antituberculosis drug development. In this study, we investigated the key interactions between InhA and damnacanthal. These compounds were previously isolated in our research, we demonstrated their potential inhibitory activity against InhA, highlighting them as promising candidates for further exploration as antitubercular agents. To better understand the variations in their inhibitory effects, molecular docking calculations were performed to analyze their binding modes and interactions within the InhA binding pocket. The lowest binding energy of ligand with –6.14 kcal/mol. The most potent compound exhibited strong interactions with InhA, specifically with Pro156 and Gln214. damnacanthal was designed. Nine newly designed compounds were obtained. The compounds exhibited docking scores ranging from –3.7 to –7.9 kcal/mol. Finally, the results provide valuable insights for the rational design of more potent InhA inhibitors with effective anti-tuberculosis activity.

1. Introduction

Tuberculosis (TB) is a highly contagious respiratory disease caused by the bacterium Mycobacterium tuberculosis (M. tuberculosis). As of 2024, 193 countries and territories representing over 99% of the world's population and TB cases submitted surveillance data.1 TB remains a major global health concern, particularly in regions with limited access to medical infrastructure and resources. M. tuberculosis's pathogenicity and resilience stem largely from its mycolic acid-rich cell wall, which is vital for maintaining the structure and function of its bacterial envelope.^{2,3} These mycolic acids are synthesized through the fatty acid synthesis (FAS-II) pathway, where InhA, an enoyl-acyl carrier protein (ACP) reductase, plays a central role. InhA catalyzes the NADHdependent reduction of 2-enoyl-ACP substrates, generating precursors critical for mycolic acid production.4 InhA is a highly attractive target for novel antitubercular drug development. Inhibiting InhA effectively disrupts cell wall biosynthesis, leading to bacterial death. Accordingly, InhA inhibitors are among the most promising candidates for next-generation TB therapies.⁵ However, the treatment of TB faces a growing challenge: the emergence of multidrug-resistant (MDR) and extensively drug-resistant (XDR) strains of M. tuberculosis. These strains have developed resistance to frontline TB drugs such as isoniazid (INH), rifampicin, ethambutol, ethionamide, and pyrazinamide, largely due to overuse and misuse. 6 This highlights the urgent need for new therapeutic agents that are not only effective but also less likely to induce resistance. Because of its crucial role in fatty acid synthesis and cell wall integrity, InhA is also the primary target of INH and other



promising antitubercular agents.⁶ Ongoing research into selective and potent InhA inhibitors represents a critical path forward in combating the global TB epidemic. In the present study, we investigated the key interactions between InhA and damnacanthal. To elucidate the significant differences in their inhibitory effects, we employed molecular simulations. Based on these findings, we modified the damnacanthal to develop novel derivatives as potential InhA inhibitors and examined their interactions with InhA using the same molecular simulations as those in our previous studies. These findings offer valuable insights into the rational design of novel derivatives as promising anti-tuberculosis agents.

2. Methods

2.1 Structure optimizations and charge distribution analysis for derivatives and NAD+

To obtain stable structures of the damnacanthal for molecular docking simulations, their 3D configurations were searched in PubChem and fully optimized with density functional theory (DFT) at the B3LYP/6-31G** level using Gaussian09.7 Charge parameters for molecular mechanics (MM) force fields were derived by evaluating the charge distributions of the through optimized structures restrained electrostatic potential (RESP) analysis⁸ with the HF/6-31G* method in Gaussian09. The hydrogen atoms of NAD+ were optimized using the B3LYP/6-31G** method, and RESP charges for the optimized structure were calculated using the HF/6-31G* method in Gaussian09.

2.2 Molecular docking simulations of inhibitors to InhA

The crystal structure of the InhA complex with its inhibitor was initially downloaded from the Protein Data Bank (PDB). Various PDB structures representing crystal structure derivatives were reviewed, with preference given to those offering higher resolution. Indeed, 11 PDB structures were retrieve, and PDB code 4OHU9 was chosen for further analysis due to its superior resolution of 1.6 Å. Although the structural information for the Met01 and Thr02 residues of InhA was missing in this PDB structure, we proceeded without complementing these residues, as they are

located far from the ligand-binding pocket of InhA. To evaluate binding mode and important interactions of InhA inhibitors in the InhA binding pocket, docked conformations to the pocket were generated using the protein-ligand docking simulation program AutoDock4.2.6.¹⁰ The InhA structure used for docking was obtained from the Protein Data Bank (PDB ID: 4OHU).⁹ The docking grid box was defined to encompass the ligand-binding pocket of InhA. Its size was set to 52 × 52 × 52 points, centered on the co-crystallized ligand in the PDB X-ray structure of the InhA complex.⁹

3. Results & Discussion

3.1 Optimized structures of InhA with its inhibitor complexes

Molecular docking simulations were carried out using the AutoDock4.2 program to explore the binding conformations of InhA-ligand complexes. The crystal structure of InhA (PDB code 4OHU)9 was employed as the initial structure for the docking simulations, because of its reported high resolution of the crystal structure. To ensure the reliability of the docking results, a re-docking simulation was performed to compare the docked conformation with the crystal structure in the binding pocket of InhA. This comparison involved calculating the root mean square deviation (RMSD) between the docked pose and the crystal structure. The docking results revealed that cluster 1 contained the largest number of candidate poses (201), with the lowest binding energy of -10.0 kcal/mol lower than those of the other clusters. The representative structure of cluster 1 was confirmed to be similar to the crystal structure, as indicated by an RMSD value of 0.88 Å as shown in Figure 1.

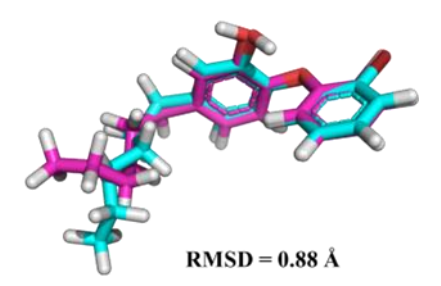


Figure 1. Superimposition of re-docked structure in the ligand-binding pocket of InhA. Cyan color indicates the PDB structure, while pink color indicates re-docked structure.





3.2 Crucial interaction of damnacanthal

To evaluate the binding mode of damnacanthal within the binding pocket of InhA, molecular docking studies were conducted. The damnacanthal was docked into InhA binding pocket, that showed lowest binding energy (-6.14 kcal/mol). The two-hydrogen bond interactions were found between hydroxyl and carbonyl of damnacanthal with Pro156 and Gln214, respectively (1.7 and 2.0 Å). Moreover, hydrophobic interactions were found with Phe149, Tyr158, Met155, Ala157, Met199, Val203, Ile215, and Leu218.

3.3 Rational design

To design novel potent inhibitors against InhA based on damnacanthal, which exhibits the highest inhibitory activity against InhA, we summarized the key interactions between damnacanthal and InhA residues in Figure 2, the hydroxyl group and oxygen atom of damnacanthal forms strong hydrogen bonds Pro156 and Gln214, respectively. with Meanwhile, the benzene ring is surrounded by hydrophobic residues of InhA. Consequently, we identified the R1, R2, and R3 sites on the benzene ring, as shown in Figure 3, and substituted the hydrogen atoms at these sites with various groups, as presented in Table 1. The design principle focuses on preserving key interactions by positioning the substituent site away from the critical interaction sites between InhA and damnacanthal. We analyzed the structure of benzene ring and identified InhA residues (Phe149, Tyr158, Met199, Val203 and NAD+) existing within 4 Å from damnacanthal as shown in Figure 3(A).

Furthermore, we examined the hydrogen atoms of the benzene ring, which exhibit interactions with these residues. To enhance the interactions, we considered hydrogen atom for substitution to enhance hydrogen bonding and hydrophobic interactions between the residues and damnacanthal. In fact, the three substituent sites (R1, R2, and R3 in Figure 3(B)) were considered and substituted by hydroxyl,

acetaldehyde and methoxymethane group, with the aim of improving both hydrophobicity and hydrogen bonding interactions.

Table 1. Chemical structures of damnacanthal and novel designed compounds, in which some of the R1, R2, and R3 groups are replaced and docking score

Code	R1	R2	R3	Docking score (kcal/mol)
N1	ОН	Н	Н	-3.7
N2	Н	ئىر 0 <	Н	-3.8
N3	Н	Н	ئمرً0 <	-5.2
N4	ОН	ОН	Н	-6.5
N5	Н	ОН	OH	-7.9
N6	ОН	Н	OH	-5.8
N7	OH	OH	OH	-7.7
N8	ОН	ئ ^{ري} 0 <	ОН	-4.4
N9	ئەر_0	ОН	ОН	-5.3

4. Conclusions

The crucial interactions between damnacanthal and the InhA residues as well as NAD+ cofactor were investigated using molecular docking calculations. The most potent compound exhibited strong hydrogen bond interactions with InhA, specifically with Pro156 and Gln214. Based on the results, nine newly designed compounds were obtained. The compounds exhibited docking scores ranging from -3.7 to -7.9 kcal/mol. This information may aid in developing novel anti-tuberculosis agents through the potent inhibition of InhA activity.





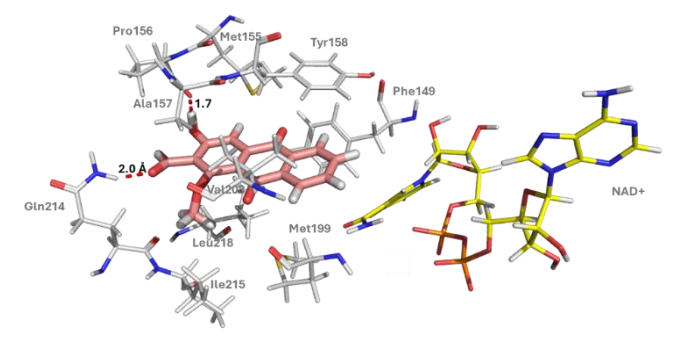


Figure 2. Binding modes and key binding interactions of damnacanthal in the InhA binding pocket.

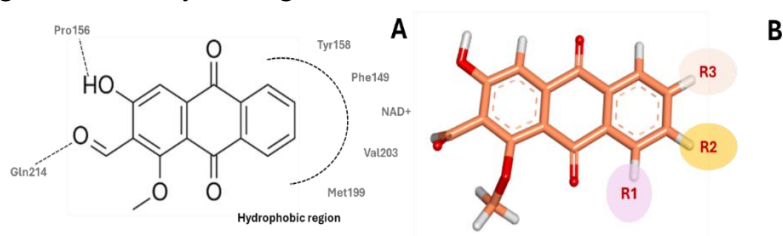


Figure 3. (A) Key interactions between damnacanthal and InhA residues. Dotted lines indicate hydrogen bonding and hydrophobic interaction sites, respectively. (B) Chemical structure of our designed derivatives based on damnacanthal, with the hydrogen atom at the R1, R2, or R3 site substituted by hydroxyl, acetaldehyde and methoxymethane group.

Acknowledgements

This study was supported by the Thailand Science Research and Innovation (TSRI), National Science, Research and Innovation Fund (NSRF), Center of Excellence for Innovation in Chemistry (PERCH-CIC) and Ubon Ratchathani University, Thailand. The financial support from Royal Golden Jubilee Ph.D. Program, Thailand to T. Pornprom (NRCT5-RGJ63020) gratefully was acknowledged. This project was funded by National Research Council of Thailand (NRCT): Contract number N42A670689. A part of this research was conducted as a part of the student exchange program between Toyohashi University of Technology and Ubon Ratchathani University, supported by the Japan Student Services Organization (JASSO).

Research ethics / Declarations

The authors declare no competing financial interest.

References

 Global Tuberculosis Report 2024. https://www.who.int/teams/globaltuberculosis-programme/tb-reports/globaltuberculosis-report-2024 (accessed February 18, 2025).

- Chollet, A.; Mourey, L.; Lherbet, C.; Delbot, A.; Julien, S.; Baltas, M.; Bernadou, J.; Pratviel, G.; Maveyraud, L.; Bernardes-Génisson, V. J. Struct. Biol. 2015, 190, 328–337.
- 3. Ando, H.; Kondo, Y.; Suetake, T.; Toyota, E.; Kato, S.; Mori, T.; Kirikae, T. *Antimicrob. Agents Chemother.* **2010**, *54*, 1793–1799.
- 4. Chollet, A.; Maveyraud, L.; Lherbet, C.; Bernardes-Génisson, V. *Eur. J. Med. Chem.* **2018**, *146*, 318–343.
- Prasad, M. S.; Bhole, R. P.; Khedekar, P. B.; Chikhale, R. V. *Bioorg. Chem.* 2021, 115, 105242.
- 6. Vilchèze, C.; Jacobs, W. R. *Microbiol. Spectrum* **2014**, *2*, MGM2–2013.
- 7. Tirado-Rives, J.; Jorgensen, W. L. *J. Chem. Theory Comput.* **2008**, *4*, 297–306.
- 8. Woods, R. J.; Chappelle, R. *J. Mol. Struct. THEOCHEM* **2000**, *527*, 149–156.
- 9. Li, H.-J.; Lai, C.-T.; Pan, P.; Yu, W.; Liu, N.; Bommineni, G. R.; Garcia-Diaz, M.; Simmerling, C.; Tonge, P. J. *ACS Chem. Biol.* **2014**, *9*, 986–993.
- 10.Hou, X.; Du, J.; Zhang, J.; Du, L.; Fang, H.; Li, M. *J. Chem. Inf. Model.* **2013**, *53*, 188–200.





Quantitative structure activity relationship and molecular docking calculations of xanthone derivatives as anti-tuberculosis agents

Wannasa Upom,¹ <u>Bongkochawan Phakamwong</u>,¹ Thimpika Pornprom,¹ Darunee Sukchit,¹ Khemmisara Sawatdee,¹ Auradee Punkvang,² Khomson Suttisintong,³ Prasat Kittakoop,^{4,5,6} Pornpan Pungpo^{1,*}

¹Department of Chemistry and Center of Excellence for Innovation in Chemistry,
Faculty of Science, Ubon Ratchathani University, Ubon Ratchathani, 34190, Thailand
²Division of Chemistry, Faculty of Science, Nakhon Phanom University, Nakhon Phanom, 48000, Thailand
³National Nanotechnology Center, NSTDA, Pathum Thani, 12120, Thailand
⁴Chulabhorn Research Institute, Laksi, Bangkok 10210, Thailand
⁵Chulabhorn Graduate Institute, Program in Chemical Sciences, Bangkok 10210, Thailand
⁶Center of Excellence on Environmental Health and Toxicology (EHT), OPS, Ministry of Higher Education,
Science, Research and Innovation, Bangkok 10210, Thailand
*E-mail: pornpan.p@ubu.ac.th

Abstract:

Tuberculosis (TB), caused by *Mycobacterium tuberculosis*, remains one of the most widespread diseases globally. A major challenge in TB treatment is the mutation of the DNA gyrase enzyme, which contributes to drug resistance. Consequently, there is an urgent need to discover novel and potent DNA gyrase inhibitors to overcome this resistance. Xanthone derivatives have emerged as promising GyrB inhibitors with potential anti-tuberculosis activity. In this study, molecular docking calculations were conducted to explore the binding modes and interactions of these derivatives. The results indicate that hydrogen bonding occurs between the oxygen atom at the R position of the ligand and the hydrogen atoms of Asp79, Thr169, and Gly83. Additionally, the xanthone derivatives exhibited π -cation interactions between their benzene ring and Arg82, as well as π - π interactions with Pro85 near the R' position. Hydrophobic interactions were also observed with Val49, Ala53, Val77, Val99, Val123, Val125, and Ile171. The resulting QSAR model is statistically reliable. These combined results contribute to the rational design of new, more potent GyrB inhibitors for tuberculosis treatment.

1. Introduction

Tuberculosis (TB) remains one of the world's most pressing public health challenges. According to the World Health Organization (WHO), an estimated 10.8 million people fell ill with TB in 2023, marking a slight increase from 10.7 million in 2022. Despite a modest decline in TB-related deaths from 1.32 million in 2022 to 1.25 million in 2023. TB has likely regained its position as the leading cause of death from a single infectious agent globally. The persistent burden of TB is exacerbated by the emergence of drug-resistant strains, particularly multidrugresistant (MDR-TB) and extensively drugresistant (XDR-TB) forms. A significant contributor to this resistance is mutations in the DNA gyrase enzyme, specifically in its GyrA and GyrB subunits. DNA gyrase, a type II topoisomerase, is essential for bacterial DNA replication and is a validated target for antibacterial Resistance agents. fluoroquinolones, which target this enzyme, underscores the urgent need to identify novel GyrB inhibitors with improved efficacy.

Among various chemical scaffolds, xanthone derivatives have shown promise due to their diverse biological activities and structural compatibility with the GyrB binding pocket. This study focuses on investigating the interaction profiles and binding affinities of xanthone derivatives using molecular docking and quantitative structure—activity relationship (QSAR) analysis. The aim is to support the rational design of new anti-TB agents capable of overcoming resistance mechanisms and enhancing treatment outcomes.

2. Methods

The structures and biological activities of xanthone derivatives were obtained from the literature.² All derivatives were constructed using the Hyperchem program and subsequently optimized using the B3LYP/6-31G(d,p) method. Molecular docking calculations were carried out using the Glide program³⁻⁵ to predict the binding orientations of potential inhibitors within the GyrB binding pocket (PDB code 4BAE).⁶ A 2D-QSAR





analysis was performed on the dataset using the SPSS software. For the molecular docking studies, three representative compounds listed in Table 1 were selected to evaluate their binding interactions with the GyrB active site.

Table 1. MIC values (μ g/mL) of the xanthone derivatives against *M. tuberculosis* H37Ra strain

3. Results & Discussion

3.1 Validation of the molecular docking calculations

A molecular docking approach was employed to investigate the key interactions between xanthone derivatives and the DNA gyrase subunit B. The results demonstrated that the docking calculations accurately predicted the binding mode and interactions of the 4BAE ligand within the GyrB binding site, yielding an RMSD of 0.72 Å. This low RMSD value indicates that the docking parameters were well-validated, ensuring high reliability of the docking predictions, as illustrated in Figure 1.

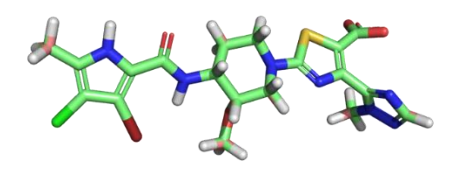


Figure 1. Superimposition of the ligand from the X-ray crystal structure (peach sticks) and the docked conformation (green sticks) of 4BAE within the GyrB binding pocket.

3.2 Molecular docking calculations analysis 3.2.1 Molecular docking calculations analysis of compound 1 – the most active compound

The oxygen atom of the hydroxyl group at the R position in compound 1 (MIC = $0.78 \mu g/mL$) forms hydrogen bonds with Asp79, Gly83, and Thr169. Additionally, a cation– π interaction is

observed between the benzene ring of compound 1 and Arg82. Moreover, hydrophobic interactions are identified with residues Val49, Ala53, Ala59, Val77, Ile84, Val123, Val125, and Ile171 (Figure 2A). These diverse molecular interactions contribute to the binding affinity and favorable orientation of compound 1 within the active site.

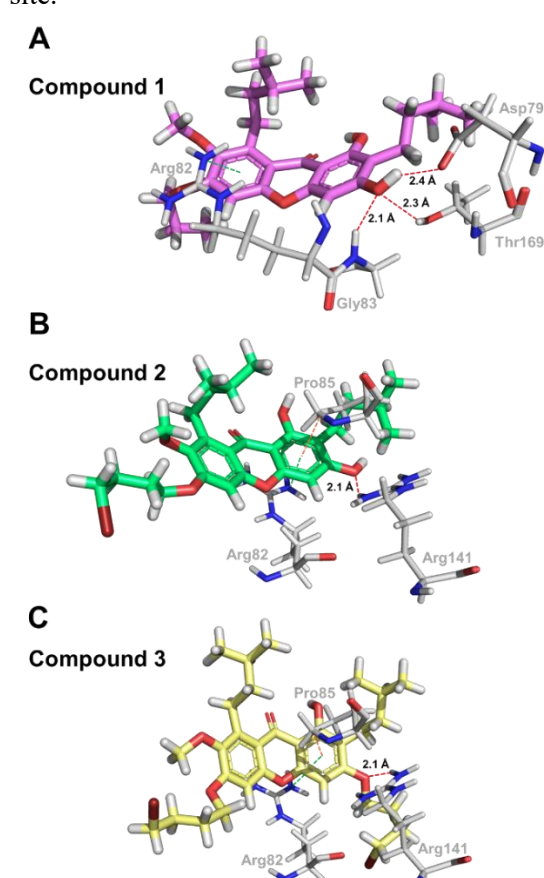


Figure 2. Binding mode of compounds 1(A), 2(B), and 3(C) in the GyrB binding pocket, as predicted by molecular docking calculations.

3.2.2 Molecular docking calculations analysis of compound 2 – a moderately active compound

Compound 2 exhibited an MIC value of $12.5 \,\mu\text{g/mL}$, which is considered moderate when compared to compounds 1 and 3. In the molecular docking analysis of compound 2, a hydrogen bond interaction is observed between the oxygen atom of its hydroxyl (OH) group and Arg141. The aromatic ring of the ligand is involved in a π -cation interaction with Arg82. A π - π interaction is also present between the





benzene ring near the R' position and the aromatic ring of Pro85. Additionally, hydrophobic interactions are observed with residues Val49, Ala53, Val77, Ile84, Val99, Val123, Val125, and Ile171 (Figure 2B). Compounds 1 and 2 share the same R group but differ at the R' position. Compound 2 has a 1-bromobutane group, while compound 1 has a propyl group. This difference affects their respective binding affinities.

3.2.3 Molecular docking calculations analysis of compound 3 – the least active compound

Compound 3 (MIC = $200.0 \,\mu\text{g/mL}$) exhibits the lowest antimicrobial activity among the three compounds. It shares the same substituent at the R' position as compound 2 but differs at the R position. A hydrogen bond interaction is observed between the oxygen atom of the R group in compound 3 and Arg141. Its aromatic ring participates in a π -cation interaction with Arg82, and a π - π interaction is also present between the benzene ring near the R' position and the aromatic ring of Pro85. Additionally, hydrophobic contacts are observed with the side chains of Val49, Ala53, Ile84, Val99, Val123, and Ile171 (Figure 2C). This structural difference influences the binding affinities of the compounds.

3.3 2D-QSAR

To further understand the structural features influencing biological activity, a 2D-QSAR analysis was analyzed. Physicochemical properties, including SA, VOL, logP, MR, POL, and mass, along with electronic properties such as C₁, C₂, C₃, C₄, O₅, C₆, C₇, C₈, C₉, C₁₀, C_{11} , C_{12} , C_{13} , C_{14} , O_{15} , and O_{16} , (Figure 3), were utilized as molecular descriptors derived from 2D-QSAR data. These descriptors were employed to investigate the relationship between molecular structure and inhibitory activity using appropriate statistical methods. A total of nine statistically significant QSAR models have been developed. The best model is Equation 1, with n = 34, $Q^2 = 0.638$, $R^2 = 0.799$, SE = 0.39663, F = 4.697, and SPRESS =0.4824. The Q² value greater than 0.6 indicates high reliability.

The derived 2D-QSAR model provides insights into the structural features that influence the antibacterial activity of the compounds, as expressed by log(1/MIC). Among the

descriptors, the atomic contribution at position O₅ shows the most significant negative impact

Figure 3. General structure of xanthone derivatives

 $\begin{array}{l} log(1/MIC) = 12.697(\pm 13.659)C_{14} \\ + 0.233(\pm 1.357)C_7 - 6.454(\pm 5.558)C_3 \\ - 13.981(\pm 6.987)C_{13} - 42.433(\pm 21.475)O_5 \\ - 3.164(\pm 1.726)C_9 - 15.470(\pm 26.832)C_4 \\ + 6.820(\pm 7.759)O_{15} - 4.940(\pm 2.780) \end{array} \qquad \begin{array}{l} \textbf{Eq 1} \end{array}$

(coefficient = -42.433), indicating that increased electron density or unfavorable electronic properties at this site may markedly reduce the inhibitory potency. Conversely, positive coefficients such as those at C_{14} (12.697) and O_{15} (6.820) suggest that these positions contribute positively to activity, and modifications enhancing favorable interactions at these atoms may improve potency.

Several other positions, such as C₃, C₄, C₉, and C₁₃, show moderate to strong negative contributions, implying that their electronic environments also play a critical role in determining biological efficacy. The best 2D-QSAR model was employed to predict the antimicrobial activity (MIC values) of the compounds, as summarized in Table 2.

3.4 Structural requirements

The structural requirements for enhanced antibacterial activity include a hydroxyl group (-OH) at the R position, which forms crucial hydrogen bonds with active site residues. A small, nonpolar alkyl group such as a propyl chain at the R' position is preferred for optimal hydrophobic interactions. Substitution at R' with bulkier groups like 1-bromobutane reduces activity. Electron-donating groups at O₅ negatively affect potency, while positive electronic contributions at C₁₄ and O₁₅ enhance activity. Therefore, maintaining favorable hydrogen bonding and hydrophobic profiles, along with optimal electronic properties, is essential for improving inhibitory efficacy.





Table 2. Experimental and predicted activities of the training and test sets derived from best 2D-QSAR model.

	log (1/MIC)				
Compound	Experiment	Predicted	Residue		
1	4.82	4.75	0.07		
2	4.83	4.84	-0.01		
2 3	4.85	4.75	0.10		
4	4.85	4.79	0.06		
5	4.56	4.92	-0.36		
6	4.60	4.99	-0.39		
7	4.61	5.50	-0.89		
8	5.42	4.83	0.59		
9	5.74	5.24	0.50		
10	4.54	4.83	-0.29		
11	4.81	4.73	0.08		
12	4.22	4.61	-0.39		
13	5.12	5.12	0.00		
14	3.93	3.70	0.23		
15	5.45	5.39	0.06		
16	4.55	4.59	-0.04		
17	5.47	5.22	0.25		
18	5.21	4.90	0.31		
19	5.48	5.37	0.11		
20	5.77	5.31	0.46		
21	5.77	4.75	1.02		
22	5.48	5.37	0.11		
23	4.64	4.77	-0.13		
24	3.53	4.34	-0.80		
25	4.89	5.41	-0.52		
26	4.66	4.75	-0.09		
27	4.86	4.75	0.11		
28	5.17	4.79	0.38		
29	5.20	4.72	0.48		
30	3.67	4.35	-0.68		
31	5.53	4.92	0.61		
32	4.35	4.88	-0.53		
33	5.22	5.42	-0.20		
34	4.70	4.92	-0.22		

4. Conclusions

This study highlights the potential of xanthone derivatives as promising GyrB inhibitors against drug-resistant *Mycobacterium tuberculosis*. Molecular docking revealed key interactions, including hydrogen bonding, π – π interactions, and hydrophobic interactions with amino acid residues at the GyrB binding site. The statistically reliable QSAR model further supports insights into the structure–activity relationship. The integrated results from this study will support the design of new potential DNA gyrase inhibitors for anti-tuberculosis therapy.

Acknowledgements

This study was supported by the Thailand Science Research and Innovation (TSRI), National Science, Research and Innovation

Fund (NSRF), Center of Excellence for Innovation in Chemistry (PERCH-CIC) and Ubon Ratchathani University, Thailand.

Research Ethics / Declarations

The authors declare no competing financial interest.

References

- 1. WHO. Global tuberculosis report 2024. https://www.who.int/teams/global-programme-on-tuberculosis-and-lung-health/tb-reports/global-tuberculosis-report-2024 (accessed April 20, 2025).
- 2. Sudta, P.; Jiarawapi, P.; Suksamrarn, A.; Hongmanee, P.; Suksamrarn, S. *Chem Pharm Bull (Tokyo)* **2013**, *61*, 194–203.
- 3. Friesner, R. A.; Banks, J. L.; Murphy, R. B.; Halgren, T. A.; Klicic, J. J.; Mainz, D. T.; Repasky, M. P.; Knoll, E. H.; Shelley, M.; Perry, J. K.; Shaw, D. E.; Francis, P.; Shenkin, P. S. *J. Med. Chem.* **2004**, *47*, 1739–1749.
- Halgren, T. A.; Murphy, R. B.; Friesner, R. A.; Beard, H. S.; Frye, L. L.; Pollard, W. T.; Banks, J. L. *J. Med. Chem.* 2004, 47, 1750–1759.
- Friesner, R. A.; Murphy, R. B.; Repasky, M. P.; Frye, L. L.; Greenwood, J. R.; Halgren, T. A.; Sanschagrin, P. C.; Mainz, D. T. *J. Med. Chem.* 2006, 49, 6177–6196.
- P, S. H.; Solapure, S.; Mukherjee, K.; Nandi, V.; Waterson, D.; Shandil, R.; Balganesh, M.; Sambandamurthy, V. K.; Raichurkar, A. K.; Deshpande, A.; Ghosh, A.; Awasthy, D.; Shanbhag, G.; Sheikh, G.; McMiken, H.; Puttur, J.; Reddy, J.; Werngren, J.; Read, J.; Kumar, M.; R, M.; Chinnapattu, M.; Madhavapeddi, P.; Manjrekar, P.; Basu, R.; Gaonkar, S.; Sharma, S.; Hoffner, S.; Humnabadkar, V.; Subbulakshmi, V.; Panduga, V. Antimicrob. Agents Chemother. 2014, 58, 61–70.





Investigation of the bioactivities of *Caesalpinia pulcherrima* (L.) SW wood extracts and *In silico* analysis of Stigmasterol as an InhA inhibitor

Pritsana Srisaengmueang,¹ <u>Darunee Sukchit</u>,¹ Khemmisara sawatdee,¹ Thimpika Pornprom,¹ Bongkochawan Pakamwong,¹ Paptawan Thongdee,⁵ Somjintana Taveepanich,¹ Kampanat Chayajarus,¹ Saisamorn Lumlong,¹ Prajakkit Rawee,¹ Jitlada Dechatiwong,¹ Jidapa Sangswan,² Kanjana Pangjit,³ Auradee Punkvang,⁴ Khomson Suttisintong,⁵ Prasat Kittakoop,^{6,7,8} Pornpan Pungpo^{1,*}

¹Department of Chemistry and Center of Excellence for Innovation in Chemistry, Faculty of Science, Ubon Ratchathani University, Ubon Ratchathani 34190, Thailand ²Department of Biological Science, Faculty of Science, Ubon Ratchathani University, Ubon Ratchathani 34190, Thailand

³College of Medicine and Public Health, Ubon Ratchathani University, Ubon Ratchathani 34190, Thailand ⁴Division of Chemistry, Faculty of Science, Nakhon Phanom University, Nakhon Phanom, 48000, Thailand ⁵National Nanotechnology Center, National Science and Technology Development Agency (NSTDA) 111 Thailand Science Park, Klong Luang, Pathum Thani 12120, Thailand ⁶Chulabhorn Research Institute, Laksi, Bangkok 10210, Thailand

⁷Chulabhorn Graduate Institute, Program in Chemical Sciences, Bangkok 10210, Thailand

⁸Center of Excellence on Environmental Health and Toxicology (EHT), OPS, Ministry of Higher Education,
Science, Research and Innovation, Bangkok 10210, Thailand

*E-mail: pornpan.p@ubu.ac.th

Abstract:

This research evaluates the chemical constituents, antioxidant activity, and antibacterial activity of crude extracts from the wood of *Caesalpinia pulcherrima* (L.) SW. Additionally, molecular simulations were performed. Crude extracts were obtained using hexane, dichloromethane, ethyl acetate, and methanol. The methanol extract yielded the highest percentage at 0.64%. Antioxidant activity was assessed using the ABTS assay at a concentration of 1000 mg/L of the ethyl acetate extract, resulting in 14.61% \pm 1.31 inhibition. Antibacterial activity was evaluated using the agar disc diffusion method at concentrations of 200, 500, and 1000 mg/mL. The ethyl acetate extract at 1000 mg/mL showed an inhibition zone of 8.33 \pm 0.58 mm against *S. aureus* ATCC 25923. Stigmasterol was identified in the ethyl acetate extract, and its inhibition of InhA was assessed, showing 95% inhibition at 64 μ M. To further investigate its inhibitory mechanism, molecular docking was conducted to analyze binding modes and interactions within the InhA binding pocket. Stigmasterol exhibited the lowest binding energy at -4.77 kcal/mol. The most active compound formed strong interactions with InhA, including hydrogen bonds with Asp150 and Arg153. These findings provide valuable insights for the rational design of more effective InhA inhibitors with enhanced anti-tuberculosis activity.

1. Introduction

Tuberculosis (TB) remains one of the leading infectious diseases worldwide, posing serious public health challenges due to the emergence of drug-resistant strains of Mycobacterium tuberculosis. The urgent need for new therapeutic agents has directed increasing interest toward bioactive compounds derived from natural products. In this context, medicinal plants represent a promising reservoir of secondary metabolites with potential antibacterial and antioxidant properties.

Natural products have attracted considerable interest as alternative sources of bioactive compounds with potential applications in

disease prevention and treatment.1 Medicinal plants, in particular, have played a significant role in traditional healthcare systems and have become the focus of modern research due to their diverse pharmacological properties and lower risk of side effects compared to synthetic drugs.² Among these, Caesalpinia pulcherrima (L.) Sw., commonly known as the peacock flower, is a tropical ornamental plant traditionally used for the treatment of various ailments including fever, bronchitis, and skin infections. Previous studies have reported the presence of flavonoids, terpenoids, and other secondary metabolites in different parts of the plant, suggesting its therapeutic potential.³ While extensive research has been conducted





on the leaves, flowers, and seeds of *C. pulcherrima*, the wood of this plant remains underexplored. Investigating the chemical profile and biological activities of the wood extract may uncover new bioactive constituents with practical applications in pharmaceutical or nutraceutical development. In this study, crude extracts from the wood of *C. pulcherrima* were prepared using solvents of varying polarity. The chemical composition, antioxidant activity, and antibacterial properties of each extract were evaluated. Additionally, the identification and bioactivity of a major compound, stigmasterol, were examined to further understand its therapeutic relevance.

2. Methods

2.1 Extraction and isolation

Dried wood of Caesalpinia pulcherrima (8.9 kg) were chopped into small pieces and ground into fine powder using a mechanical herbal grinder. The powdered plant material was wrapped in muslin cloth and sequentially extracted using 40 L of each solvent n-hexane, dichloromethane, ethyl acetate, and methanol in that order. Each extraction was performed by maceration kept at room temperature for 7 days. After the extraction period, the mixtures were filtered. The filtrates were concentrated under reduced pressure using a rotary evaporator at 40°C to remove the bulk of the solvent. The DCM extract was column chromatography on alumina, eluting with different solvents such as hexane, hexane: EtOAc: MeOH, EtOAc: MeOH and MeOH. The LD8 fraction, examined by TLC using hexane: EtOAc (3:1v/v) solvent system showed single spot. This fraction was crystallized with DCM and Hexane that afforded a compound (3.0101%) as white needle crystal which was identified as stigmasterol based on spectroscopy (¹H, ¹³C NMR) data.

2.2 ABTS Cation Radical Decolorization Assay

The ABTS⁺⁺ radical scavenging activities of the extracts were determined according to the literature.^{3,4} 7 mM of ABTS⁺⁺ solution was prepared from 2,2-azino-bis(3-ethylbenzothiazo-line-6-sulfonic acid) and K₂S₂O₃. The solution was kept in the dark for 24 h at room temperature, and the absorbance of the solution was measured at 734 nm. The solutions of the extracts were prepared in 1000

mg/mL and added to vial. Immediately after, the ABTS⁺⁺ solution was added and incubated at room temperature in the dark. The absorbance of the mixer was measured at 734 nm after 10 min incubation (Each absorbance was taken to be the mean of triplicate measurements). The results were reported as the % inhibition value.

2.3 Antibacterial activity

The antibacterial activity of the crude extract was evaluated using the agar disc diffusion method against S. aureus (Gram-positive) Bacterial suspensions were cultured in Luria Bertani (LB) broth and incubated at 37°C for 16-18 hours. A sterile cotton swab was used to evenly spread the bacterial suspension on LB agar plates. Sterile paper discs (6 mm in diameter) were placed on the inoculated agar plates, and 20 µL of each test solution was applied to the discs using a sterile micropipette. plates were then incubated 35 ± 2 °C for 48 hours. After incubation, the antibacterial activity was assessed measuring the diameter of the inhibition zones around each disc in millimeters (mm).

2.4 Enzyme inhibition assay (InhA)

The inhibitory activity of the compound was expressed as the percentage of InhA inhibition, based on the initial reaction velocity, relative to a control reaction without the inhibitor.

2.5 Molecular docking simulations of inhibitors to InhA

To evaluate binding mode and important interactions of InhA inhibitors in the InhA binding pocket, docked conformations to the pocket were generated using the protein-ligand docking simulation program AutoDock4.2.6. The InhA structure used for docking was obtained from the Protein Data Bank (PDB ID: 4OHU). The docking grid box was defined to encompass the ligand-binding pocket of InhA. Its size was set to $68 \times 68 \times 68$ points, centered on the co-crystallized ligand in the PDB X-ray structure of the InhA complex.

3. Results & Discussion

3.1 Extraction and isolation

Dried wood of Caesalpinia pulcherrima (8.9 kg) was sequentially extracted with hexane, dichloromethane, ethyl acetate, and methanol. The highest crude extract yield was obtained from methanol (0.6414%), followed by ethyl acetate (0.1903%), dichloromethane



(0.1796%), and hexane (0.1365%), indicating that polar solvents were more effective in extracting phytochemicals. Further purification of the dichloromethane extract by column chromatography led to the isolation of a pure which identified compound, was stigmasterol. The structure was confirmed by ¹H and ¹³C NMR.

3.2 Antioxidant activity by ABTS assay

The ABTS radical scavenging activity of the crude extracts from Caesalpinia pulcherrima wood was evaluated at a concentration of 1000 mg/L and compared with the standard antioxidant, Trolox. As shown in Figure 1, Trolox exhibited the highest ABTS⁺ scavenging activity (approximately 82%), serving as a positive control. Among the crude extracts, the methanol extract showed the highest activity (~38%), followed by ethyl acetate (~14%). The dichloromethane and hexane extracts exhibited minimal scavenging effects, with values less than 5%. These results suggest that polar solvents, particularly methanol, were more effective in extracting antioxidant compounds from the wood of C. pulcherrima.

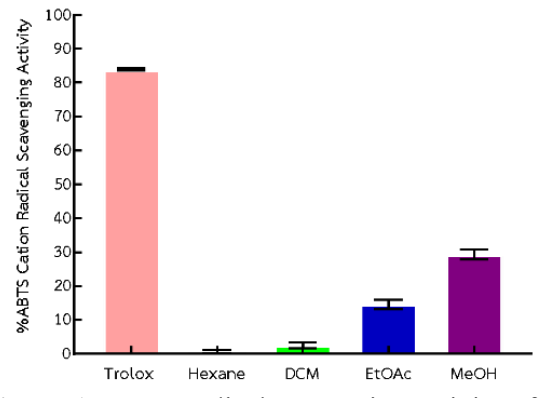
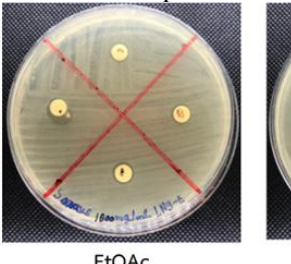


Figure 1. ABTS radical scavenging activity of Caesalpinia pulcherrima wood crude extracts obtained using different solvents (1000 mg/L), compared with Trolox as standard.

3.3 Antibacterial activity

The ethyl acetate and methanol crude extracts Caesalpinia pulcherrima demonstrated antibacterial activity against S.aureus at concentrations of 500 and 1000 mg/L. At 500 mg/L, both extracts produced inhibition zones of 7.00 ± 0.00 mm. When the concentration was increased to 1000 mg/L, the ethyl acetate extract showed a greater inhibition

zone of 8.33 ± 0.58 mm compared to the methanol extract of 7.50 ± 0.71 mm. These findings suggest that bioactive compounds extracted by moderate polar (EtOAc) and polar solvents antibacterial (MeOH) possess properties. The observed activity could be attributed to the presence of secondary metabolites such as flavonoids, phenolics, or terpenoids, which have been reported to disrupt microbial membranes and inhibit bacterial enzymes.4,5 Previous studies have shown that ethyl acetate and methanol are effective solvents for extracting antibacterial compounds from medicinal plants.6





EtOAc

MeOH

Figure 2. Antibacterial activity of ethyl acetate and methanol crude extracts of Caesalpinia pulcherrima wood (1000 mg/L) against S. aureus using agar disc diffusion method.

3.4 Enzyme inhibition assay (InhA)

Stigmasterol was identified in the ethyl acetate extract, and its inhibition of InhA was assessed, showing 95% inhibition at 64 µM.

Molecular 3.5 docking simulations inhibitors to InhA

To evaluate the binding mode of stigmasterol within the InhA binding pocket, molecular docking studies were performed. Stigmasterol was docked into the InhA active site, yielding the lowest binding energy of -4.77 kcal/mol. Two hydrogen bond interactions were observed: one between the hydroxyl group of stigmasterol and Asp150, and another between its carbonyl group and Arg153 as shown in Figure 3.

4. Conclusions

This study demonstrated that polar solvents, particularly methanol and ethyl acetate, are effective in extracting bioactive phytochemicals from Caesalpinia pulcherrima wood. Methanol yielded the highest crude extract and exhibited the strongest antioxidant





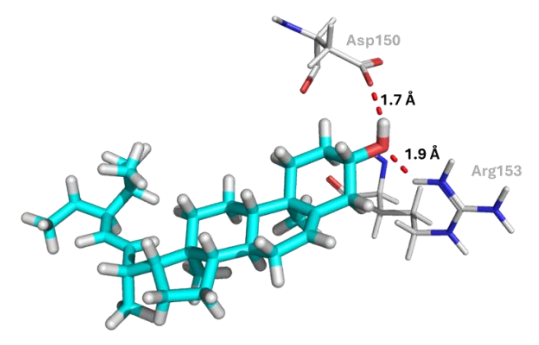


Figure 3. Binding modes and key binding interactions of Stigmasterol in the InhA binding pocket.

antibacterial activity against S. aureus. A pure compound, stigmasterol, was isolated from the dichloromethane extract and identified via NMR spectroscopy. Stigmasterol exhibited significant inhibitory activity against InhA enzyme (95% at 64 µM), and molecular docking studies revealed strong binding interactions with key residues Asp150 and Arg153 within the InhA active site. These findings suggest that C. pulcherrima wood promising compounds contains with antioxidant, antibacterial, and potential antitubercular properties.

References

- 1. Newman, D. J.; Cragg, G. M. *J. Nat. Prod.* **2020**, *83*, 770–803.
- Atanasov, A. G.; Waltenberger, B.; Pferschy-Wenzig, E. M.; Linder, T.; Wawrosch, C.; Uhrin, P.; Temml, V.; Wang, L.; Schwaiger, S.; Heiss, E. H.; Rollinger, J. M.; Schuster, D.; Breuss, J. M.; Bochkov, V.; Mihovilovic, M. D.; Kopp, B.; Bauer, R.; Dirsch, V. M.; Stuppner, H. *Biotechnol. Adv.* 2015, 33, 1582–1614.
- 3. Pulipati, S.; Pallavi, G.; Sujan, B.; Babu, K.; Babu, P. *Int. J. Biomed. Pharm. Res.* **2012**, *3*, 360–365.
- 4. Cowan, M. M. Clin. Microbiol. Rev. 1999, 12, 564–582.
- 5. Cushnie, T. P. T.; Lamb, A. J. *Int. J. Antimicrob. Agents* **2011**, *38*, 99–107.
- 6. Qin, L.; Chen, S.; Xie, L.; Yu, Q.; Chen, Y.; Xie, J. *Process Biochem.* **2022**, *121*, 248–256.





Bioactive extraction from bamboo, roselle, and monk fruit for a fiber-rich wellness drink with sustainable packaging

Ratchaphong Katerung,^{1,*} Narissara Uthai,¹ Duangrutai Thumrongchote,¹ Supakorn Boonyuen²
¹Department of Home Economics, Faculty of Home Economics Technology, Rajamangala University of Technology Krungthep, Bangkok, 10120, Thailand

²Faculty of Science and Technology, Thammasat University, Amphoe Khlong Luang, Pathum Thani 12120 *E-mail: vkatrung@gmail.com

Abstract:

This study investigates the extraction, characterization, and application of bioactive compounds from various species of bamboo (Bambusoideae), with an emphasis on optimizing the retention and controlled release of flavonoid-rich extracts for multifunctional use. Eight bamboo species were evaluated for agronomic performance and phytochemical composition, with *Dendrocalamus sericeus* Munro (Sang-Mon bamboo) exhibiting the highest total flavonoid content, reaching a peak during the post-monsoon period (October-November). Flavonoid structures were elucidated using UV-Vis spectroscopy and HPLC analysis. Antibacterial assays demonstrated significant inhibition zones against Staphylococcus aureus and Escherichia coli, while cytotoxicity assessments confirmed the safety of the extracts at concentrations below 100 ppm in fibroblast cell lines. In addition, silver nanoparticles synthesized via green methods using Sang-Mon bamboo flavonoids exhibited enhanced antioxidant activity, as measured by DPPH and ABTS radical scavenging assays. Encapsulation using lysosomemimetic vesicles enabled sustained release, indicating strong potential for cosmetic and biomedical applications. These findings contributed to the formulation of a fiber-enriched instant wellness beverage, combining bamboo leaf extract, Hibiscus sabdariffa (roselle), Siraitia grosvenorii (monk fruit), and citrus-derived soluble fiber. The beverage is designed to support digestive health, metabolic balance, muscle recovery, and hydration. Advanced eco-friendly extraction and encapsulation technologies were employed to preserve bioactivity and improve nutrient bioavailability. The final product offers a sustainable, plant-based alternative to synthetic sports drinks, addressing consumer demand across ASEAN and global markets while enhancing socio-economic opportunities for local agricultural communities through value-added bamboo-based innovations.

1. Introduction

Bamboo, a member of the Poaceae family (subfamily Bambusoideae), comprises over 1,250 species found primarily in tropical and subtropical regions of Asia, South America, and parts of Africa. While its stems and shoots have been widely utilized in construction, furniture, and food industries, increasing attention has turned toward the medicinal and bioactive potential of bamboo, particularly its leaves.¹⁻⁷ Historically, bamboo leaves have been used in traditional Asian medicine to treat fever, detoxify the body, and improve cardiovascular health. Extracts from various bamboo species, such as Phyllostachys nigra and Bambusa vulgaris, have demonstrated antioxidant, antiaging, and antibacterial properties, largely due to their high content of flavonoids and phenolic compounds.8-12

In Thailand, more than 80 species of bamboo are native or naturalized. Among them, *Dendrocalamus sericeus* Munro (commonly known as Sang Mon bamboo) and *Bambusa*

vulgaris Schrad. ex J.C.Wendl. are of significant agricultural and economic value. *D. sericeus*, indigenous to northern Thailand, is known for its large, straight culms and durable leaves, whereas *B. vulgaris* is widely distributed and commonly used in traditional remedies and functional foods. ¹³⁻²⁰

Recent studies have highlighted the potential of bamboo leaf extracts in combating oxidative stress and bacterial infections, yet research on certain species—such as D. sericeus—remains limited.21-25 Thus, the present study aims to investigate bioactive the compounds, antioxidant antibacterial capacity, and properties of leaf extracts from *Dendrocalamus* sericeus and Bambusa vulgaris, with the goal of promoting their value in pharmaceutical and nutraceutical applications.



2. Methods

2.1 Sample Collection and Extraction

Leaves of *Dendrocalamus sericeus* and *Bambusa vulgaris* were collected from Prachin Buri, Thailand (September 2024). Two extraction methods were used:

Maceration: 40 g of dried leaves were soaked in 200 mL of 95% ethanol, shaken at 150 rpm for 7 days, filtered, and evaporated under vacuum. Soxhlet: 40 g of sample were extracted in 200 mL of 95% ethanol for 8 hours, followed by vacuum evaporation. Extracts were stored at 4 °C in amber bottles.

2.2 Antioxidant Assays

2.2.1 DPPH Assay

Adapted from Sharma and Tej, 26 100 μ L of extract (10–100 ppm) was mixed with 900 μ L of 0.08 mM DPPH, incubated in the dark for 30 min, and measured at 515 nm. % inhibition was calculated using the equation:

% Inhibition = $(AB-AS)/AB\times100$

2.2.2 ABTS Assay

Following Re et al., ²⁷ ABTS•+ was prepared and diluted to absorbance 0.70 at 734 nm. 100 μL of extract (25–100 ppm) was added, reacted for 6 min, and absorbance was measured at 734 nm.

2.2.3 FRAP Assay

Following Benzie and Strain, ²⁸, ²⁹ FRAP reagent was mixed and preheated. 200 µL of extract was added to 2.8 mL reagent, incubated for 4 min, and absorbance measured at 539 nm. Results were reported as µmol Fe²⁺ equivalents.

2.3 Total Phenolic Content

Using the Folin–Ciocalteu method,³⁰ 100 µL of extract was reacted with Folin reagent, sodium carbonate, and water. After 2 h incubation in the dark, absorbance was read at 731 nm. Results were expressed as µg GAE/mg dry weight.

2.4 Total Flavonoid Content

Based on Onanong et al.,³¹ extract was reacted sequentially with NaNO₂, AlCl₃, NaOH, and water. After incubation, absorbance was measured at 510 nm. Flavonoid content was expressed as µg QE/mg dry weight.

2.5 Antibacterial Activity

The disc diffusion method³⁶ was used against S. aureus and *E. coli*. Extracts (10 mg/L in methanol) were applied (50 μ L) to sterile discs and placed on nutrient agar. Penicillin (10 mg/L) served as the positive control. Inhibition zones were measured after 24 h incubation at 37 ± 2 °C.

3. Results & Discussion

Ethanol was selected as the extraction solvent due to its effectiveness, safety, and ability to preserve bioactive compounds such as polyphenols and flavonoids.³² As shown in Table 1 and Figure 1, both *Dendrocalamus sericeus* and *Bambusa vulgaris* leaf extracts exhibited notable antioxidant activity and high flavonoid content.

These findings are consistent with previous studies,³³ suggesting that both bamboo species share similar phytochemical profiles. The strong antioxidant properties observed are attributed to the presence of flavonoids, which are efficiently extracted with ethanol and remain structurally stable during the process.³⁴ This supports the potential use of bamboo leaves as a natural source of health-promoting compounds for

food, pharmaceutical, and nutraceutical applications.

Table 1. Antioxidant activity of both types of bamboo leaf crude extracts by DPPH assay, ARTS assay and FRAP assay

Types of	Extraction	DPPH IC ₅₀	ABTS IC ₅₀	FRAP values
bamboo	method	(ppm)	(mM)	(mM/g.)
Dendrocalamus	Maceration	37.07±0.02 ^c	5.72±0.03 ^b	0.14±0.00 ^a
sericeus Munro	Soxhlet	32.41±0.07 ^a	5.30±0.02ª	0.12±0.00 ^b
Bambusa	Maceration	43.61±0.25 ^d	18.15±0.06 ^d	0.12±0.00 ^b
vulgaris Schrad	Soxhlet	33.01±0.44 ^b	17.42±0.21 ^c	0.10±0.00°
ascorbic acid (vit	amin C)	1.23±0.00	1.20±0.00	0.20±0.00

Different superscript letters (a, b, c, etc.) within the same column indicate statistically significant differences (p < 0.05).

Table 1 summarizes the antioxidant activities of *Dendrocalamus sericeus* and *Bambusa vulgaris* leaf extracts using ethanol via immersion and Soxhlet methods. The Soxhlet method showed stronger antioxidant activity in DPPH and ABTS assays, with the lowest IC_{50} found in *D. sericeus* (32.41 \pm 0.07 ppm and 5.30 \pm 0.02 mM, respectively). In contrast, the FRAP assay showed higher iron (II) recovery with the immersion method, especially in *B. vulgaris* (0.14 \pm 0.00 Fe mM/g). Compared to vitamin C, both extracts showed lower activity but remain promising natural antioxidant sources, with Soxhlet extraction providing the highest overall efficiency.





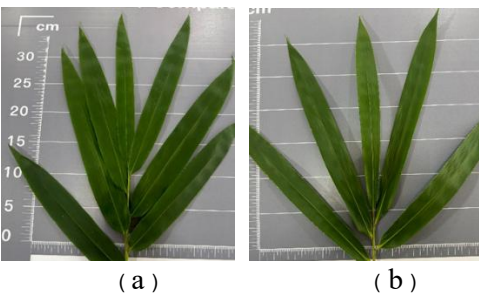


Figure 1. Characterisitics of bamboo leaves: *Dendrocalamus sericeus Munro* (a) and *Bambusa vulgaris* Schrad (b)

Previous studies have shown that phenols and flavonoids are key antioxidants in bamboo. These compounds play a vital role in free radical scavenging and have potential for use in food, pharmaceutical, and nutraceutical industries. This study examined how leaf type and extraction method affect phenolic and flavonoid content (Table 2).

Table 2. Total phenolic compounds (TPC) and total flavonoid compounds (TFC) content

· · · · · · · · · · · · · · · · · · ·					
	Extraction	TPC	TFC		
Types of bamboo	method	(µg GAE/mg dry wt.)	(µg QE/mg dry		
	metriod		wt.)		
Dendrocalamus	Maceration	54.87±0.01 ^a	123.46±12.35ª		
sericeus Munro	Soxhlet	46.64±0.01°	115.23±7.13 ^b		
Bambusa vulgaris	Maceration	50.75±0.01 ^b	61.73±0.00°		
Schrad	Soxhlet	41.15±0.01 ^d	45.27±7.13 ^d		

Different superscript letters (a, b, c, etc.) within the same column indicate statistically significant differences (p $\!<\!0.05$).

Table 2 shows that the extraction method significantly influenced the total phenolic (TPC) and flavonoid content (TFC) in both Dendrocalamus sericeus and Bambusa vulgaris leaf extracts. Solvent immersion yielded higher TPC and TFC than Soxhlet extraction in both species, with D. sericeus showing the highest values (TPC: $54.87 \pm 0.007 \mu g$ GAE/mg; TFC: 123.46 ± 12.35 µg QE/mg). The superior performance of maceration is likely due to reduced heat exposure and longer solvent contact time, which help preserve heat-sensitive compounds. These results, supported by antioxidant activity (Table 1), confirm that immersion is more effective for extracting bioactive compounds. Mass spectrometry analysis further indicated phenolic structures (m/z 430, 329, 213), consistent with prior findings³⁵ that associate phenols and flavonoids with antioxidant activity in bamboo.

Table 3 shows that *Dendrocalamus sericeus* leaf extracts inhibited *E. coli* and *S. aureus* more effectively than *Bambusa vulgaris*, likely due to higher flavonoid and polyphenol content. Although less potent than penicillin, the extracts show promise as natural antibacterial agents. MIC and MBC results are summarized in Table 4.

Table 3. Antibacterial activity of various bamboo leaf extracts (n=3)

Types of bamboo leaves	Inhibition zone (mm)		
Types of barriboo teaves	E. coli	S. aureus	
Dendrocalamus sericeus Munro	5.75 ± 0.71 ^a	3.10 ± 0.20 ^a	
Bambusa vulgaris Schrad	3.25 ± 0.41 ^b	1.50 ± 0.71 ^b	
Penicillin antibiotics	7.25 ± 0.08	7.05 ± 0.18	

Different superscript letters (a, b, c, etc.) within the same column indicate statistically significant differences (p < 0.05).

Table 3 shows that *Dendrocalamus sericeus* leaf extract exhibited stronger antibacterial activity than *Bambusa vulgaris*, with larger inhibition zones against *E. coli* (5.75 mm) and *S. aureus* (3.10 mm), though still less effective than penicillin.

In the study to find the Minimum Inhibitory Concentration (MIC) and Minimum Bactericidal Concentration (MBC), a color change was used to indicate bacterial growth: purple means no growth, pink means growth. Both bamboo leaf extracts showed purple color in the first two wells, indicating the lowest concentration needed to stop bacterial growth (MIC). For the MBC test, samples from wells without growth were placed on agar plates. The lowest concentration that prevented bacterial growth on the agar was recorded as the MBC. The results are shown in Table 4.

Table 4. presents the results of the Minimum Inhibitory Concentration (MIC) and Minimum Bactericidal Concentration (MBC) tests for extracts from *Dendrocalamus sericeus* Munro leaves and *Bambusa vulgaris* Schrad leaves

Types of bamboo leaves	MIC	MBC	MIC	MBC
	E. coli	E. coli	S. aureus	S. aureus
Dendrocalamus sericeus Munro	500	500	500	500
Bambusa vulgaris Schrad	500	500	500	500

From Table 4, both *Dendrocalamus sericeus* Munro and *Bambusa vulgaris* Schrad leaf extracts inhibited and killed *E. coli* and S. aureus at 500 ppm (MIC and MBC). The MBC/MIC ratio was 1, indicating strong antibacterial effectiveness. These results





support previous studies and suggest these bamboo extracts have potential as natural antibacterial agents for food, beverages, and medical uses

Acknowledgements

This research project was supported by the Science, Research and Innovation Fund (Fundamental Fund), Chemistry Program, Faculty of Science and Technology, Thammasat University, and the Department of Home Economics, Faculty of Home Economics Technology, Rajamangala University of Technology Krungthep (Phra Nakhon Tai).

4. Conclusions

The ethanol extraction of Dendrocalamus sericeus Munro and Bambusa vulgaris Schrad efficiently yielded antioxidant compounds, with Soxhlet extraction showing stronger antioxidant activity. However, solvent immersion produced higher phenolic and flavonoid contents, key compounds for antioxidant effects. Dendrocalamus sericeus Munro extract also inhibited E. coli and S. aureus growth, with antibacterial activity comparable to penicillin. Both extracts had MIC and MBC values of 500 ppm and an MBC/MIC ratio of 1, indicating strong antibacterial effectiveness. Overall, these bamboo leaf extracts show promising antioxidant and antibacterial potential.

References

- Lu, B.; Chen, J.; Huang, W.; Wu, D.; Xu, W.; Xie, Q.; Li, L. Afr. J. Biotechnol. 2011, 10, 8448–8455.
- Jan, E. G.; Wolter, E. H.; Claudia, M. D. M. Perennial Grasses for Bioenergy and Bioproducts Production 2018, 175–216.
- 3. Goyal, A. K.; Kar, P.; Sen, A. *Biology of Useful Plants and Microbes* **2013**, 197–208.
- 4. Goyal, A.; Brahma, B. *Int. J. Fundam. Appl. Sci.* **2014**, *3*, 2–10.
- 5. Sarawood, S.; Atchara, T. *Agric. Nat. Resour.* **2017**, *51*, 499–503.
- 6. Hong, E.-J.; Jung, E.-M.; Lee, G.-S.; Kim, J.Y.; Na, K.-J.; Park, M.-J.; Kang, H.-Y.; Choi, K.- C.; Seong, Y.H.; Choi, I.-G.; Jeung, E.-B. J. Ethnopharmacol. **2010**, *128*, 594–599.

- Mária, H. F.; Antonio, L. B.; Mariana, S. C.; Flávia, V. B.; Célia, M. L. F.; Maria, T. P. S. C. Food Res. Int. 2019, 124, 222–229.
- 8. Biswajeet, A.; Amulyaratna, B.; Prafulla, K. S.; Durga, P. M.; Sukumar, P.; Bimalendu, C.; Suchismeeta, B. *Adv. Bamboo Sci.* **2024**, *9*, 100110.
- 9. Soejatmi, D.; Wong, K. M. For. Bull. (BOT) **2004**, 32, 73–75.
- 10. Shukla, R.; Sumit, G.; Sajal, S.; Dwivedi, P. K.; Mishra, A. *Int. J. Biopharm. Phytochem. Res.* **2012**, *1*, 9–15.
- 11. Basumatary, A.; Middha, S. K.; Usha, T.; Brahma, B. K.; Goyal, A. K. Res. Plant Biol. 2015, 5.
- 12. Tang, T. K. H.; Liese, W. J. Bamboo Rattan **2011**, 10, 1–12.
- 13. Sahoo, A.; Ogra, R. K.; Sood, A.; Ahuja, P. S. *Grassl. Sci.* **2010**, *56*, 116–125.
- 14. Kim, C. Y.; Lee, H. J.; Jung, S. H.; Lee, E. H.; Cha, K. H.; Kang, S. W.; Um, B. H. *J. Korean Soc. Appl. Biol. Chem.* **2009**, *52*, 613–619.
- 15. Loa, J.; Chow, P.; Zhang, K. *Cancer Chemother. Pharmacol.* **2009**, *63*, 1007–1016.
- Lv, Z. L.; Lin, X.; Miao, Z. H.; Guo, H. X.;
 Wang, J. A. H.; Lei, M. L.; Pan, Y.; Zhang,
 B. L. Sci. Res. Essays 2012, 7, 3789–3796.
- 17. Seki, T.; Maeda, H. *Anticancer Res.* **2010**, *30*, 111–118.
- Zhang, Y.; Bao, B.; Lu, B.; Ren, Y.; Tie, X.; Zhang, Y. J. Chromatogr. A 2005, 1065, 177–185.
- Tanaka, A.; Zhu, Q.; Tan, H.; Horiba, H.; Ohnuki, K.; Mori, Y.; Yamauchi, R.; Ishikawa, H.; Iwamoto, A.; Kawahara, H.; Shimizu, K. Molecules 2014, 19, 8238– 8260.
- 20. Jin, Y.-C., Yuan, K., Zhang, J. *Molecules* **2011**, *16*, 4318–4327.
- 21. Wang, J.; Yue, Y. D.; Tang, F.; Sun, J. *Molecules* **2012**, *17*, 12297–12311.
- 22. Singh, S. R.; Dalal, S.; Singh, R.; Dhawan, A. K.; Kalia, R. K. *Acta Physiol. Plant.* **2013**, *35*, 419–430.
- 23. Chaiyalad, S.; Sungkaew, S.; Siripatanadilok, S. *Thai J. For.* **2013**, *32*, 1–8.
- 24. Thanapisit, P. Sci. Technol. J. **2015**, 23, 22–34.
- 25. GBIF Secretariat. GBIF Backbone Taxonomy 2022.





- 26. Sharma-Om, P.; Tej, B. K. Food Chem. **2009**, 113, 1202–1205.
- 27. Re, R.; Pellegrini, N.; Protegente, A.; Pannala, A.; Yang, M. *Free Radic. Biol. Med.* **1999**, *26*, 1231–1237.
- 28. Benzie, I. F. F.; Strain, J. J. *Anal. Biochem.* **1996**, *239*, 70–76.
- 29. Benzie, I. F. F.; Strain, J. J. Methods Enzymol. **1999**, 299, 15–27.
- 30. Pitchaporn, W.; Naret, M.; Sirithon, S. *Food Chem.* **2014**, *157*, 457–463.
- 31. Onanong, K.; Sirithon, S.; Nathida, W.; Naret, M. *J. Funct. Foods* **2011**, *3*, 88–99.
- 32. Aiko, S.; Tsukasa, S.; Eiichi, S.; Noriyuki, Y.; Kazumi, Y.; Tadashi, T. *J. Herb. Pharmacother.* **1991**, *33*, 159–167.
- Boris, M. P.; Denis, U.; Abir, B.; Dejan, A.; Teodora, K.; Malik, A.; Noureddine, E.; Yacine, B. *J. Mol. Liq.* **2024**, *415*, 126333.
- 34. Yonggang, D.; Ge, Z.; Gonghui, S.; Yiming, W.; Wei, L.; Shitong, R. *Eur. Polym. J.* **2022**, *162*, 110898.
- 35. Haimei, L.; Yongsheng, C.; Qingxia, P.; Xinjia, T.; Guo, C.; Hua, Z.; Rian, Y. *Ind. Crops Prod.* **2022**, *178*, 114609.
- 36. Abu, H. D. A.; Nur, Q. A. R.; Muhammad, H. M. Y.; Kian-Hui, C.; Mohd, L. K.; Noor, H. U.; Shafinas, A.; Nur, S. R.; Mardiana, S.; Muhammad, H. S. *Biocatal. Agric. Biotechnol.* **2023**, *54*, 102930.





Preparation of bioactive ionic liquids for extraction of polyhydroxylated fatty alcohols from avocado (*Persea americana*)

<u>Kristoffer Rem Labing-isa</u>,^{1,*} Sanya Sureram,² Chulabhorn Mahidol,² Somsak Ruchirawat,^{1,2,3} Prasat Kittakoop^{1,2,3}

¹Chulabhorn Graduate Institute, Program in Chemical Sciences, Laksi, Bangkok, Thailand 10210

²Chulabhorn Research Institute, Kamphaeng Phet 6, Talat Bang Khen, Laksi, Bangkok, Thailand 10210

³Center of Excellence on Environmental Health and Toxicology, (EHT) OPS, Ministry of Higher Education,

Bangkok 10400, Thailand

*E-mail: kristoffer@cgi.ac.th

Abstract:

Ionic liquids have emerged as promising and sustainable alternative to conventional solvents in response to increasing concerns over the environmental and health hazards associated with traditional methods used for the extraction of bioactive natural products. Ionic liquids have interesting properties including tunability and recyclability. In this study, cholinium-based ionic liquids were synthesized and evaluated as an extraction solvent system, in combination with co-solvents, e.g., water, ethanol, and hexane, for the extraction of polyhydroxylated fatty alcohols from the seeds and pulp of *Persea americana* (avocado). Although the synthesized cholinium-based ionic liquids could extract polyhydroxylated fatty alcohols from the avocado matrix under the tested conditions, separation of the ionic liquids from co-solvents was difficult, and thus hampering the recycling of ionic liquids. Therefore, these ionic liquids may not be suitable for the extraction of bioactive natural products. However, we found that the ionic liquid, choline laurate (Ch-IL12), exhibited antibacterial activity against the selected bacterial strains, for example, *Escherichia coli*, *Staphylococcus epidermidis*, *Staphylococcus aureus*, and *Enterococcus faecalis*.

1. Introduction

Polyhydroxylated fatty alcohols (PFAs) found in the avocado fruits were previously found to have virucidal and antiviral activities.1 Amongst the avocado tissues of the fruit being used to extract these compounds, seed has the highest concentrations of PFAs.2 However, their traditional extraction and processing methodologies normally use organic solvents including hexane3 and chloroform-methanol mixtures,4 which pose challenges in scalability and cost-effectiveness, as well as in the environmental impact that could limit their widespread use in commercial products. Ionic liquids (ILs) have emerged as a revolutionary alternative solvents in extracting bioactive natural products, offering a greener solution to these issues because of its interesting properties including tunability and recyclability.5

This study synthesized and assessed cholinium-based ionic liquids as an extraction solvent system in conjunction with co-solvents such as water, ethanol, and hexane to extract PFAs from *Persea americana* (avocado) seeds and pulp. PFAs, avocadene (1) and avocadyne (2), are the major compounds in avocado seeds and pulp, and their structures are shown in Figure 1. Avocadene (1) and avocadyne (2) have

interesting biological activities, for example, a potent inhibitor of fatty acid oxidation,⁶ anthelmintic activity,⁷ and mosquito larvicidal activity.⁸ Avocatin B, a mixture of avocadene (1) and avocadyne (2), could selectively induce apoptosis of leukemia and leukemia stem cells,⁹ and the analytical method was developed for avocatin B using LC-MS method.¹⁰

Figure 1. Chemical structures of common PFA compounds found in avocado, avocadene (1) and avocadyne (2).

2. Methodology

2.1 Preparation of ionic liquids

The ionic liquids (ILs) were synthesized following the method reported by Petkovic, ¹¹ by dropwise addition of the corresponding acid (1:1) to aqueous cholinium bicarbonate. A mixture was kept stirring overnight at ambient temperature and pressure. The synthesized ILs were characterized by comparison of ¹H-Nuclear Magnetic Resonance (NMR) spectra





with those reported in the literature. NMR spectra (in D₂O) were recorded on 400 MHz NMR spectrometer.

2.2 PFA extraction from avocado

The avocado fruits were bought from a local market in Bangkok, Thailand, in November 2024. The avocado seed was separated from the fruit and was hammered into small pieces. Ground avocado seed and pulp were stored in a refrigerator until further use. ILs were mixed with one of the co-solvents, water, ethanol, and hexane, in the ratio of 1:2 (weight by volume), and these solvent systems were used for extraction. Avocado pulp or seed was mixed with each solvent system using the ratio of 1:4 solid to liquid (weight by volume). Avocado pulp or seed was soaked in each solvent system for 3 days. After filtration, the extract was placed in a refrigerator at 4°C for 1 day for the solvent system using water. For the solvent systems with ethanol or hexane, they were kept at -80 °C; this process is to separate ILs from water, ethanol, and hexane.

2.3 Antibacterial and antifungal analysis

All of the synthesized cholinium-based ILs were tested against various gram positive, gram negative bacteria and fungus following the Kirby-Bauer Disk Diffusion Susceptibility Test Protocol using Mueller-Hinton Agar media.¹³ Microorganisms tested for antimicrobial activity Staphylococcus aureus. Staphylococcus epidermidis, Enterococcus faecalis, Escherichia coli, Salmonella typhi, Shigella flexneri, and Candida albicans. The size of the discs (HIMEDIA, SD067-5CT) in the antimicrobial assay is 0.6 cm. ILs were dissolved in ethanol to achieve a-1mg per disc concentration, and the discs were left to dry for 1 day before using for antimicrobial testing. Positive controls were ciprofloxacin and ampothericin B.

3. Results & Discussion 3.1 Synthesis of ILs

Five cholinium-based ionic liquids with varying molecular carbon chains were synthesized, namely choline acetate (Ch-IL02), choline butyrate (Ch-IL04), choline hexanoate (Ch-IL06), choline octanoate (Ch-IL08), and choline laurate (Ch-IL12). These ILs were identified by analysis of NMR data, as well as by data comparison from literature.^{6,12} The ¹H

NMR spectra (in D_2O) of these ILs revealed signals at the following δ_H /ppm:

Choline acetate (Ch-IL02): 3.94 (m, 2H, -O-CH₂-), 3.39 (m, 2H, -CH₂-N-), 3.08 (s, 9H, -N-CH₃), 1.79 (s, 3H, -CO-CH₃).

Choline butyrate (Ch-IL04): 4.04 (m, 2H, -O-CH₂-), 3.49 (m, 2H, -CH₂-N-), 3.18 (s, 9H, -N-CH₃), 2.13 (t, 2H, -CH₂-), 1.53 (m, 2H, -CH₂-), 0.87 (t, 3H, -C-CH₃).

Choline hexanoate (Ch-IL06): 4.02 (m, 2H, -O-CH₂-), 3.48 (m, 2H, -CH₂-N-), 3.16 (s, 9H, -N-CH₃), 2.12 (t, 2H, -CH₂-), 1.51 (m, 2H, -CH₂-), 1.25 (m, 4H, -CH₂-), 0.84 (t, 3H, -C-CH₃).

Choline octanoate (Ch-IL08): 4.00 (m, 2H, -O-CH₂-), 3.47 (m, 2H, -CH₂-N-), 3.16 (s, 9H, -N-CH₃), 2.10 (t, 2H, -CH₂-), 1.50 (m, 2H, -CH₂), 1.25 (m, 8H, -CH₂-), 0.84 (t, 3H, -C-CH₃).

Choline laurate (Ch-IL12): 4.01 (m, 2H, -O-CH₂-), 3.49 (m, 2H, -CH₂-N-), 3.17 (s, 9H, -N-CH₃), 2.12 (t, 2H, -CH₂-), 1.51 (m, 2H, -CH₂-), 1.26 (s, 16H, -CH₂-), 0.85 (t, 3H, -C-CH₃).

3.2 Extraction of PFAs

We found that the ILs-solvent systems employed in this work could extract PFAs at different levels. Among the ILs-solvent systems, choline butyrate, Ch-IL04-hexane solvent system, was found to efficiently extract avocadene (1) and avocadyne (2) from avocado seed. As shown in Figure 2, a crude extract using Ch-IL04-hexane solvent system showed signals of both avocadene (1) and avocadyne (2). In a crude extract of avocado seeds using Ch-IL04-hexane solvent system (Figure 2, bottom), a peak at δ_H 5.82 ppm is a characteristic of avocadene (1), while at δ_H 2.18 ppm is of avocadyne (2). These results demonstrated that the Ch-IL04-hexane solvent system could extract both PFAs 1 and 2 from avocado seeds. Efforts have been made for recovering ILs from the extract using lower temperatures at -80 °C in order to turn liquid ILs to become solid, which will be collected and used for the next extraction. However, the liquid ILs did not turn to be solid under the solvent systems used for the extraction, suggesting that lowering temperature could not assist ILs recovery. There are a few recovery methods for ILs, for example, distillation, membrane separation, extraction, aqueous twophase system, and adsorption.14 Further investigation on ILs recovery for cholinium-





based ionic liquids presented in this work should be performed in the future.

3.3. Antibacterial assay

Cholinium-based ionic liquids were tested against various gram-positive and gramnegative bacteria, as well as the fungus *Candida albicans*, to assess antibacterial and antifungal activities.

Positive controls were 5-mg ciprofloxacin per disc for antibacterial test, and 10-mg ampothericin B for antifungal test. As shown in Table 1, it was found that amongst the synthesized ionic liquids, Ch-IL12 has antibacterial activity against the bacterial strains *E. coli*, *S. epidermidis*, and *E. faecalis* with the zone inhibitions of 1.0 cm, 1.5 cm, and

2.0 cm, respectively. In addition, Ch-IL12 showed antibacterial activity against *S. aureus* with the zone inhibition of 1.0 cm.

4. Conclusions

Cholinium-based ionic liquids were synthesized and used to extract polyhydroxylated fatty alcohols from avocado. Among the solvent mixtures used, Ch-IL04hexane solvent system could efficiently extract avocadene (1) and avocadyne (2) from avocado seed. However, it was difficult to recover ionic liquids for recycling. The ionic liquid Ch-IL12 showed antibacterial activity against a few bacterial strains including S. aureus, E. coli, S. epidermidis, and E. faecalis.

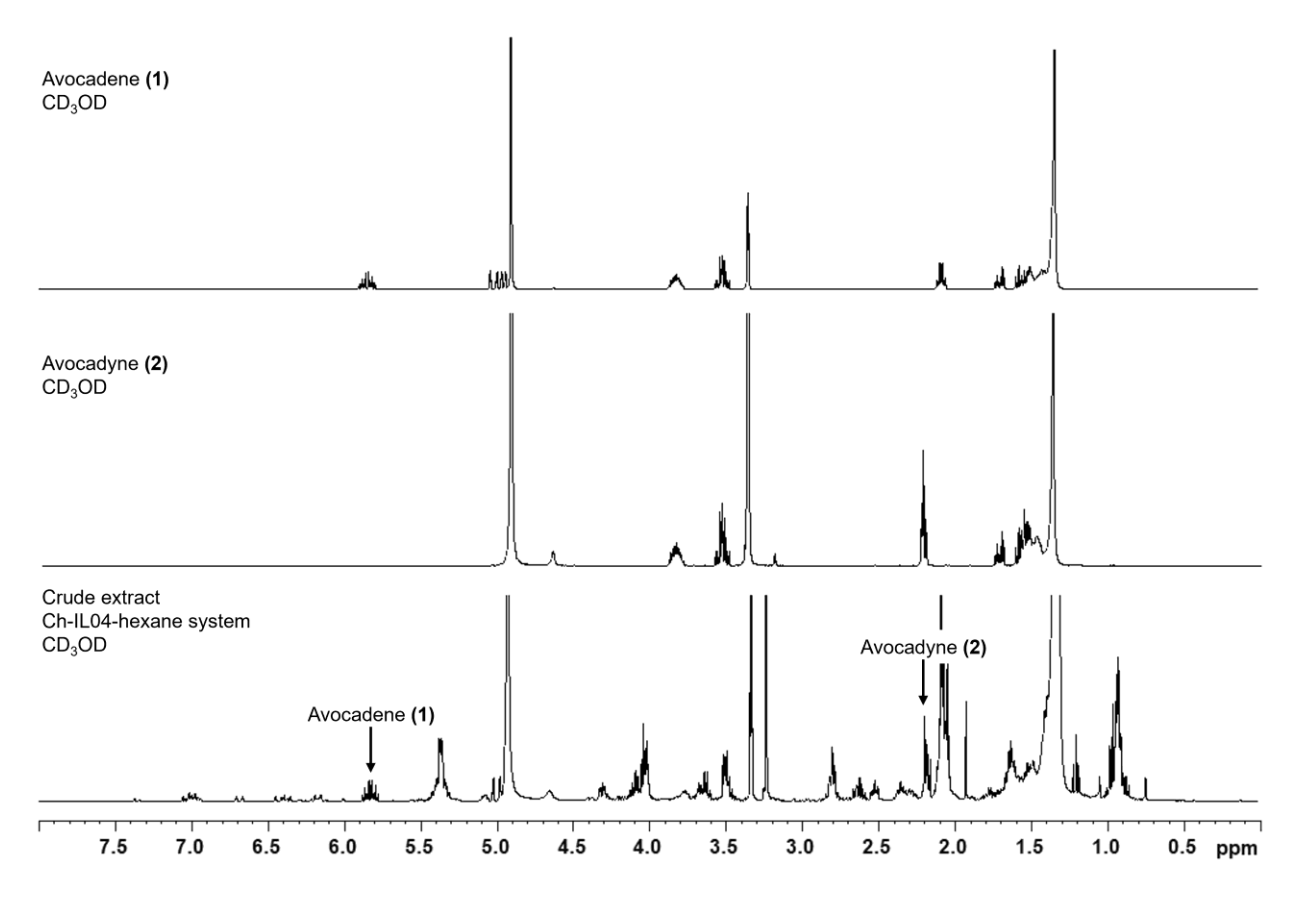


Figure 2. NMR spectra (in CD₃OD) of a crude extract of avocado seeds using Ch-IL04-hexane solvent system (bottom), avocadyne (2) (middle), and avocadene (1) (top).





Table 1. Inhibition zones of choline-ionic liquids against various bacteria and fungus.

Choline-	E.	S.	E.	C.	S.	S.	S.
IL	coli	epidermidis	faecalis	albicans	typhi	flexneri	aureus
Ch-IL02	NA	NA	NA	NA	NA	NA	NA
Ch-IL04	NA	NA	NA	NA	NA	NA	NA
Ch-IL06	NP	NP	NP	NA	NA	NA	NA
Ch-IL08	NA	NA	NA	NA	NA	NA	NA
Ch-IL12	1.0 cm	1.5 cm	2.0 cm	NA	NA	NA	1.0 cm

NA means that there is no activity against the bacteria, and NP means that the test is not yet performed.

Acknowledgements

This work is supported by the grant funded by the National Research Council of Thailand (NRCT), Contract number N42A670689. This work is supported in part by the grant from the Center of Excellence on Environmental Health and Toxicology (EHT), OPS, Ministry of Higher Education, Science, Research and Innovation. We acknowledge the financial support and facilities of the Chulabhorn Research Institute (CRI) and the Chulabhorn Graduate Institute (CGI), as well as the grant from the NRCT and Thailand Science Research and Innovation (TSRI). Kristoffer Rem Labingisa thanks the grant from the Chulabhorn Graduate Institute Scholarship Commemorating Princess Chulabhorn's 60th Birthday Anniversary Commemoration Scholarship, and thanks the Thailand International Cooperation Agency (TICA).

References

- Darshana, D.; Chutiwitoonchai, N.; Paemanee, A.; Sureram, S.; Mahidol, C.; Ruchirawat, S.; Kittakoop, P. ACS Food Sci. Technol. 2023, 3, 1759–1767.
- Rodríguez-Sánchez, D. G.; Pacheco, A.; Villarreal-Lara, R.; Ramos-González, M. R.; Ramos-Parra, P. A.; Granados-Principal, S.; Díaz de la Garza, R. I.; García-Rivas, G.; Hernández-Brenes, C. Molecules 2019, 24, 2354.
- Rosenblat, G.; Meretski, S.; Segal, J.; Tarshis, M.; Schroeder, A.; Zanin-Zhorov, A.; Lion, G.; Ingber, A.; Hochberg, M. Arch. Dermatol. Res. 2011, 303, 239–246.
- Ahmed, N.; Smith, R. W.; Chen, P. X.; Rogers, M. A.; Spagnuolo, P. A. Food Chem. 2025, 463, 140811.
- Ventura, S. P. M.; e Silva, F. A.; Quental, M. V.; Mondal, D.; Freire, M. G.;

- Coutinho, J. A. P. Chem. Rev. 2017, 117, 6984–7052.
- Tcheng, M.; Minden, M. D.; Spagnuolo, P. A. J. Food Biochem. 2022, 46, e13895.
- 7. Fahs, H. Z.; Refai, F. S.; Gopinadhan, S.; Moussa, Y.; Gan, H. H.; Hunashal, Y.; Battaglia, G.; Cipriani, P. G.; Ciancia, C.; Rahiman, N.; et al. *Nat. Commun.* **2025**, *16*, 305.
- Louis, M.; Rani, V. P.; Krishnan, P.; Reegan, A. D.; Balakrishna, K.; Ignacimuthu, S.; Packiam, S. M.; Maheswaran, R.; Shirota, O. Appl. Biochem. Biotechnol. 2023, 195, 2636– 2647.
- 9. Lee, E. A.; Angka, L.; Rota, S.-G.; Hanlon, T.; Mitchell, A.; Hurren, R.; Wang, X. M.; Gronda, M.; Boyaci, E.; Bojko, B.; et al. *Cancer Res.* **2015**, *75*, 2478–2488.
- 10. Ahmed, N.; Smith, R. W.; Henao, J. J. A.; Stark, K. D.; Spagnuolo, P. A. *J. Nat. Prod.* **2018**, *81*, 818–824.
- Petkovic, M.; Ferguson, J. L.; Gunaratne, H. Q. N.; Ferreira, R.; Leitão, M. C.; Seddon, K. R.; Rebelo, L. P. N.; Pereira, C. S. *Green Chem.* 2010, 12, 643–649.
- 12. Sharma, M.; Prakash Chaudhary, J.; Mondal, D.; Meena, R.; Prasad, K. *Green Chem.* **2015**, *17*, 2867–2873.
- 13. Kirby-Bauer Disk Diffusion Susceptibility Test Protocol. https://asm.org/protocols/kirby-bauer-disk-diffusion-susceptibility-test-pro (accessed May 14, 2025).
- 14. Khoo, Y. S.; Tjong, T. C.; Chew, J. W.; Hu, X. Sci. Total Environ. **2024**, 922, 171238.





Shellfish "Royal Purple" pigment discovered via HPLC on a 2,500-year old marble jar of the Persian King Darius the Great

Zvi C. Koren*

The Edelstein Center for the Analysis of Ancient Artifacts, Department of Chemical Engineering Shenkar College of Engineering, Design and Art, Ramat Gan, Israel *E-mail: zvi@shenkar.ac.il

Abstract:

Royal Purple (or Shellfish Purple) is a designation used to describe regal textiles dyed with the purple pigment extracted from a certain gland of some Muricidae sea snails inhabiting the Mediterranean. These purple and violet garments conferred upon the wearer an aura of power and sacredness and, thus, only sovereigns, military generals, eminent officials, and high priests wore such textiles. This molluskan pigment is the most mystifyingly complex of all the natural colorants used in antiquity. In the current research, high-performance liquid chromatography (HPLC) coupled with photodiode array (PDA) detection was used for the microchemical analysis of residual decorative purple paint pigments on the surface of a 2,500-year old stone jar. This pear-shaped marble vessel contains carved quadrilingual inscriptions praising the Persian King Darius I. The major colorants identified in the purple pigment are 6,6'-dibromoindigo, 6-monobromoindigo, and 6,6'-dibromoindirubin, with traces of indigo and 6-bromoisatin. This analysis establishes that a marine mollusk was the source of the purple pigment, which is also known as Tyrian Purple of the ancients – a rare find. A comparison with the relative dye compositions of various Muricidae species suggests that the biological provenance of this ancient pigment was probably an indigo-deficient *Hexaplex trunculus* sea snail.

1. Introduction

Royal robes, cloaks, mantles, and textile furnishings were distinct in that these items were dyed in whole, or in part, with the glandular fluid extracted from certain sea snails that produced reddish-purple and bluish-purple (violet) pigments. The reddish product of "shellfish purples" was also referred to historically as Royal Purple, Imperial Purple, and Tyrian Purple, the latter name invoking the name of the Phoenician city Tyre where these molluskan pigments were produced. The violet - bluish - variety has also been termed as "Biblical Blue", which refers to the colors of some of the vestments worn by the Israelite High Priest as well as certain textile furnishings of King Solomon's Temple in Jerusalem. The mollusks that produced these highly colorful pigments belong to the Muricidae family, and in the Mediterranean region, three species of sea snails were known to produce such pigments, and their modern taxonomic names are Hexaplex trunculus, Bolinus brandaris, and Stramonita haemastoma. 1-4

The discoverers of the purple pigment that can be extracted from these sea snails are undoubdetly those people of the Aegean Sea are from about 4,000 years ago. These purple pigments were originally used as paint pigments for the production of certain motifs in frescos. However, it was probably the Phoenicians who succeeded in con being able to chemically convert the pigment – a water-insoluble colorant – into one that is water-soluble, a dye, which can then be used for the dyeing of textiles.

In the current work, a unique marble vessel, or jar, associated with King Darius I – the "Great" – of Ancient Persia, and thus dated from about 2,500 years ago, had splotches of purple residues on the outside of the container. There was no residual pigmentation on the interior of the vessel. A close examination also showed that the base, the underside of the vessel, also showed residual purple spots. It is, thus, supposed that most probably the entire outside of the vessel was painted purple, and today, much of this paint pigment has rubbed off of the object. The investigation was to identify these residual purple pigments on the vessel.

2. Methods

The optimal method for analyzing natural organic colorants from flora and fauna is the technique known as HPLC (high-performance liquid chromatography), and the detection is enabled by the photo-diode array (PDA) detector attached to it. The resulting





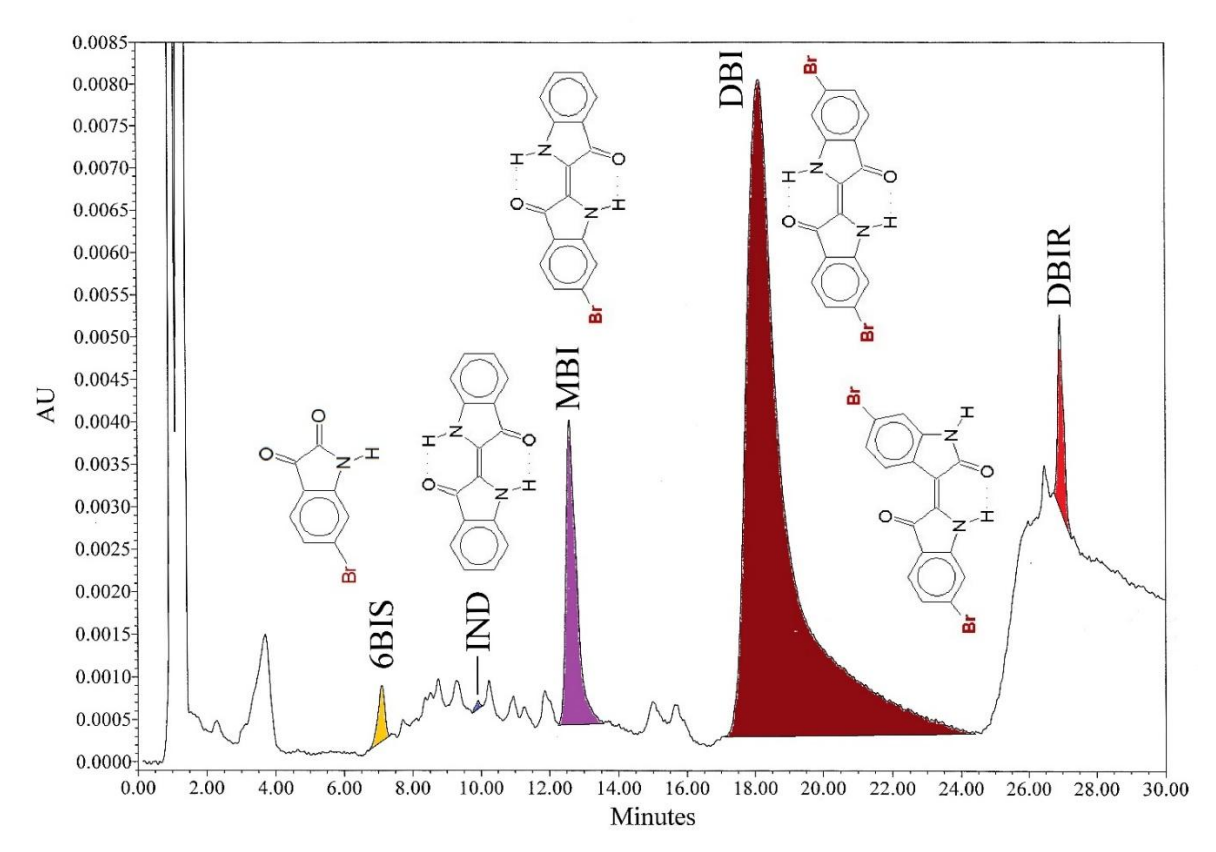


Figure 1. HPLC chromatogram of the DMSO-extracted purple pigment from the Darius jar at 300 nm. The detected dyes are, as follows: 6-bromoisatin (6BIS), indigo (IND), 6-monobromoindigo (MBI), 6,6'-dibromoindigo (DBI), and 6,6'-dibromoindirubin (DBIR).

chromatographic property of a unique retention time for each separated dye component as well as a spectrometric property, the dye's UV/Vis absorption spectrum, are double identifying features that are instrumental in identifying each dye in the purple mixture.

2.1 Dye extraction

In order to extract and dissolve the purple pigment, which is the least soluble of all natural colorants, a suitable solvent is needed. Though, pyridine and DMF (dimethyl formamide) have been shown to be effective solvents for these colorants, however, the optimal solvent has been shown to be DMSO (dimethyl sulfoxide). This has been used for the purple pigment on the King Darius jar, at 100 °C for 10 minutes. A purple sample the size of the tip of a needle, was inserted into a 2-mL glass vial, with the addition of 400 µL of DMSO. The mixture was heated for 10 minutes in a dry-bath heater, with shaking, set to 100 °C. The reddish-purple pigment produces a blue solution, which after cooling, was filtered through a 0.45-u nylon

filter (with polypropylene housing). Exactly 20-μL of this solution was then injected into the HPLC.

2.2 HPLC system

The chromatographic system used has been detailed elsewhere, and is hereby summarized.^{5,6} An all-Waters reverse-phase HPLC-PDA system was used with a ternary mobile phase consisting of water, methanol, and an aqueous 5% phosphoric acid solution.

3. Results & Discussion

The HPLC-produced chromatogram at 300 nm of a purple extract from the King Darius jar is shown in Figure 1. In the figure, the molecular structures of the identified dye components are shown, together with their abbreviated names.⁷ The identification of a brominated indigoid dye in a pigment automatically implies that the dyestuff source of this colorant is a shellfish, as only they produce such a brominated pigment. Hence, the presence of DBI, the common dye of all shellfish purple pigments signifies that the





pigment was indeed used to paint a royal object, as only kings and emperors were able to utilize such precious pigments.

4. Conclusions

The detection of the brominated indigoid dyes in the purple paint residue on the jar associated with King Darius I proves that this vessel is indeed a royal object. This is a rare instance where the shellfish purple pigment was used to paint an entire object – a royal marble jar.

Acknowledgements

The author is grateful to the Edelstein Foundation for supporting this research into the natural dyes used in antiquity.

References

- Cardon, D. Natural Dyes Sources, Tradition, Technology and Science; Archetype Publications: London, 2007; Ch. 11
- 2. Cooksey, C. J. Molecules 2001, 6, 736–769.
- 3. Wouters, J. Dyes Hist. Archaeol. **1992**, 10, 17–21
- 4. Karapanagiotis, I. *Sustainability* **2019**, *11*, 1–23.
- 5. Koren, Z. C. *Microchim. Acta* **2008**, *162*, 381–392.
- 6. Koren, Z. C. *Dyes Hist. Archaeol.* **2008**, *21*, 26–35.
- 7. Koren, Z. C. Heritage 2023, 6, 2186–2201.

.





Kinetic model comparison and analysis in citronella leaves (*Cymbopogon winterianus*) extraction using microwave hydro-distillation

Patar Jonathan Sipahutar, Mahfud*

Department of Chemical Engineering, Institut Teknologi Sepuluh Nopember, Indonesia *E-mail: mahfud@chem-eng.its.ac.id

Abstract:

Microwave-assisted extraction methods have shown significant advancements in essential oil extraction processes. Among these, microwave hydro-distillation (MHD) has been recognized for its ability to produce high-quality essential oils. This study aims to analyze and evaluate the kinetic model the extraction process of citronella leaves (*Cymbopogon winterianus*). The variables include feed-to-solvent (F/S) ratios of 0.1, 0.15, and 0.2, microwave powers were 150, 300 and 450 watt and extraction time for 180 minutes with 20 minutes interval. The result suggest that the Power Law and Hyperbolic model were slightly better at representing the experimental data of MHD.

1. Introduction

Citronella oil, derived from the leaves and stems Cymbopogon nardus and Cymbopogon winterianus, is a key essential oil with significant commercial value due to its applications in perfumery, pharmaceuticals, cosmetics, and food flavoring. Indonesia, as one of the major producers of citronella oil, has experienced consistent export growth, with citronella ranked as the third-largest essential oil export after patchouli and vetiver oils.1 However, conventional extraction methods such as hydro-distillation are increasingly considered inefficient due to long processing times, significant solvent consumption, and thermal degradation of thermolabile compounds.2 To address these limitations, the is exploring non-conventional extraction techniques that offer improved efficiency and sustainability.

Microwave-assisted extraction methods. including Microwave Hvdro-distillation (MHD) and has emerged as promising alternatives. This technique offers faster heating, higher yields, and better retention of bioactive compounds without extensive use of solvents.3, 4 Prior studies have demonstrated successful application of these methods in essential oil extraction. Furthermore, there remains a lack of comprehensive comparative analysis between kinetic modeling and statistical optimization under various process conditions.

This study aims to develop kinetic models and perform. The development lies in the simultaneous evaluation of kinetic models. The research scope includes parameter estimation

and model validation, contributing to both scientific understanding and industrial application.

2. Methods

2.1 Microwave hydro-distillation (MHD) of Citronella leaves (*Cymbopogon winterianus*)

This study employed a combination of kinetic modeling to evaluate the extraction of citronella oil from *Cymbopogon winterianus* using Microwave hydro-distillation (MHD) under atmospheric pressure (1 atm). The raw material was cut to a uniform size of 0.5 cm, and three feed-to-solvent (F/S) ratios were investigated: 0.1, 0.15, and 0.2. Distilled water (300 mL) was used as the solvent for MHD. Extraction was performed at varying microwave power levels of 150, 300, and 450 W for up to 180 minutes, and the essential oil was collected at fixed intervals

2.2 Kinetic modelling

Kinetic modeling was performed using five widely accepted mathematical models: First-order, Power Law, Hyperbolic, Weibull and Elovich. These models have been widely used in extraction processes involving essential oils and plant-based materials due to their ability to describe diffusion, adsorption, and phase equilibrium phenomena.

The first-order kinetic model, as introduced by Lagergren (1898) and refined by Ho (2004) and Reddad et al. (2002) can be written as:

$$\frac{dC_t}{dt} = k_1(C_s - C_t)$$
 Eq 1

Assumes the rate of extraction is proportional to the difference between the equilibrium concentration (C_0) and the concentration at time t (C_t),⁵ then equation 1 becomes:





$$C_t = C_0 (1 - e^{(-k_1 t)})$$
 Eq 2
To capture non-linear mass transfer, the Power

To capture non-linear mass transfer, the Power Law model as shown in equation 3 describes extraction via diffusion in non-swelling systems, with B representing the system constant and n the diffusion exponent. This model expresses the extraction mechanism by diffusive compounds through a non-swelling system.⁶

$$q = Bt^n$$
 Eq 3

The Hyperbolic model, adapted from Peleg, accounts for a fast initial extraction phase that decreases over time, transitioning from first- to zero-order kinetics. Parameters C₁ and C₂ represent initial rate and saturation effects, respectively.⁶

$$q = \frac{C_1 t}{(1 + C_2 t)}$$
 Eq 4

Weibull's exponential model incorporates scale (D) and shape (m) parameters to represent extraction as either exponential or sigmoidal curves.⁶

$$q = 1 - \exp\left(-\frac{t^m}{D}\right) \qquad \text{Eq 5}$$

Finally, Elovich's model is employed to describe extraction systems governed by desorption or surface reactions, where the rate decreases logarithmically over time. E₀ and E₁ are the parameters of the Elovich's equation.⁶

$$q = E_0 + E_1 \ln t \qquad \qquad \mathbf{Eq} \ \mathbf{6}$$

Table 1. Comparison of several kinetic models in the extraction process

Models	Equation	Constants
1st Order	$q = C_0(1 - e^{(-k_1 t)})$	k_1, C_0
Power Law	$q = Bt^n$	B, n
Hyperbolic	$q = \frac{C_1 t}{(1 + C_2 t)}$	C_1, C_2
Weibull	$q = 1 - \exp\left(-\frac{t^m}{D}\right)$	m, D
Elovich	$q = E_0 + E_1 \ln t$	E_0, E_1

Each model was fitted to the experimental yield data to evaluate its suitability in describing the extraction dynamics. These models offer distinct advantages depending on the mass transfer mechanism and the nature of the extracted compounds.⁶ Data fitting and parameter estimation were conducted using Microsoft Excel Solver. Root Mean Square Error (RMSE) and the coefficient of

determination (R^2) were used to assess the accuracy of model predictions as shown by the equation 1 and 2.7

$$RMSE = \sqrt{\frac{1}{n}\sum_{i=1}^{n}(q_{\exp i} - q_{\operatorname{calc} i})^{2}} \qquad \text{Eq 7}$$

$$R^{2} = 1 - \frac{\sum_{i=1}^{n} (q_{\exp i} - q_{\operatorname{calc} i})^{2}}{\sum_{i=1}^{n} (q_{\exp i} - \bar{q}_{\exp i})^{2}}$$
 Eq 8

Where $q_{\exp i}$ and $q_{\operatorname{calc} i}$ are calculated by experimental yields and models of oil extracted, $\bar{q}_{\exp i}$ is experimental data average. Then n is the number of experimental data.

3. Results & Discussion

The comprehensive modeling and optimization approach used in this study provides an understanding of the kinetics and process behavior of citronella oil extraction using microwave-based techniques. The data obtained from citronella extraction using MHD at three power levels (150, 300, and 450 W) and three feed-to-solvent (F/S) ratios (0.1, 0.15, and0.2) were used to evaluate model performance. Five kinetic models were applied to the experimental data. Figures 1 presents a graphical comparison of each kinetic model and experimental results for the MHD method at power 150 and three F/S which has determined. The experimental yield data were plotted against time and fitted to estimate model parameters. A comparison between the predicted and experimental data was conducted to evaluate the accuracy of each model.

The Power Law model consistently achieved the lowest RMSE (average 0.0334), indicating strong predictive accuracy, especially in early and mid-phase extraction periods. This model effectively described the diffusion-controlled behavior of the system.⁶ On the other hand, the Hyperbolic model exhibited the highest average R² value (0.9943), showing its robustness in capturing the transition from the rapid to equilibrium phase of extraction.⁸ The First-order model also demonstrated reasonable fit, with RMSE and R² values close to those of the top two models (RMSE = 0.0389, R² = 0.9940), supporting its applicability in single-phase mass transfer systems.⁶





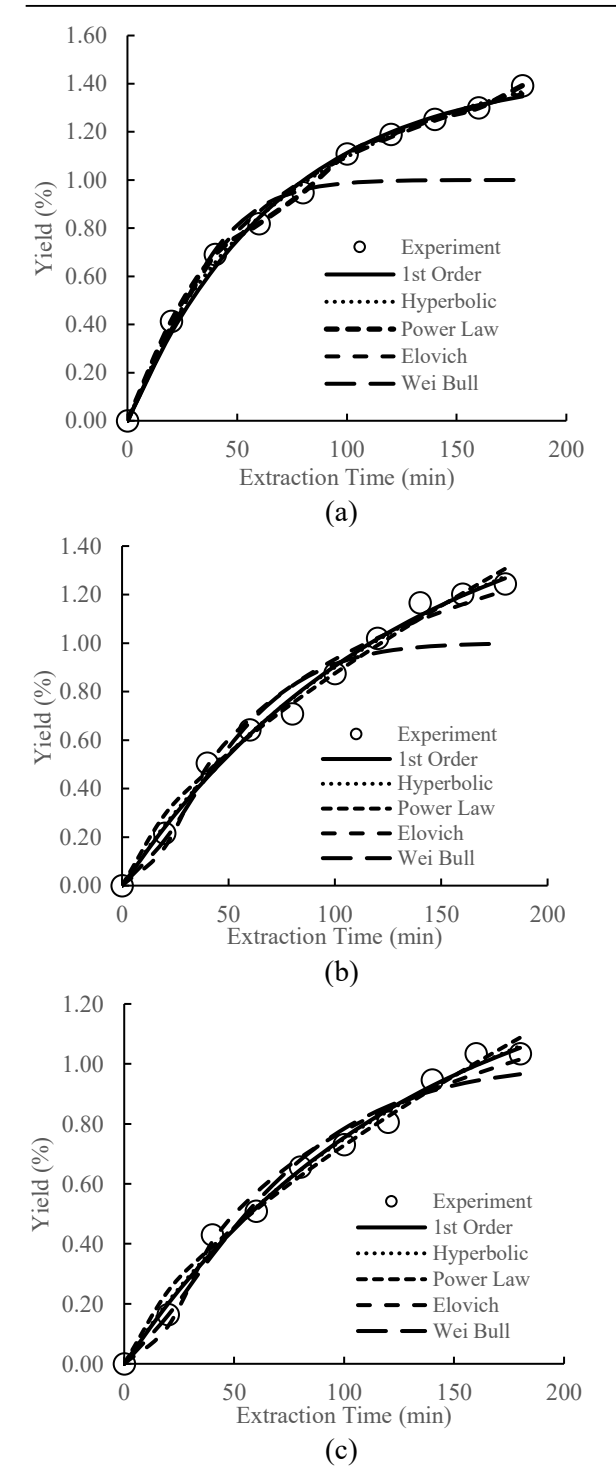


Figure 1. Comparison of kinetic models with experimental data for citronella extraction using the MHD method at 150 W and an F/S ratio of (a) 0.1, (b) 0.15, and (c) 0.2.

Conversely, the Weibull model presented the least accurate predictions, with an RMSE of 0.2877 and R^2 of 0.8160, suggesting its inadequacy in this particular system, possibly

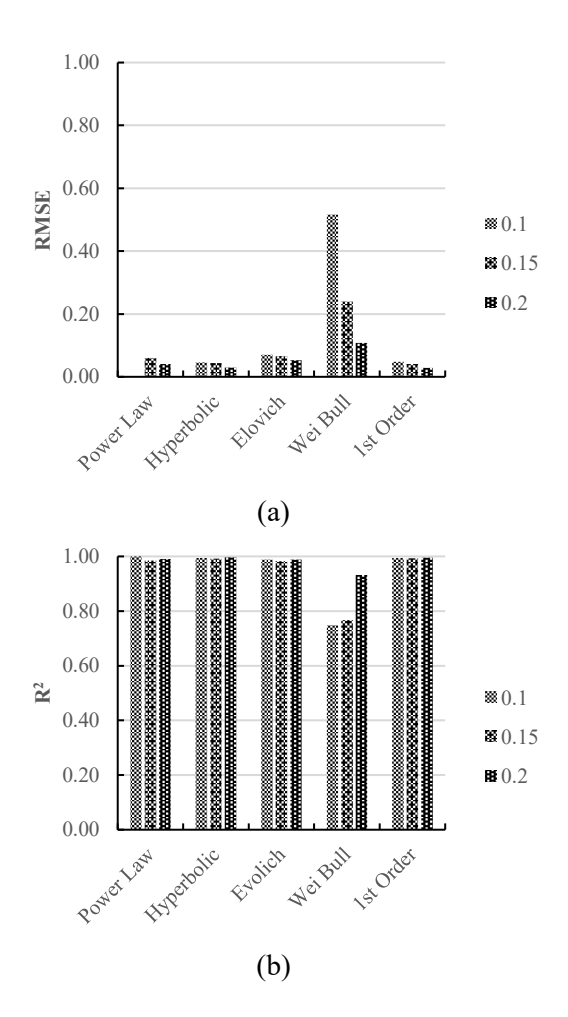
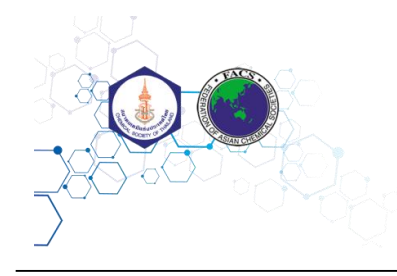


Figure 2. Results of (a) RMSE and (b) R² for each predictive calculation method.

due to its greater flexibility in handling sigmoid-type curves which were not characteristic of the citronella extraction profile.⁶ From these findings, it can be concluded that the Power Law and Hyperbolic models are most suitable for modeling citronella extraction kinetics under microwave-assisted conditions, while the Weibull and Elovich models were less representative of the observed phenomena.

4. Conclusions

This study demonstrated that Microwave Hydrodistillation (MHD) effectively extract citronella oil, with Power Law and Hyperbolic models providing the best kinetic fit. The research contributes to the growing body of knowledge on green extraction technologies and suggests further investigation into





compound-specific kinetics and compositional analysis for broader industrial applications.

Acknowledgements

This work supported by Department of Chemical Engineering, Laboratory of Chemical Reaction Process and Biomass Conversion, Institut Teknologi Sepuluh Nopember, Surabaya, Indonesia.

Research Ethics / Declarations

Authors declare no conflict of interest.

References

- 1. Sulaswatty, A.; Syahbana, M.; Haznan, R.; Tursiloadi, A. S. *Quo Vadis Minyak Serai Wangi Dan Turunannya*; LIPI Press: Jakarta, 2019.
- 2. Ferhat, M. A.; Meklati, B. Y.; Smadja, J.; Chemat, F. *J. Chromatogr. A* **2006**, *1112*, 121–126.
- 3. Lucchesi, M. E.; Chemat, F.; Smadja, J. *J. Chromatogr. A* **2004**, *1043*, 323–327.
- 4. Kusuma, H. S.; Mahfud, M. *Period. Polytech. Chem. Eng.* **2017**, *61*, 82–92.
- Kusuma, H. S.; Rohadi, T. I.; Daniswara,
 E. F.; Altway, A.; Mahfud, M. Korean
 Chem. Eng. Res. 2017, 55, 574–577.
- 6. Haqqyana, H.; Finish, V.; Tania, W.; Suyadi, A. M.; Septya Kusuma, H.; Altway, A.; Mahfud, M. *Mor. J. Chem.* **2020**, *8*, 64–71.
- 7. Mahfud, M.; Masum, Z.; Bhuana, D. S.; Altway, A.; Yuniati, Y. *J. Appl. Eng. Sci.* **2022**, *20*, 881–888.
- 8. Silou, T.; Bassiloua, J. B.; Kama Niamayoua, R. *Eur. J. Biol. Biotechnol.* **2021**, *2*, 105–110.





Catalytic ethanol dehydration to ethylene over zeolite A synthesized from sugarcane bagasse ash

<u>Darunee Sukchit</u>, ¹ Saisamorn Lumlong, ¹ Malee Prajuabsuk, ¹ Chan Inntam, ¹ Supakorn Boonyuen, ² Duangkamol Gleeson, ³ Auradee Punkvang, ⁴ Sasijuta Wattanarach, ⁵ Parjaree Thavorniti, ⁵ Bunjerd Jongsomjit, ^{6,7} Pornpan Pungpo^{1,*}

Department of Chemistry and Center of Excellence for Innovation in Chemistry, Faculty of Science,
Ubon Ratchathani University, Ubon Ratchathani, 34190, Thailand

²Department of Chemistry, Faculty of Science and Technology, Thammasat University, Pathum Thani 12120, Thailand

³Department of Chemistry & Applied Computational Chemistry Research Unit, School of Science, King Mongkut's Institute of Technology Ladkrabang, Bangkok 10520, Thailand

⁴Division of Chemistry, Faculty of Science, Nakhon Phanom University, Nakhon Phanom, 48000, Thailand ⁵National Metal and Materials Technology Center, National Science and Technology Development Agency (NSTDA), Pathum Thani 12120, Thailand

⁶Center of Excellence on Catalysis and Catalytic Reaction Engineering, Department of Chemical Engineering, Faculty of Engineering, Chulalongkorn University, Bangkok 10330, Thailand

⁷Bio-Circular-Green-Economy Technology & Engineering Center, BCGeTEC, Department of Chemical Engineering, Faculty of Engineering, Chulalongkorn University, Bangkok 10330, Thailand

*E-mail: pornpan.p@ubu.ac.th

Abstract:

The catalytic dehydration of ethanol to ethylene is a crucial process in the petrochemical industry, as ethylene serves as a key building block for various derivatives such as polyethylene, ethylene glycol, ethylbenzene, and styrene. In this study, sugarcane bagasse ash waste from the Mitr Phol Sugar Factory in Amnat Charoen Province, Thailand, was utilized as a feedstock to synthesize zeolite A via the hydrothermal method. The study aims to evaluate the catalytic performance of zeolite A derived from sugarcane bagasse ash as a heterogeneous catalyst for the dehydration of ethanol to ethylene. The catalysts were characterized using XRD analysis. For the catalytic test, zeolite A was used in gas-phase ethanol dehydration at temperatures ranging from 250 to 350 °C. The results revealed that ethylene conversion increased as the reaction temperature rose from 250 to 350 °C. Zeolite A from sugarcane bagasse ash exhibited high acidity, resulting in 51.0% conversion toward ethylene at 350 °C. The heterogeneous catalyst, zeolite A from sugarcane bagasse ash, demonstrates significant potential for the efficient dehydration of ethanol to ethylene.

1. Introduction

Green chemical production interdisciplinary field that integrates chemistry, chemical engineering, and ecology, with the primary goal of reducing the fossil carbon footprint. In recent years, platform chemicals derived from biomass have attracted significant attention. Among them, bioethanol produced through the fermentation of feedstocks such as sugarcane bagasse and maize starch has emerged as a promising alternative. The transformation of bioethanol has gained increasing interest due to its wide range of technological applications. It serves as a precursor for the synthesis of various chemical intermediates, including ethylene, diethyl ether, acetaldehyde, ethyl acetate, and acetic acid. these, ethylene is particularly Among important, acting as a key building block for numerous derivatives such as polyethylene, polyvinyl chloride, and styrene.

Ethylene is one of the most critical raw materials in the chemical industry, used extensively in the production of various polymeric products like polyethylene, polyvinyl chloride, and polystyrene. 1-3 Currently, ethylene is primarily produced through naphtha cracking, a highly energyintensive process. However, dwindling fossil feedstock reserves, coupled with the growing global demand for energy in both industrial and domestic sectors, are increasingly impacting ethylene production. Moreover, the naphtha cracking process contributes substantially to degradation, environmental particularly through greenhouse gas emissions and ecotoxicity. 4-6 Therefore, there is an urgent need to explore renewable and sustainable alternatives





to reduce reliance on finite fossil resources and to mitigate the environmental impact associated with ethylene production.

Zeolites are widely regarded as excellent catalysts for the dehydration of ethanol to ethylene. Their high surface area, superior cation-exchange efficiency, and low production costs make natural zeolites particularly effective as catalysts. Among the zeolite family, zeolite-A (Na₁₂[AlO₂SiO₂]₁₂·27H₂O) is one of the most important members.⁷⁻⁹ Zeolite A has a three-dimensional cubic structure with an equal silica-to-alumina ratio. The equivalent numbers of aluminum atoms and mobile cations (sodium) confer a high cation-exchange capacity, making it more effective than other types of zeolites. This characteristic establishes zeolite-A as a suitable support material for catalytic applications.

This study investigates the catalytic performance of zeolite A in the conversion of ethanol to ethylene. The zeolite A catalysts were synthesized via the hydrothermal method using sugarcane bagasse ash as the raw material. The synthesized zeolite A catalysts were thoroughly characterized using X-ray diffraction (XRD). Their catalytic activity was then evaluated in the ethanol dehydration process.

2. Methods

2.1 Materials

Analytical reagent grade chemicals were used in the current work: NaAlO₂ (anhydrous, Al (Al₂O₃): 50-56%, Na (as Na₂O): 37-45%, Sigma-Aldrich, USA), NaOH (Carlo Erba Reagents, France, \geq 97.0%), and CH₃OH (Merck, Germany, \geq 99.0%). Deionized water was prepared using the water deionizer (WaterPro PS, Labconco, USA).

2.2 Synthesis of zeolite A

10 g of fly ash and 12 g of NaOH were ground in a mortar for 10 minutes and then transferred into a vessel. The solid mixture was melted for 90 minutes at 550°C in a furnace, then allowed to cool. NaAlO₂ was added to the product after fusion to adjust the SiO₂/Al₂O₃ ratio to approximately 1. The mixture was then ground for an additional 5 minutes, transferred to a polypropylene reagent bottle, and deionized water (liquid-solid ratio of 4.5–5.5) was added for thorough stirring. The mixture was

subjected to a hydrothermal reaction and maintained at a constant temperature in an oven at 90°C for 16 hours. After cooling at the end of the reaction period, the product was washed until the pH reached about 7. The solid product, after filtration, was dried overnight at 90°C for 16 hours

2.3 Characterization of the catalyst2.3.1 X-ray diffraction analysis (XRD)

The phase and crystal structure of zeolite A were determined by X-ray diffraction (XRD) (X'Pert Pro, PANalytical, Netherlands) with Cu K α radiation ($\lambda = 1.5406$ Å) at 40 kV and 30 mA.

2.4 Reaction study

The catalytic dehydration reaction of ethanol was conducted in a fixed-bed continuous-flow glass tube microreactor. First, 0.1 g of the catalyst sample and 0.05 g of quartz wool were packed inside the central glass tube reactor, which was positioned within an electric furnace. A pretreatment step was performed at 200°C under nitrogen flow for 1 hour to remove moisture from the surface of the catalyst. Subsequently, the liquid ethanol was vaporized at 120°C with nitrogen gas flowing at 60 ml/min, using a controlled injection system with a single syringe pump to maintain a volumetric flow rate of 0.397 ml/h for ethanol feeding. The gas stream then entered the reactor with a weight hourly space velocity (WHSV) of 3.1 $g_{ethanol}/g_{cat}\cdot_h$. The operating temperature range was set between 250°C and 350°C under atmospheric pressure. The gaseous products were analyzed using a Shimadzu GC-14B gas chromatograph with a flame ionization detector (FID) and a capillary column (DB-5) at 150°C. During the reaction tests, results were recorded at least three times for each temperature.

3. Results & Discussion

3.1 Characterizations of catalysts

3.1.1 X-ray diffraction analysis (XRD)

The identification of the synthesized material as zeolite A was confirmed by X-ray diffraction (XRD) analysis. The diffraction peaks of the synthesized product correspond well to the characteristic reflections of zeolite A, matching previously published data on synthesized zeolite A from fly ash. These results indicate that the material synthesized from bagasse ash via the hydrothermal method is zeolite A.



3.2 Catalytic activity of ethanol dehydration3.2.1 Reaction study

Table 2 illustrates the effect of reaction temperature on ethanol conversion over the zeolite A catalyst, with ethylene (C₂H₄) identified as the principal product. The data clearly indicate that ethanol conversion increases with temperature, highlighting the significant role of thermal energy in promoting the dehydration reaction.

At 250 °C, ethanol conversion remained low (1.6%), implying that the thermal energy available at this temperature is inadequate to activate the catalyst surface or drive the endothermic dehydration process. A moderate increase to 11.3% conversion was observed at 300 °C, suggesting the onset of catalytic activity as active acid sites on the zeolite become more energetically accessible. This initiates the dehydration mechanism, wherein ethanol undergoes protonation followed by elimination of water to yield ethylene. A pronounced rise in conversion was observed at 350 °C, reaching 51.0%, which marks the optimal condition among those studied. This significant enhancement is attributed to improved molecular mobility, increased interaction between ethanol molecules and acidic sites.

Overall, increasing the reaction temperature effectively enhances the conversion of ethanol to ethylene, with 350 °C identified as the most favorable temperature under the examined conditions. The results confirm that zeolite A is a promising catalyst for ethanol dehydration to ethylene, particularly at elevated temperatures where both catalytic site activation and reaction kinetics are optimized.

Table 2. Ethanol conversion of zeolite A.

Catalyst	Temperature (°C)	Ethanol conversion (%)
Zeolite A from	250	1.6
sugarcane bagasse	300	11.3
ash	350	51.0

4. Conclusions

In this study, zeolite A synthesized from sugarcane bagasse ash waste from the Mitr Phol Sugar Factory was successfully employed as a heterogeneous catalyst for the gas-phase dehydration of ethanol to ethylene. The catalyst exhibited favorable physicochemical properties, including high acidity and welldefined porous structure, as confirmed by various characterization techniques. Catalytic performance tests showed that the ethanol conversion, and ethylene selectivity increased with reaction temperature, achieving 51.0% conversion at 350 °C. These findings indicate that zeolite A derived from sugarcane bagasse ash is a promising and sustainable catalyst for efficient ethylene production from renewable bioethanol.

Acknowledgements

The research on the "Catalytic ethanol dehydration to ethylene over zeolite A synthesized from sugarcane bagasse ash" by Ubon Ratchathani University, Department of Chemistry, has received funding support from the NSRF. The Thailand Graduate Institute of Science and Technology (SCA-CO-2565-17147-TH) is acknowledged for financial support to D. Sukchit. Additional support from Ubon Ratchathani University, National Metal and Materials Technology Center, and National Science and Technology Development Agency (NSTDA) are gratefully acknowledged for supporting this research. We would like to thank the Mitr Phol Sugar Factory in Amnat Charoen Province, Thailand, for kindly providing the ash used in this study.

Research Ethics / Declarations

The authors declare no competing financial interest.

References

- Janlamool, J.; Jongsomjit, B. J. Oleo Sci. 2017, 66, 1029–1039.
- 2. Kamsuwan, T.; Jongsomjit, B. *Eng. J.* **2016**, *20*, 63–75.
- 3. Krutpijit, C.; Jongsomjit, B. *J. Oleo Sci.* **2017**, *66*, 1355–1364.
- 4. Bokade, V. V.; Yadav, G. D. *Appl. Clay Sci.* **2011**, *53*, 263–271.





- 5. Chaichana, E.; Boonsinvarothai, N.; Juntadech, N.; Jongsomjit, B. *J. Porous Mater.* **2019**, *26*.
- Chen, Y.; Wu, Y.; Tao, L.; Dai, B.; Yang, M.; Chen, Z.; Zhu, X. J. Ind. Eng. Chem. 2010, 16, 717–722.
- 7. Hong, M.; Yu, L.; Wang, Y.; Zhang, J.; Chen, Z.; Dong, L.; Zan, Q.; Li, R. *Chem. Eng. J.* **2019**, *359*, 363–372.
- 8. Sathupunya, M.; Wongkasemjit, S. *J. Eur. Ceram. Soc.* **2003**, *34*, 1293–1303.
- 9. Sukchit, D.; Prajuabsuk, M.; Lumlong, S.; Inntam, C.; Punkvang, A.; Wattanarach, S.; Thavorniti, P.; Jongsomjit, B.; Wongyai, K.; Gleeson, D.; Shanmugam, P.; Boonyuen, S.; Pungpo, P. ACS Omega 2025, 10, 5981–5992.
- 10. Tohdee, K.; Semmad, S.; Nonthawong, J.; Praserthdam, P.; Pungpo, P.; Jongsomjit, B. S. Afr. J. Chem. Eng. **2024**, 49, 273–284.





Green synthesis of silver nanoparticles using crude extract from peels of Musa ABB cv. Kluai 'Namwa' for antibacterial activity

Khemmisara sawatdee,¹ Pritsana Srisaengmueang,¹ Darunee Sukchit,¹ Bongkochawan Pakamwong,¹ Thimpika Pornprom,¹ Kampanat Chayajarus,¹ Saisamorn Lumlong,¹ Prajakkit Rawee,¹ Jitlada Dechatiwong,¹ Jidapa sangswan,² Auradee Punkvang,³ Paptawan Thongdee,⁴ Khomson Suttisintong,⁴ Pornpan Pungpo¹,*

¹Department of Chemistry and Center of Excellence for Innovation in Chemistry, Faculty of Science, Ubon Ratchathani University, Ubon Ratchathani 34190, Thailand ²Department of Biological Science, Faculty of Science, Ubon Ratchathani University, Ubon Ratchathani 34190, Thailand

³Division of Chemistry, Faculty of Science, Nakhon Phanom University, Nakhon Phanom, 48000, Thailand
⁴National NanoTechnology Center, NSTDA, 111 Thailand Science Park, Klong Luang,
Pathum Thani 12120, Thailand

*E-mail: pornpan.p@ubu.ac.th

Abstract:

In this study, environmentally friendly silver nanoparticles (AgNPs) were synthesized using herbal extracts derived from peels of Musa~ABB~cv.~Kluai~'Namwa'. The synthesis process and important parameters, including silver nitrate (AgNO₃) concentration, temperature, and solution pH, were investigated. Optimal conditions for AgNPs synthesis were determined and the obtained results are 5 and 10 mM of AgNO₃ concentration at 80°C, with pH values of 10. The successful formation of AgNPs was confirmed by a color change from light yellow to dark brown and characterization using UV-visible spectrophotometry, shown as a maximum absorption peak at 412 to 442 nm. The antibacterial activity of the synthesized AgNPs against S.~aureus and E.~coli was evaluated using the agar disc diffusion method. The AgNPs synthesized under the 10 mM AgNO₃ and pH 10 condition exhibited the highest inhibition zones, measuring 8.00 ± 1.00 mm for E.~coli and 10.00 ± 0.00 mm for S.~aureus. These findings highlight the potential of agricultural waste, such as banana peels, for the green synthesis of AgNPs. Moreover, the synthesized AgNPs demonstrated promising antibacterial properties, supporting their application in sustainable antimicrobial development and value-added agricultural waste management.

1. Introduction

The increasing global concern environmental sustainability has prompted the development of eco-friendly approaches for the synthesis of nanomaterials. Among them, silver nanoparticles (AgNPs) have attracted considerable attention due to their unique physicochemical properties and spectrum antimicrobial activity. Conventional methods for AgNPs synthesis often involve toxic chemicals and high energy consumption, which pose risks to both human health and the environment. In response, green synthesis methods using biological resources have emerged as sustainable alternatives that align with the principles of green chemistry.¹

Plant-based extracts, particularly from agricultural waste, have shown promising potential as reducing and stabilizing agents in the synthesis of metal nanoparticles. These natural extracts contain a rich array of phytochemicals such as phenolics, flavonoids,

and alkaloids, which facilitate the reduction of metal ions into nanoparticles without the need for hazardous reagents.² Among various wastes, banana peels agricultural abundantly available, inexpensive, and rich in bioactive compounds, making them an ideal candidate for green nanotechnology applications.³ In this study, silver nanoparticles were synthesized using peel extracts of Musa ABB cv. Kluai 'Namwa', a widely cultivated banana variety in Thailand. The synthesis process was optimized by investigating the effects of silver nitrate concentration, temperature, and pH on nanoparticle formation. Furthermore, the antibacterial activity of the synthesized AgNPs was evaluated against Staphylococcus aureus and Escherichia coli, two common pathogenic bacteria. This research not only explores an environmentally benign method for AgNPs synthesis but also highlights the value-added utilization of agricultural waste





for sustainable antimicrobial material development.

2. Methods

2.1 Preparation of banana peel extract (BE)

Fresh peels of *Musa ABB cv. Kluai 'Namwa'* were washed thoroughly with tap water followed by distilled water to remove dirt and impurities. The cleaned peels were then cut into small pieces and sun-dried at 30-40°C for 48 hours. The dried peel was ground into powder using an electric blender. 1 g of the dried peel powder was boiled in 100 mL of deionized water at 70°C for 15 minutes. The mixture was allowed to cool to room temperature and filtered through Whatman No. 1 filter paper. The resulting filtrate was collected as the banana peel extract (BE) and stored at 4 °C for further use in nanoparticle synthesis.

2.2 Green synthesis of silver nanoparticles

The green synthesis of silver nanoparticles (AgNPs) was carried out using BE (Musa ABB cv. Kluai 'Namwa') as a natural reducing and stabilizing agent. A 0.5% (w/v) BE solution was prepared by diluting the extract with deionized water. To enhance the dispersion of the extract, 5% (v/v) ethanol was added, followed by the addition of silver nitrate and 10 mM). The total volume of the reaction mixture was maintained at 50 mL, and the incubated at mixtures were different temperatures (room temperature, 60°C, 70°C, and 80°C) for 30 minutes under constant stirring. To investigate the effect of pH on nanoparticle formation, the reaction mixtures were adjusted to different pH values: unadjusted pH (approximately 5.5), pH 7, and pH 10. The pH adjustments were carried out using a 1 M NaOH solution. Each condition was tested while keeping other parameters constant to evaluate the influence of pH on the efficiency of Ag+ ion reduction nanoparticle stability.

2.3 Characterization by UV-vis spectroscopy The formation and optical properties of the synthesized silver nanoparticles were characterized using UV-vis spectrophotometry. The absorption spectra of the reaction mixtures were recorded in the wavelength range of 200–800 nm using a UV-vis spectrophotometer.

2.4 Antibacterial activity

The antibacterial activity of the synthesized silver nanoparticles (AgNPs) was evaluated using the agar disc diffusion method against Staphylococcus aureus (Gram-positive) and Escherichia coli (Gram-negative). Bacterial suspensions were cultured in Luria Bertani (LB) broth and incubated at 37°C for 16-18 hours. A sterile cotton swab was used to evenly spread the bacterial suspension on LB agar plates. Sterile paper discs (6 mm in diameter) were placed on the inoculated agar plates, and 20 µL of each test solution was applied to the discs using a sterile micropipette. The plates were then incubated at $35 \pm 2^{\circ}$ C for 48 hours. After incubation, the antibacterial activity was assessed by measuring the diameter of the inhibition zones around each disc in millimeters (mm).

3. Results & Discussion

3.1 Color change of the silver nanoparticle solution

The banana peel extract was used to reduce Ag⁺ ions, causing the solution to change color from light yellow to dark brown after the addition of AgNO₃. This color change was observed after heating the reaction mixture at 80°C for 30 minutes. The synthesis was conducted using a 1:10 ratio of banana peel extract (25 mL) to silver nitrate (5 mM, 2.5 mL), with the solution showing a gradual increase in color intensity as the reaction proceeded. This indicates the successful reduction of Ag+ ions and the formation of silver nanoparticles (AgNPs). The color transition from yellow to brown is characteristic of the formation of AgNPs, as confirmed by the UV-vis spectrophotometric analysis showing an absorption peak at 412-442 nm.

3.2 Characterization by UV-vis spectroscopy

The formation and optical properties of the synthesized silver nanoparticles (AgNPs) were characterized using UV-vis spectrophotometry. The absorption spectra of the reaction mixtures were recorded in the wavelength range of 200–800 nm. A distinct surface plasmon resonance (SPR) band was observed within the range of 412–442 nm, confirming the formation of AgNPs. The variation in absorption peak positions and intensities corresponded to different synthesis conditions, such as AgNO₃ concentrations (Figure 1 a), temperature





(Figure 1 b, d), and pH values (Figure 1 c, e). These results indicate the successful reduction of Ag^+ ions to Ag^0 nanoparticles and the dependence of particle characteristics on the synthesis parameters.

3.3 Optimization parameters using UV-Vis spectroscopy for the synthesis of AgNPs

The green synthesis of silver nanoparticles (AgNPs) was optimized by evaluating the effects of AgNO₃ concentration, temperature, and pH using UV-vis spectrophotometry in the wavelength range of 200–800 nm. The characteristic surface plasmon resonance (SPR)

band of AgNPs was used as an indicator of successful nanoparticle formation. As shown in Figure 1a, various concentrations of AgNO₃ (1–10 mM) were investigated while keeping the extract concentration and temperature constant. The SPR peak appeared between 412–442 nm and increased in intensity with increasing AgNO₃ concentration, reaching a maximum at 5 and 10 mM. This suggests that higher precursor concentrations enhance the formation of AgNPs due to the increased availability of Ag⁺ ions.

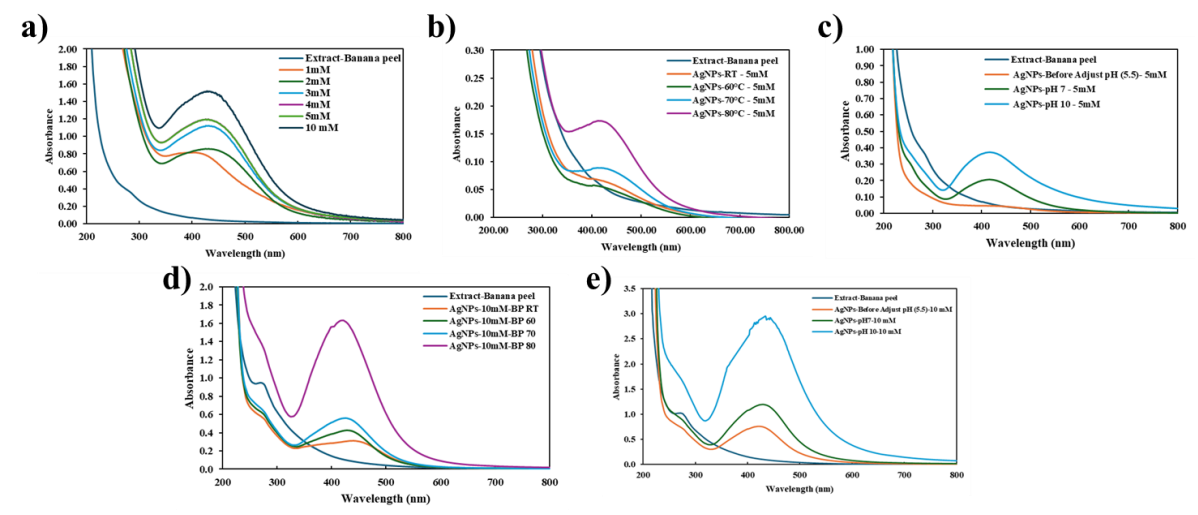


Figure 1. UV-vis absorption spectra of silver nanoparticles synthesized using banana peel extract under different reaction conditions: (a) effect of AgNO₃ concentration, (b) effect of temperature at 5 mM AgNO₃, (c) effect of pH at 5 mM AgNO₃ and 80 °C, d) effect of temperature at 10 mM AgNO₃, and e) effect of pH at 10 mM AgNO₃ and 80 °C

The effect of temperature was studied at room temperature, 60 °C, 70 °C, and 80 °C using 5 mM AgNO₃ (Figure 1b). The SPR peak became sharper and more intense at higher temperatures, particularly at 80 °C, indicating faster reduction of silver ions and more uniform formation nanoparticle under conditions. The influence of pH was examined at three levels: unadjusted (5.5), neutral (pH 7), and alkaline (pH 10) (Figure 1c). The results revealed that the intensity of the SPR peak increased significantly at pH 10, suggesting that alkaline conditions promote more efficient reduction and stabilization of nanoparticles. Overall, the optimal conditions for AgNP synthesis using banana peel extract were found to be 5-10 mM AgNO₃, a reaction temperature of 80 °C, and pH 10.

3.4 Antibacterial study of AgNPs

The antibacterial activity of silver nanoparticles synthesized using banana peel extract was evaluated against E. coli and S. aureus by the agar disc diffusion method. As shown in Figure 2 and Table 1, no inhibition zones were observed for DI water, BE, or silver nitrate (AgNO₃), indicating no intrinsic antibacterial activity from these components. In contrast, biosynthesized AgNPs demonstrated clear antibacterial effects. The AgNPs synthesized at pH 10 using 5 mM AgNO₃ showed inhibition zones of 7.67 ± 0.58 mm against E. coli and 8.00 ± 1.37 mm against S. aureus. Greater activity was observed with AgNPs synthesized at pH 10 using 10 mM AgNO₃, which produced inhibition zones of 8.00 ± 1.00 mm for E. coli and 10.00 ± 0.00 mm for S. aureus. These results suggest that the antibacterial activity of





AgNPs increases with higher silver nitrate concentration under alkaline conditions. Therefore, the synthesized AgNPs possess promising antibacterial potential, especially against *S. aureus*.

Table 1. Inhibition zone diameters (mm) of BE-synthesized silver nanoparticles (AgNPs) and control treatments against *E. coli* and *S. aureus* using the agar disc diffusion method.

Treatments	Inhibition Zones Diameter (mm)			
	E. coli	S. aureus		
DI water	6.00 ± 0.03	6.00 ± 0.12		
BP-Extract	6.00 ± 0.21	6.00 ± 0.86		
$AgNO_3$	6.00 ± 0.43	6.00 ± 0.32		
AgNPs-5mM-pH 10	7.67 ± 0.58	8.00 ± 1.37		
AgNPs-10mM- pH 10	8.00 ± 1.00	10.00 ± 0.15		

^{*}For the values of 6 mm we considered no antibacterial activity as 6 mm is the diameter of the test discs.

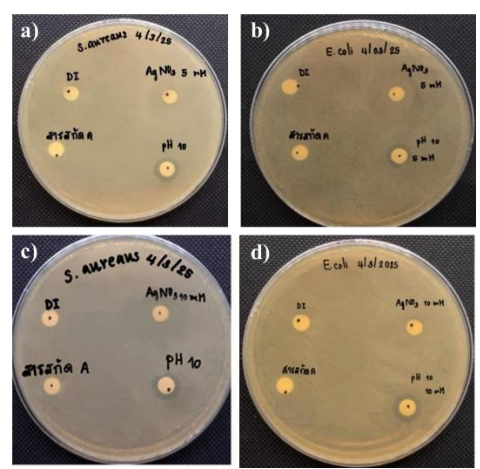


Figure 2. a) *S. aureus* (AgNPs-5mM-pH10), b) *E. coli* (AgNPs-5mM-pH 10), c) *S. aureus* (AgNPs-10mM-pH 10) and d) *E. coli* (AgNPs-10mM-pH 10)

4. Conclusions

This study demonstrated the successful green synthesis of silver nanoparticles (AgNPs) using banana peel extracts from *Musa ABB cv. Kluai 'Namwa'* as a sustainable and environmentally friendly reducing agent. The effects of synthesis parameters, including silver nitrate concentration, temperature, and pH, were systematically investigated. Optimal synthesis conditions were identified at 10 mM AgNO₃, 80°C, and pH 10, under which the formation of

AgNPs was confirmed by characteristic surface plasmon resonance peaks in the UV-vis range (412–442 nm). The biosynthesized AgNPs exhibited notable antibacterial activity, particularly against S. aureus and E. coli, with the highest inhibition zones observed under optimal conditions. These findings underscore the potential of utilizing agricultural waste in the eco-friendly synthesis of nanomaterials and support the development of value-added, sustainable antimicrobial agents.

Acknowledgements

This study was supported by Science, Research and Innovation Fund (NSRF), Center of Excellence for Innovation in Chemistry (PERCH-CIC) and Ubon Ratchathani University, Thailand. National Nanotechnology Center, Department of Biological Science, Faculty of Science, Ubon Ratchathani University, Ubon Ratchathani, Thailand, National Science and Technology Development Agency (NSTDA) Thailand are gratefully acknowledged for supporting this research.

Research Ethics / Declarations

The authors declare no competing financial interest.

References

- 1. Iravani, S.; Varma, R. S. *Environ Chem. Lett.* **2020**, *18*, 703–727.
- 2. Ameen, F.; Srinivasan, P.; Selvankumar, T.; Kamala-Kannan, S.; Al Nadhari, S.; Almansob, A.; Dawoud, T.; Govarthanan, M. *Bioorg. Chem.* **2019**, *88*, 102970.
- 3. Bag, S. S.; Bora, A.; Golder, A. K. *Curr. Nanomater.* **2020**, *5*, 47–65.





Magnetic CoFe₂O₄/MIL-53/carbon aerogel composite for efficient organic dye adsorption in wastewater treatment

Kamonphat Narkwan, Paramasivam Shanmugam, <u>Supakorn Boonyuen</u>*

Department of Chemistry, Faculty of Science and Technology, Thammasat University, Pathum Thani 12120,

Thailand

*E-mail: chemistrytu@gmail.com

Abstract:

Dye adsorption using nanocomposites has emerged as a highly effective and sustainable approach for the removal of organic dyes from wastewater, addressing the critical issue of water pollution and ensuring environmental safety through enhanced adsorption capacity, selectivity, and reusability. In this study, magnetic CoFe₂O₄ nanoparticles supported on biomass-derived carbon aerogels (CA) from chitosan and metal-organic framework (MIL-53)-based aerogels were synthesized using a simple hydrothermal process. The obtained CoFe₂O₄/MIL-53/CA composites are lightweight, low-density, cost-effective, eco-friendly, and easily collected after the adsorption process. The structural, morphological, and physicochemical properties of the synthesized CoFe₂O₄/MIL-53/CA composites were characterized using Fourier transform infrared (FTIR) spectroscopy, X-ray diffraction (XRD), scanning electron microscopy (SEM), nitrogen (N₂) adsorption-desorption analyses, and transmission electron microscopy (TEM). The adsorption performance of the CoFe₂O₄/MIL-53/CA composite was evaluated for both cationic and anionic dyes. The CoFe₂O₄/MIL-53/CA composite exhibited superior adsorption properties compared to pristine CoFe₂O₄, MIL-53, and CA materials. This study introduces a novel CoFe₂O₄/MIL-53/CA composite with enhanced adsorption efficiency, recyclability, and environmental sustainability. The synergistic combination of magnetic nanoparticles, MOF-based aerogels, and biomass-derived carbon aerogels results in a high-performance adsorbent, offering significant potential for practical wastewater treatment applications.

1. Introduction

Synthetic dyes are extensively utilized in a wide range of industries, including textiles, pharmaceuticals. cosmetics. processing. These dyes, due to their complex structures and resistance biodegradation, are frequently discharged into water bodies as persistent organic pollutants. Dye-contaminated effluents not only impair water quality by reducing dissolved oxygen levels and light penetration but also pose significant ecological and human health risks if left untreated. Various physical, chemical, and biological methods have been employed for the removal of dyes from wastewater, including ion exchange, membrane filtration, photocatalysis, and coagulation. Among these, adsorption has emerged as one of the most effective and widely adopted techniques, due to its simplicity, high removal efficiency, cost-effectiveness, and ease of operation.² The success of adsorption-based treatments largely depends physicochemical properties of the adsorbent, such as surface area, porosity, surface functionality, and regeneration potential. In carbon-based recent years, materials particularly carbon aerogels and metal organic

frameworks (MOFs) like MIL-53 have gained prominence as advanced adsorbents for dye removal. Carbon aerogels are characterized by their ultrahigh surface area, low density, and hierarchical porous structure, allowing for strong interactions with dye molecules through electrostatic attraction, hydrogen bonding, and π – π stacking.^{3, 4} MOFs such as MIL-53 offer highly tunable pore geometries, high chemical stability, and accessible functional groups that facilitate multiple adsorption mechanisms including coordination bonding and π - π interactions.^{5, 6} However, both carbon aerogels and MOFs suffer from a critical limitation: the lack of facile separation from aqueous media post-adsorption. This hampers their scalability and reuse in real-world applications.⁷ To this limitation, overcome magnetic nanoparticles, particularly cobalt ferrite (CoFe₂O₄), have been explored due to their excellent chemical stability superparamagnetic behavior, which allow for easy recovery of the adsorbent using an external magnetic field.8 While CoFe₂O₄ offers outstanding magnetic separability, its relatively low surface area limits its adsorption performance when used alone. To address these





individual limitations and harness their complementary strengths, composite adsorbents integrating CoFe₂O₄, MIL-53, and carbon aerogels have emerged as a promising solution. Such ternary hybrid systems offer synergistic properties, combining the high adsorption capacity of porous materials with the recoverability magnetic nanoparticles. 9-11 The integration enhances dye uptake while enabling rapid, separation and recyclability of the adsorbent, making them well-suited for practical and sustainable wastewater treatment. 12-14

In this study, we report the synthesis and evaluation of a novel CoFe₂O₄/MIL-53/chitosan-derived carbon aerogel composite as an efficient, magnetically recoverable adsorbent for the removal of organic dyes from aqueous solutions. The aim is to create a multifunctional composite that unifies high surface area, tailored porosity, active surface chemistry, and magnetic separability, thereby advancing the development of robust, reusable, and scalable materials for environmental remediation.

2. Methods

Materials

All reagents were of analytical grade and used without further purification. Chitosan, iron(III) chloride hexahydrate (FeCl₃·6H₂O), cobalt(II) chloride hexahydrate (CoCl₂·6H₂O), terephthalic acid, sodium hydroxide (NaOH), and N,N-dimethylformamide (DMF) were obtained from commercial suppliers. Distilled water was used throughout the experiments.

Synthesis Procedures

2.1 Synthesis of chitosan-derived carbon aerogel (CA)

Chitosan powder (1 g) was dispersed in 10 mL of distilled water and transferred into a stainless-steel autoclave. The sealed autoclave was heated at 180 °C for 5 hours. The hydrothermal product was collected via centrifugation at 3000 rpm for 5 min, washed thoroughly with distilled water and ethanol to remove residual impurities, and frozen at 2 °C for 48 hours. The frozen sample was subsequently lyophilized for 48 hours to obtain the carbon aerogel (CA).

2.2 Synthesis of MIL-53

MIL-53 was synthesized via a solvothermal method by dissolving FeCl₃·6H₂O (1 mmol)

and terephthalic acid (2.0 mmol) in 10 mL of DMF. The solution was transferred to a stainless-steel autoclave and heated at 180 °C for 5 hours. The product was collected by centrifugation, washed with hot ethanol, and dried in an oven to yield MIL-53 crystals.

2.3 Synthesis of Cobalt Ferrite (CoFe₂O₄)

CoFe₂O₄ nanoparticles were synthesized via a co-precipitation method. FeCl₃·6H₂O (2.0 mmol) and CoCl₂·6H₂O (1.0 mmol) were dissolved in 10 mL of distilled water. NaOH solution was added dropwise under stirring until the pH exceeded 10. The mixture was transferred into an autoclave and heated at 180 °C for 6 hr. The resulting solid was separated by centrifugation, washed with ethanol and water, and dried at 60 °C.

2.4 Fabrication of CoFe₂O₄/MIL-53/CA composite

Equal masses of CoFe₂O₄, MIL-53, and CA (1:1:1 ratio) were dispersed in 20 mL of ethanol and sonicated for 30 minutes to ensure homogeneous mixing. The suspension was then dried in an oven at 60 °C. The resulting hybrid material was designated as the CoFe₂O₄/MIL-53/CA composite.

2.5 Characterization techniques

2.5.1 Fourier transform infrared spectroscopy (FTIR)

FTIR analysis was performed to identify functional groups and confirm chemical interactions. Samples were ground and analyzed using ATR-FTIR in the 4000–400 cm⁻¹ range (insert instrument name, model, and manufacturer).

2.5.2 X-ray diffraction (XRD)

XRD patterns were recorded to examine phase composition and crystallinity. The samples were scanned and the diffraction peaks compared with standard JCPDS cards using X'Pert HighScore Plus software.

2.5.3 Transmission electron microscopy (TEM)

TEM analysis was conducted to investigate particle size and internal structure. Images were processed using ImageJ software to estimate average particle dimensions.

2.5.4 Adsorption experiments

Effect of Adsorbent Dosage and Contact Time Methylene blue (MB) and methyl orange (MO) solutions (10 ppm, 20 mL each) were treated with 15, 20, 25, and 30 mg of the CoFe₂O₄/MIL-53/CA composite. Adsorption





was monitored at 2-hr intervals using a UV–Vis spectrophotometer to evaluate dye removal efficiency. Effect of Initial Dye Concentration Dye solutions (10–80 ppm, 20 mL) were treated with 30 mg of each adsorbent (composite, CA, MIL-53, CoFe₂O₄). After 8 hr, residual dye concentrations were determined spectrophotometrically.

3. Results & Discussion

A comprehensive set of characterization techniques was employed to evaluate the structural, morphological, and physicochemical properties of the synthesized CoFe₂O₄/MIL-53/CA composite. The primary goal was to confirm the successful integration of cobalt ferrite nanoparticles, MIL-53 metal-organic framework, and chitosan-derived carbon aerogels into a unified hybrid material. The results presented below demonstrate the formation of a well-defined composite with preserved structural features from each component, suitable for dye adsorption applications. The analysis includes X-ray diffraction (XRD), Fourier-transform infrared spectroscopy (FTIR), scanning microscopy (SEM), transmission electron microscopy (TEM), and dye adsorption performance under various experimental conditions.

3.1 X-ray diffraction (XRD) analysis

Figure 1 presents the X-ray diffraction (XRD) patterns of the synthesized materials: carbon aerogel (CA), MIL-53, CoFe₂O₄, and the CoFe₂O₄/MIL-53/CA composite. The XRD profiles provide clear evidence of the successful formation of the composite and confirm the retention of the crystalline phases of its individual components. The diffraction pattern of MIL-53 shows distinct peaks at 2θ values of 17.34°, 24.20°, 27.90°, 33.12°, 35.60°, 39.85°, 40.88°, 49.42°, 54.00°, and 62.46°, which are consistent with its reported crystallographic planes, indicating the formation of a highly framework. 15 ordered metal-organic carbon aerogel (CA) exhibits broad peaks centered at approximately $2\theta = 10.34^{\circ}$ and 19.68°, typically associated with the (002) and (101) planes of disordered graphitic carbon, reflecting the partially amorphous nature of biomass-derived aerogels.16 For CoFe₂O₄, characteristic reflections were observed at 20 values of 18.20°, 26.22°, 30.16°, 35.48°,

43.13°, 53.64°, and 62.54°, corresponding to the (111), (220), (311), (400), (422), (511), and (440) crystal planes, respectively. These peaks match well with the standard JCPDS card No. 00-022-1086, confirming the formation of spinel-structured cobalt ferrite.¹⁷ composite CoFe₂O₄/MIL-53/CA, all major diffraction peaks from the three constituents are clearly visible, indicating that the crystal structures of MIL-53, CA, and CoFe₂O₄ remain intact during composite formation. Notably, prominent peaks at $2\theta = 35.5^{\circ}$ and 62.56° , attributed to the (311) and (440) planes of CoFe₂O₄, are well preserved in the composite spectrum. This confirms the successful integration of the magnetic nanoparticles within the hybrid framework without significant structural distortion.

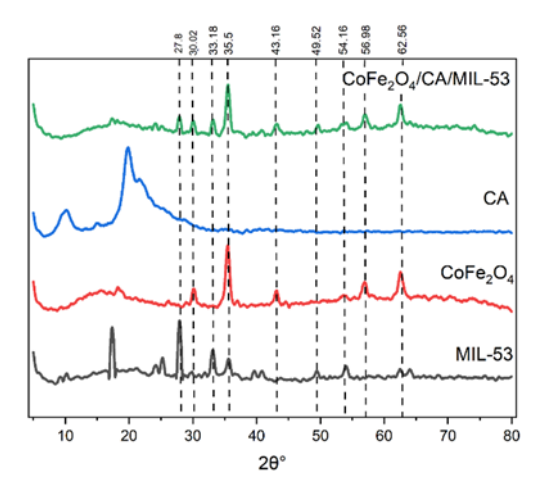


Figure 1. XRD pattern of CoFe₂O₄/MIL-53/CA composite, carbon aerogel (CA), CoFe₂O₄ and MIL-53.

3.2 Fourier transform infrared Spectroscopy (FTIR) analysis

FTIR spectroscopy was conducted in the range of 500–4000 cm⁻¹ to investigate the functional groups present in the individual components and the CoFe₂O₄/MIL-53/CA composite. The spectra of carbon aerogel (CA), MIL-53, CoFe₂O₄, and the composite are shown in Figure 2. In the carbon aerogel spectrum, broad absorption bands at 3362 and 2861 cm⁻¹ correspond to O–H and N–H stretching vibrations, respectively—characteristic of chitosan-derived carbon materials. These bands are also present in the composite, indicating the retention of hydroxyl and amino groups after hybridization. The MIL-53 spectrum exhibits a





strong band at 1681 cm⁻¹, attributed to the asymmetric stretching of carboxylate groups (C=O), along with a peak at 1400 cm⁻¹ corresponding to symmetric C-O stretching. features are indicative of terephthalate linkers in the MOF structure. A band at 1281 cm⁻¹, observed in both MIL-53 and the composite, is assigned to C-O stretching in aromatic esters. Importantly, a distinct absorption band near 534 cm⁻¹ characteristic of Fe-O stretching is evident in CoFe₂O₄, MIL-53, and the composite spectrum. This confirms the successful incorporation of CoFe₂O₄ nanoparticles into the hybrid matrix without significant disruption of the original chemical framework. Overall, the FTIR data validate the successful integration of all three components into a chemically stable and functionally active composite structure. 18

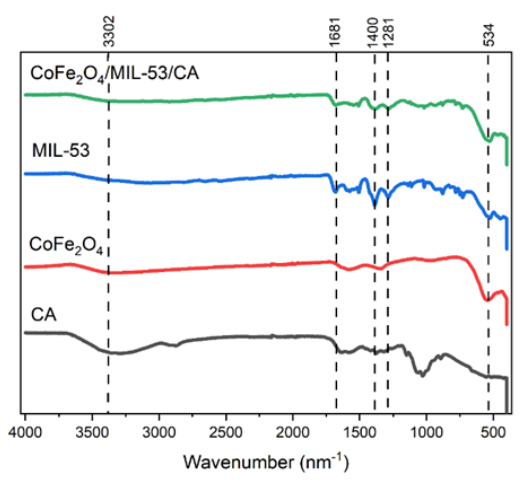


Figure 2. FTIR spectra of CoFe₂O₄/MIL-53/CA composite, carbon aerogel (CA), CoFe₂O₄ and MIL-53

3.3 Transmission electron microscopy (TEM) analysis. The morphology, particle size, and structural integration of the CoFe₂O₄/MIL-53/CA composite were investigated using high-resolution transmission electron microscopy (HRTEM), with representative micrographs shown in Figure 3a–b.

Figure 3a illustrates the general morphology of the composite, where irregularly shaped clusters are observed, exhibiting a particle size distribution ranging from 26 to 120 nm. This range is notably larger than the crystallite size of 15.67 nm calculated via the Scherrer equation, suggesting that the observed particles agglomerated or composed polycrystalline domains. Higher magnification in Figure 3b reveals faceted nanoparticles with well-defined boundaries, indicative of high crystallinity. The morphology of individual particles shows distinct faceted surfaces, further supporting the formation of well-ordered nanostructures. The high-resolution TEM image displays clear lattice fringes with an interplanar spacing of approximately 0.25 nm, consistent with the (311) planes of CoFe₂O₄. This confirms the retention of the crystalline structure of CoFe₂O₄ within the composite matrix. These combined observations validate the successful incorporation of CoFe₂O₄ nanoparticles within the MIL-53 and carbon aerogel framework, while maintaining their crystallinity and benefiting from the porous, high-surface-area support structure.

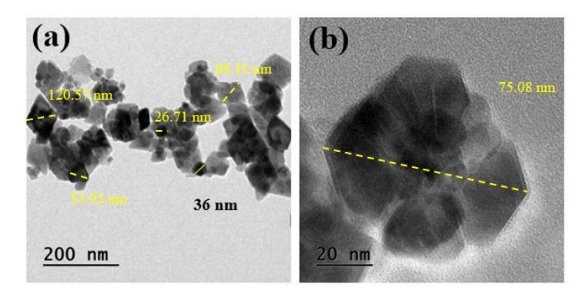


Figure 3. HRTEM images of CoFe₂O₄/MIL-53/CA composite at normal (a) and high (b) resolutions

3.4 Effect of adsorbent dosage

The influence of adsorbent dosage on dye removal efficiency was evaluated for both methylene blue (MB) and methyl orange (MO), and the results are illustrated in Figure 4.

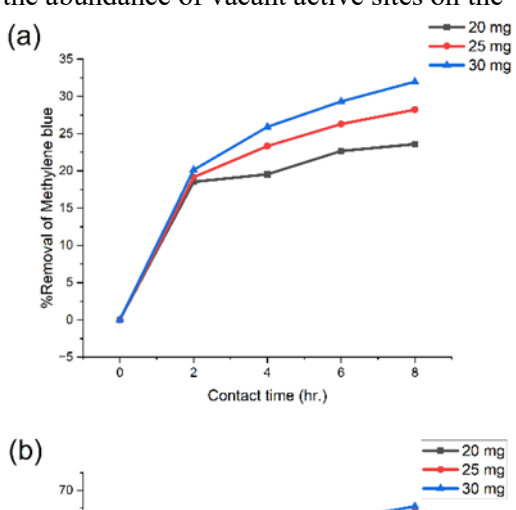
The data clearly demonstrate that increasing the adsorbent dosage significantly enhances dye removal performance. As the dosage increased from 20 mg to 30 mg, the removal efficiency for MB improved from 20.12% to 31.94%, while MO removal rose more markedly from 36.02% to 65.46%. This improvement can be attributed to the increase in available surface area and active adsorption sites, which provides more opportunities for dye molecules to bind. The higher dosage ensures more active surface coverage and reduces the mass transfer resistance between the dye molecules and



adsorbent surface, thereby facilitating a more effective adsorption process.

3.5 Effect of Contact Time and Initial Dye Concentration

The effect of contact time and initial dye concentration on the adsorption behavior of MB and MO is shown in Figure 4. The adsorption process exhibited a biphasic pattern: a rapid uptake phase during the initial 1–2 hours, followed by a plateau as equilibrium was approached. This trend was observed consistently across all initial concentrations tested. The initial rapid adsorption is attributed to the abundance of vacant active sites on the



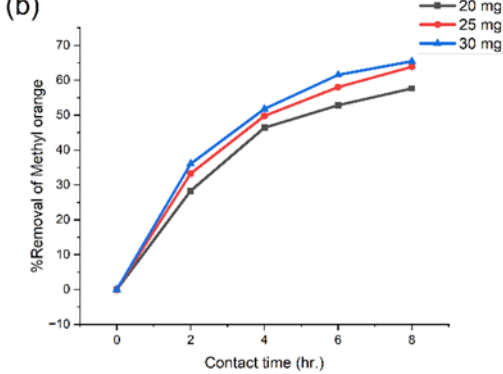


Figure 4. Effect of dosage and contact time (a) methylene blue (b) methyl orange

surface of the composite material. As the active sites become progressively occupied, the rate of adsorption slows due to reduced availability of binding sites and increasing resistance to intraparticle diffusion. This is particularly evident at higher dye concentrations, where competition among dye molecules for available sites becomes more significant. Interestingly, the overall adsorption profile remained similar across different dye concentrations, indicating a concentration-independent adsorption

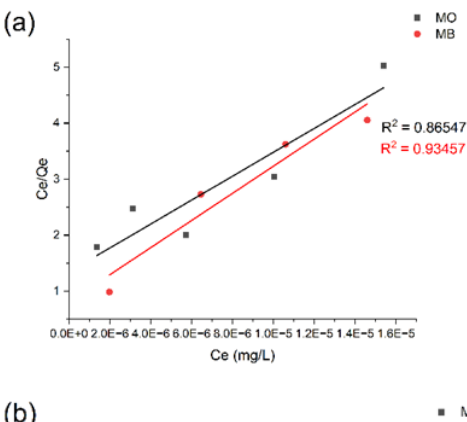
mechanism under the tested conditions. This suggests that the CoFe₂O₄/MIL-53/CA composite offers consistent adsorption performance and maintains structural integrity across a range of contaminant concentrations, making it a promising candidate for practical wastewater treatment applications.

3.6 Adsorption Isotherm Analysis

To elucidate the adsorption mechanism of MB and MO onto the CoFe₂O₄/MIL-53/CA composite, equilibrium adsorption data were analyzed using the linearized forms of both the Langmuir and Freundlich isotherm models.¹⁶ These models provide insight into the nature of the adsorbent-adsorbate interactions and surface characteristics. The Freundlich isotherm. an empirical model, describes adsorption on heterogeneous surfaces and assumes a multilayer adsorption process. Its logarithmic form relates the equilibrium adsorption capacity (Qe, mg/g) and the equilibrium concentration (Ce, mg/L) through the Freundlich constants Kf and n, which reflect adsorption capacity and intensity, respectively. As illustrated in Figure 5a, the plots of log O_e versus log Ce for both MO and MB exhibit reasonably linear relationships, with correlation coefficients (R²) of 0.8875 for MO and 0.8783 for MB. The slightly higher R² value for MO suggests a better fit to the Freundlich model, indicating that the adsorption of MO is more influenced by the heterogeneity of the composite. The presence of multiple types of binding sites with varying energy levels on the composite surface supports the applicability of the Freundlich model. In contrast, the Langmuir isotherm assumes monolayer adsorption on a homogeneous surface with a finite number of identical adsorption sites and no adsorbate-adsorbate interactions. The linearized Langmuir plots of C_e/Q_e versus C_e are shown in Figure 5b, with correlation coefficients of 0.9346 for MB and 0.8655 for MO. The higher R² value for MB indicates a better fit to the Langmuir model, suggesting that MB adsorption occurs predominantly via monolayer coverage on a uniform surface. Taken together, these results imply that the CoFe₂O₄/MIL-53/CA composite exhibits dual adsorption characteristics: MB primarily undergoes monolayer adsorption on relatively homogeneous regions, while MO adsorption is better explained by multilayer



coverage on heterogeneous surface sites. This highlights the versatility and multifunctionality of the composite for treating various dye pollutants in aqueous environments.



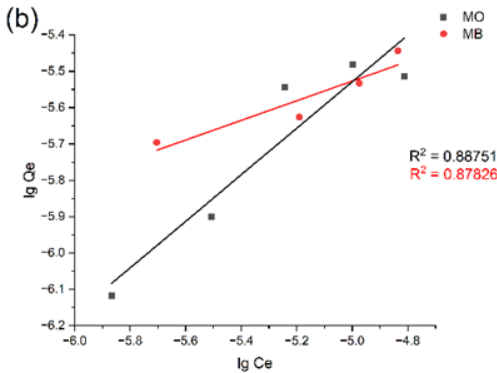


Figure 5. Isotherm model fits of adsorption (a) Langmuir isotherm (b) Freundlich isotherm

3.7 Adsorption Kinetics

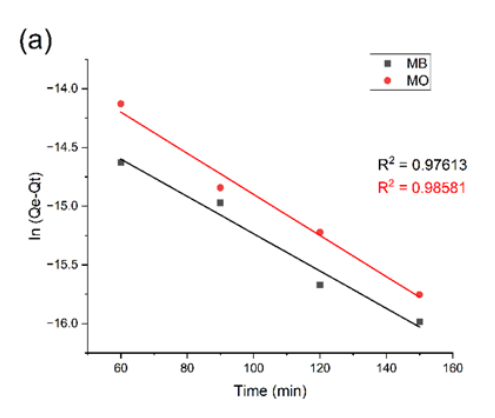
To elucidate the adsorption mechanism of methylene blue (MB) and methyl orange (MO) onto the CoFe₂O₄/MIL-53/CA composite, the experimental data were fitted to two widely used kinetic models: the pseudo-first-order and pseudo-second-order models. These models help describe the rate and possible mechanism of adsorption by evaluating how dye uptake varies with time. The pseudo-first-order kinetic model assumes that the rate of occupancy of adsorption sites is proportional to the number of unoccupied sites.

Its linearized form is expressed in Equation:

$$\log(q_e - q_t) = \log(q_e) - \frac{k_1}{2.303}t$$
 Eq 1

where Q_e and Q_t are the amounts of dye adsorbed at equilibrium and at time t, respectively, and k_1 is the rate constant. The linear plots of $\ln(Q_e - Q_t)$ versus time are shown in Figure 6a. The correlation coefficients (\mathbb{R}^2)

obtained were 0.9761 for MB and 0.9858 for MO, indicating an excellent fit to the pseudo-first-order model, particularly in the case of MO. These high R² values suggest that the rate-limiting step in the adsorption process is likely physisorption involving weak interactions between the dye molecules and the adsorbent surface.



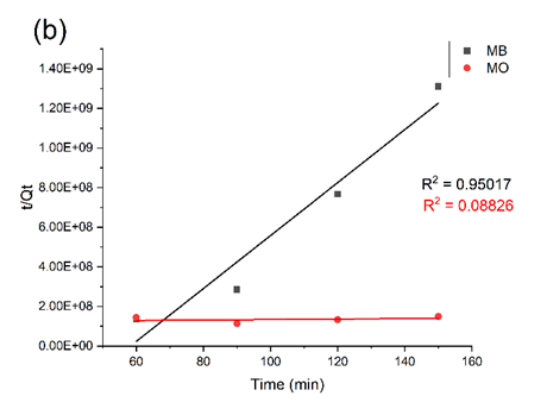


Figure 6. Pseudo-first order (a) and pseudo-second order kinetic fits (b) of adsorption of the dyes.

The pseudo-second-order kinetic model, which assumes that the adsorption rate is dependent on the square of the number of unoccupied sites (typically associated with chemisorption), was also evaluated. The linear plots of t/Q_t versus t are presented in Figure 6b. The correlation coefficient for MB was 0.9502, showing a reasonably good fit, while MO exhibited a much lower R^2 value of 0.0883, indicating that this model does not adequately describe the adsorption kinetics of MO under the current experimental conditions.

In summary, the adsorption kinetics of both MB and MO are better described by the pseudo-first-order model, suggesting a physisorption-





dominated process. Although MB exhibits reasonable agreement with both models, it slightly favors the pseudo-first-order mechanism. These findings further confirm the composite's capability for rapid dye uptake and its suitability for practical wastewater treatment applications.

4. Conclusions

In this study, a novel composite adsorbent composed of CoFe₂O₄, MIL-53, and chitosanderived carbon aerogel was successfully synthesized using hydrothermal, solvothermal, and freeze-drying techniques. The composite was thoroughly characterized using XRD, FTIR, SEM, and TEM analyses, which confirmed the effective integration of all components. XRD patterns revealed structural modifications and potential incorporation of MIL-53 into the composite framework, while FTIR spectra confirmed the presence of characteristic functional groups from each precursor. SEM and TEM imaging indicated that the composite possessed a nanostructured morphology with particle sizes ranging from 26 to 120 nm, and HRTEM analysis showed distinct lattice fringes, with SAED confirming its polycrystalline nature. The adsorption performance of the composite was evaluated using methylene blue (MB) and methyl orange (MO) as model pollutants. The adsorption process was found to be strongly influenced by adsorbent dosage and contact time. Kinetic modeling demonstrated that the adsorption of both dyes followed pseudo-first-order kinetics, indicating physisorption-dominated mechanism. Isotherm analysis revealed that MB adsorption fit the Langmuir model well, suggesting monolayer adsorption, whereas MO adsorption was better described by the Freundlich model, indicating multilayer adsorption on heterogeneous surfaces.

Overall, the CoFe₂O₄/MIL-53/CA composite exhibited promising adsorption efficiency, structural stability, and reusability, making it a strong candidate for practical application in dye-contaminated wastewater treatment. The study also highlights the critical role of nanostructuring and surface area in enhancing adsorption capacity, supporting the development of advanced multifunctional adsorbents for environmental remediation.

Acknowledgements

This study was also supported by the Thammasat University Research Fund, Contract No. TUFT 032/2568.

References

- Adeogun, A. I.; Osideko, O.; Idowu, M.; Balogun, A. O.; Areo, O. M.; Bello, O. S. SN Appl. Sci. 2020, 2, 795.
- Ahmad, R.; Kumar, R.; Haseeb, A. *Ecotoxicol. Environ. Saf.* **2021**, 220, 113160.
- 3. Farmahini, A. H.; Krishnamurthy, S.; Friedrich, D.; Brandani, S.; Sarkisov, L. *Carbon Capture Sci. Technol.* **2019**, *1*–2, 100006.
- Chen, Z.; Zheng, X.; Chen, Y.; Li, J.; Huang, Y.; Zhang, S.; Yang, W. ChemBioEng Rev. 2022, 9, 472–490.
- 5. Doydora, S. A.; Yotapukdee, N. *Water Sci. Technol.* **2022**, *86*, 2878–2889.
- Wattanachira, S.; Suksaroj, T. T.; Suksaroj, C. *IOP Conf. Ser. Earth Environ. Sci.* 2020, 514, 052001.
- Khan, M. A.; Ali, A.; Khan, N. A.; Shah,
 S. S.; Wang, J.; Wang, Y. Mater. Adv.
 2021, 2, 4825–4834.
- 8. Ali, I.; Asim, M.; Khan, T. A. *J. Environ. Manage.* **2012**, *113*, 170–183.
- 9. Crini, G. *Bioresour. Technol.* **2006**, *97*, 1061–1085.
- Ghosh, A.; Debnath, S.; Saha, B.; Chattopadhyay, K. K. Appl. Surf. Sci. 2022, 574, 151568.
- 11. Li, Y.; Liu, Y. *J. Environ. Eng. Sci.* **2013**, *12*, 231–240.
- 12. Paramasivam, S.; Wei, W.; Kun, Q.; Zhifeng, J.; Junwei, L.; Jimin, Xie. *Mater. Sci. Eng. B: Solid-State Mater.* **2019**, *248*, 114387.
- 13. Kant, R.; Awasthi, A.; Shrivastava, M.; Bajpai, P. K. *ACS Omega* **2021**, *6*, 31626–31638.
- 14. Srinivasan, R.; Muthusamy, S.; Sivasamy, A. *ACS Omega* **2021**, *6*, 15044–15056.
- 15. Pathania, D.; Katwal, R.; Kaur, H. *Int. J. Phytopharm.* **2016**, *5*, 70–78.
- Ali, I.; Gupta, V. K. Advances in Water Treatment by Adsorption Technology. In Industrial Applications of Nanomaterials; Jawaid, M.; Rahman, M. M.; Mishra, A. K., Eds.; Woodhead Publishing: Cambridge, 2017; pp 503–533.





- 17. Huang, Y.; Ma, Y.; Zhang, M.; Zhang, Y.; Tang, Z.; Liu, Y.; Li, C. *Carbon Res.* **2024**, *1*, 100012.
- 18. Crini, G.; Lichtfouse, E. *Environ. Chem. Lett.* **2014**, *17*, 145–155.
- 19. Banerjee, S.; Chattopadhyaya, M. C. *Arab. J. Chem.* **2017**, *10*, S1629–S1638.





Sustainable carbon aerogel/graphene oxide composite for efficient dye removal from wastewater

Nuntikan Kongkharat, Paramasivam Shanmugam, Supakorn Boonyuen*
Department of Chemistry, Faculty of Science and Technology, Thammasat University,
Pathum Thani 12120, Thailand
*E-mail: nuntikan.kon@gmail.com

Abstract:

Water pollution caused by organic dyes is a significant environmental concern due to their toxicity, persistence, and resistance to degradation. Developing efficient, sustainable, and cost-effective adsorbents for dye removal is crucial for wastewater treatment. In this study, a composite of dried Chinese jujube-derived carbon aerogel and graphene oxide (CA-GO) was synthesized using a hydrothermal method followed by freeze-drying. The resulting CA-GO composites are were characterized using XRD., FTIR, SEM/EDS, HRTEM and BET analysis. The adsorption efficiency of CA-GO and carbon aerogels was evaluated for both cationic and anionic dyes. The results indicated that CA-GO exhibited superior adsorption efficiency compared to carbon aerogel, primarily due to the enhanced surface properties imparted by graphene oxide. Additionally, the composite demonstrated a greater affinity for cationic dyes, such as Methylene Blue, compared to anionic dyes, such as Congo Red. This study highlights a sustainable and efficient approach to dye adsorption, with potential applications in wastewater treatment, energy storage, and biotechnology.

1. Introduction

Synthetic dyes are extensively used in industries such as textiles, printing, and food processing, leading to the discharge of highly colored and toxic wastewater. These dyes, particularly azo-based compounds, are resistant biodegradation and pose significant environmental and health hazards. Traditional dye removal methods physical (e.g., filtration, flotation), chemical (e.g., oxidation), and biological treatments often suffer from limitations such as high cost, secondary pollution, or low efficiency against complex dye molecules.¹⁻³ In contrast, adsorption has emerged as a superior alternative due to its cost-effectiveness, simplicity, and removal efficiency.4 Carbon aerogels. especially those derived from biomass such as dried Chinese jujube, offer a sustainable solution due to their high porosity, surface area, and tunable surface chemistry.⁵ Incorporating graphene oxide (GO) into carbon aerogels can enhance adsorption performance through increased functional group availability and improved structural integrity. This study aims to develop and characterize a carbon aerogel-graphene oxide (CA-GO) composite and evaluate its adsorption capacity for representative cationic (Methylene Blue) and anionic (Congo Red) dyes, providing insights into its potential application in wastewater treatment.6-8

The current research, Methylene Blue (MB) and Congo Red (CR) were selected as model dyes to represent typical cationic and anionic pollutants commonly found in industrial wastewater. Their distinct molecular structures and charge properties provide a robust framework for evaluating the adsorption behavior of the synthesized materials. The primary objectives of this study are to synthesize a carbon aerogel/graphene oxide (CA/GO) composite and to investigate its adsorption efficiency toward MB and CR.⁹ The study further aims to analyze the influence of key parameters such as contact time and dye concentration on adsorption performance. Adsorption isotherms and kinetics models are applied understand the mechanism involved.10 Additionally, comprehensive characterization of the CA/GO composite including functional groups, surface area, porosity, and morphology is conducted to elucidate the relationship between material structure and adsorption capacity. 12 The outcomes of this study are expected to demonstrate the potential of CA/GO as a sustainable and effective adsorbent for wastewater treatment applications.

2. Methods

2.1 Instrumentation and Equipment

The synthesis of carbon aerogels and CA/GO composites was conducted using a





hydrothermal reactor, ultrasonic bath, hot air oven (Memmert UN30), centrifuge, and freeze dryer (Labconco FreeZone). Dye adsorption studies were carried out using a UV-Vis spectrophotometer (Shimadzu UV1900) and a pH meter. Material characterization was performed using scanning electron microscopy (ThermoScientific Phenom), field emission scanning electron microscopy (FESEM, ZEISS), and transmission electron microscopy (JEOL TEM). Crystalline structure was determined by X-ray diffraction (Rigaku SmartLab), and chemical structures were analyzed using Fourier-transform infrared spectroscopy (FTIR, Thermo Scientific Nicolet iS50).

2.2 Materials

Dried Chinese jujube (Ziziphus jujuba) was purchased from a local market and used as the carbon source. Commercial graphene oxide (Nippon Shokubai), methylene blue (MB), Congo red (CR) dyes (QREC), hydrochloric acid (37% AR grade, ACL Labscan), sodium hydroxide (AR grade, QREC), and deionized water were used throughout the study without further purification.

2.3 Synthesis of carbon aerogel (CA)

Twenty-five grams of dried Chinese jujube were washed, chopped, and blended with 20 mL of deionized water to obtain a homogeneous mixture. The mixture was subjected to hydrothermal treatment at 180 °C for 12 hours. The resulting product was washed several times with distilled water, centrifuged at 3000 rpm for 5 minutes, and then frozen for 48 hours. The sample was subsequently freezedried at –51 °C for 48 hours to obtain the carbon aerogel (CA), which served as a scaffold for the CA/GO composite.

2.4 Synthesis of Carbon Aerogel/Graphene Oxide Composite (CA/GO)

To synthesize the CA/GO composite, 0.75 g of carbon aerogel and 0.25 g of graphene oxide were dispersed in 20 mL of purified water, followed by sonication for 30 minutes. The mixture was frozen for 48 hours and then freeze-dried at -51 °C for 36 hours to yield the final CA/GO composite.

2.5 Preparation of Dye Solutions

Stock solutions of MB and CR (100 ppm) were prepared by dissolving 0.0500 g of each dye in deionized water and adjusting the final volume to 500 mL in a volumetric flask.

2.6 Effect of contact time

Three milligrams of CA/GO were added to eight test tubes, each containing 5 mL of 2.5 ppm MB solution. The tubes were vortexed and left to stand at room temperature for different durations ranging from 10 to 80 minutes at 10-minute intervals. After adsorption, the supernatant was analyzed using UV-Vis spectroscopy (200–800 nm). The same procedure was repeated for CR.

2.7 Effect of adsorbent dosage

To study the influence of adsorbent dosage, 10 ppm solutions of MB and CR were prepared. Various amounts of CA/GO (5, 10, 15, 20, and 25 mg) were added to the dye solutions and allowed to interact for 150 minutes at room temperature. Post-adsorption dye concentrations were determined using UV-Vis spectrophotometry.

3. Results & Discussion

This section presents a comprehensive analysis of the synthesized adsorbents and their performance in dye removal. The results encompass material characterization and adsorption behavior of carbon aerogel (CA) and carbon aerogel/graphene oxide (CA/GO) composites. Key factors affecting adsorption efficiency—such as contact time, adsorbent dosage, initial dye concentration, and solution pH—were systematically investigated using Methylene Blue (MB) and Congo Red (CR) as model dyes. These dyes were selected to represent typical cationic and anionic contaminants in industrial effluents. In addition to adsorption performance, structural and morphological characterizations, including phase analysis, surface functionality, and porosity, were performed to elucidate the mechanisms involved. The findings are presented and discussed in the following sections.



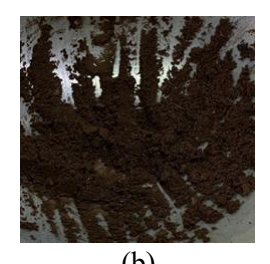


Figure 1. The physical appearance and color of the synthesized sample (a) CA (b) CA/GO





3.1 Characterization of Samples

X-ray diffraction analysis

The XRD pattern of the synthesized carbon aerogel (CA) exhibits a broad peak centered at $2\theta \approx 22.47^{\circ}$, which is characteristic of amorphous carbon and corresponds to the (002) plane. This broad diffraction feature confirms the predominantly disordered structure of the carbon framework, consistent with previous reports on biomass-derived carbon materials. ^{10,} 11, 19 In contrast, the XRD pattern of graphene oxide (GO) displays a sharper and more intense peak at $2\theta \approx 26.41^{\circ}$, along with a secondary broad peak around $2\theta \approx 43.71^{\circ}$, which may be attributed to the (100) plane, indicating partial in-plane ordering of sp²-hybridized carbon atoms. For the CA/GO composite, the diffraction profile shows a broad peak centered at $2\theta \approx 22.04^{\circ}$, similar to the CA sample, indicating that the amorphous carbon matrix remains dominant in the composite structure. Additionally, a smaller peak observed at $2\theta \approx$ 47.44° suggests the presence of residual crystalline domains or partial graphitization, possibly introduced through the incorporation of GO.¹³ This subtle structural ordering implies improved interfacial interaction between the carbon aerogel and graphene oxide within the composite framework.

Fourier transform infrared (FTIR) spectra

The FTIR spectra confirm the presence of key functional groups in CA, GO, and the CA/GO composite. For GO, peaks at 1734 cm⁻¹ and 1554 cm⁻¹ correspond to C=O stretching of carboxylic acids and C=C stretching of sp² carbon domains, respectively. The CA spectrum shows a broad O-H band at 3352 cm⁻¹, C-H stretching near 2932 cm⁻¹, a C=O band at 1699 cm⁻¹, and a C-O-C stretching band at 1024 cm⁻¹. The CA/GO composite exhibits combined features of both materials, with O–H stretching at 3387 cm⁻¹, C– H at 2924 cm⁻¹, C=O at 1701 cm⁻¹, and C-O bands at 1160 and 1025 cm⁻¹. These spectral shifts and intensified bands suggest successful integration of GO into the aerogel matrix. 14, 15 The abundance of oxygen-containing functional groups enhances adsorption potential by offering active sites for hydrogen bonding and electrostatic interactions with dye molecules.

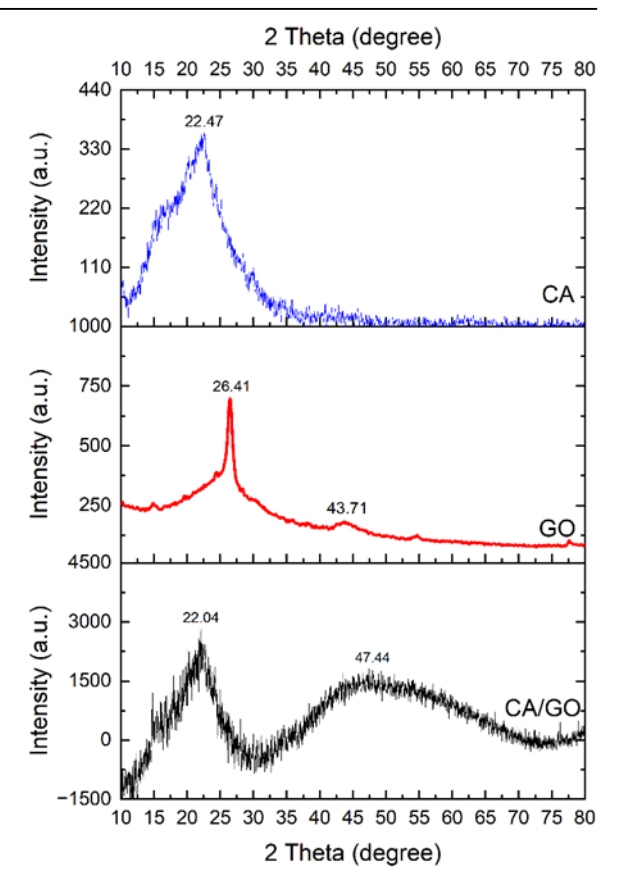


Figure 2. XRD pattern of Carbon aerogel (CA), Graphene oxide (GO) and Carbon aerogel/Graphene oxide composite (CA/GO).

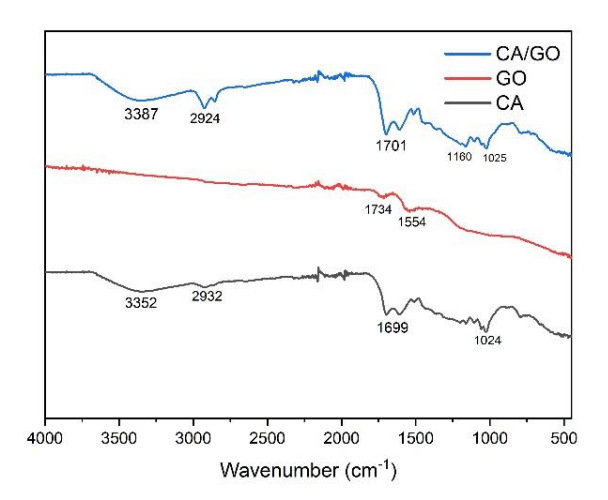
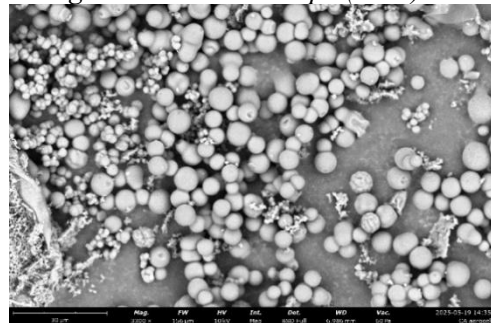


Figure 3. FTIR spectra of Carbon aerogel, Graphene oxide and Carbon aerogel/Graphene oxide composite (CA/GO).



Scanning Electron Microscope (SEM)



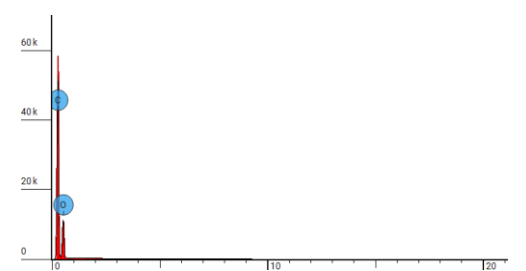


Figure 4. Scanning electron micrograph (top) and SEM-EDS (bottom) of carbon aerogel (CA)

SEM micrographs of the carbon aerogel (CA) reveal the presence of spherical particles, a morphology likely influenced by the celluloserich structure of the dried Chinese jujube precursor. This morphology is characteristic of biomass-derived carbon materials and suggests a porous framework conducive to adsorption. Elemental analysis via SEM-EDS confirmed that the CA primarily consists of carbon (C) and oxygen (O), as expected from cellulose-based carbon materials. FESEM analysis of the CA/GO composite shows a distinct layered, lamellar structure, indicative of successful incorporation of graphene oxide into the carbon aerogel matrix. This layered morphology increases surface area and enhances structural complexity, both of which are advantageous for dye adsorption.¹⁶ The observed features are consistent with the typical morphology of composites. graphene-based SEM-EDS analysis of the composite further confirmed the presence of carbon and oxygen as the major elements, supporting the composite's composition and structural integrity.

The TEM image of the CA/GO composite reveals a porous, interconnected network composed of thin, wrinkled graphene oxide sheets uniformly distributed within the carbon aerogel matrix. The sheet-like morphology and good dispersion of GO layers confirm its successful incorporation into the aerogel

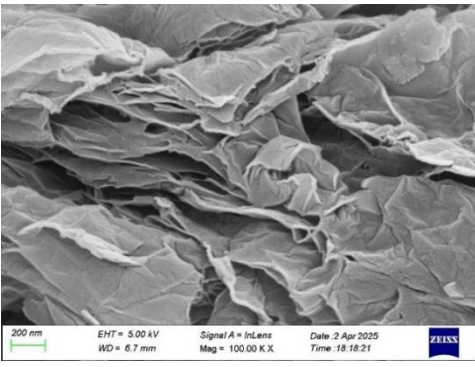


Figure 5. FESEM micrograph of carbon aerogel/graphene oxide composite (CA/GO).

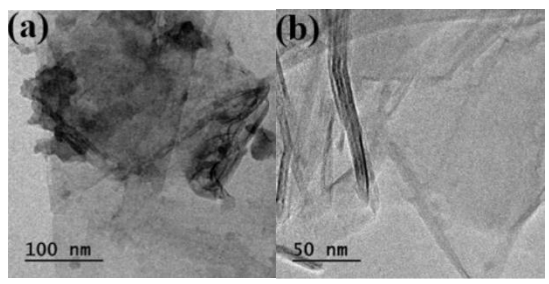


Figure 6. Transmission electron micrograph of Carbon aerogel/Graphene oxide composite (CA/GO).

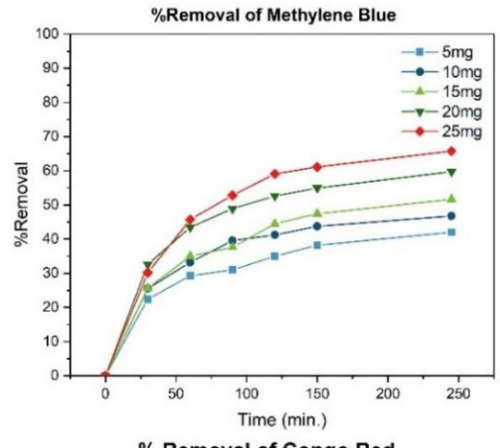
framework.¹⁷ Partial stacking of the graphene sheets is also observed, contributing to the enhanced surface area and structural stability of the composite.

Effect of adsorbent dosage

Figure 7 illustrates the influence of adsorbent dosage on the removal efficiency of Methylene Blue (MB) and Congo Red (CR), each at an initial concentration of 10 ppm in 20 mL solution. An increase in adsorbent dosage from 5 mg to 25 mg significantly enhances dye removal efficiency for both dyes. In the case of MB, removal occurs rapidly during the initial contact time and gradually plateaus as equilibrium is approached, indicating the saturation of available active sites. This behavior reflects the increased availability of adsorption sites with higher dosages, which facilitates more efficient dye uptake. Similarly, for CR, a consistent improvement in removal efficiency is observed with increasing adsorbent dosage. 18 The highest removal rate is achieved at 25 mg, suggesting that greater surface area and active site availability contribute positively to adsorption capacity.







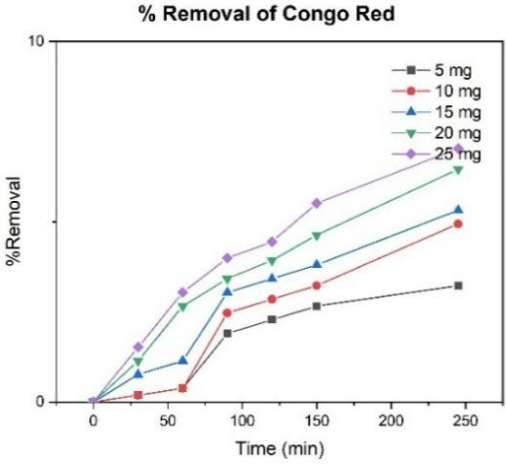


Figure 7. Effect of adsorbent dosage on removal efficiency of Methylene Blue and Congo Red.

However, the overall removal efficiency of MB is markedly higher than that of CR at equivalent dosages. This difference can be attributed to stronger electrostatic interactions between the cationic MB molecules and the negatively charged surface of the CA/GO composite, which are further enhanced by the incorporation of graphene oxide. The smaller molecular size of MB also facilitates easier diffusion into the porous network. In contrast, the anionic nature and larger molecular structure of CR likely result in weaker interactions and more restricted access to internal adsorption sites. These findings align with previous studies indicating that graphene oxide-containing composites exhibit higher affinity for cationic dyes such as MB similar to previous report. 19, 20

4. Conclusions

In this study, a carbon aerogel/graphene oxide (CA/GO) composite was successfully synthesized via a simple hydrothermal method

followed by freeze-drying. Characterization by XRD, SEM, FTIR, and TEM confirmed the formation of a porous, layered composite with an amorphous carbon structure and abundant surface functional groups, including hydroxyl, carbonyl, and carboxyl moieties. These groups contribute to the material's strong adsorption capability through hydrogen bonding and electrostatic interactions.

Adsorption experiments revealed that CA/GO exhibits significantly higher removal efficiency for the cationic dye Methylene Blue (MB) compared to the anionic dye Congo Red (CR). This enhanced performance is attributed to the strong electrostatic attraction between the positively charged MB and the negatively charged GO-containing surface, as well as the smaller molecular size of MB, which facilitates diffusion into the porous network.

The composite also demonstrated good reusability across multiple adsorption—desorption cycles, with only a slight decrease in efficiency, indicating its potential for practical wastewater treatment applications.

For future work, incorporating magnetic components into the composite is recommended to simplify adsorbent recovery. Additionally, investigating adsorption at higher dye concentrations and varying temperatures would allow for more comprehensive isotherm modeling and kinetic analysis. Further BET surface area measurements and complementary characterization techniques are also suggested to confirm the aerogel's structural classification and provide deeper insights into its adsorption behavior.

Acknowledgements

This study was also supported by the Thammasat University Research Fund, Contract No. TUFT 032/2568.

References

- Gusain, R.; Gupta, K.; Joshi, P.; Khatri, O. P. Adv. Colloid Interface Sci. 2019, 272, 102009.
- Maleki, H.; Durães, L.; García-González, C. A.; del Gaudio, P.; Portugal, A.; Mahmoudi, M. Adv. Colloid Interface Sci. 2016, 236, 1–27.
- 3. Karaaslan, M. A.; Kadla, J. F.; Ko, F. K. In *Lignin in Polymer Composites*; Faruk, O.,





- Sain, M., Eds.; William Andrew Publishing: Oxford, 2016; pp 67–93.
- 4. Kimura, R.; Ferré-Pujol, P.; Nishina, Y. *Carbon* **2025**, *238*, 120296.
- Nguyen, N. T.; Tran, M. Q.; Le, H. Q.; Bui, T. V.; Nguyen, K. D. *J. Environ. Manage*. 2021, 295, 113118.
- Le, H. V.; Dao, N. T.; Bui, H. T.; Le, P. T. K.; Le, K. A.; Tran, A. T. T.; Nguyen, K. D.; Ho, P. H. ACS Omega 2023, 8, 33412–33425.
- 7. Joshi, P.; Sharma, O. P.; Ganguly, S. K.; Srivastava, M.; Khatri, O. P. *J. Colloid Interface Sci.* **2021**, *608*, 2870–2883.
- 8. Azizian, S.; Eris, S. In *Interface Science* and *Technology*; Elsevier: Amsterdam, 2021; Vol. 33.
- 9. Oladoye, P. O.; Ajiboye, T. O.; Omotola, E. O.; Oyewola, O. J. *Results Eng.* **2022**, *16*, 100678.
- 10. Patil, A. V.; Sawant, S. A.; Sonkawade, R. G.; Vhatkar, R. S. *J. Energy Storage* **2023**, *72*, 108533.
- 11. Macias, C.; Rasines, G.; García, T. E.; Zafra, M. C.; Lavela, P.; Tirado, J. L.; Ania, C. O. *Gels* **2016**, *2*, 34–45.
- 12. Wang, M.; Shao, C.; Zhou, S.; Yang, J.; Xu, F. *RSC Adv.* **2017**, *7*, 38220–38228.
- 13. Xu, W.; Li, Y.; Wang, H.; Du, Q.; Li, M.; Sun, Y.; Cui, M.; Li, L. *ACS Omega* **2021**, *6*, 29243–29253.
- 14. Cai, K.; Zheng, M.; Xu, H.; Zhu, Y.; Zhang, L.; Zheng, B. *Carbohydr. Polym.* **2021**, *257*, 117624.
- 15. Zhang, M.; Xue, Y.; Zhou, H.; Xiang, A.; Deng, Y. *Int. J. Biol. Macromol.* **2025**, *308*, 142662.
- Shi, Y.; Song, G.; Li, A.; Wang, J.; Wang, H.; Sun, Y.; Ding, G. Colloids Surf., A 2022, 641, 128595.
- Wang, Z.; Song, L.; Wang, Y.; Zhang, X. F.; Yao, J. J. Phys. Chem. Solids 2021, 150, 109839.
- Tian, X.; Zhu, S.; Peng, J.; Zuo, Y.; Wang, G.; Guo, X.; Zhao, N.; Ma, Y.; Ma, L. Electrochim. Acta 2017, 241, 170–178.
- 19. Mohamed, E. N.; Abd-Elhamid, A. I.; El-Bardan, A. A.; et al. *Sci. Rep.* **2023**, *13*, 14265.
- Zaman, A.; Orasugh, J. T.; Banerjee, P.;
 Dutta, S.; Ali, M. S.; Das, D.;
 Bhattacharya, A.; Chattopadhyay, D.
 Carbohydr. Polym. 2020, 246, 116661.





Impact of electron beam irradiation on physicochemical properties of okara powder

Danita Sornkeawthanadet, <u>Thajanyawan Sahaspornchaikul</u>, Krittiya Khuenpet* Department of Food Science and Technology, Thammasat University, Thailand *E-mail: krittiya23@tu.ac.th

Abstract:

Okara, a nutrient-rich by-product, has limited use in food applications due to its undesirable physicochemical properties. This study investigated the impact of electron beam irradiation on okara powder to determine its potential for food use. The powder was irradiated at 0, 2.5, 5, and 7.5 kGy, and its chemical and physical properties were analyzed. Irradiation did not significantly affect moisture and protein content but resulted in a decrease ($p \le 0.05$) in fat, crude fiber, and lightness (L*), while increasing ΔE values, indicating noticeable color changes. Water holding capacity (WHC) decreased by 11.75%, whereas oil holding capacity (OHC) increased by 15.06%. The highest phenolic content (0.665 mg GAE/g) was observed at 5 kGy, though antioxidant activity declined. Scanning Electron Microscopy revealed increased porosity in irradiated samples. The observed changes suggest that electron beam irradiation modifies okara powder and may improve its functionality as a food ingredient.

1. Introduction

Okara is the insoluble by-product obtained after extracting soy milk from ground soybeans. During production, approximately 1.1 - 1.2 kg of wet okara are generated from every 1 kg of soybeans, depending on the water-to-soybean ratio and filtration efficiency. Although commonly treated as waste, okara contains a rich composition of dietary fiber, protein, fat, vitamins, minerals, and bioactive compounds such as isoflavones, saponins, and phytosterols. These attributes highlight okara's potential as a valuable raw material for functional food development.

However, its utilization remains limited due to unsuitable physicochemical properties, such as low solubility and poor dispersibility. Electron irradiation (EBI), a non-thermal processing technique, has been shown to induce molecular changes in food materials, including polysaccharide depolymerization and protein modification.² These changes may enhance hydration properties and functional characteristics. This study aimed to investigate the effects of EBI on the physicochemical properties of okara powder to improve its potential for future food applications.

2. Methods

2.1 Preparation of okara powder

Fresh okara was obtained from Green Spot Co., Ltd., Pathum Thani Province, Thailand. The sample was dried using a tray dryer (Model: CD-1, PML, Thailand) at 55°C for 8–10 hours. After drying, the okara was ground into a fine powder using a fine powder grinder and sieved

through an 80-mesh screen to obtain uniform particle size. The grinding process was carried out at the Institute of Food Research and Product Development, Kasetsart University. The powdered samples were then packed in sealed aluminum foil bags and stored at room temperature prior to electron beam irradiation.

2.2 Electron beam irradiation

Okara powder was subjected to electron beam irradiation at doses of 2.5, 5.0, and 7.5 kGy. The irradiation process was conducted at the Irradiation Center, Thailand Institute of Nuclear Technology (Public Organization).

- 2.3 Evaluation of the effects of irradiation on the physicochemical properties of okara powder
- **2.3.1 Moisture, protein, fat and crude fiber contents** were determined following AOAC methods.³
- **2.3.2 Color values (L*, a*, b*)** were measured using a colorimeter. The total color difference (ΔE) was calculated using the following equation:

$$\Delta E = [(\Delta L)^2 + (\Delta a)^2 + (\Delta b)^2]^{1/2}$$
 Eq 1

2.3.3 Water holding capacity (WHC) and oil holding capacity (OHC) were determined using the modified method of Bashir & Aggarwal.⁴

2.3.4 Total phenolic content (TPC) and antioxidant activity

TPC was determined using the Folin–Ciocalteu reagent method, and antioxidant activity (free radical scavenging activity) was evaluated using the DPPH assay, both according to the method described by Morodi et al.⁵



2.3.5 The microstructure was analyzed using scanning electron microscopy (SEM, Model: JSM-5410LV, JEOL, Japan).

2.3.6 Experimental design and statistical analysis

A Completely Randomized Design (CRD) with three replications (n = 3) was used. All results are presented as mean \pm SD. Differences among treatments were analyzed using one-way ANOVA, followed by Duncan's Multiple Range Test (DMRT) to determine significant differences at p < 0.05. Statistical analyses were performed using SPSS Statistics version 27.0.1 (IBM Corporation, Armonk, NY, USA).

3. Results & Discussion

3.1 Moisture, protein, fat and crude fiber contents

Table 1 indicates that moisture and protein contents of okara powder were not significantly different (p > 0.05) between irradiated and non-irradiated samples. The use of electron beam irradiation at doses up to 7.5 kGy involves low energy input and short exposure time, resulting in minimal thermal effects and limited molecular disruption. As a result, it has minimal impact on the properties and nutritional quality of food products.⁶ Similar observations were reported by Bashir and Aggarwal,⁴ who found that gamma irradiation did not significantly change the moisture or protein content of chickpea flour.

In contrast, a significant decrease in fat content was observed with increasing irradiation doses. This reduction can be attributed to the oxidative degradation of lipids induced by EBI, leading to the formation of free radicals that break down fat molecules. The interaction between ionizing radiation and lipids in food occurs randomly, and the presence of water activity further contributes to the oxidation process.⁷

Crude fiber content exhibited a gradual decline with increasing radiation doses. This is likely due to the high levels of dietary fiber present in okara, which primarily consists of complex, non-digestible polysaccharides commonly found in plant cell walls.^{1,8} Ionizing radiation has the ability to disrupt internal chemical bonds within these fiber structures. As the radiation dose increases, the energy exposed to the system also increases, resulting in more

extensive breakdown of the fiber matrix⁹ and a measurable reduction in crude fiber content.

3.2 Color

According to the results in Table 2, the lightness value (L*) of irradiated okara powder decreased compared to the non-irradiated sample. This reduction is likely attributed to the Maillard reaction induced by irradiation. The Maillard reaction is a non-enzymatic browning process that occurs between reducing sugars and amino acids.

Table 1. Effect of electron beam irradiation (EBI) on moisture, protein, fat and crude fiber contents of okara powder

Treatment	Moisture	Protein	Fat	Crude Fiber
	$content^{ns} \\$	$content^{ns}$	(g/100 g)	(g/100 g)
	(g/100 g)	(g/100 g)		
Control	$6.48 \pm$	$23.24 \pm$	$2.84^a \pm$	17.67a ±
	0.12	0.20	0.06	0.09
EBI 2.5	$6.46 \pm$	$23.12 \pm$	$2.69^{ab} \pm$	$17.38^{b} \pm$
	0.05	0.18	0.06	0.05
EBI 5.0	$6.45 \pm$	$23.24 \pm$	$2.60^{b} \pm$	$17.20^{c} \pm$
	0.06	0.06	0.06	0.02
EBI 7.5	$6.31 \pm$	$23.13 \pm$	$2.39^c \pm$	$17.08^{c} \pm$
	0.14	0.21	0.10	0.05

Note: EBI 2.5, EBI 5.0, and EBI 7.5 represent samples treated with electron beam irradiation at doses of 2.5, 5.0, and 7.5 kGy

As the irradiation dose increased, the L* value declined from 79.32 ± 0.08 in the control to 77.51 ± 0.07 at 7.5 kGy. These results are consistent with the findings of Bashir & Aggarwal,⁴ who reported that the L* value of chickpea flour decreased with increasing gamma irradiation dose due to enhanced Maillard reaction.

In addition, the redness (a*) and yellowness (b*) values of electron beam-irradiated okara were higher than those of the non-irradiated samples. The total color difference (ΔE) tended to increase with increasing irradiation dose, indicating that the Maillard reaction occurred more intensively, leading to greater color differences between the irradiated and non-irradiated samples. However, these color changes in irradiated okara were not visually perceptible to the naked eye, as illustrated in the images presented in Figure 1.

 $^{^{}a,b,c}$ Values with different superscript letters within the same column are significantly different (p \leq 0.05).

ns indicates no significant difference (p > 0.05).





Table 2. Effect of electron beam irradiation (EBI) on color values (L*, a*, b*, \triangle E), water and oil holding capacity (WHC, OHC), total phenolic content and, DPPH radical scavenging capacity of okara powder

powder								
Treatment	L*	a*	b*	ΔΕ	WHC (g/g)	OHC (g/g)	Total Phenolic (mg GAE/g)	DPPH radical scavenging capacity (mg GAE/g)
Control	$79.32^a\pm$	1.84° ±	17.18° ±	-	5.53a ±	$1.66^{c} \pm$	$0.528^c \pm$	$0.125^a\pm$
	0.08	0.03	0.17		0.18	0.03	0.077	0.006
EBI 2.5	$78.47^{b} \pm$	$2.03^{b} \pm$	$18.09^{b} \pm$	$1.28^{b} \pm$	$5.28^{b} \pm$	$1.75^{b} \pm$	$0.616^{ab} \pm$	$0.120^{b} \pm$
	0.08	0.04	0.27	0.09	0.07	0.02	0.017	0.004
EBI 5.0	$77.37^c \pm$	$2.27^a \pm$	$18.56^a \pm$	$2.32^a \pm$	$5.05^{c} \pm$	$1.86^a \pm$	$0.665^a\pm$	0.121^{ab} \pm
	0.22	0.12	0.09	0.48	0.25	0.03	0.040	0.007
EBI 7.5	77.51° ±	$1.97^{b} \pm$	$18.47^a \pm$	$2.23^a \pm$	$4.88^{d}\pm$	$1.91^{a} \pm$	$0.600^{b} \pm$	$0.119^{b} \pm$
	0.07	0.05	0.35	0.25	0.15	0.09	0.071	0.004

Note: EBI 2.5, EBI 5.0, and EBI 7.5 represent samples treated with electron beam irradiation at doses of 2.5, 5.0, and 7.5 kGy $^{a, b, c, d}$ Values with different superscript letters within the same column are significantly different (p \leq 0.05).



Figure 1. Images of okara powder irradiated with electron beam (EB)

3.3 Water holding capacity (WHC) and oil holding capacity (OHC)

The water holding capacity (WHC) of okara powder decreased with increasing doses of electron beam irradiation, as shown in Table 2. The control sample exhibited the highest WHC $(5.53 \pm 0.18 \text{ g/g})$, while the lowest value was observed at 7.5 kGy $(4.88 \pm 0.15 \text{ g/g})$.

These results associate with previous work by Zhang et al.,11 who reported that the WHC of okara ranged between 3.5-6.5 g/ml. A significant decrease in WHC ($p \le 0.05$) was observed with increasing doses of electron beam irradiation, demonstrating a reduction in the water retention capacity of the samples. Okara is primarily composed of insoluble dietary fiber, including cellulose hemicellulose.1 Irradiation damages the fiber structure, reducing the number of sites available for water molecule retention, thus lowering the WHC.9 These observations are reliable with previous reports showing that irradiation induces molecular degradation, which can change certain properties such as solubility.² In addition, irradiation has been shown to modify polysaccharide structures through mechanisms such as cross linking, grafting, and chain

scission.¹² Moreover, irradiation disrupts the molecular structure of lignocellulose, a major component of insoluble dietary fiber, which leads to a decrease in its water retention capacity.⁹ It also causes protein denaturation by breaking hydrogen bonds and exposing hydrophobic regions, resulting in reduced water-binding ability of the proteins.²

Regarding oil holding capacity (OHC), which is a functional property important for flavor retention and shelf-life improvement in food products, the results revealed that non-irradiated okara had significantly lower OHC than irradiated samples ($p \le 0.05$). A significant increase in OHC ($p \le 0.05$) was observed with increasing electron beam doses, indicating an enhanced oil retention capacity. As shown in Table 1, the protein content of okara ranged from 23.12-23.24 g/100 g (dry basis). Irradiation causes protein denaturation and exposes hydrophobic regions by disrupting hydrogen bonds, enabling proteins to bind more effectively with oil.²

3.4 Total phenolic content (TPC)

According to Table 2, the total phenolic content (TPC) of irradiated okara powder was higher than that of the non-irradiated sample. This increase may be attributed to the release of phenolic compounds from glycosidic linkages or the degradation of high molecular weight phenolics into smaller, more extractable forms. Radiation can cleave the chemical bonds of polyphenols, resulting in the release of watersoluble low-molecular-weight phenolics.¹³ These findings are consistent with those of Variyar et al.,¹⁴ who reported an increase in free





phenolic compounds (aglycones) in soybeans irradiated with gamma rays at doses ranging from 0.5 to 5 kGy. Electron beam irradiation at 5 kGy resulted in the highest TPC in okara flour, followed by a decline as the radiation dose increased. The observed decrease in antioxidant activity may be due to free radical formation during irradiation, 15 which may react with antioxidants through radical-mediated reactions, leading to their degradation. 16

3.5 Antioxidant activity (DPPH assay)

DPPH assay results in Table 2 show that nonirradiated okara had the highest antioxidant activity (0.125 \pm 0.006 mg GAE/g), which significantly decreased after irradiation. The lowest value was observed at 7.5 kGy (0.119 \pm 0.004 mg GAE/g) (p ≤ 0.05). This reduction may be attributed to the degradation of lipidsoluble antioxidants caused by irradiationinduced lipid oxidation.¹⁰ Vital et al.¹⁷ also reported higher antioxidant capacity in nonirradiated okara compared to irradiated samples. At higher doses, such as 5.0 kGy, a slight increase in antioxidant activity was observed (0.121 \pm 0.007 mg GAE/g), although the difference was not statistically significant. This response may be linked to partial breakdown of polysaccharide chains, which can generate smaller fragments with more exposed hydroxyl groups. These structural changes reduce hydrogen bonding within the polymer network and may enhance radical scavenging ability, as previously suggested by Mukhtar et al.18

3.6 Microstructure analysis

Electron beam treatment caused visible changes in the surface morphology of okara powder, as shown in Figure 2. While the control sample appeared compact and smooth, the irradiated sample showed a more porous and disrupted matrix. These changes likely resulted from the breakdown of chemical bonds in fiber and protein structures during irradiation. Although increased porosity was observed, the damage to the fiber network may have led to the loss of key water-binding sites, which corresponds with the reduced water holding capacity observed in treated samples.

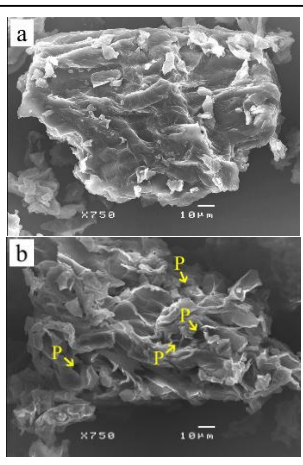


Figure 2. Scanning electron microscope (× 750) of okara powder: (a) Control, (b) Electron beam 5.0 kGy. P indicates pores formed on the surface after irradiation.

4. Conclusions

This study showed that electron beam irradiation affected both structural and functional properties of okara powder. Moisture and protein contents remained stable, while fat and crude fiber decreased as radiation dose increased. The changes in color values, with decreased L* and increased a* and b*, suggest browning reactions may have occurred. WHC and antioxidant activity were reduced in irradiated samples, likely due to disruption of fiber networks and the loss of antioxidant compounds. In contrast, OHC and TPC content increased, potentially because of molecular breakdown and better extractability of bioactive components. Structural observations under SEM revealed a more porous and fragmented surface in irradiated samples. Electron beam treatment, particularly at moderate doses, could be used to improve the value and functionality of okara in food applications.

Acknowledgements

The authors gratefully acknowledge the Research Fund, Faculty of Science and Technology, Thammasat University, for financial support. Sincere thanks are also extended to Green Spot Co., Ltd. for their kind provision of okara used in this study.





References

- 1. Unsanusuwanakul, A.; Thongkrajang, K. *Araharn* **2022**, *52*, 24–36.
- Gupta, A. D.; Singh, R.; Jaiswal, V.; Rawat, K. P.; Singh, H.; Bhadauria, V.; Punia, R. *Food Technol.* 2020, 44, 212–229.
- 3. AOAC. *Official Methods of Analysis*, 17th ed.; Association of Official Analytical Chemists: Washington, DC, USA, 2000.
- 4. Bashir, K.; Aggarwal, M. *LWT Food Sci. Technol.* **2016**, *69*, 614–622.
- Morodi, V.; Kaseke, T.; Fawole, O. A. *Processes* 2022, 10, 1629.
- 6. Arapcheska, M.; Spasevska, H.; Ginovska, M. Curr. Trends Nat. Sci. 2020, 9, 100–106.
- 7. Sinanoglou, V.; Strati, I.; Kokkotou, K.; Lantzouraki, D.; Makris, C.; Zoumpoulakis, P. *J. Spectrosc.* **2015**, *2015*, 1–10.
- 8. Li, B.; Qiao, M.; Lu, F. Food Rev. Int. **2012**, 28, 231–252.
- Li, X.; Wang, B.; Hu, W.; Chen, H.; Sheng,
 Z.; Yang, B.; Yu, L. Food Chem. X 2022, 14,
 100274.
- Hamza, H.; Jimenez-Araujo, A.; Ben Miloud, N.; Guillen-Bejarano, R.; Ghorbal, A.; Rodríguez-Arcos, R.; Benabderrahim, M. A.; Elfalleh, W. Food Biosci. 2023, 56, 103288.
- 11. Zhang, M.; Feng, X.; Liang, Y.; He, M.; Geng, M.; Huang, Y.; Teng, F.; Li, Y. *Innov. Food Sci. Emerg. Technol.* **2022**, *79*, 103049.
- 12. Choi, J.-I.; Kim, H.-J. *Carbohydr. Polym.* **2013**, *97*, 358–362.
- 13. Jamshidi, M.; Barzegar, M.; Sahari, M. A. *Int. Food Res. J.* **2014**, *21*, 1289–1296.
- 14. Variyar, S.; Limaye, P.; Sharma, A. *J. Agric. Food Chem.* **2004**, *52*, 3385–3388.
- 15. Tewari, K.; Kumari, S.; Vinutha, T.; Singh, B.; Dahuja, A. *J. Radioanal. Nucl. Chem.* **2014**, *303*, 2041–2051.
- 16. Sajilata, M. G.; Singhal, R. S. *Radiat. Phys. Chem.* **2006**, *75*, 297–300.
- 17. Vital, A. C.; Croge, C.; Felix da Silva, D.; Araújo, P.; Gallina, M.; Matumoto-Pintro, P. *J. Food Sci. Technol.* **2018**, *55*.
- 18.Mukhtar, R.; Shah, A.; Noor, N.; Gani, A.; Ahmed Wani, I.; Ahmad Ashwar, B.; Masoodi, F. A. *Int. J. Biol. Macromol.* **2017**, *104*, 1313–1321





Green synthesis of silver nanoparticles using *Caesalpinia pulcherrima* flower extracts: Evaluating their phytochemicals and antioxidant activity

Neethiyarasu Dhino Dhithesh, Mathi Kandiah* School of Science, BMS Campus, 591, Galle Road, Colombo 06, Sri Lanka *E-mail: mathi@bms.edu.lk

Abstract:

The contemporary advancement of nanobiotechnology, where nanoparticles are green synthesised using biological bottom-up approach to overcome the limitations of conventional methods has gained attention in numerous fields, including medicine. This study aimed to green synthesize silver nanoparticles (AgNPs) using five varieties of Caesalpinia pulcherrima (CP) (Orange, Yellow, Red, Pink Yellow and Pink) in an environmentally friendly and sustainable approach and determine their antioxidant, photocatalytic and antibacterial properties. The AgNPs were synthesised at optimum temperature at 90 °C for 60 minutes and were characterized using UV-visible spectrum, that showed a plasmon resonance peak between 400-460 nm. Transmission electron microscopy analysis revealed the synthesised CP AgNPs are spherical in shape and 20 nm in size. The biosynthesized AgNPs could be used in treating free radical-mediated diseases and multidrug resistant bacterial infections and minimize environmental pollution by degrading organic dyes to non-toxic intermediate compounds.

1. Introduction

Nanotechnology is a growing field of science and engineering concerned with the study, manipulation, and application of materials with at least one dimension in the nanoscale (1-100 nm) to fabricate materials, systems, and technologies with fundamentally distinct traits and functionalities. 1 It allows the utilization of nanoparticles with unique physical, chemical, optical, and electrical properties in a wide array of fields, placing them at the forefront of technology.² Asghari et al. nanobiotechnology as a branch of study that investigates the unique physicochemical and biological features of nanoparticles and their applicability in various fields, including health and agriculture (Figure 1).3 Using physical, biological chemical. and techniques. nanoparticles (NPs) are fabricated. Physical and chemical approaches are stereotypical approaches that have drawbacks. (Figure 2). These methods consume high energy, form hazardous by-products, utilize compounds, and produce substandard products with less purity. The limitations are overborne by biological techniques or "green synthesis".

Green synthesis is the eco-friendly technique of NP synthesis utilizing biological samples such as plants, microbes, and fungi. Plant green synthesis has numerous advantages, including fast, high-yield production, low cost, and non-toxicity.^{7,8} AgNPs synthesis utilizes water,

maintaining a non-toxic, environmentally friendly approach over organic solvents in plant extracts.⁹

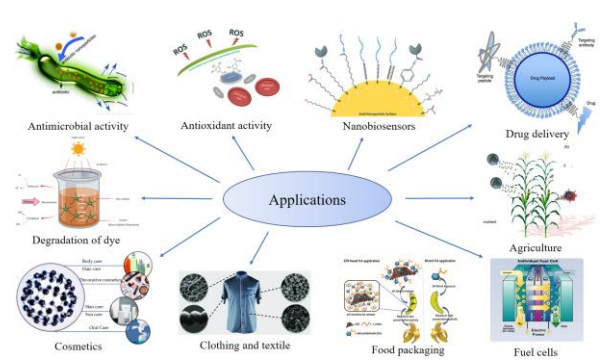


Figure 1. Applications for nanotechnology

Silver nanoparticles (AgNPs) are fabricated in this research due to their unique properties; unlike zinc, gold, and copper, silver has distinctive properties such as thermal and electrical conductivity, chemical stability, and catalytic activity. Due to their size and high surface-to-volume ratios, nanoparticles exhibit different physical and chemical properties than their conventional counterparts, including biological traits, electrical and thermal conductivity, and photocatalytic activity. Furthermore, AgNPs demonstrate surface plasmon resonance (SPR) and are highly resistant to bacteria, rendering them excellent for biological application. 12





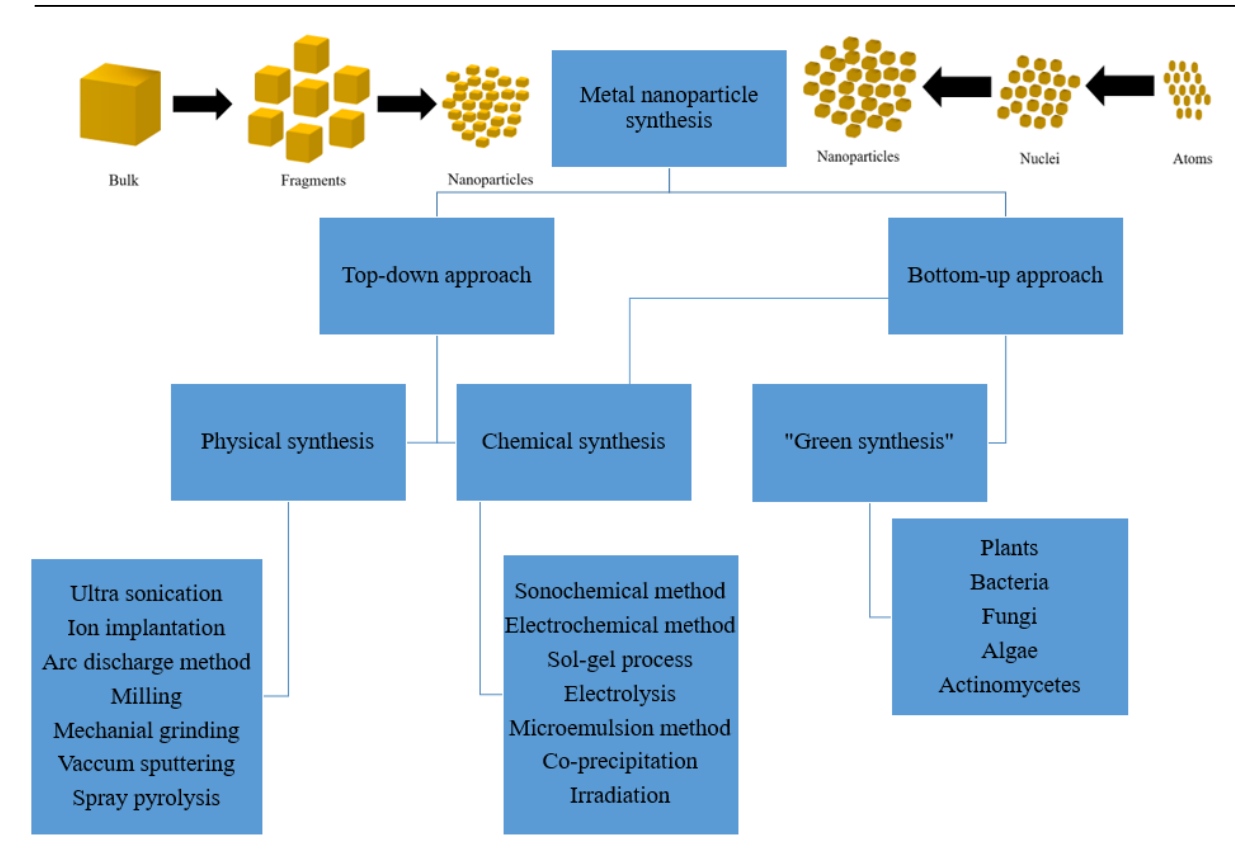


Figure 2. The approaches for nanoparticle synthesis

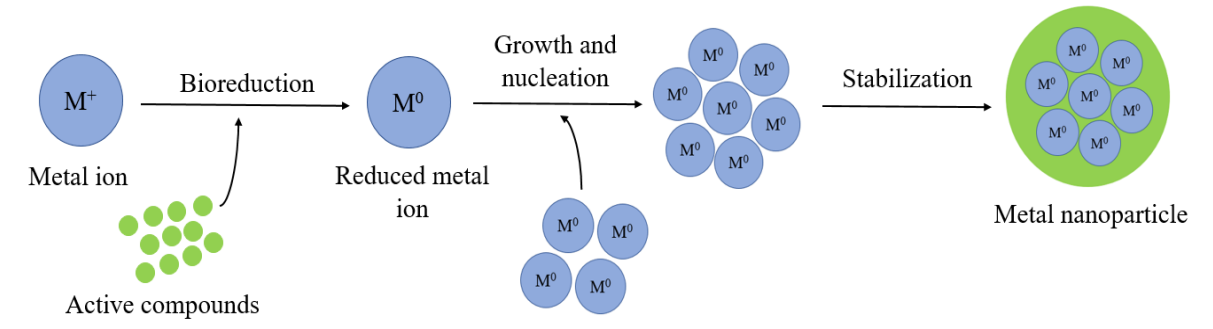


Figure 3. Mechanism of AgNPs green synthesis

In green synthesis of metal nanoparticles (MNP), a metal solution is added to a biological extract and, with the help of active compounds present in the biological sample at different conditions such as concentrations, pH, temperature, pressure, and time, the bio reduction occurs.

During the reduction process, the monovalent or divalent metal ions are reduced to a zero-valent state by the present phytochemicals and other factors including temperature, pH, pressure, and reaction time. This is accompanied by nucleation and growth and

eventually stabilization, where phytochemicals function as capping agents and stabilize the nucleation, forming nanoparticles (Figure 3). 13,14

In this research, *Caesalpinia pulcherrima* (CP) flower extracts were used to synthesize AgNPs. CP, also known as peacock flower, is a member of the Fabaceae family of legumes (Figure 4). Traditional medicinal and herbal advantages from various parts of China have been well recognized across the world. It is used for treating fevers, ulcers, asthma, tumors, and skin







Figure 4. Caesalpinia pulcherrima of Fabaceae family (Sharma, Goyal and Bhat, 2013)

diseases. They are known for their medicinal properties against malaria, cholera, and bronchitis and have been used due to their anti-inflammatory, antioxidant, analgesic, antidiabetic, and anthelmintic properties. Studies identify that CP is rich in phenols that have high antioxidants and antibacterial properties. ^{14–16} Floral waste is produced when *Caesalpinia pulcherrima* is used as an ornamental plant. NP synthesis using floral waste prevents wastage of resources. Khatami et al reported the similar research using hay to synthesize AgNPs. ¹⁷

Antioxidants, found naturally in the body or from food, protect against harmful oxidants. When oxidants like ROS, free radicals, and RNS overwhelm antioxidants, oxidative stress occurs, damaging cells and increasing disease risk. Research shows that nanoparticles from antioxidant-rich natural sources can replace toxic synthetic antioxidants like BHT-Q and BHA, which have been linked to health issues such as allergies, DNA damage, and liver cancer, supporting the move toward green synthesis (Figure 5). ^{18–20}

The objectives of this study are to green synthesis AgNPs from five different CP flower extracts and assess their antioxidant, photocatalytic, and antibacterial properties. Testing for total flavonoid content, total phenolic content, total antioxidant capacity, 2,2-diphenyl-1-picrylhydrazyl (DPPH) scavenging activity and median inhibition concentration (IC₅₀) tests will be conducted to assess antioxidant activity.

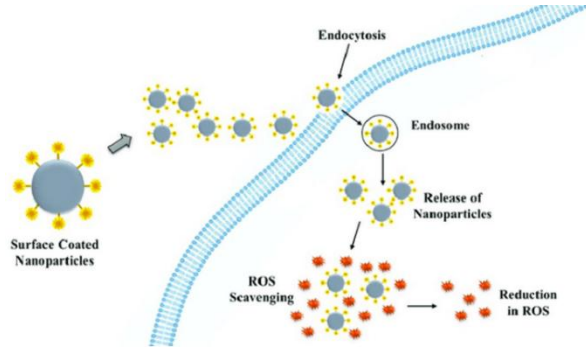


Figure 5. Antioxidant mechanism of nanoparticles (adapted from Bhardwaj *et al.*, 2020)

2. Methodology

All procedures followed good laboratory practice and safety protocols (COSHH and bioCOSHH).

2.1 Sample collection and preparation Five varieties of *Caesalpinia pulcherrima* (CP) flowers were collected from home gardens in Colombo, Sri Lanka (Figure 6). Flowers were air-dried for 10 days, ground, and 2 g was boiled with 50 mL distilled water for 10 minutes. Extracts were filtered and stored at 4 °C.

2.2 Phytochemical analysis

Conducted as outlined in Table 1.

2.3 Green synthesis of AgNPs

1 mL of extract was mixed with 9 mL of 1 mM AgNO₃ and incubated at 90 °C for 60 minutes. Absorbance was measured at 320–520 nm.

2.4 Optimization of AgNPs

Synthesis was optimized at various temperatures and times; absorbance was recorded at 320–520 nm.

2.5 Dilution

Extracts and AgNPs were diluted at a 1:15 ratio and stored at 4 °C.

2.6 TEM Analysis

RF AgNPs were centrifuged, dried at 40 °C, and sent to SLINTEC for TEM analysis.

2.7 TFC, TPC, TAC determination

TFC: AlCl₃ colorimetric assay, results in μg QE/100 g. *TPC*: Folin-Ciocalteu assay, results in g GAE/100 g. *TAC*: Phosphomolybdenum assay, results in g AAE/100 g. All assays were in triplicate.

2.8 DPPH scavenging and IC₅₀.

DPPH assay assessed antioxidant activity at 517 nm. IC50 was determined using five







Figure 6. Different varieties of Caesalpinia pulcherrima flowers used in AgNPs synthesis

Table 1. Procedures for the phytochemical analysis (Roghini and Vijayalakshmi, 2018).

Phytochemical	Procedure	Expected positive results
Tannins	2 mL of 5% FeCl ₃ was added to 1 mL of the extract	Formation of greenish black or dark blue colour
Terpenoids	2 mL of Chloroform and 2 mL of H ₂ SO ₄ was added to 0.5 mL of the extract	Reddish brown colour Formation at the interface
Saponins	2 mL of the extract and 2 mL of distilled water was added to a graduated cylinder and shook well for 15 minutes	Formation of 1cm layer of foam
Carbohydrate	1 mL of Molisch's reagent was added to 2 mL of extract and followed by addition of few drops of concentrated H ₂ SO ₄	Formation of reddish or purple ring
Proteins	Few drops of 0.2% ninhydrin were added to 2 mL of the extract	Formation of mauve or purple colour
Steroids	1 mL of Chloroform was added to 1 mL of the extract, followed by the addition of few drops of H_2SO_4	Formation of brown ring
Anthraquinones	Few drops of 10% NH ₄ OH was added to 1 mL of extract	Pink coloured precipitate formation





Table 2.	Phytochemical Phytochemical	Lanalysis	test results
I abic 2.	1 Hy to chichine a	i amary sis	test results

Phytochemical	OF	YF	RF	PYF	PF	Results
Tannins	V	V	V	V	V	
Terpenoids	$\sqrt{}$	$\sqrt{}$	$\sqrt{}$	\checkmark	$\sqrt{}$	
Saponins	$\sqrt{}$	\checkmark	\checkmark	\checkmark	$\sqrt{}$	
Carbohydrate	$\sqrt{}$	$\sqrt{}$	$\sqrt{}$	$\sqrt{}$	$\sqrt{}$	
Proteins	×	×	×	×	×	
Steroids	×	×	×	×	×	
Anthraquinone s	×	×	×	×	×	

concentrations (20–100%) and equation (1).

Inhibition (%) =
$$\left(Acontrol \left(\frac{Asample}{Acontrol} \right) \right) x \ 100$$
 (1)

3. Results

3.1 Phytochemical Analysis

The colour change indicated the presence of phytochemicals in the extract (Table 2). According to the results obtained the presence of carbohydrates, tannins, saponins and terpenoids were confirmed.

3.2 Green synthesis of AgNPs

The formation of AgNPs was observed initially by the change from pale yellowish colour to reddish-brown colour in all the samples after incubated at 90 °C for 60 minutes. as shown in Figure 7.

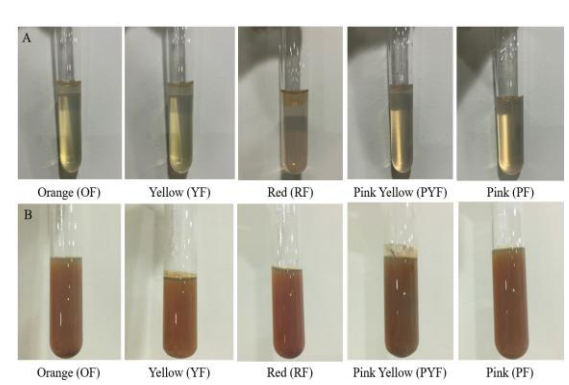


Figure 7. Green synthesis of AgNPs. (A) CP water extracts mixed with silver nitrate before incubation and (B) AgNPs produced after incubation for 60 minutes at 90°C.

3.3 Characterization of AgNPs

The peaks at 420 nm and 440 nm in the UV-Vis spectrum confirmed the formation of AgNPs for all the five varieties (Figure 8).





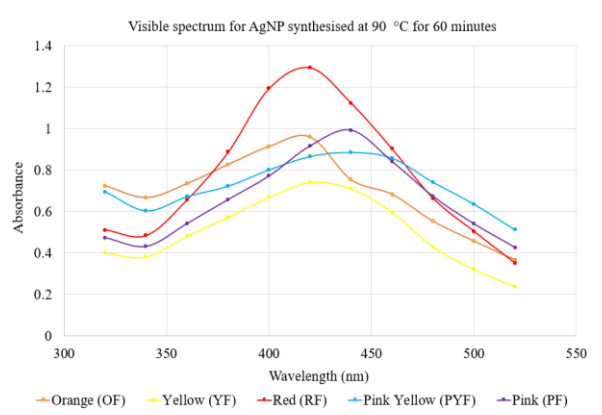


Figure 8. Visible spectrum for AgNPs synthesised at 90°C for 60 minutes.

Transmission Electron Microscope analysis reveals the AgNPs to be spherical and around 40 nm in size (Figure 9).

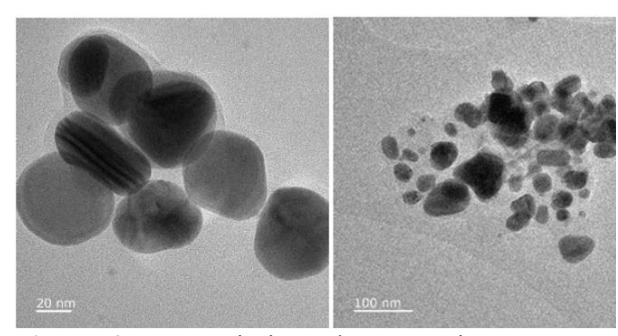


Figure 9. Transmission Electron Microscope images of RF AgNPs

3.4 Determination of antioxidant activity3.4.1 Total flavonoid content (TFC)

TFC analysis indicated that AgNPs contained has higher TFC than the extracts and RF AgNPs has the highest TFC (Figure 10). The significance difference between extracts and AgNPs was compared by One-way ANOVA.

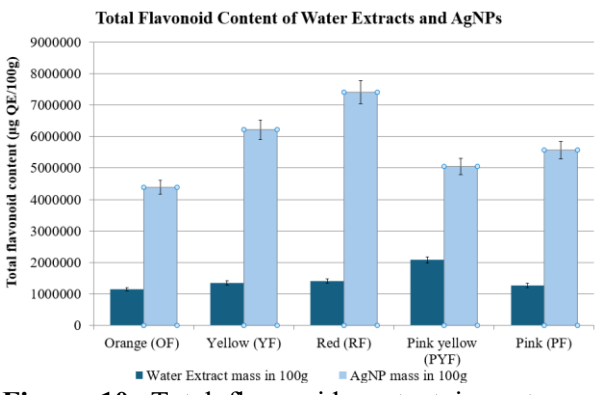


Figure 10. Total flavonoid content in water extracts and AgNPs

3.4.2 Total phenolic content (TPC)

TPC analysis indicated that AgNPs contained have higher TPC than the extracts on average and OF, YF and PYF AgNPs have the highest TPC (Figure 11). The significance difference between extracts and AgNPs was compared by One-way ANOVA.

3.4.3 Total antioxidant capacity (TAC)

TAC analysis indicated that AgNPs contained has higher TAC than the extracts and PYF AgNPs have the highest TAC (Figure 12). The significance difference between extracts and AgNPs was compared by One-way ANOVA.

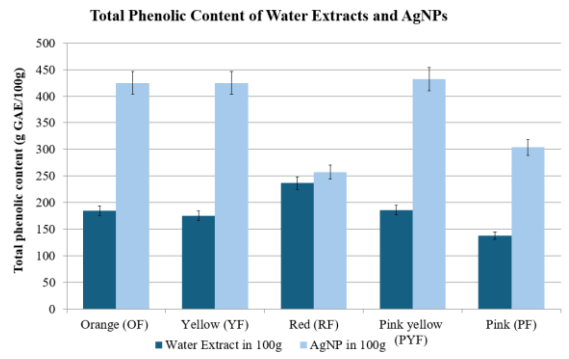


Figure 11. Total phenolic content in water extracts and AgNPs

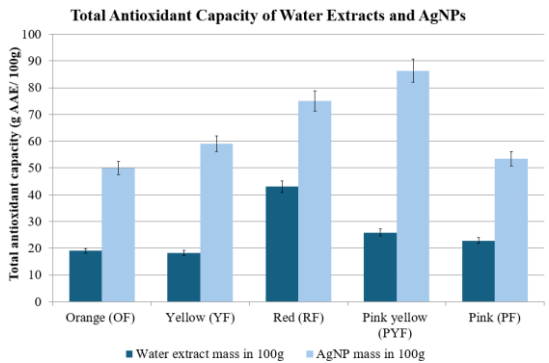


Figure 12. Total antioxidant capacity in water extracts and AgNPs

3.4.4 Determination of DPPH scavenging activity

AgNPs when compared to the extracts showed similar levels of % DPPH scavenging activity excluding RF and PYF (Figure 13).





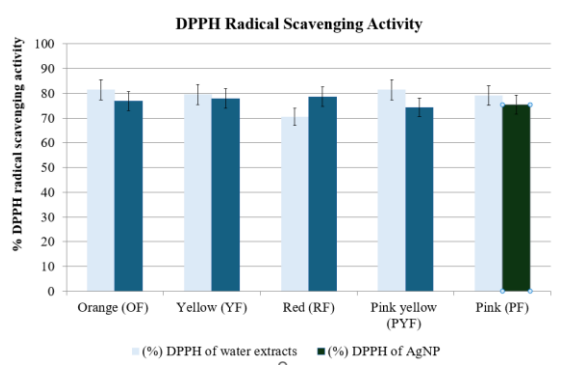


Figure 13. % DPPH scavenging activity of water extracts and AgNPs

3.4.5 Determination of median inhibitory concentration (IC₅₀) of DPPH

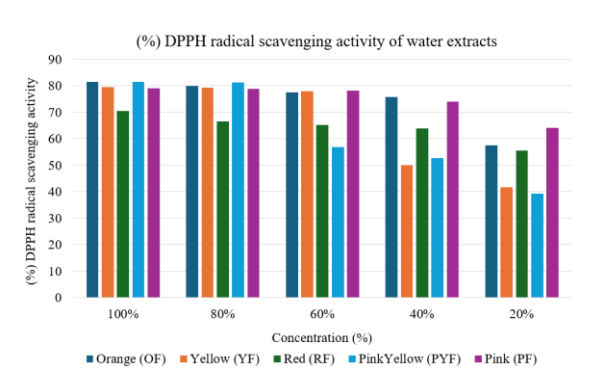


Figure 14. IC₅₀ of water extracts

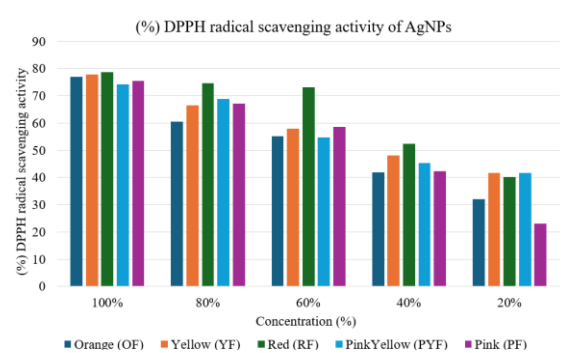


Figure 15. IC₅₀ of AgNPs

Table 3. IC₅₀ of water extracts and AgNPs

		2
Sample	IC ₅₀ of water	IC ₅₀ of AgNPs
Sumpre	extracts (%)	(%)
OF	0.34	0.54
YF	0.30	0.42
RF	0.28	0.32
PYF	0.38	0.44
PF	0.84	0.55

The IC_{50} of PF AgNPs was lower than its extracts, which indicates a higher antioxidant capacity (Table 3) (Figures 14–15).

4. Conclusion

This study successfully demonstrated the green synthesis of silver nanoparticles (AgNPs) using five varieties of Caesalpinia pulcherrima flowers, offering an eco-friendly and sustainable alternative to conventional methods. The synthesized AgNPs exhibited strong antioxidant, activities, with superior performance compared to crude water extracts. Characterization confirmed their nanoscale size, spherical shape, and semiconductor properties. These findings highlight the potential of CP-based AgNPs in biomedical and environmental applications, particularly for treating oxidative stress-related diseases, Therefore, a detailed understanding of the properties of each variety is facilitated by these research findings, allowing a better alleviation of the dilemma faced by humankind and the environment.

Acknowledgements

The authors thank BMS for funding.

Research Ethics / Declarations

Authors declare no conflict of interest.

References

- 1. Nasrollahzadeh, M.; Mahmoudi-Gom Yek, S.; Motahharifar, N.; Ghafori Gorab, M. *The Chemical Record* **2019**, *19* (12), 2436–2479.
- 2. Khan, I.; Saeed, K.; Khan, I. *Arabian Journal of Chemistry* **2019**, *12* (7), 908–931.
- 3. Asghari, F.; Jahanshiri, Z.; Imani, M.; Shams-Ghahfarokhi, M.; Razzaghi-Abyaneh, M. Antifungal Nanomaterials: Synthesis, Properties, and Applications. In *Nanobiomaterials in Antimicrobial Therapy*; Grumezescu, A. M., Ed.; William Andrew Publishing, 2016; pp 343–383.
- 4. Ying, S.; Guan, Z.; Ofoegbu, P. C.; Clubb, P.; Rico, C.; He, F.; Hong, J. *Environmental Technology & Innovation* **2022**, *26*, 102336.
- 5. Dikshit, P. K.; Kumar, J.; Das, A. K.; Sadhu, S.; Sharma, S.; Singh, S.; Gupta,





- P. K.; Kim, B. S. *Catalysts* **2021**, *11* (8), 902.
- 6. Osman, A. I.; Zhang, Y.; Farghali, M.; Rashwan, A. K.; Eltaweil, A. S.; Abd El-Monaem, E. M.; Mohamed, I. M. A.; Badr, M. M.; Ihara, I.; Rooney, D. W.; Yap, P.-S. *Environ Chem Lett* **2024**, 22(2), 841–887.
- 7. Ahmad, S.; Munir, S.; Zeb, N.; Ullah, A.; Khan, B.; Ali, J.; Bilal, M.; Omer, M.; Alamzeb, M.; Salman, S. M.; Ali, S. *International Journal of Nanomedicine* **2019**, *14*, 5087–5107.
- 8. Moodley, J.; Cairncross, L.; Naiker, T.; Constant, D. *BMC Cancer* **2018**, *18*(1), 312.
- 9. Beyene, H. D.; Werkneh, A. A.; Bezabh, H. K.; Ambaye, T. G. *Sustainable Materials and Technologies* **2017**, *13*, 18–23.
- 10. Ahmed, T.; Ogulata, R. T. *Journal of Natural Fibers* **2022**, *19*(14), 8463–8484.
- Gong, X.; Jadhav, N. D.; Lonikar, V. V.; Kulkarni, A. N.; Zhang, H.; Sankapal, B. R.; Ren, J.; Xu, B. B.; Pathan, H. M.; Ma, Y.; Lin, Z.; Witherspoon, E.; Wang, Z.; Guo, Z. Advances in Colloid and Interface Science 2024, 323, 103053.
- 12. Mlalila, N. G.; Swai, H. S.; Hilonga, A.; Kadam, D. M. *Nanotechnology, Science and Applications* **2016**, *10*, 1–9.
- 13. Shah, A. D.; Langenberg, C.; Rapsomaniki, E.; Denaxas, S.; Pujades-Rodriguez, M.; Gale, C. P.; Deanfield, J.; Smeeth, L.; Timmis, A.; Hemingway, H. *The Lancet Diabetes & Endocrinology* **2015**, *3*(2), 105–113.
- Torres, A.; Niederman, M. S.; Chastre, J.; Ewig, S.; Fernandez-Vandellos, P.; Hanberger, H.; Kollef, M.; Li Bassi, G.; Luna, C. M.; Martin-Loeches, I.; Paiva, J. A.; Read, R. C.; Rigau, D.; Timsit, J. F.; Welte, T.; Wunderink, R. European Respiratory Journal 2017, 50(3), 1700582.
- 15. Moteriya, P.; Chanda, S. *Journal of Genetic Engineering and Biotechnology* **2018**, *16* (1), 105–113.
- 16. Nadar Rajivgandhi, G.; Chackaravarthi, G.; Ramachandran, G.; Kanisha Chelliah, C.; Maruthupandy, M.; Alharbi, M. S.; Alharbi, N. S.; Khaled, J.

- M.; Li, W.-J. *Journal of King Saud University Science* **2022**, *34* (2), 101795.
- 17. Khatami, M.; Sharifi, I.; Nobre, M. A. L.; Zafarnia, N.; Aflatoonian, M. R. *Green Chemistry Letters and Reviews* **2018**, *11*(2), 125–134.
- 18. Nagaich, U.; Gulati, N.; Chauhan, S. *Journal of Pharmaceutics* **2016**, *2016*(1), 7141523.
- 19. Nimse, S. B.; Pal, D. *RSC Adv.* **2015**, *5*(35), 27986–28006.
- Lourenço, S. C.; Moldão-Martins, M.;
 Alves, V. D. Molecules 2019, 24(22), 4132.





Sponsors













































